

Fatigue-fluage du Polyamide 6,6 renforcé

Ilan Raphael

▶ **To cite this version:**

Ilan Raphael. Fatigue-fluage du Polyamide 6,6 renforcé. Autre [cond-mat.other]. École Nationale Supérieure des Arts et Métiers, 2019. Français. ⟨NNT : 2019ENAM0048⟩. ⟨tel-02612939v1⟩

HAL Id: tel-02612939

https://pastel.hal.science/tel-02612939v1

Submitted on 19 May 2020 (v1), last revised 22 May 2020 (v2)

HAL is a multi-disciplinary open access archive for the deposit and dissemination of scientific research documents, whether they are published or not. The documents may come from teaching and research institutions in France or abroad, or from public or private research centers.

L'archive ouverte pluridisciplinaire **HAL**, est destinée au dépôt et à la diffusion de documents scientifiques de niveau recherche, publiés ou non, émanant des établissements d'enseignement et de recherche français ou étrangers, des laboratoires publics ou privés.



HAL Authorization

2019-ENAM-0048

ParisTech
INSTITUT DES SCIENCES ET TECHNOLOGIES
PARIS INSTITUTE OF TECHNOLOGY

Arts et Métiers Institute of Technology

École doctorale n° 432 : Sciences des Métiers de l'Ingénieur

Doctorat ParisTech

THÈSE

pour obtenir le grade de docteur délivré par

l'École Nationale Supérieure des Arts et Métiers

Spécialité doctorale "Mécanique des Matériaux"

présentée et soutenue publiquement par

Ilan RAPHAEL

le 5 décembre 2019

Cyclic-creep of reinforced Polyamide 6,6 under fatigue loading

Directeurs de thèse : **Nicolas SAINTIER & Lucien LAIARINANDRASANA**
Co-encadrant de thèse : **Gilles ROBERT**

Jury

C. NADOT-MARTIN	Institut Pprime	Présidente
A. BERNASCONI	Politecnico di Milano	Rapporteur
C. PLUMMER	EPFL	Rapporteur
J-L. BOUVARD	CEMEF - Mines ParisTech	Examinateur
B. HUNEAU	École Centrale de Nantes	Examinateur
L. LAIARINANDRASANA	CdM - Mines ParisTech	Examinateur
N. SAINTIER	Arts et Métiers ParisTech	Examinateur
G. ROBERT	Solvay Performance Polyamides	Examinateur

Arts et Métiers ParisTech, Centre de Bordeaux-Talence
I2M, UMR CNRS 5295, Département DuMAS
Esplanade des Arts et Métiers 33400 Talence, France

THESE

¡ Vive hoy !
¡ Arriesga hoy !
¡ Hazlo hoy !
¡ No te dejes morir lentamente !
¡ No te impidas ser feliz !

Pablo Neruda

Penguins never give up.

David Attenborough

Contents

Contents 1

Acknowledgements 1

Introduction 3

1 State of the Art 7

1.1 Reinforced polyamide 6,6 . . . 7

1.1.1 A composite material . . . 7

1.1.1.1 History and usage . . . 7

1.1.1.2 Manufacturing process . . . 8

1.1.2 A semi-crystalline matrix . . . 9

1.1.2.1 Global description . . . 9

1.1.2.2 Formation and structure of the spherulite . . . 10

1.1.2.3 Spherulite observation . . . 11

1.1.2.4 The shish-kebab structure . . . 13

1.1.2.5 Crystallinity . . . 13

1.1.2.6 Glass transition temperature . . . 14

1.1.3 Reinforcements for an improved mechanical performance . . . 14

1.1.3.1 Short glass fibers . . . 14

1.1.3.2 Microstructure induced by the injection molding . . . 15

1.1.3.3 On the importance of the fiber-matrix interface . . . 15

Adhesion at the interface . . . 16

Spherulitic structures along fibers . . . 16

1.2 Macroscopic mechanical properties . . . 17

1.2.1 Mechanical anisotropy . . . 17

1.2.1.1 Quasi-static tensile tests . . . 17

1.2.1.2 Fatigue testing . . . 18

1.2.2 Effect of the mechanical loading . . . 20

1.2.2.1 Mean stress effect . . . 20

1.2.2.2 Frequency effect . . . 20

1.2.3 Environmental effects . . . 22

1.2.3.1 Temperature . . . 22

1.2.3.2 Relative humidity . . . 22
1.2.3.3 Other types of aging . . . 23
1.2.4 Influence of the spherulite size . . . 24
1.2.5 Notches and geometrical defects . . . 25
1.2.6 Cyclic creep . . . 28
1.3 Fatigue life assessment . . . 30
1.3.1 Mechanical parameters under cyclic loading . . . 30
1.3.2 Life assessment criteria . . . 31
1.3.2.1 Stress-based approach . . . 31
1.3.2.2 Strain-based approach . . . 34
1.3.2.3 Energy-based approach . . . 34
1.3.2.4 Modulus-based approach . . . 35
1.3.2.5 Cyclic strain rate-based approach . . . 35
1.4 Damage mechanisms . . . 38
1.4.1 Experimental techniques . . . 38
1.4.2 Damage mechanisms in the neat polymer . . . 38
1.4.2.1 Quasi-static tensile tests . . . 38
1.4.2.2 Fatigue tensile tests . . . 39
1.4.2.3 Creep tests . . . 40
1.4.3 Damage mechanisms in the composite material . . . 41
1.4.3.1 Quasi-static tensile tests . . . 41
1.4.3.2 Fatigue tensile tests . . . 42
1.5 Numerical modeling . . . 45
1.5.1 Through process modeling . . . 45
1.5.2 Macroscopic mechanical modeling . . . 45
1.5.2.1 Constitutive modeling . . . 45
1.5.2.2 The GTN damage model . . . 47
1.5.3 Modeling at the microscopic scale . . . 48
1.5.4 Micro-mechanical modeling . . . 48
1.5.4.1 Microstructure modeling: context and methods . . . 49
1.5.4.2 Microstructure modeling: results . . . 50
1.5.4.3 Spherulite modeling . . . 53
Growth modeling . . . 53
Mechanical modeling . . . 53
1.6 Bibliography . . . 55

2 Materials and methods **67**
2.1 Testing specimens . . . 67
2.1.1 Material . . . 67
2.1.2 Microstructure of the composite . . . 67
2.1.3 Spherulitic microstructure . . . 69
2.1.4 Smooth specimen geometry . . . 69
2.1.5 Notched specimens . . . 70
2.1.6 Specimen conditioning . . . 70
2.2 Experimental set-up . . . 74

2.2.1 In-lab testing . . . 74
2.2.1.1 Quasi-static testing . . . 74
2.2.1.2 Fatigue testing . . . 74
2.2.1.3 Local strain measurements using DIC . . . 75
2.2.1.4 Definitions . . . 76
2.2.2 In-situ synchrotron testing . . . 77
2.3 Observation techniques . . . 79
2.3.1 Transmission cross-polarized light microscopy . . . 79
2.3.2 Scanning Electron Microscopy . . . 80
2.3.3 Micro-tomography . . . 80
2.3.4 Atomic Force Microscopy . . . 81
2.3.5 Digital Image Correlation . . . 81
2.4 Bibliography . . . 83

3 Voiding mechanisms at the micro-scale 85
3.1 Further study of the usual damage mechanisms . . . 85
3.1.1 Fiber failure . . . 86
3.1.2 Cavitation . . . 87
3.1.3 Debonding . . . 89
3.2 Spherulitic damage . . . 91
3.2.1 Specimens geometry and loading conditions . . . 91
3.2.2 Tomographic observations on short fatigue cracks . . . 91
3.2.3 Fractography analysis of fatigued PA66 specimens . . . 96
3.2.3.1 Spherulite observation . . . 96
3.2.3.2 Spherulite orientation . . . 100
3.2.4 On the importance of the spherulite nucleus . . . 101
3.2.5 Fractography analysis of fatigued composite specimens . . . 104
3.3 Bibliography . . . 106

4 Fatigue behavior at the macro-scale 107
4.1 Durability criteria for smooth specimens . . . 107
4.1.1 A cyclic strain rate based criterion . . . 107
4.1.2 Effect of water-intake . . . 108
4.1.3 Improving the strain-rate based durability criterion . . . 108
4.1.3.1 Experimental method . . . 109
4.1.3.2 Mixed criterion: anelastic energy and cyclic strain rate 109
4.1.3.3 Identification on a smaller database . . . 112
4.1.3.4 Further remarks on the mixed criterion . . . 115
4.1.3.5 Conclusion on the mixed criterion . . . 116
4.2 Experimental study on notched specimens . . . 116
4.2.1 Quasi-static testing . . . 116
4.2.1.1 Unreinforced PA66 . . . 116
4.2.1.2 Reinforced PA66 . . . 119
4.2.2 Fatigue testing . . . 119
4.2.2.1 Unreinforced PA66 . . . 119

4.2.2.2 Reinforced PA66 . . . 121
4.2.3 Durability criteria . . . 125
4.2.4 Further comments about the criteria . . . 127
4.3 F.E. analyses . . . 129
4.3.1 F.E. models . . . 129
4.3.2 Parametric identification for constitutive models . . . 130
4.3.2.1 Parameters' identification for quasi-static tensile test . . . 130
4.3.2.2 Adjustments for fatigue loading . . . 132
4.3.3 Cyclic strain rate . . . 133
4.3.3.1 Global strain rate . . . 133
Unreinforced PA66 . . . 133
Reinforced PA66 . . . 133
4.3.3.2 Local cyclic strain rate . . . 133
Unreinforced PA66 . . . 136
Reinforced PA66 . . . 137
4.3.4 GTN model and void growth . . . 139
4.3.4.1 Parameters GTN model . . . 139
4.3.4.2 Damage growth . . . 139
Unreinforced PA66 . . . 139
Reinforced PA66 . . . 141
4.3.5 Application of the criterion . . . 141
4.4 Bibliography . . . 143

5 Microstructure modeling **145**
5.1 FFT modeling . . . 145
5.1.1 Method . . . 145
5.1.1.1 Microstructure segmentation . . . 145
5.1.1.2 Considered volume . . . 146
5.1.1.3 Periodic microstructure . . . 146
5.1.1.4 Material model . . . 147
5.1.1.5 Parameter identification . . . 148
5.1.1.6 Fiber-matrix interface . . . 148
5.1.1.7 Loadings . . . 149
5.1.2 FFT modeling, results and analysis . . . 150
5.1.2.1 Material behavior . . . 150
Strain rate in the matrix . . . 150
Comparison with the composite material . . . 150
Distribution of the local mechanical fields in the matrix . . . 151
5.1.2.2 Main damage mechanisms . . . 152
Fiber failure . . . 153
Damage at fiber end . . . 153
Crazing . . . 155
Cavitation . . . 155
5.2 FE modeling . . . 161
5.2.1 Method . . . 161

5.2.1.1 Microstructure segmentation and meshing 161
5.2.1.2 Constitutive model 163
5.2.1.3 Loading 163
5.2.2 FE modeling, results and analysis 163
5.2.2.1 Cyclic loading 163
5.2.2.2 Matrix damage growth 164
Note on the damage model 164
Localization and growth of damage 164
5.3 Bibliography 167

6 Outlooks and conclusion **169**
6.1 Outlooks 169
6.1.1 At the macro-scale 169
6.1.1.1 Notched specimens 169
6.1.1.2 Multi-axial loading 169
6.1.1.3 Towards other materials 170
6.1.1.4 Adaptation for industrial use 170
6.1.1.5 Calibration of the damage model 170
6.1.2 At the micro-scale 171
6.1.2.1 Measuring local strains 171
6.1.2.2 Influence of the spherulite morphology 171
6.1.2.3 Microstructure modeling 172
6.1.2.4 Tomography, a non-destructive tool? 173
6.1.3 Towards the nano-scale 174
6.1.3.1 Molecular dynamics, a quick review 174
6.1.3.2 Why it matters... 174
6.1.3.3 ... And what it could bring 175
6.2 General conclusion 175
6.3 Bibliography 177

7 Résumé étendu **179**
7.1 Introduction 179
7.2 État de l'Art 181
7.2.1 Polyamide 6,6 renforcé 181
7.2.2 Propriétés mécaniques 182
7.2.2.1 Anisotropie du matériau 182
7.2.2.2 Chargement mécanique 182
7.2.2.3 Effet de l'environnement 182
7.2.2.4 Influence de la taille des sphérolites 183
7.2.2.5 Effet d'entaille 183
7.2.2.6 Fluage cyclique 184
7.2.3 Calculs de durée de vie 184
7.2.4 Mécanismes d'endommagement 185
7.3 Approfondissement des mécanismes d'endommagement 187
7.3.1 Endommagement sphérolitique 187

7.3.2 Structure de la sphérolite orientée . . . 188
7.3.3 Retour au matériau composite . . . 189
7.4 Échelle Macroscopique . . . 189
7.4.1 Critère mixte . . . 189
7.4.2 Étude expérimentale des éprouvettes entaillées . . . 191
7.4.3 Modélisation par Éléments-Finis . . . 191
7.4.3.1 Le modèle . . . 191
7.4.3.2 Vitesse de déformation cyclique et critère . . . 193
7.4.3.3 Modèle GTN . . . 194
7.5 Échelle Microscopique . . . 195
7.5.1 Calculs FFT . . . 195
7.5.1.1 Mise en place . . . 195
7.5.1.2 Champs mécaniques dans la matrice . . . 196
7.5.1.3 Principaux mécanismes d'endommagement . . . 196
7.5.1.4 Cas de la cavitation . . . 197
7.5.2 Calculs Éléments-Finis . . . 197
7.5.2.1 Mise en place . . . 197
7.5.2.2 Résultats . . . 198
7.6 Conclusion . . . 198

A Processing of tomographic data **I**
A.1 The tomographic image . . . I
A.1.1 A 3D volume . . . I
A.1.2 Information and artifacts . . . II
A.2 Usual filtering and segmentation tools . . . II
A.2.1 Denoising . . . II
A.2.2 Thresholding . . . III
A.2.3 Morphological operations . . . III
A.3 Analysis tools . . . IV
A.3.1 Quantitative analysis . . . IV
A.3.2 Toward numerical modeling . . . IV
A.4 Bibliography . . . V

B Molecular dynamics **VII**
B.1 The force field . . . VII
B.2 The PE model . . . IX
B.3 For a PA66 model . . . IX
B.3.1 A full model of the polymer chain . . . IX
B.3.2 A coarse-grain approach . . . X
B.4 The time-scale in MD calculations . . . X
B.5 The choice of boundary conditions . . . XI
B.6 Bibliography . . . XI

List of Figures **XIII**

Acknowledgements

I would first like to express my deepest gratitude to Andrea Bernasconi and Christopher Plummer for their thorough examination of the manuscript and the highly interesting discussion at the defense.

My most sincere thanks also go to Carole Nadot-Martin for presiding the jury as well as to Jean-Luc Bouvard and Bertrand Huneau for the passionate discussion. All of you took the time and effort to examine and debate this work, and your remarks and comments helped improve its quality.

Beginning a PhD is like starting a long mountain hike.

As for any challenging adventure, you need the advices from the best guides you can get. I wish to warmly thank my guides for this journey, Nicolas Saintier and Lucien Laiarinandrasana, for their expert advices. This extends to the most incredible industrial sponsor, Gilles Robert, for his trust and support during the past three years. Without you three, this work would not have been so rewarding nor have produced all these results.

For this kind of adventure you also need to have a good team to travel with: Alexandre Gaspard Messager and Bastien Balthazar Vayssette, your daily support, your crazy sense of humor and your friendship made this experience an unforgettable one.

A special mention for Mathias Cousté who I had the pleasure to work with during his internship at the lab. Good luck with your own PhD!

From the nicest of welcomes I received in 2016 by the old crew Héloïse Rolland, Mohand Ouarabi and Luis Pallarès, to those who will still be the trail in 2020 - Camille Rousseau, Louise Le Barbenchon, Marie Pirotais - I have met some incredible comrades!

To the Italian family, Lorenzo Cappelli, Pietro Del Sorbo and Enrico Panietteri, grazie mille per tutti!

I also have to mention the numerous ambitious projects of Simon Dousset, that greatly contributed to this incredible trip, and the precious help of Lucien Cadieu for the last rehearsals before the defense.

Finally, a special thanks to Sarah Benart for your daily encouragements and invaluable kindness. You were a constant support throughout this adventure.

Like any mountain trip, the experience and dedication of the people from the lab was a precious help on a daily basis.

The crazy *R0-48* team: Jonathan Merzeau for his drone-building skills and Mohammed El May for his tacos expertise which is only rivaled by the cheese-nan mastery of Yves Chemisky.

The *fatigue* team: Thierry Palin-Luc, Charles Brugger and Christophe Bois, thank you for your advices throughout this work.

The *expert* team: Florence Duville your help was key in organizing almost anything, Matthieu Lasserre your knowledge in computers, politics and lab's old gossips was a precious source of inspiration, Jérémie Béga your expertise in using the SEM made a lot of this work possible, and last but not least Christophe Lemaire -one of many other gossips expert- who was always a pleasure to encounter in the lab.

The *advisors* team: Azita Ahmadi and Olivier Caty for your the time you took to monitor the evolution of this thesis work over three years and for your valuable advices.

I would also like to acknowledge the role of some of my former supervisors in giving me the desire to start this thesis: Emilie Santos during my internship at the Amsterdam Medical Center, Olivier Mayeur during my final-year project at the Laboratoire de Mécanique de Lille, Guillaume Dilasser during my internship at the CEA Saclay.

Finally, my infinite gratitude goes to my entire family for their constant support. To my grand-parents, to my parents and to my brother, you inspired me on this journey and gave me both the taste for hiking and doing science, as well as the means to do so.

To my family, to my comrades...

Introduction

Since the mid-20^{th} century, uncontrolled human activity has caused temperatures and carbon dioxide levels to rise at unprecedented rates while biodiversity is eroding at scales close to a mass extinction.

Laws and regulations are needed in order to reduce the human impact on climate and nature. As such, legislators have called for a reduction of emissions in the transport industry.

One way to engineer more fuel efficient vehicles is to reduce their overall weight. Composite materials can thus be used in order to replace some of the metallic parts and obtain lighter cars. This, far from being a miracle solution to the issue of climate change, is a small contribution to a much more complex issue.

However, materials providers and car manufacturers need to be confident in the mechanical properties and the durability of these new composite materials. The evolution of the mechanical properties and the progressive damage under repeated loading constitute the focus of what is called *fatigue of materials*.

Development of fatigue studies began in the second half of the 19^{th} century for metallic materials, and is often linked to investigations by Rankine and Wöhler following the Meudon rail accident in 1842. Later major crashes and disasters that were catastrophic fatigue failure prompted progress in research and engineering, most notably:

- during WWII, Tipper[1] investigated failure of steels when Liberty ships suffered hull cracks in the cold North Atlantic waters.
- significant progresses were made in the understanding of notch effect - or why it is better for planes to have round windows - as two de Havilland Comet passenger planes broke up in mid-air in 1954.

With the industrialization of plastics and composite materials during the 20^{th} century, new studies were needed on the mechanical properties and underlying physics of this new class of materials.

[1] Constance Tipper was the first female full-time faculty member at Cambridge University Department of Engineering. She demonstrated that there is a critical temperature below which the fracture mode in steel changes from ductile to brittle. She was the first person to use a scanning electron microscope to examine metallic fracture faces.

After the first works on the fatigue of short-glass fibers reinforced polyamides in the 1990s by Sato and Horst, several research team have contributed to this field as for example Prof. Bernasconi from Politecnico di Milano in Italy, Prof. Sonsino from Fraunhofer LBF in Germany, Prof. Fatemi from the University of Memphis in the USA, etc. In France, several teams also contributed to the research regarding fatigue of reinforced polyamides: Prof. Nadot-Martin and CNRS Senior Researcher Castagnet from the Pprime Institute, Ass. Prof. Marco from ENSTA Bretagne, Prof. Meraghni from ENSAM Metz, and Prof. Saintier from ENSAM Bordeaux. From these labs, a number of PhD thesis have been dedicated to the topic including the works of Ghorbel, Arif, Klimkeit, Despringre, Rolland and Fouchier[2]. Furthermore, the french community can also rely on the extensive works performed on the creep of polymer materials, mostly at the Centre des Matériaux of Mines ParisTech, and on the properties and structures of semi-crystalline polymers.

The present work is part of a larger research project that includes two other PhD theses by Caroline Goutal and Prashanth Santharam at the Pprime Institute and ENSTA Bretagne respectively. The research of Caroline Goutal is focused on the optimization of a multiaxial energy-based fatigue criterion, while the work of Prashanth Santharam follows a thermo-mechanical approach.

This project is performed in collaboration with a number of industrial partners, among them: Solvay Perfomance Polyamides (that directly funded this research), Trelleborg Vibracoustic, e-Xstream engineering, PSA and Promold.

The present work aims at completing the existing description and understanding of the fatigue behavior and damage of short-glass fibers reinforced thermoplastic polymers and the study of a strain rate based fatigue criteria.

After a state of the art on the existing research in chapter 1, we will then introduce the materials and methods of this study (chapter 2). The work will then focus on the evaluation of damage mechanisms in the material as observed using micro-tomography and scanning electron microscopy (chapter 3). In order to fully address the polymer damage mechanisms, additional observations are performed on the pure polymer matrix and are used to shed light on spherulitic damage mechanisms and their strong similarities with static creep damage, where strain rate is known to drive the durability. Transitioning at the macroscopic scale in chapter 4, the mechanical response of smooth and notched specimens is investigated in order to establish a cyclic strain rate based durability criterion, unifying the composite fatigue behavior on a wide range of loading conditions including R ratio effect, frequency effect, fiber orientation effect and humidity. Using micro-structure modeling, chapter 5 will complete the picture by confronting the experimental evaluation of local damage with computed local mechanical fields and durability criteria. Finally, we will conclude this work with a number of remarks and outlooks for future research.

[2]The work of Fabre could probably be added to this list, if it wasn't confidential until March 2020...

Note that this thesis manuscript is based on several articles already published at the time of writing or to appear in the coming months:

- Rolland, H., Saintier, N., **Raphael, I.**, Lenoir, N., King, A., & Robert, G. (2018). "In-situ fatigue damage mechanisms in short fibre reinforced PA66 as observed by synchrotron X-ray microtomography". *Composites Part B: Engineering*, 143, 217–229. https://doi.org/10.1016/j.compositesb.2017.12.051

- **Raphael, I.**, Saintier, N., Robert, G., Béga, J., & Laiarinandrasana, L. (2019). "On the role of the spherulitic microstructure in fatigue damage of pure polymer and glass-fiber reinforced semi-crystalline polyamide 6.6". *International Journal of Fatigue*, 126, 44–54.
https://doi.org/10.1016/j.ijfatigue.2019.04.036

- **Raphael, I.**, Saintier, N., Rolland, H., Robert, G., & Laiarinandrasana, L. (2019). "A mixed strain rate and energy based fatigue criterion for short fiber reinforced thermoplastics". *International Journal of Fatigue*, 127, 131–143.
https://doi.org/10.1016/j.ijfatigue.2019.06.003

- **Raphael, I.**, Saintier, N., Robert, G. & Laiarinandrasana, L. "Fatigue properties of notched short glass fiber reinforced polyamide 6,6 specimens".

- **Raphael, I.**, Saintier, N., Rolland, H., Mareau, C., Robert, G., & Laiarinandrasana, L. "Micro-mechanical modeling of fatigue damage mechanisms in short fiber reinforced thermoplastic".

However results are presented here with more context and sometimes more details.

NB: An extended abstract in French is provided in chapter 7.
NB: Un résumé étendu en français est fourni en chapitre 7.

NB 2: But the full English version is of course much better ;)

Chapter 1

State of the Art

There is pleasure in recognizing
old things from a new viewpoint

Richard Feynman

The purpose of this first chapter is to make a literature review on the different topics that will be covered in this work. It aims at giving a clear view of the existing research relevant to what will later be presented. As most of the results introduced here have already been extensively discussed in multiple papers and PhD thesis, all references will be given so that the reader might obtain more information. However some points that are rarely covered in works on fatigue of composite materials will be more detailed (e.g. on semi-crystalline structures).

1.1 Reinforced polyamide 6,6

1.1.1 A composite material

1.1.1.1 History and usage

On February 28, 1935, Wallace Carothers and his team first synthesized Polyamide 6,6 (PA66). *Nylon*, as it would be commercially known, was the result of a decade long effort to produce new polymers, that started from fundamental research until practical application.

Indeed, in 1926, Charles Stine, then research head at DuPont, launched what he called "a radical departure from previous policy" with a program of "pure science" aiming at "establishing or discovering new scientific facts" in several areas including organic synthesis and polymerization [1]. He hired a Harvard instructor, Wallace Carothers, to lead this work. Along with his team[1], Carothers synthesized neoprene for the first time in April 1930, before focusing on the invention of a polymer that could be turned into fibers.

[1]French chemist Gerard Berchet worked under the supervision of Carothers and played a pivotal role in the invention of both neoprene and nylon... as he was the one actually doing the experiments!

When they produced the first PA66 fibers, it quickly became apparent that this new polymer could have a huge economic potential. It was presented in 1938 by Stine, who by then had become DuPont vice-president, as revolutionary [2]:

> "Though wholly fabricated from such common raw materials as coal, water and air, nylon can be fashioned into filaments as strong as steel, as fine as the spider's web, yet more elastic than any of the common natural fiber and possessing a beautiful luster."

It is thus in the form of threads that PA66 became known worldwide in multiple usages from stockings to parachutes including toothbrush bristles... and the first flag planted on the Moon by the crew of Apollo 11.

Polyamide 6 (PA6), then widely known as *Perlon*, was developed just a few years after PA66 in order to reproduce its properties without patent violations. It was synthesized in January 1938 by Paul Schlack, while working at IG Farben in Nazi Germany [3].

With the later development of the plastics usage in industries, polyamides were no longer restricted to the textile market. Polyamide usage became common in various applications such as pipes or parts for the automotive industry. In the latter case bulk PA66 is often reinforced with short glass fibers in order to further improve its mechanical strength while remaining lightweight. This forms a composite material that can be efficiently used to replace metallic alloys in the vehicles.

The market for both PA66 and PA6 was estimated at USD 25.7 billion in 2017 and is expected to register a 6% annual growth rate in 2019-2025. The increased usage of technical plastics, in ever more demanding applications, requires better control of the manufacturing process, better understanding of the material microstructure and better modeling of its mechanical properties.

1.1.1.2 Manufacturing process

In order to meet the high production rates of the automotive industry, parts made of short glass fiber reinforced polyamide are injection molded (fig. 1.1). This also allows for the precise manufacturing of parts with complex geometries.

Injection molding uses a screw inside a heated barrel in order to mix the polymer and the glass fibers. The screw is rammed forward in order to inject the molten compound in the mold cavity. Pressure in maintained during the solidification of the material. This cooling is accelerated by water running through channels inside the mold walls. The mold then opens, ejector pins push the part out of the cavity and the mold closes again for the next injection.

This cycle takes between a few seconds and a couple of minutes, depending on the size of the part.

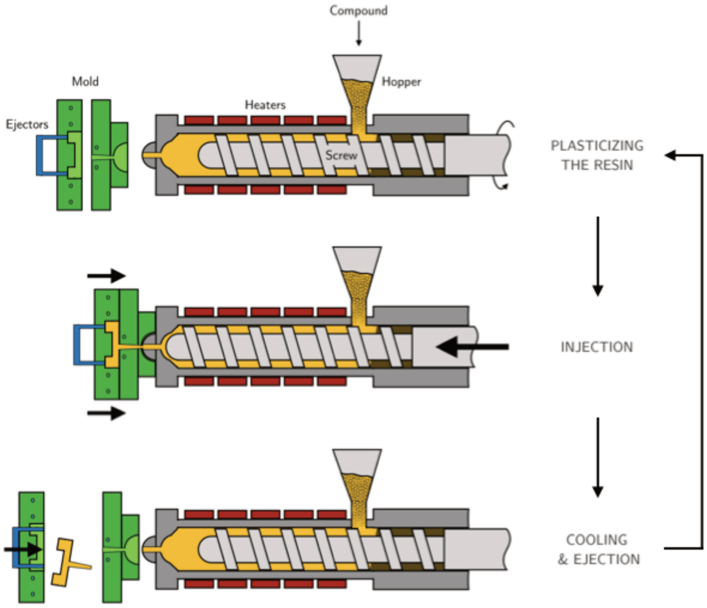


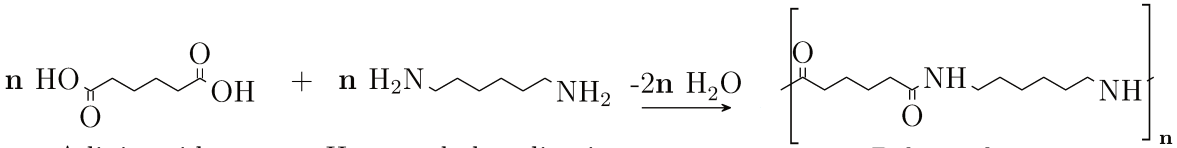
Figure 1.1: Injection molding process.

1.1.2 A semi-crystalline matrix

1.1.2.1 Global description

In a composite material the role of the matrix is to maintain the reinforcements and transfer stress between them.

Polyamide 6,6 is one of the most common type of poylamides. It is synthesized by polycondensation of hexamethylenediamine and adipic acid, with the formation of amide bonds from the amine and acide functions. Water is removed to drive the reaction towards the polymerisation:



Adipic acid Hexamethylenediamine Polyamide 6,6

Each of the two reactants contains six carbon atoms, hence the name “polyamide 6,6”. Note that PA6 is produced differently, by ring opening of caprolactam - that has six carbons.

Depending on the degree of polymerization, a polyamide macromolecule can be composed of between 10^3 and 10^6 monomers.

Polyamide 6,6 is a semi-crystalline polymer. Its molecules can locally thus be in either in a crystalline or an amorphous state. The same macromolecule can have a section of its chain in a crystalline state and an other section in an amorphous state.

The overall organization of the semi-crystalline polymer will be described below.

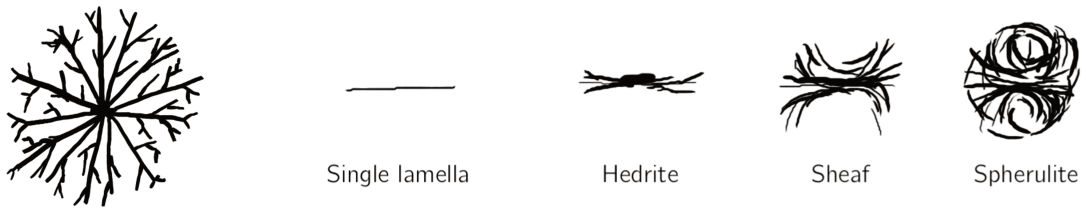
1.1.2.2 Formation and structure of the spherulite

Semi-crystalline thermoplastics often crystallize as spherulites. Spherulites are spherical crystal colonies. Their formation is usually described during crystallization experiments on thin films [4] and two categories can be made depending on the formation process [5]. Category 1 spherulites initiates on a nucleation point and forms via radial growth (fig. 1.2(a)) while category 2 spherulites forms from a single folded chain crystal.

This first lamella will form the "nucleus" of the future spherulite. These pre-spherulitic structures have been reported to be randomly oriented [6] in thin films. Further crystallization make them grow into a hedrite, a sheaf and later a full spherulite (fig. 1.2(b)) [7].

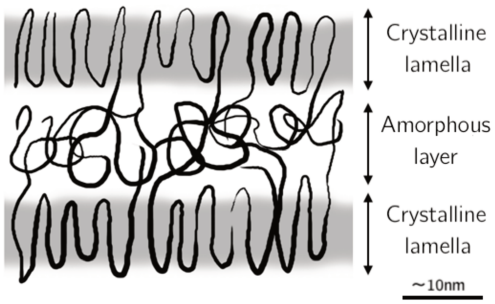
Multiple mechanisms have been put forth to explain the formation of such spherulite from a single point or lamella. These scenarios -as well as much more detailed information- can be found in the review by Crist and Schultz [8]. However experimental evidence on the mechanisms of spherulite growth in bulk material is, understandably, lacking.

In the case of the polymer studied and process conditions, spherulites are considered to be composed of an array of crystalline lamellae between which the polymer is in an amorphous state (fig. 1.2(c)). Lamella thickness is around 10 nm, as is the distance between to successive lamellae.

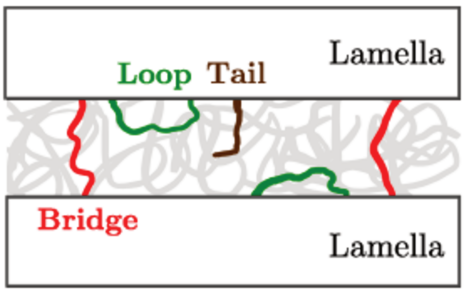


(a) Fully radial *category 1* spherulite.

(b) Formation of a *category 2* spherulite in a thin film



(c) Semi-crystalline arrangement of polymer chains



(d) Chains configuration

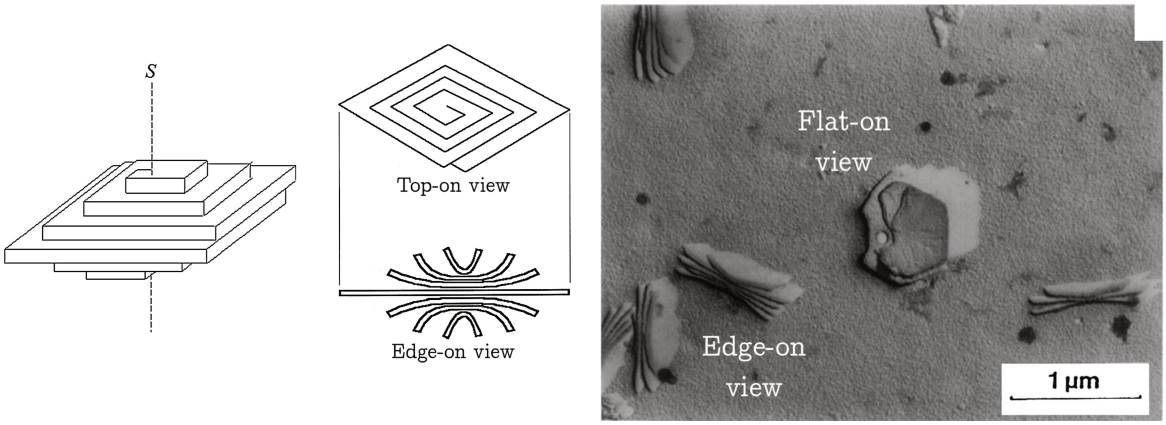
Figure 1.2: Structure of spherulites in a semi-crystalline thermoplastic as usually described.

As polymer chains are long compared to the lamellar structure, a polymer chain can be in several local configurations [9; 10]. Regular or irregular folding of a macromolecule that exits and re-enters a lamella results in the formation of a *loop*. A polymer

chain that goes from one lamella to the next one will form a *bridge*. Finally a polymer chain that exits a crystalline lamella and ends in the amorphous zone is called a *tail* (fig. 1.2(d)).

Spherulite growth continues linearly with time until it encounters neighboring growing spherulites. The average size of the spherulites depends of the cooling conditions and the density of potential nucleating sites for crystallization.

Traditional observations on thin films and 2D description of the structure might be largely incomplete to properly describe the three-dimensional structure of spherulites [11]. A few deeper analysis can be found in the literature regarding cellulose triacetate [4], poly(4-methylpentene-1) [6] and poly(oxyethylene) [12]. They describe a *rose-petal assembly* and a *square outline* of the spherulites when observed under a top plan view. These observations are consistent with the proliferation of spherulites *via* spiral growth (fig. 1.3).



(a) Sketch of spiral growth from a giant screw dislocation. From Crist [8].

(b) Top flat-on view and side edge-on view. From Crist [8].

(c) TEM image of iPS hedrites grown from a still melt. From Vauhan [13].

Figure 1.3: Spiral growth of spherulite.

1.1.2.3 Spherulite observation

Detailed observation of spherulites is crucial if one wants to link the fatigue damage to the spherulitic structure of the polymer. However, unlike with grains observations in metals where crystallographic observations can be made using EBSD and grain boundaries can be observed in tomography by various techniques [14], observation of spherulites is much less standardized. Multiple observation techniques can be found in the literature [8], but the full understanding of the complex tridimensional nature of bulk polymer's spherulite is still an issue.

Traditional observations are made using cross-polarized light microscopy (see fig. 1.4 and section 2.3.1). Thanks to the birefringence of the material, spherulites appear with a typical Maltese-Cross pattern [15; 16]. Such methods require the observation to be made on thin film (obtained by casting, compression or cut from samples using a micro-

tome), making it delicate for a number of applications. In particular the observation of damage by this technique is difficult and may lead to ambiguous conclusions. It is also worth mentioning that obtaining longitudinal thin slices of the fiber reinforced material using a microtome is possible but arduous. The polymer around the fibers is damaged by the process and it is difficult to observe the spherulites in these regions. Moreover, as it is based on optical microscopy, this technique is better suited for large spherulites.

Observations of spherulites and damage can also be made using Atomic Force Microscopy (AFM) [17; 18]. Once again, published observations have mostly been performed on thin films, yielding the same aforementioned limitations.

Cryo-fractography and/or chemical etching have also successfully been used in a some studies [19; 20] and especially for PA6 [21; 22], for PEHD [23; 24] and for PA11 [25]. However they are not easily implemented and chemical attacks to reveal spherulites can be very tricky to manage. This might explain the very few (convincing) examples that can be found in the literature.

It is worth noting that spherulites in PA6 and PA66 are not visible using tomography [22; 26] - at least with the technology currently available, although new techniques are presently under development using nano-tomography.

Finally, X-Ray scattering was also extensively used as a way to describe the organization of matter within spherulites [27; 28]. Together with cross-polarized microscopy, this technique was used to classify at least four types of spherulitic structures[2], as detailed in the work of Magill [29].

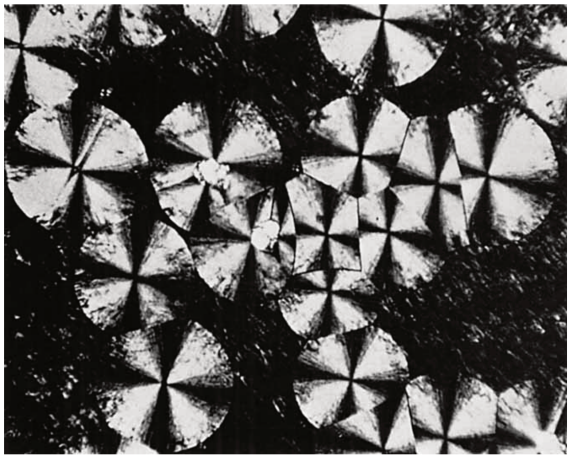


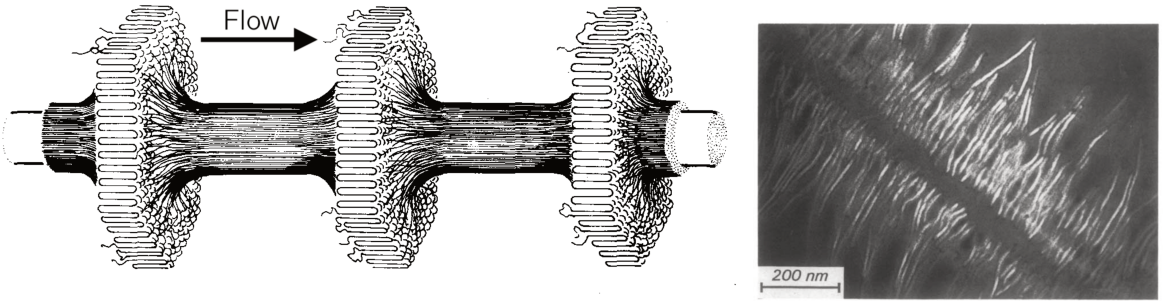
Figure 1.4: PA610 spherulites as observed using cross-polarized microscopy. From Magill [29].

[2]The different types of spherulitic structures depend on the fusion and cooling conditions but differ from the categories introduced in section 1.1.2.2. The distinction, mostly based on the details of the organization of the polymer chains in the spherulite, is out of the scope of this work but can be found in the literature [11; 28; 29].

1.1.2.4 The shish-kebab structure

Spherulite is not the only form of semi-crystalline arrangement. In the some cases during the flow of a polymer melt, molecules will extend and orient in the direction of the shear stress. This affects the morphology of the crystallized structure. The most common form of flow-induced oriented morphology is the *shish-kebab* structure (fig. 1.5). This structure was evidenced experimentally by KELLER & MACHIN [30] and the name was coined by LINDENMEYER[3].

The usual description is that the center of the structure (i.e. the *shish*) is a long crystalline assembly of aligned extended polymer chains. Nucleation sites on the surface of the shish allow for the lateral growth of crystalline lamellae, thus forming the *kebab*.



(a) Shish-kebab structure. From PENNINGS [32].

(b) Electron Spectroscopic Imaging of a PE shish-kebab. From HUONG [33].

Figure 1.5: Shish-kebab structure in semi-crystalline thermoplastics.

Contrarily to spherulites, shish-kebab are oriented structures. They can form during flow induced crystallization of the polymer [34] when the strain in the melt strongly orients the macro-molecules.

1.1.2.5 Crystallinity

As describded above, the semi-crystalline polymer is composed of two phases: a crystalline and an amorphous[4]. The degree of crystallinity can be defined with respect to the volume (v_c) or to the mass (χ_c) as:

[3]LINDENMEYER made a theoretical prediction for the folding of long polymer chains, which he introduced in his 1967 paper [31] with:

> I never saw a folded chain
> I never hope to see one,
> But I can tell you anyhow
> I'm damn near sure there be one.

Which is pretty cool.

[4]More recent observations have evidenced the existence of two amorphous phases: the Rigid Amorphous Phase (RAP) and the the Rigid Mobile Phase (MAP) [35]. The RAP can be seen as an interphase between the crystalline lamella and the MAP. These two phases behave differently and their ratio have been reported to directly influence the glass transition temperature in PA6 [36]. The concept of RAP and MAP is still the subject of current research in the community.

$$v_c = \frac{V_c}{V_{tot}} \text{ and } \chi_c = \frac{M_c}{M_{tot}} \tag{1.1}$$

with V_c (resp. M_c) the volume (resp. mass) of the crystalline phase and V_{tot} (resp. M_{tot}) the total volume (resp. mass) of the specimen.

The degree of crystallinity can be determined using density measurements, differential scanning calorimetry, X-ray diffraction, infrared spectroscopy or nuclear magnetic resonance. Note that the degree of crystallinity (a scalar value) cannot describe the morphology, size and variability of the spherulites in the bulk.

1.1.2.6 Glass transition temperature

Glass transition temperature T_g is a key parameter for the mechanical behavior of polymers.

Under T_g the amorphous polymer chains have little movement. The polymer is in a glassy and rigid state. The amorphous phase cannot undergo large strain without failure.

Above T_g, thermal motion is higher and the amorphous polymer chain can move. The material is in a rubbery state and can accommodate larger strains.

The glass transition temperature depends of the water intake, cystallinity, amorphous orientation and RAP content of the polymer [36].

1.1.3 Reinforcements for an improved mechanical performance

Adding rigid objects in the thermoplastic matrix helps to improve its mechanical performances by finding a good compromise between stiffness, brittleness and failure characteristics. Multiple types of reinforcement can be used (e.g. mineral particles, metallic powders, fibers...) to obtain a variety of final properties.

1.1.3.1 Short glass fibers

In this work, reinforcements are short glass fibers. They are referred to as *short* because of their sub-millimetric length, as opposed to long fibers with lengths of a few centimeters.

These fiber offer the compromise of improving the mechanical properties while still allowing for the injection molding process.

Final mechanical properties are strongly influenced by the properties of the fibers. In our case, E-glass is used. Fibers are cylinders $10\mu m$ in diameter with an average length of $350\mu m$, although lengths usually vary from 50 to $500\mu m$.

Similar to all composite materials, the material is often characterized by the fraction of these reinforcements, by weight or volume. In our case the fraction for glass fibers is 30% by weight.

However, knowing the volume fraction is not sufficient as the short glass fibers are not randomly oriented and evenly distributed in the bulk material. As failure characteristic is a *local* mechanism, gaining a good understanding of it thus requires

a precise description of the microstructure from which the studied volume of interest will be extracted.

1.1.3.2 Microstructure induced by the injection molding

Injection molding induces a characteristic microstructure in the composite: fibers orientation is heterogenous throughout the thickness of the plate. This microstructure has been extensively described in the literature and is usually referred to as a *skin-shell-core* microstructure (fig. 1.6).

In a typical 3.2mm thick plate, the *skin* is a 50μm thick layer of randomly oriented fibers formed at the surface of the plate. Here fibers are frozen in their positions by the thermal shock between the hot injected material and the cold mold walls during the injection molding process. Beneath this skin, is the *shell* layer. This is the thickest layer, with 1.4mm. In the shell, because of the shear stress in the molten material flow, fibers are oriented in the mold flow direction (MFD). Finally, at the center of the plate, is a 300μm thick layer referred to as the *core*. In this layer, fibers are perpendicular to the MFD. This orientation is caused by an extensional flow as the molten material enters the mold cavity.

The reader shall refer to the articles written by the following authors for more details regarding fiber orientation in injection molded composite materials: Horst [37], Bernasconi [38], Arif [39; 40], Ayadi [41] and Rolland [42].

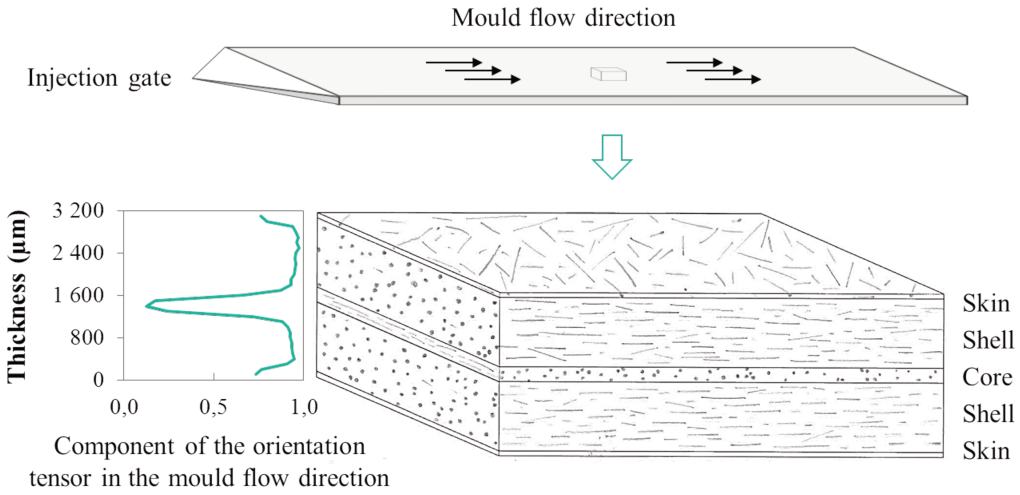


Figure 1.6: Heterogeneous fiber orientation in an injection molded plate. From Rolland [43].

1.1.3.3 On the importance of the fiber-matrix interface

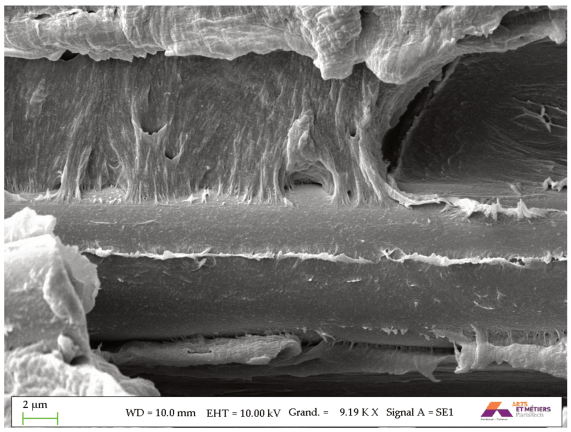
When stress is applied to the material, it is transferred from the matrix to the fibers. The fiber-matrix interface thus plays a critical role in the mechanical performance of the composite material.

Adhesion at the interface Adhesion between the glass fibers and the polymer matrix is paramount in order in obtain good mechanical properties (section 1.1.3.3). In order to obtain good bonding, glass fibers usually receive a surface chemical treatment (*sizing*). Aminosilane coupling agents bond to both the glass surface and the polymer molecules. Interfacial interaction is thus composed of both hydrogen and covalent bonds. This ensures a stronger interface than with only hydrogen bonds in the case of non-treated glass fibers [44].

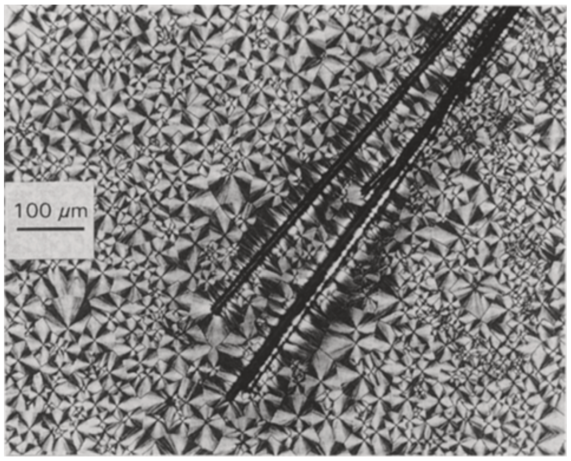
Sizing is performed during the manufacturing of the fibers, while they are still arranged in long bundles. This has a major consequence: when glass fibers are later cut or broken to form *short* fibers, their tips have not been treated.

The interested reader can find much more details in works focusing on this subject. For example Bergeret [45] and Rudzinski [46] studied the influence of sizing on the aging of the material and the evolution of its mechanical properties. More recently, Gabet [47] studied the properties and optimization of this interface.

Spherulitic structures along fibers Due to the presence of fibers in the melt, nucleation of the crystalline structures can in some cases occur along the fibers. This phenomenon is referred to as *transcrystallinity*. Spherulites nucleated on the surface of fibers grow radially and form a transcrystalline layer (section 1.1.3.3). They are smaller and have a larger aspect ratio than those nucleated in the matrix. According to Mourglia-Seignobos [48], transcrystallinity caused by glass fibers is very limited in the material studied in the present work.



(a) SEM observation of the fatigue damage at the fiber-matrix interface.



(b) Transcrystalline spherulitic morphology around glass fibers in thin film of melt-crystallized PA66. From Shiao [49].

Figure 1.7: Fiber-matrix interface in fiber reinforced polymers.

1.2 Macroscopic mechanical properties

1.2.1 Mechanical anisotropy

The injection process orients most of the fibers in the direction of the flow. In order to study the influence of this anisotropy on the mechanical properties of the material specimens are usually machined or cut at different angles with respect to the mold flow direction (MFD) as shown on fig. 1.8. Note that a given specimen taken for example at 45° with respect to the injection flow, will later be referred to as a "45°" specimen.

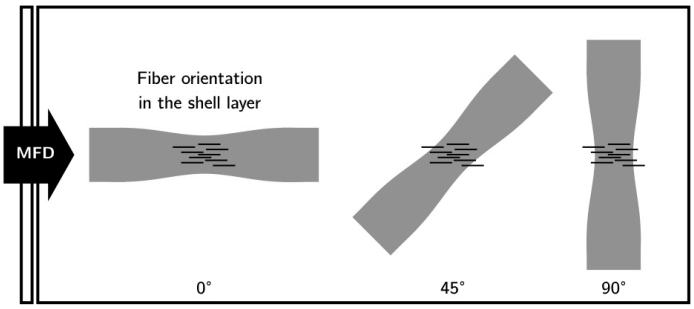


Figure 1.8: Specimen orientation in an injection molded plate.

1.2.1.1 Quasi-static tensile tests

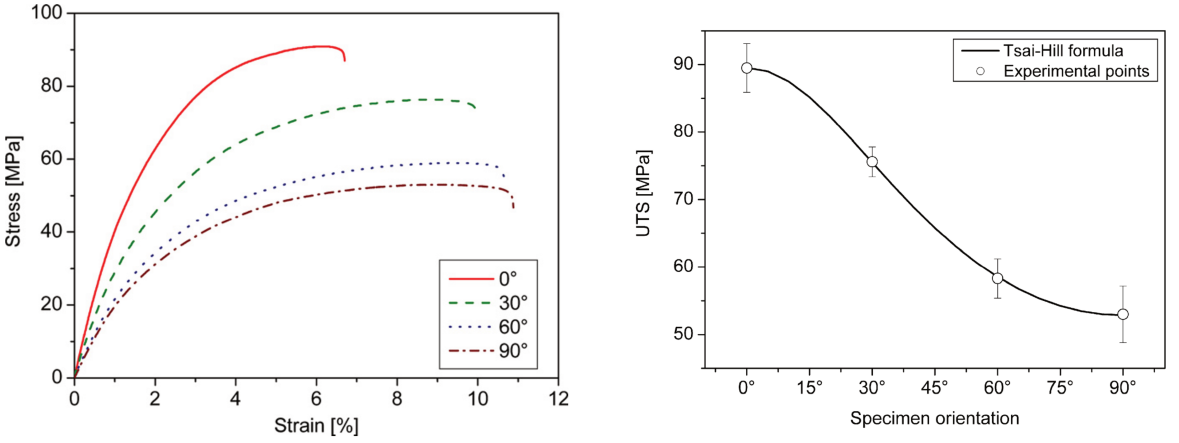
Bernasconi *et al.* [50] studied reinforced PA6 (PA6-GF30). Quasi-static tensile testing was performed on 0°, 30°, 60°, and 90° specimens. For every specimen the stress-strain curved increased rapidly before reaching a flat plastic[5] region with limited strain hardening. The ultimate tensile stress (UTS) is only slightly higher to the stress at break for all specimens, the presence of fibers probably preventing extensive necking. Results showed the decreasing values of elastic modulus and UTS for increasing values of the orientation angle of specimens. Strain at break was also higher for increased values of the orientation angle (fig. 1.9(a)). The Tsai–Hill criterion allowed for an accurate prediction of the dependence of the UTS values upon the orientation angle (fig. 1.9(b)):

$$\left(\frac{\sigma_1}{\sigma_{1,u}}\right)^2 + \left(\frac{\sigma_2}{\sigma_{2,u}}\right)^2 - \frac{\sigma_1\sigma_2}{\sigma_{1,u}^2} + \left(\frac{\tau_{12}}{\tau_{12,u}}\right)^2 = 1 \tag{1.2}$$

with σ_i the normal stress applied in the i-direction, τ_{ij} the shear stress applied in the i-j plane. The values $\sigma_{i,u}$ are the experimental values of the UTS for specimens taken at 0° and 90°. The value of τ_{12} was determined for $\theta = 30°$ using:

$$\sigma_u(\theta) = \left[\frac{\cos^2(\theta)(\cos^2(\theta) - \sin^2(\theta))}{\sigma_{1,u}^2} + \frac{\sin^4(\theta)}{\sigma_{2,u}^2} + \frac{\cos^2(\theta)\sin^2(\theta))}{\tau_{12,u}^2}\right]^{-1/2} \tag{1.3}$$

[5]Plastic deformation is assumed, although it would require the unloading of the specimen to formally distinguish from non-linear elasticity.



(a) Tensile stress–strain curves.

(b) Interpolation of the UTS by the Tsai–Hill criterion.

Figure 1.9: Results from tensile testing for different specimen orientations. From Bernasconi [50].

1.2.1.2 Fatigue testing

Similar analysis, also by Bernasconi *et al.* [50], has been made in the case of fatigue loading.

They reported a decreased fatigue strength with increasing orientation angle (fig. 1.10(a)) and showed the good predictive capabilities of a modified Tsai–Hill criterion (fig. 1.10(b)):

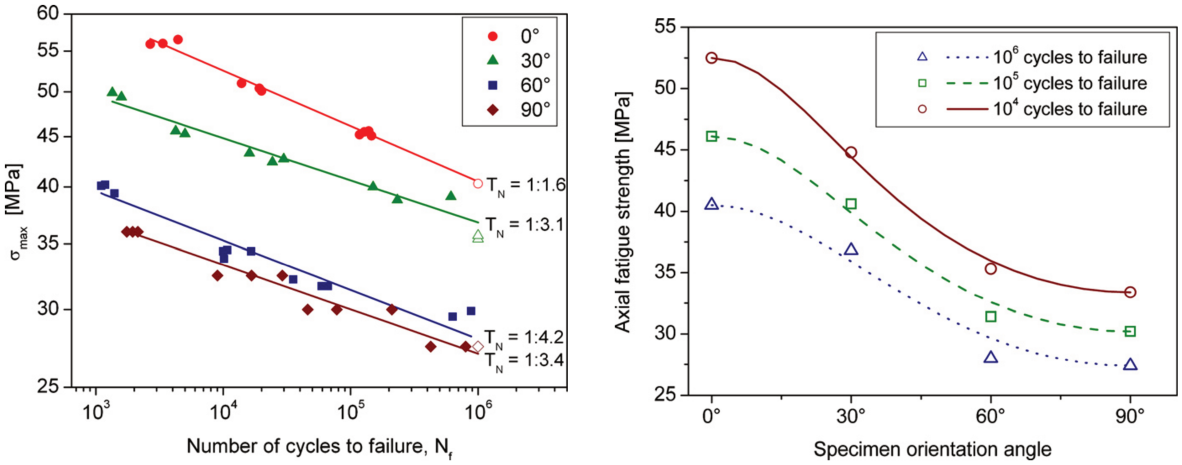
$$\left(\frac{\sigma_{1,\max}}{\sigma_{1,fat(N)}}\right)^2 + \left(\frac{\sigma_{2,\max}}{\sigma_{2,fat(N)}}\right)^2 - \frac{\sigma_{1,\max}\,\sigma_{2,\max}}{\sigma^2_{1,fat(N)}} + \left(\frac{\tau_{12,\max}}{\tau_{12,fat(N)}}\right)^2 = 1 \qquad (1.4)$$

with $\sigma_{i,\max}$ (resp. $\tau_{ij,\max}$) the maximal value of the normal stress applied in the i-direction (resp. of the shear stress applied in the i-j plane) during one loading cycle. The values $\sigma_{i,fat(N)}$ and $\tau_{12,fat(N)}$ are experimental fatigue strength for a specimen life of N loading cycles.

The orientation angle also has a direct impact on the macroscopic fatigue crack propagation, as observed on the surface of 20wt% short carbon fiber reinforced PPS notched specimens by Tanaka *et al.* [51]. As shown on fig. 1.11, the macroscopic crack path is nearly perpendicular to the loading axis for the cases of 0° and 90° specimens. For 45° specimens, the crack path was inclined because the crack often propagated along fibers.

In 0° specimens crack needs to either get around fibers or break them in order to propagate (fig. 1.12(a)). Main propagation mechanisms contributing to the crack advance are thus damage at fiber end and fiber failure.

In 45° and 90° specimens, crack mainly propagates along the length of fibers by decohesion at the fiber-matrix interface (figs. 1.12(b) and 1.12(c)).



(a) S–N curves. Bright symbols indicate test interrupted at 10^6 cycles (run-outs).

(b) Interpolation of the fatigue strength values by a Tsai–Hill type criterion.

Figure 1.10: Results from fatigue testing for different specimen orientations - RH50, R=0.1, 4Hz. From Bernasconi [50].

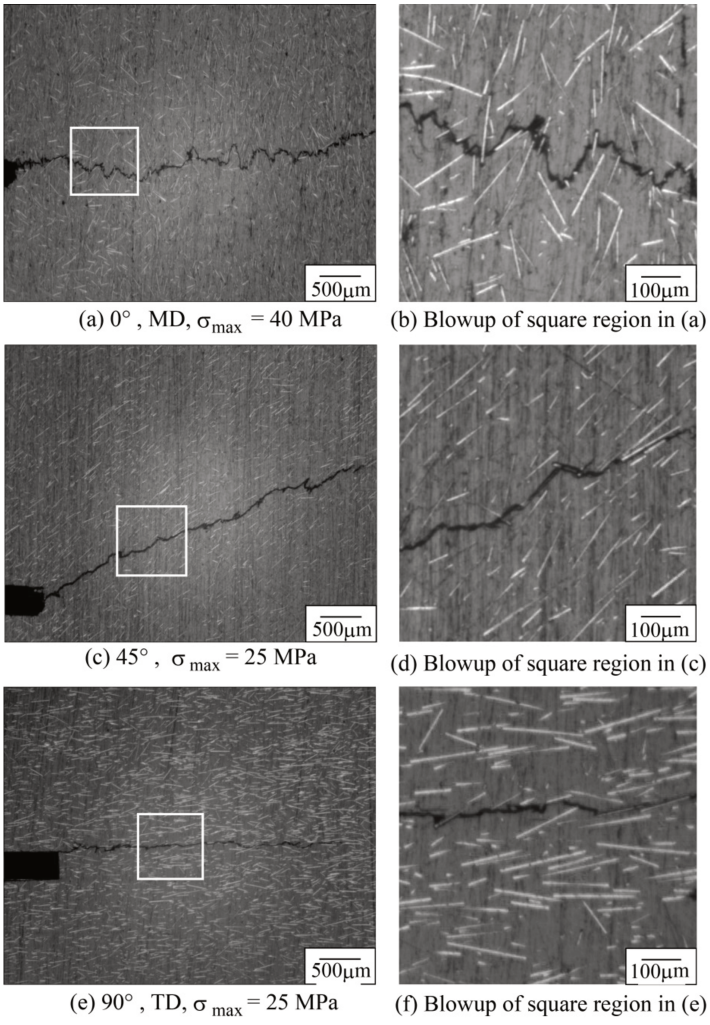


Figure 1.11: Fatigue cracks in 0°, 45° and 90° notched specimens of under R=0.1. From Tanaka [51].



(a) 0° microstructure (b) 45° microstructure (c) 90° microstructure

Figure 1.12: Schematics of fatigue crack propagation mechanisms.

1.2.2 Effect of the mechanical loading

1.2.2.1 Mean stress effect

Mean stress effect has a major impact on the material behavior which exhibits significant visco-elasticity at ambient temperature that may in turn have a strong effect on its durability.

Studies are performed by running tests a different load ratios $R = \sigma_{min}/\sigma_{max}$. Mallick [52] showed that an increased mean stress causes a lower fatigue strength (fig. 1.13) on PA66GF33.

When addressing the mean stress effect usual approach consists in the use of classical empirical models that explicitly embed a mean stress effect (eg. modified Goodman and Gerber equations [52; 53], Chaboche model [54]).

As noted by Robert [55], when analyzing lines of constant life for reinforced PA66 (fig. 1.13), data might be considered as linear, especially for 0° specimens. Nevertheless, at higher load ratios, the drop of properties accelerates, which proves the need for a parabolic correlation. Modifications of the Gerber equation, such as proposed by Mallick [52], are needed to properly account for the mean stress effect and the induced cyclic creep phenomenon. Indeed under fatigue loading the mean strain increases during testing[6]. This is taken into account in the proposed correction of the Gerber equation.

1.2.2.2 Frequency effect

Due to their viscous nature, polymers and their composites are sensitive to the strain rate. This has a direct impact on the properties under all types of loading conditions quasi-static, dynamic and fatigue.

In fatigue, the effect of the loading frequency is complex:

- **At high frequencies**, the material has higher strength which could improve the fatigue lifetime [37]. However a higher frequency also induces heat build-up of

[6]This phenomenon will be detailed in section 1.2.6.

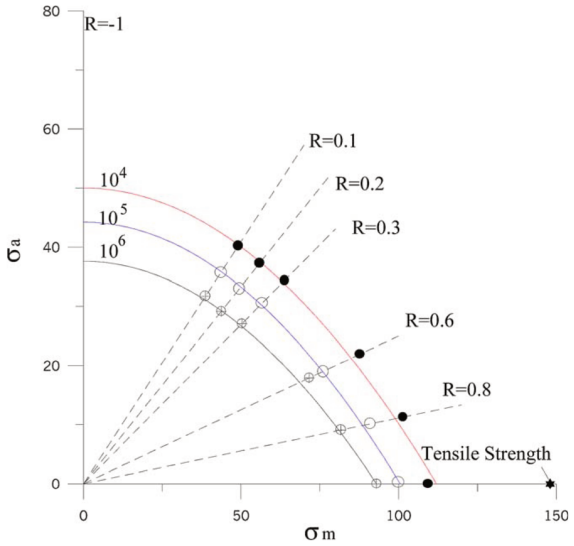


Figure 1.13: Haigh diagram: Relationship between stress amplitude σ_a and mean stress σ_m, with modified Gerber equation. From Mallick [52].

the specimen, which will decreases its mechanical performances. This temperature increase has a linear dependence to the frequency [56]. Overall increasing frequency induces a strong decrease of the fatigue strength [57].

- **At low frequencies**, the fatigue test can become dominated by the cyclic creep. Higher cyclic strain rates can induce some heat build up in the specimen [37] which has a detrimental effect on fatigue life.

Zhou [58] reported an *optimal frequency* of 2Hz as the transition between the regimes for PA66GF30 (fig. 1.14). This is similar to the 1Hz reported by Horst [37].

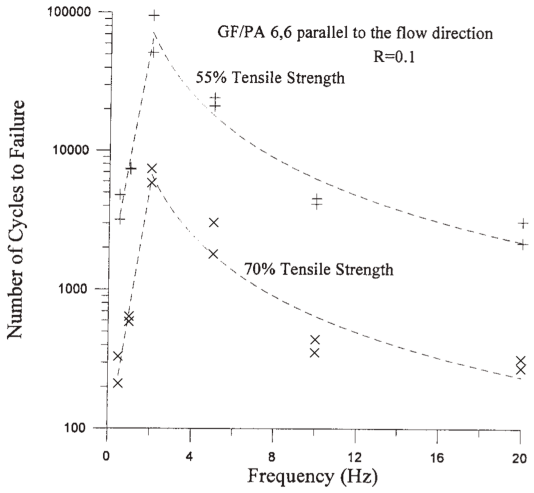


Figure 1.14: Effect of loading frequency in fatigue life. 0° specimens, R=0.1. From Zhou [58].

It is important to note that, because it is directly linked to heat build-up in the specimen, the frequency effect depends of multiple other factor such as temperature,

sample water uptake and thickness. It is also strongly dependant on the convection conditions at the specimen surface.

1.2.3 Environmental effects

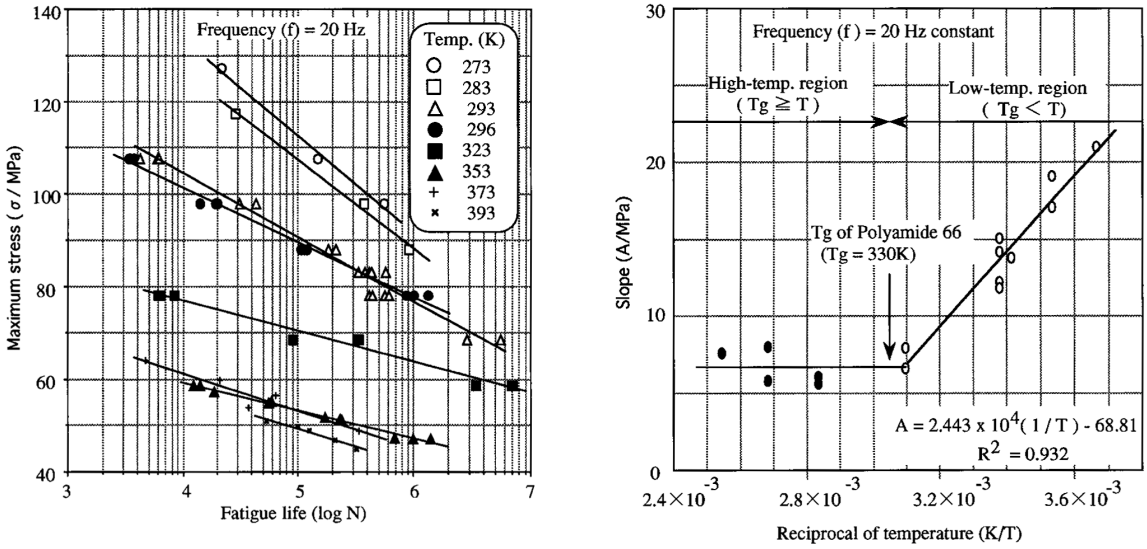
Polyamide 6,6 is sensitive to its environment. The impact of temperature, humidity and radiations on the mechanical properties and aging of the material should therefore be studied.

1.2.3.1 Temperature

Temperature has a direct effect on the mechanical response of the composite material.

For quasi-static loading, a lower temperature increases the modulus of the material as well as its UTS [59].

During fatigue loading at a given applied stress, the higher the temperature, the lower the lifetime of the specimen (fig. 1.15(a)). The slope of the S-N curves decreases as the temperature increases up to T_g. Above T_g the slope becomes independent of the temperature (fig. 1.15(b)).



(a) Dependence of S-N curves on ambient temperature

(b) Relationship between ambient temperature and slope of the S-N curve

Figure 1.15: Influence of temperature on the S-N curves of RH0 PA66GF33. From Handa [60].

1.2.3.2 Relative humidity

Polyamides are hydrophilic materials, especially PA6 and PA66. Water uptake causes swelling and mass increase of the material.

Water molecules insert themselves in the macro-molecular network, exclusively in the amorphous phase, and form hydrogen bonds with the polymer chains (fig. 1.16). In

doing so, they replace parts of the bonds in the amide functional group with a weaker link [61]. Water thus modify the mechanical properties of the polymer.

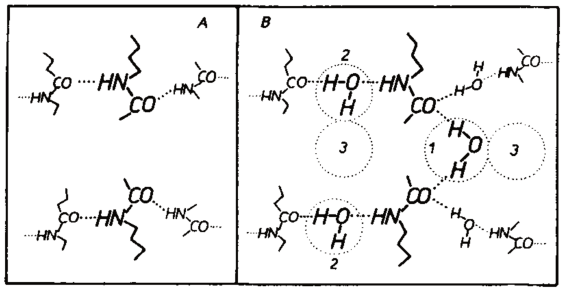


Figure 1.16: Model of displacement of sorbed water in PA6. From Puffr [62].
A. Dry amorphous polyamide.
B. Wet polyamide at saturated vapor pressure:
1, firmly bound water;
2, loosely bound water;
3, sites for capillary condensed water.

For quasi-static loading of PA6GF35, Ferreno *et al.* showed that water uptake reduces the rigidity and increases the ductility of the material (with a lower UTS and a higher strain at break).

During fatigue loading at a given applied stress, the higher the water uptake, the lower the lifetime of the specimen (fig. 1.17). However as it is more ductile, the material is better able to resist the advance of the fatigue crack in the last stage of its lifetime. In the wet material the process zone at crack tip is larger [63], the required energy for crack advance is higher [64] and crack propagation rates are lower [63; 65].

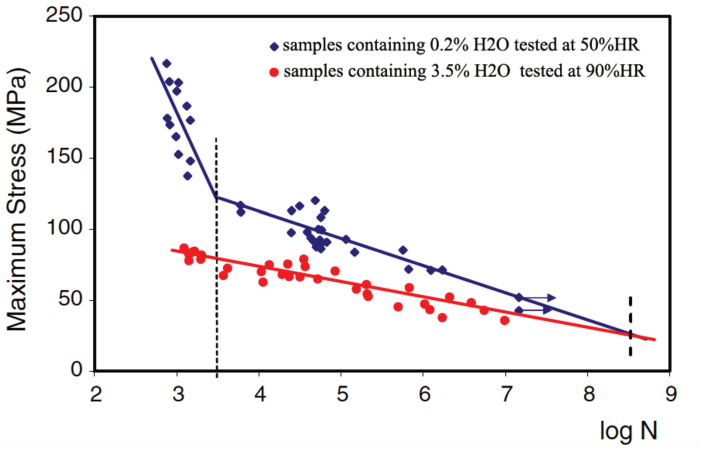


Figure 1.17: S-N curves for PA66GF30, R=-1, f=10Hz, T=23°C. From Barbouchi [66].

1.2.3.3 Other types of aging

Durability of the material can be affected by a vast diversity of external factors, some of which can occur simultaneously. Aging refers to the progressive degradation of

the properties of the material. It may of course be caused by long term or repeated mechanical stress but also by a number of environmental stresses: temperature and moisture as we have seen, but also saline atmosphere, presence of micro-organisms, contact with chemical products and exposure to high-energy electromagnetic waves (UV light, X-rays, Gamma-rays) [45].

Oxidative degradation mechanisms of the polymer, whether thermal- or photo-oxidation, have similarities [67]. A visible effect is the yellowing of the polymer [68].

Moreover, the oxidation causes embrittlement of the material. As noted by Okamba-Diogo [69], in an aged polymer specimen, cavitation is facilitated and the degradation of the number of polymer chains acting as links in the amorphous phase will induced a brittle failure.

1.2.4 Influence of the spherulite size

For metallic materials, the influence of the grain size on the mechanical properties have long been investigated. Similarly, it can be expected that the spherulite size has an impact on the overall properties of the polymer. However very few studies have been dedicated to this question.

Karger-Kocsis [70] processed PA6 in different conditions of temperature and injection speed in order to obtain various microstructural characteristics. By conducting Fatigue Crack Propagation (FCP) tests, it was suggested that an increased spherulite size improves resistance to crack propagation (higher ΔK_{th} see fig. 1.18(a)) but increased the propagation rate once the crack is propagating. The fracture toughness K_c was not significantly affected.

Yet it must be noted that the spherulite size was not the only parameter to vary due to the change in processing conditions: relative thickness of the skin layer and crystallinity were also modified. Any conclusion should thus be made carefully. Furthermore, the author remarked that it was highly probable that FCP resistance goes through a maximum both in function of crystallinity and spherulite size.

A study by Way [71] on the effect of spherulite size on the fracture properties of polypropylene focused on quasi-static testing. Samples were compression molded and spherulite radii between $40\mu m$ and $160\mu m$ were obtained by varying the cooling rate.

Results showed a major influence of the spherulite radius on the profile of the stress-strain curve (fig. 1.18(b)). As the spherulite size decreases, the fracture mode shifted from brittle to ductile. This change in failure mechanisms was supported by fractography observations and might be linked to a change of damage scenario. Indeed the authors noted that for specimens with large spherulites the fracture surface was "highly-faceted" and that these "polyhedrons" were typical of inter-spherulitic failure (fig. 1.18(c)).

Moreover they showed that the crystallinity and spherulite radius were linked, with larger spherulites being more crystalline (fig. 1.18(d)).

Interestingly, the yield stress increased with the spherulite radius until a maximum was reached and the yield stress started decreasing (fig. 1.18(e)). The explanation

proposed by the authors is a balance between the effect of the microstructure (larger spherulites are more crystalline and thus have higher strength) and the effect of the boundaries (larger spherulites obtained at slower cooling rates have weaker boundaries due to voiding and segregation of impurities, strain is thus less accommodated by spherulite deformation and more by inter-spherulitic damage).

As the authors noted "potential strength of slow-cooled spherulites is large but the problem is boundary cohesion". Subsequently various heat treatment were allegedly tried to strengthen the boundaries but with moderate success.

The existence of an optimal spherulite size before a negative impact of an increased radius on the mechanical properties might explain why the earlier study of Starkweather [72] only reported a decrease of the yield stress with increasing size on PA66 (see fig. 1.18(b), spherulites are obtained with nucleating agent). Although one could note that the results of Starkweather indicated a higher yield stress for a spherulite radius lower than $1.5\mu m$. The point was not taken into account in the correlation but might suggest an optimal radius size of about $2\mu m$ for PA66.

Another mean of controlling the spherulite size is by using nucleating agents. However Way [71] considered that crystallization would then start at higher temperature preventing the formation of an *advantageous* slow-cooled microstructure.

1.2.5 Notches and geometrical defects

Industrial parts often have complex geometries and structural heterogeneities such as notches induce stress concentrations in the material and lower its mechanical performances. This is often referred to as the *notch effect*.

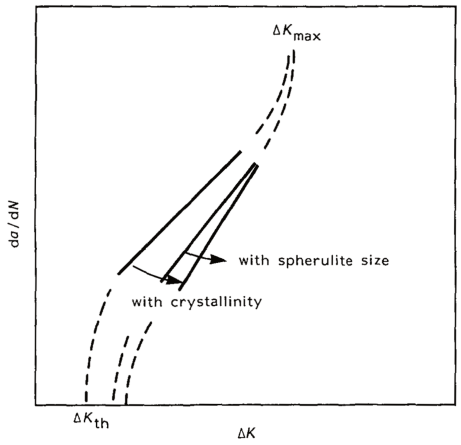
Tools for predictions of fatigue failure from stress concentrations have first been developed for metals. In particular the theory of critical distances (TCF) proposed by Taylor [73]. The critical stress within a given characteristic region of interest (point, line, area, volume), in the vicinity of the notch (fig. 1.19), is taken as the fatigue damage parameter to assess fatigue life.

The equations are:

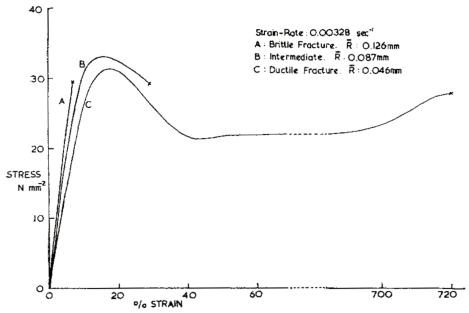
$$\begin{aligned}
\text{Point method: } \sigma_{av} &= \Delta\sigma_1\left(r=\frac{l_0}{2},\theta=0\right)\\
\text{Line method: } \sigma_{av} &= \frac{1}{2l_0}\int_0^{2l_0}\Delta\sigma_1\left(r,\theta=0\right)dr\\
\text{Area method: } \sigma_{av} &= \frac{2}{1.1\pi l_0^2}\int_{-\pi/2}^{\pi/2}\int_0^{l_0}\Delta\sigma_1\left(r,\theta\right)r dr d\theta\\
\text{Volume method: } \sigma_{av} &= \frac{3}{2\pi(1.54l_0)^3}\int_0^{2\pi}\int_0^{\pi/2}\int_0^{1.54l_0}\Delta\sigma_1\left(r,\theta,\varphi\right)r^2\sin\phi dr d\theta d\varphi
\end{aligned} \tag{1.5}$$

with the critical distance l_0 calculated by the empirical El Haddad equation:

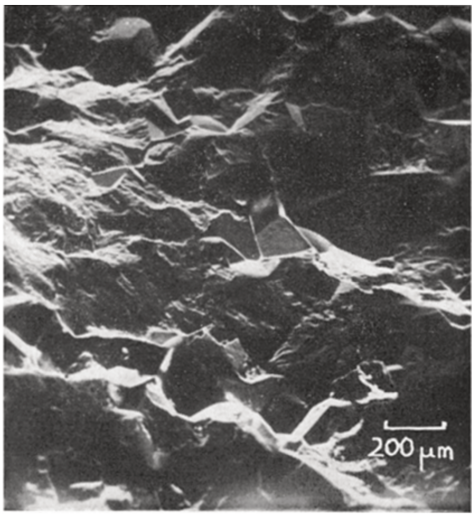
$$l_0 = \frac{1}{\pi}\left(\frac{\Delta K_{th}}{\Delta f_{-1}}\right)^2 \tag{1.6}$$



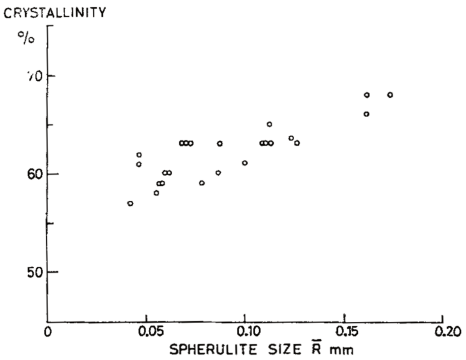
(a) Schematic of the effects of crystallinity and spherulite size on the FCP response of PA6. From Karger-Kocsis [70].



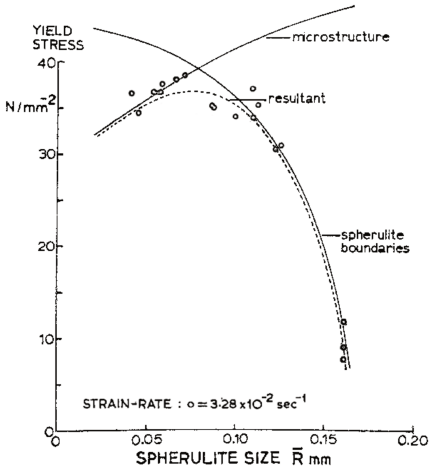
(b) Effect of spherulite size on the stress-strain curve for PP. From Way [71]



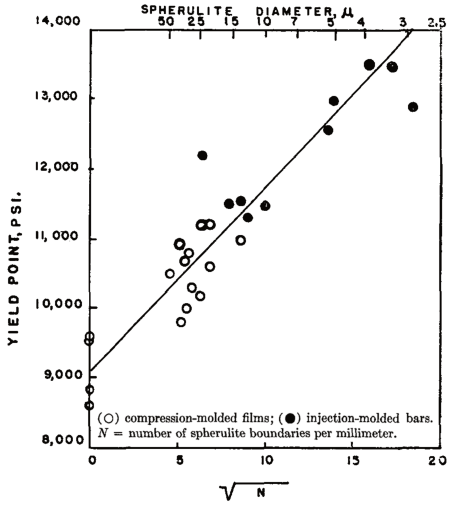
(c) Highly-faceted surface produced by the fracture of PP specimens with large spherulites. From Way [71]



(d) Crystallinity vs. spherulite size in PP. From Way [71]



(e) Effect of the spherulite size on the yield stress in PP, with possible interpretation. Adapted from Way [71]



(f) Effect of the spherulite size on the yield stress in PA66. From Starkweather [72]

Figure 1.18: Influence of the spherulite size on the material properties.

with ΔK_{th} the range of threshold value for fatigue crack propagation, and Δf_{-1} the range of fully reversed axial fatigue limit.

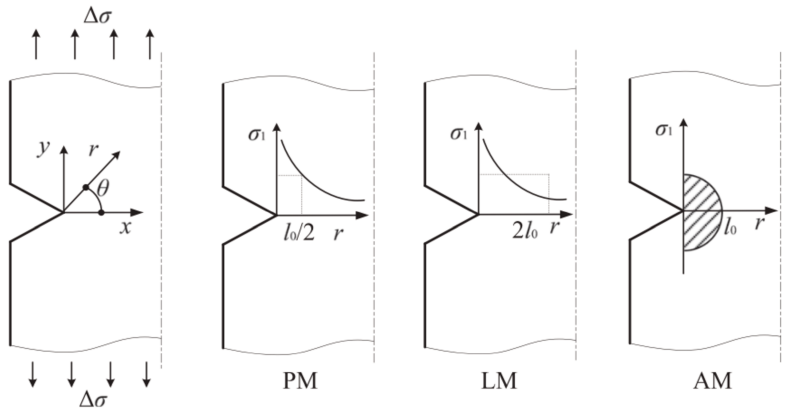


Figure 1.19: Schematic diagrams of Point, Line, and Area methods in TCD. From Luo [74].

For injected thermoplatics, notches can be machined or molded. In this latter case, the presence of notches also induces a change in the local fiber orientation.

Sonsino [75] studied notched PA66GF35 specimens under purely alternative loading (R=-1). Holes were molded at the center of the gauge length with various radii (from 5 to 0.2 mm) inducing a stress concentration factor K_T ranging from 1 to 9.8. Several observations were reported (fig. 1.20):

- fatigue lifetime is reduced with increasing notch severity (higher K_T).
- notch severity has little effect on the slope of the S-N curves, unlike what is usually reported for metals.
- the slope of the S-N curve remains constant (up to 10^7 cycles).
- sensitivity to the notch becomes almost imperceptible at high temperatures (T=130°C).

Bernasconi studied notched specimens by combining synchrotron tomography [38] and DIC strain fields measurements [76]. Results showed that fiber orientation in the proximity of molded notches was not significantly influenced by the position of the injection gate position. Moreover, the maximum local strain values measured at notch root using DIC was related to the fiber orientation pattern of an area larger than that examined by micro-CT. This highlights the necessity to have a good description of the anisotropic microstructure, at the scale of the specimen.

Bernasconi therefore also concluded that in order to accurately model the strain field using FEM around molded notches, it would be required to include information about local fiber orientation and resulting local elastic constants. This justified the later use of *Through Process Modeling* (see section 1.5.1) for the proper numerical simulation of molded notched components [77].

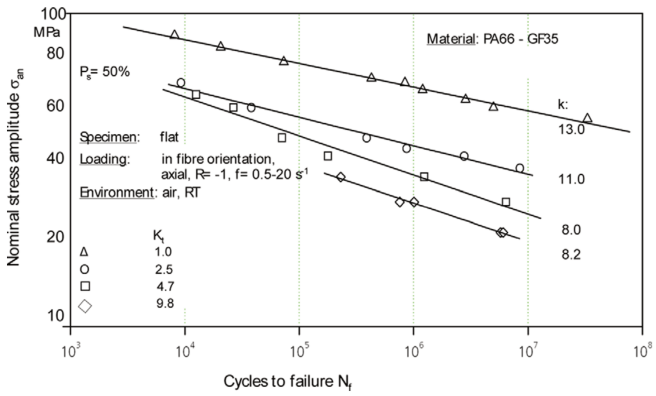


Figure 1.20: Influence of notches on the fatigue strength of PA66GF35. From Sonsino [75].

Finally, Laiarinandrasana *et al.* [78] combined infrared thermography measurements and synchrotron laminography observations for the study of PA66GF35 specimens with molded notches under fatigue loading. This aimed at correlating the maximum dissipation area, evaluated from temperature mappings, with the maximum damage area evaluated from laminography. Moreover laminography provides valuable insight on the various local sources of dissipation due to stress concentration in the bulk material. For example, laminography evidenced a curved notch root under mechanical loading and this change in geometry helped to explain that the maximum dissipation was not located right at the edge of the initial straight notch. Laminography also used to evaluate the micro-porosity within the material. This is important for accurate evaluation of the dissipation sources from thermal measurements as micro-porosity impacts the specific mass and specific heat. Imaging and thermal measurements are thus quite complementary to gain a good understanding of the notch effect.

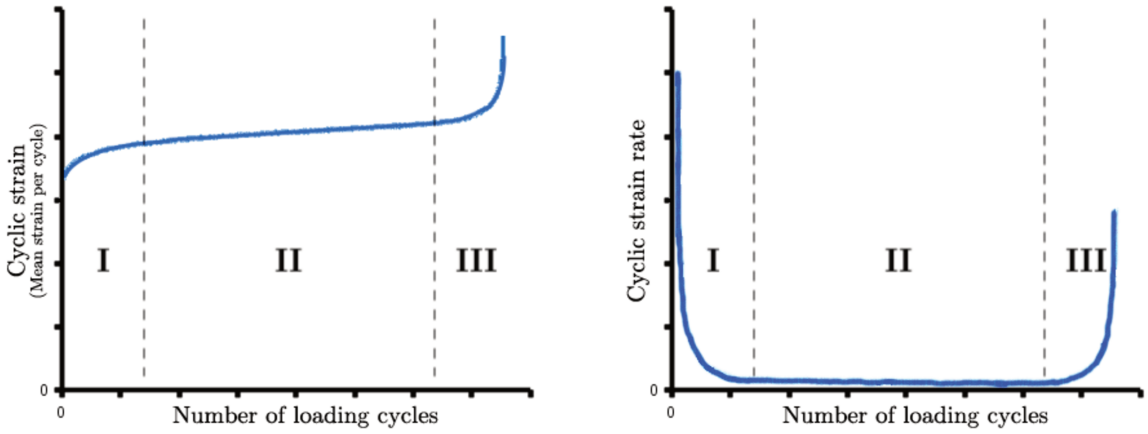
1.2.6 Cyclic creep

Under a fatigue loading with a positive mean stress, the mean strain increases with the number of applied loading cycles.

This effect is reported by several authors and referred to as either *ratcheting* [53], *creep* [37], *fatigue creep* [48], *cyclically induced creep* [79] or *cyclic creep* [57]. In the rest of this work, this phenomenon will be called *cyclic creep* and is key to understand the mechanical response of polymers under fatigue loading.

Plotting the mean strain per cycle - or *cyclic strain* - versus the number of loading cycles yields a curve similar to what would be obtained for a creep test (fig. 1.21). However it should be noticed that the *cyclic strain rate* is much higher that it would be for stationary creep at the same (mean) stress. Parameters of the cyclic loading (stress amplitude, frequency, etc.) have a direct effect on the cyclic creep [53].

Similar to creep, three stages can be defined. During primary creep the cyclic strain increases rapidly until the cyclic strain rate become almost constant. Secondary creep is then reached. This is the longest of the stages, where the cyclic strain steadily increases with the applied loading cycles. Microscopic damage grows progressively in the bulk



(a) Cyclic strain

(b) Cyclic strain rate

Figure 1.21: Schematic of a typical evolution of the cyclic strain and cyclic strain rate during fatigue loading, with controlled load. (For cyclic loading with controlled displacement, cyclic stress relaxation would be observed).

material[7]. Finally, as strain localizes and macroscopic damage begins to expand in the material, tertiary creep is reached. This stage is more pronounced for neat polymer than for the composite material where strain is limited by the presence of fibers. The cyclic strain increases rapidly, until final failure of the specimen.

[7]Damage mechanisms for the neat and reinforced polymer will be presented in section 1.4

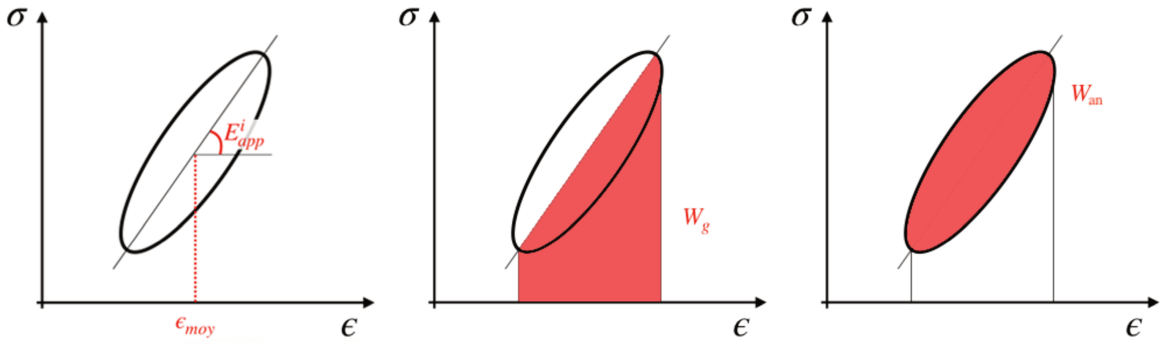
1.3 Fatigue life assessment

Being able to predict the durability of the material is key especially for industrial applications where engineers need to be able to design parts that meet specific requirements. Having a proper durability criterion means that the iterative engineering process of a new part can be done numerically and the costly validation by experimental testing can be limited to an already optimized design.

1.3.1 Mechanical parameters under cyclic loading

Macroscopic parameters, representative of the material effective behavior, are the base of fatigue life assessment approaches.

When considering a load cycle during an uniaxial test on a viscoelastic composite several mechanical quantities can be considered of interest for monitoring. Figure 1.22 illustrates some of these parameters.



(a) Modulus and mean strain (b) Given strain energy W_g (c) Anelastic energy W_{an}

Figure 1.22: Usual mechanical parameters.

- **Apparent modulus,** E_{app} (fig. 1.22(a)). For composite materials a decrease in the apparent modulus is often associated with the development of cyclic damage in the specimen. However it should be noticed that due to the visco-elastic behavior of the polyamide matrix the direct link between damage and modulus drop is not straight forward in our case. The apparent modulus at the i^{th} cycle, E^i_{app}, is calculated from the strain and stress amplitudes as :

$$E^i_{app} = \frac{\sigma^i_{max} - \sigma^i_{min}}{\varepsilon^i_{max} - \varepsilon^i_{min}} \tag{1.7}$$

- **Given total strain energy density per cycle** W_g (fig. 1.22(b)). When considering multiaxial fatigue criteria the given elastic strain energy density is a parameter that is considered to efficiently describe multiaxial fatigue data by many authors [80]. As an energy parameter it is naturally sensitive to the mean stress effect (at constant stress amplitude the given strain energy increases as the mean stress increases).

In the case of our study, since the purely elastic strain energy is difficult to address unambiguously (and independently of a model choice), the total given strain energy over a cycle is considered here and computed as follows:

$$W_g = \int_{t_0}^{t_f} < \sigma \dot{\varepsilon}_t > \ \mathrm{d}t \tag{1.8}$$

where <> stands for the Macaulay brackets, σ the axial stress component and ε_t for the total axial strain component. The total given strain energy W_g is the amount of energy given to the material during loading.

- **Anelastic strain energy per cycle** W_{an} (fig. 1.22(c)). In a general thermodynamic framework, the hysteresis area results from the contribution of intrinsic dissipation, stored energy variation and thermomechanical coupling sources. For pure polyamide, Benaarbia *et al.* [81] have shown that the latter are negligible for PA66 so that the anelastic strain energy density W_{an} per cycle can be written as follows:

$$W_{an} = \int_{cycle} \sigma \ \mathrm{d}\varepsilon = W_s + D_i \tag{1.9}$$

where W_s stands for the stored energy density per cycle and D_i for the intrinsic dissipation (that can be evaluated from thermal measurements under certain conditions, see [82]). It should be noticed that the balance between W_s and D_i is not constant over the whole fatigue life.

- **Axial mean strain** ε_{cycl} (fig. 1.22(a)). Under load controlled fatigue, the mean strain is calculated for every cycle and is classically associated with a ratcheting effect. Yet, for polymer materials and as detailed above, the evolution of this mean strain drift is generally considered as cyclic creep rather than ratcheting that may be associated to different physical deformation mechanisms.

1.3.2 Life assessment criteria

The aim of a fatigue criterion[8] is to determine the number of cycles the material can withstand prior to failure. A criterion can be based on one or several parameters relative to the loading or the mechanical response of the material. Multiple criteria can be found in the literature, often adapted from the formalism developed for metallic materials.

1.3.2.1 Stress-based approach

Simple shear-stress based criteria can be formulated as reported by Launay [86]:

[8] These are not always binary criteria for a given fatigue life (like the Sines and Crossland criteria) but for convenience reasons we will also call a *criterion* a way to compute an estimated fatigue life. This is way shorter than *fatigue life assessment model* and this is quite usually done in the literature [83–85].

$$\log N_f = \frac{\sigma_0 - \Delta J_2(\underline{\underline{\sigma}})}{b} \tag{1.10}$$

with σ_0 and b parameters of the criterion and ΔJ_2 a scalar measure of the octahedral shear-stress intensity. ΔJ_2 can be calculated using the equivalent von Mises stress or the Hill stress to better account for the anisotropy of the material. However these criteria are not sensitive to the mean stress, contrary to what is observed experimentally for polymer based composite material.

Launay [86] subsequently proposed variations of the Crossland, Sines and Dang Van criteria in order to include a dependence to the hydrostatic pressure (maximal or mean value), but with only moderate success, especially on RH50 specimens, probably because of the wide nature of specimens and loading conditions (fig. 1.23).

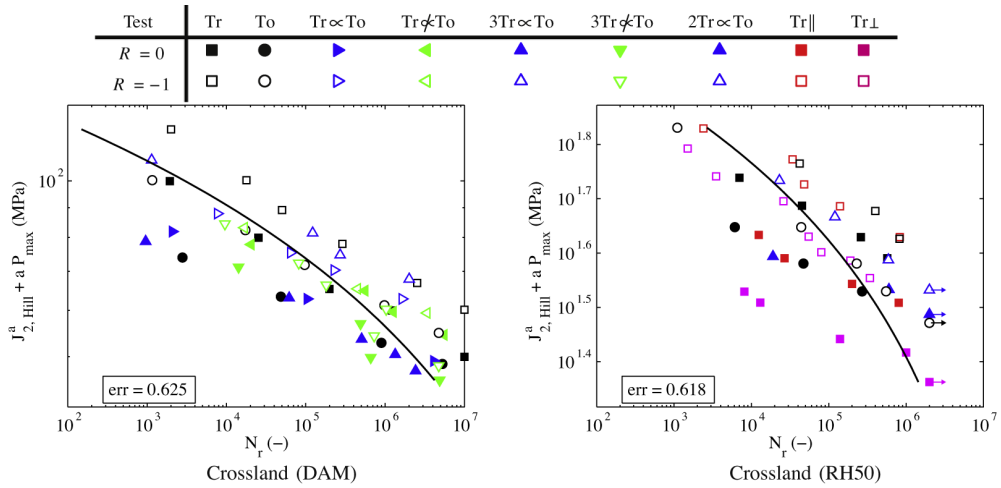


Figure 1.23: Study on tubular and dogbone specimens. From Launay [86].

Bernasconi [50] used a modified Tsai-Hill criterion in order to account for fiber orientation. This yields good results (see fig. 1.10(b)), although being very sensitive to the microstructure of the tested specimen.

Simpler stress-based criteria are tested under multiaxial loading by Klimkeit [83]:

$$\sigma = a(N_f)^{-1/b} \tag{1.11}$$

with a and b parameters of the criterion. σ is chosen a measure of the stress, and Klimkeit tested the maximal principal stress (*principal stress criterion*) and the von Mises stress (*von Mises stress criterion*). These criteria were applied at then end of a TPM with elastic calculations being performed over one loading cycle. Neither of the criteria yielded good results for all the specimen and loading conditions (fig. 1.24).

Fatemi [56] proposed a criterion that seems to yield good results for fully reversed loading of PBT and PA6 specimens under various temperatures and fiber orientations (fig. 1.25). The number of cycles is successfully correlated with an equivalent stress amplitude:

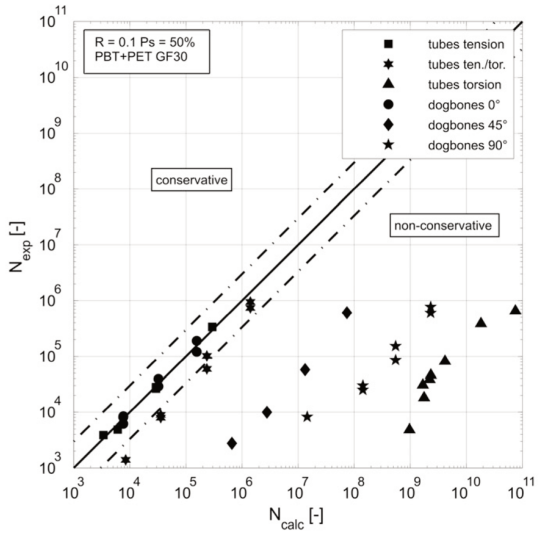


Figure 1.24: Comparison between experimental and assessed fatigue lives using a Principal Stress criterion on PBT-PET GF30 specimens at R=0.1. From Klimkeit [83].

$$\sigma_{eq} = 96.3 \left[\frac{\sigma_u - \sigma_a}{\alpha(\theta)\,\sigma_u^{-0.6}\,(2\sigma_a)^{1.6}} + 1 \right]^{-0.36} \tag{1.12}$$

with σ_u the ultimate tensile strength of the material and σ_a the stress amplitude.

This is branded by the authors as having only "one material parameter" α which can be expressed as a function of fiber orientation θ:

$$\alpha(\theta) = -0.0005\,\theta + 0.118 \tag{1.13}$$

Overall this "general" fatigue life model seems to have six empirical parameters and an explicit dependence to the fiber orientation.

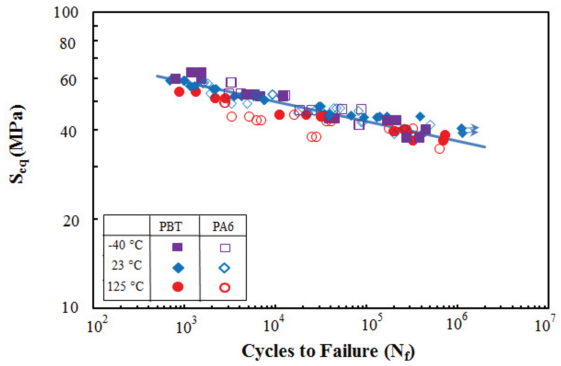


Figure 1.25: Equivalent stress amplitude vs. fatigue life for PBT and PA6 specimens at various temperatures - R=-1 - 0°, 18°, 45°, 90°. From Fatemi [56].

1.3.2.2 Strain-based approach

Launay [86] also proposed a version of the Manson-Coffin equation, initially introduced for predicting the durability of metals in low cycle fatigue under uni-axial loading:

$$\Delta\varepsilon_{vp} \cdot (N_f)^b = C \tag{1.14}$$

with b and C materials parameters and $\Delta\varepsilon_{vp}$ the amplitude of the visco-plastic strain in the direction of the stabilized cycle:

$$\Delta\varepsilon_{vp} = \min_{\underline{\underline{\varepsilon}}^1} \max_{t\in[0,T_{cycle}]} \left[\sqrt{\frac{2}{3}(\underline{\underline{\varepsilon}}^1 - \underline{\underline{\varepsilon}}_{vp}(t) : \underline{\underline{\varepsilon}}^1 - \underline{\underline{\varepsilon}}_{vp}(t)} \right] \tag{1.15}$$

However, as the authors noted themselves "this criterion does not appear to be relevant for reinforced polyamide in dry or conditioned state" as it yields poor results.

1.3.2.3 Energy-based approach

Several types of energy-based criteria have been proposed in the literature, often adapted from the correlation proposed by Morrow [87] for metals between the fatigue life and the dissipated energy per cycle.

Klimkeit [83] studied various types of specimens under multiaxial loading and after TPM and used such a modified criterion:

$$\gamma W_{an} \cdot (N_f)^b = C \tag{1.16}$$

with W_{an} the anelastic energy determined as the area of the hysteresis loop and γ a specific parameter for taking mean stress into account as proposed by Kujawski [88]:

$$\gamma^2 - \frac{\sigma_m}{\sigma_a}\gamma - 1 = 0 \tag{1.17}$$

This yielded satisfactory results for PBT-PET GF30 and PA66 GF35, especially at a load ratio R=-1 for which the criterion was identified. Predictions are much less convincing for R=0.1, especially for PA66 GF35 were they are widely non-conservative.

A similar approach but in a viscoelastic framework was applied by Fouchier [85] at the end of TPM for uniaxial loading at R=0.1 and R=-1. Results were good and proved the importance of the mean stress correction, even though some discrepancies appeared for 45° specimens going up to one decade between the calculated and experimental number of cycles to failure.

Launay [86] also adapted the original criterion by introducing:

$$(W_d^{vp} + \alpha W_d^{ve}) \cdot (N_f)^b = C \tag{1.18}$$

with W_d^{vp} and W_d^{ve} the viscoplastic and viscoelastic dissipated energies. The results obtained using this method are good for tests performed at the load ratios R=0 and R=-1.

Other variations were also used by Kujawski [88], Klimkeit [89] and Launay [86] considering respectively the total strain energy, the elastic strain energy and the anelastic strain energy.

1.3.2.4 Modulus-based approach

Mourglia-Seignobos [48] introduced a criterion based on the apparent modulus $E(T)$ measured in the stabilized regime, at the self-heating temperature T:

$$\frac{\sigma_{max}}{E(T)} = -\lambda \log N_f + \beta \tag{1.19}$$

with λ and β two parameters independent of the temperature.

While not taken into account explicitly in the criterion, the effect of the mean-stress, frequency or damage might be embedded in the variable $E(T)$. Although this is not shown by the authors.

1.3.2.5 Cyclic strain rate-based approach

When considering a visco-elastic material under cyclic loading, cyclic creep may play an important role in the durability of the material while embedding a mean stress sensitivity (see sections 1.2.2.1 and 1.2.6).

This approach closely resembles those for creep of thermoplastic specimens. Under a static imposed load, the secondary creep rate $\dot{\varepsilon}_{crp}$ can directly be related to the time to failure t_f using the Monkman-Grant relationship [90]: $\dot{\varepsilon}_{crp}^{\alpha} \cdot t_f = \varepsilon_c$, where α and ε_c are two parameters of the material. But while many studies have been performed on static creep (a time dependent phenomenon), not much data exists for cyclic creep (a cycle dependent phenomenon) during stress-controlled fatigue testing.

Horst [37] studied a polyamide 6 reinforced with 30wt% short glass fibers and showed that a parameter based on the evolution of the cyclic strain rate (determined from the measurement of the global displacement rate in stage II) could unify fatigue results for two sets of specimens sampled at different positions on an injection molded plate.

Mourglia-Seignobos [48] also showed that this parameter unifies results at different testing temperatures (25°C, 65°C, 140°C) on a polyamide 6,6 reinforced with 30wt% short glass fibers.

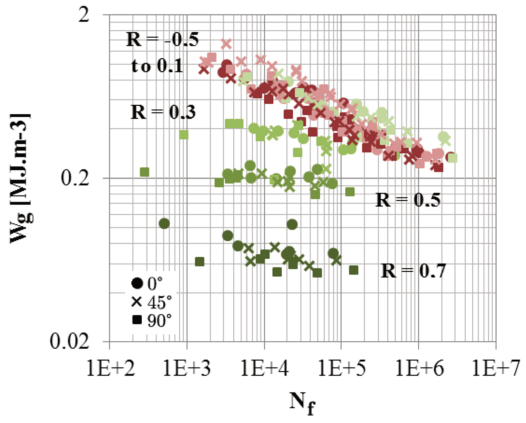
Bernasconi [57] showed that the cyclic strain rate unifies fatigue results for various loading frequencies (1-4 Hz), also on a polyamide 6,6 reinforced with 30wt% short glass fibers.

More recently Rolland [43] used a large data base of more than two hundred fatigue tests to identify a cyclic strain rate based criterion that yields particularly good results for positive load ratios. Whereas the energetic parameters all embed a load-ratio sensitivity (figs. 1.26(a) and 1.26(b)), the cyclic strain rate is the only parameter unifying fatigue results over most of the database (fig. 1.26(c)).

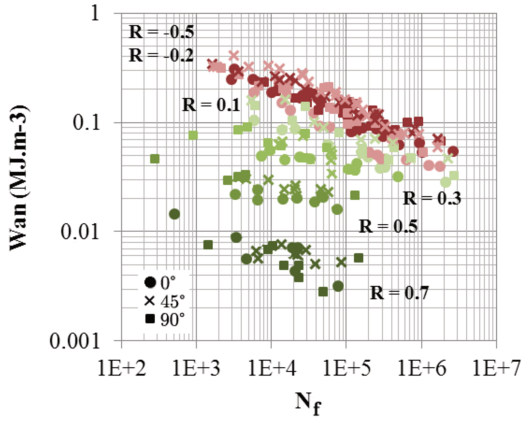
The lifetime was thus estimated from the cyclic strain rate $\dot{\varepsilon}_{cycl}$ at mid fatigue life:

$$N_f = A\left(\frac{\dot{\varepsilon}_{cycl}}{\dot{\varepsilon}_0}\right)^n \tag{1.20}$$

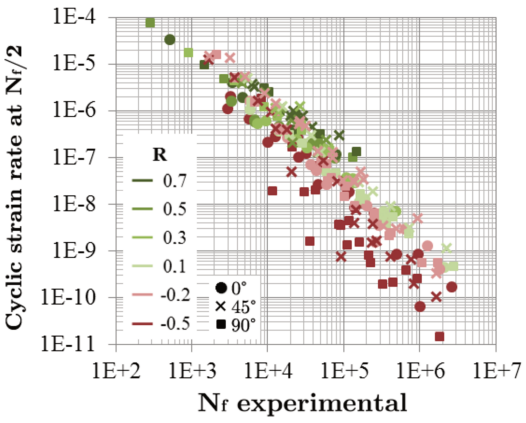
The calculated lifetime is then compared with the one obtained experimentally. Figure 1.26(d) shows that the estimate of the experimental lifetime by this quantity is very good, except for the results obtained at negative load ratio and especially at $R = -0.5$.



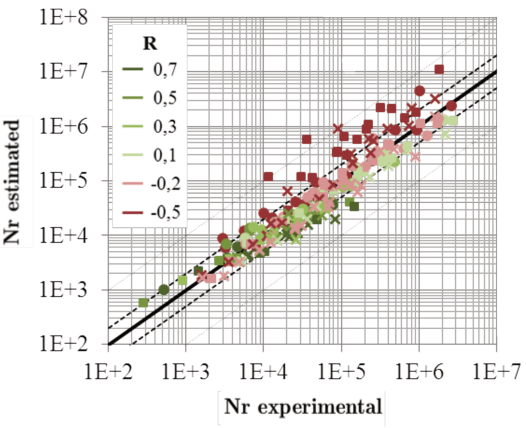
(a) W_g vs. N_f



(b) W_{an} vs. N_f



(c) Cyclic strain rate vs. N_f



(d) Estimated service life using eq. (1.20) vs. experimental number of cycle to failure. Scatter bands of factor 2 and 10 are marked in dashed and dotted lines respectively

Figure 1.26: Study of PA66GF30 specimens - RH50 - f = 3Hz - forced convection. From Rolland [43]

When considering a criterion based on the cyclic strain rate, the question often arises of what is hidden being such a parameter. Is it viscosity, plasticity and/or damage? And how to differentiate these different phenomena.

Although not discussed by the aforementioned authors that used such type of strain-rate based criterion, one could argue that the distinction between viscosity, plasticity and damage becomes tenuous at lower scales.

In the complex internal structure of semi-crystalline polymers, mechanical loading triggers chain mobility and disentanglement. This in turn can induce chain scission, cavitation and crystal plasticity [91; 92]. Crystalline lamella fragmentation has been reported to occur at very low strain levels, even without a cavitation phenomenon [18]. In that case, fragmentation of the crystalline lamella leaves the polymer chains in an amorphous state and does not necessarily lead to the formation of *voids*. All those mechanisms that are very local (nano to micro scale), complex and inhomogeneous within a spherulite [93] contribute to the progressive strain increase during fatigue loading.

Cyclic creep is thus here considered as the macroscopic consequence of these mechanisms, where viscous chain mobility, plastic deformation and damage process are almost indistinguishable.

1.4 Damage mechanisms

1.4.1 Experimental techniques

In order to investigate the damage process in the material several techniques can be used. The choice of the technique depends if the investigation is conducted post-mortem on broken samples, ex-situ on in-situ during mechanical loading. Post-mortem observations of a broken sample are the most easy to perform and are usually done using SEM[9]. This allows for a detailed imaging of the fracture surface, and is of relative easy and standard use.

Some authors have performed thin slices on broken fatigue-damaged polymer in order to use cross-polarized microscopy[10] for observation of damage close to spherulites [79].

Ex-situ observations, meaning the mechanical test has to be interrupted and sample taken out of the testing machine for observation, is nowadays often be performed using micro-tomography[11]. This allows for the assessment of the damage in the bulk of the material.

In-situ testing allows for the testing and observation to be performed in the same place, and more and more often at the same time.

SEM and micro-tomography can be used for in-situ testing, providing adequate setup is available.

Moreover, damage monitoring can be performed using acoustic emission [94; 95]. Damage mechanisms can be differentiated and their position evaluated.

Surface damage process during fatigue crack propagation has also been directly observed by some authors using an optical microscope mounted on the testing machine [51].

Other studies focusing on damage at lower scales on polymers include in-situ observations using AFM [17; 18; 96; 97] and X-ray scattering [48].

1.4.2 Damage mechanisms in the neat polymer

1.4.2.1 Quasi-static tensile tests

Regarding micro-damage in the polymer during quasi-static tensile testing, Galeski *et al.* [98] analyzed spherulitic damage in bulk PA6 during quasi-static tensile testing. By performing observations using cross-polarized microscopy and Transmission Electron Microscopy (TEM) on thin sections cut from the neck regions of deformed specimens, they noted that "equatorial regions of the spherulites are particularly susceptible to microvoiding mechanisms".

Transition or competition between the different types of micro-mechanisms (chain slip, disentanglement, cavitation, crystal plasticity, lamella fragmentation) is complex.

[9] Details on observation using SEM are given in section 2.3.2

[10] Details on observations using cross-polarized microscopy are given in section 2.3.1

[11] Details on observations using micro-tomography are given in section 2.3.3

The complexity stems from the scale involved and from the complicated and poorly understood spherulitic structure where they take place (see section 1.1.2.2).

Yet it is now established that nano-voiding is induced by the local presence of a triaxial stress state and that larger micrometric cavities are subsequently developed when the lamellar structure is transformed into a fibrillar, or crazing, structure [92].

Crazing is a transition between damage initiation and the growth of micro-cracks and is widely described in the literature from an experimental [99] as well as a theoretical [100] point of view. Crazing occurs when amorphous polymer chains orient themselves under the applied stress. Slip can then occurs in the crystalline lamellae, as well as chain scission or disentanglement [101]. Connector bridges progressively break and damage progresses as a crack that will eventually lead to failure.

However Detrez [18] used AFM observations to show that lamella fragmentation can occur before the generation of crazes, and thus in the very early stages of loading.

It also worth mentioning that cavitation is the one early stage of damage during tensile loading but this is not necessarily true in other modes of deformation than uniaxial tension. Bartczak [93] reported that "morphological transformations from initial isotropic structure into microfibrils [...] can take place without formation of any cavities or microvoids in the regime of plane-strain or uniaxial compression".

1.4.2.2 Fatigue tensile tests

Early fatigue damage as cavitation and micro-cracks was studied in the neat polymer in three previous works that tried to link these damage marker with the spherulitic microstructure of the polymer.

The first one concerns the earlier work of Andrews and Walker [79] regarding fatigue fracture in PE under low loading frequency (0.01-1Hz). They observed slices of damaged samples and reported "short cracks running straight for distances comparable to the spherulite size and frequently along the inter-spherulite boundaries" (see arrows on fig. 1.27).

Later Bretz [65; 102] suggested that semi-crystalline polymers fracture both in an inter-spherulitic and an intra-spherulitic manner (also called *trans-spherulitic* by the authors). The authors performed uniaxial fatigue testing at $10Hz$, but precise loading conditions are unclear. The quality of the images is lacking of sufficient details to make firm conclusion and, as noted by the authors themselves, more work is needed in this area [102].

More recently, the work of Mourglia-Seignobos [48] focused on damage initiation at the nano- and micro-scales, within the semi-crystalline polymer. The following scenario was suggested for fatigue induced damage:

- Cavities grow in the polymer. Cavities diameters are in the 20-220 nm range.
- During the first stages of fatigue, the number of those cavities increases but their volumes remain unchanged.
- Cavities grow to reach the size of a few microns.

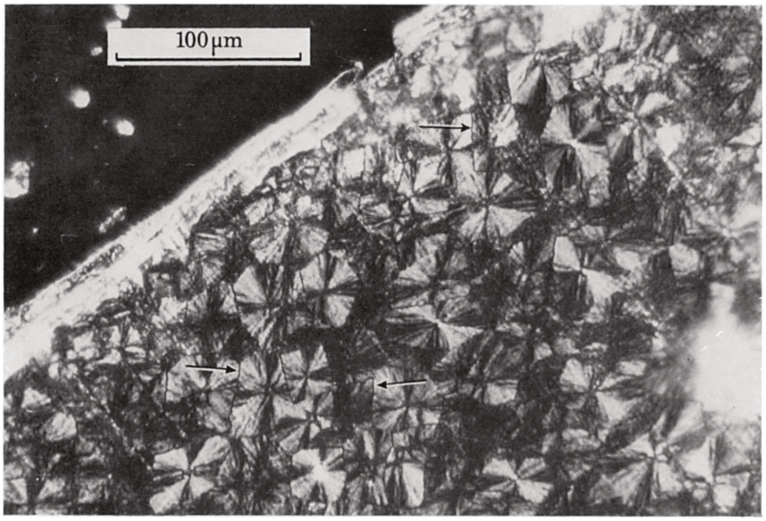


Figure 1.27: Section of polyethylene after fatigue showing "many inter-spherulitic cracks". From Andrews [79].

- Cavities join to form micro-cracks.
- Micro-cracks grow and join forming a macro-crack leading to the specimen failure.

Based on SAXS measurements, Mourglia-Seignobos reported cavitation to occur in domains oriented perpendicularly to the stress. The authors suggest that this damage is *very likely* located in the equatorial plane of spherulites, between crystalline lamellae.

As no general agreement seems to exist, further understanding and observations evidencing this spherulitic fatigue damage are required, especially in order to validate a damage scenario.

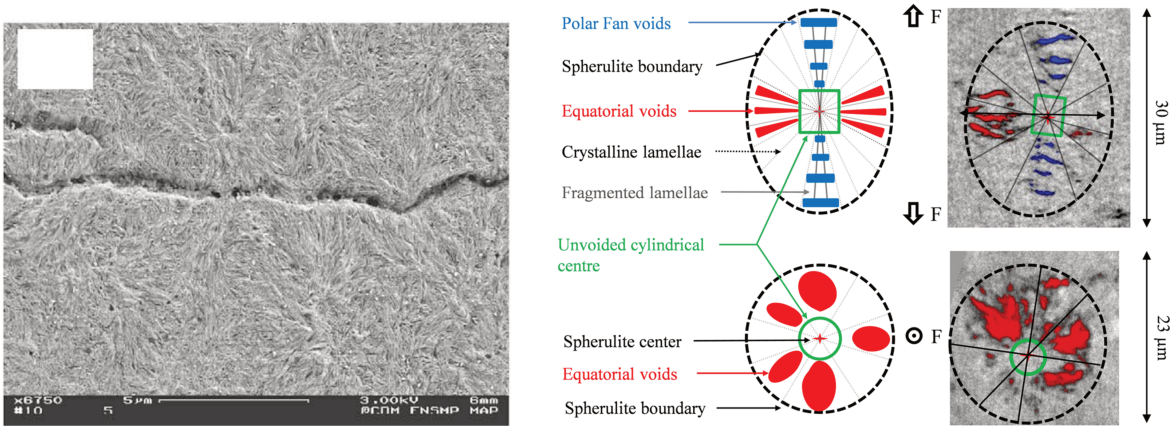
1.4.2.3 Creep tests

As we will detail in the rest of the manuscript, creep and fatigue damage have some similarities for polymer materials. It is thus worth detailing some of the most important factors of creep damage. We will here limit ourselves to quick overview on creep damage mechanisms of unreinforced semi-crystalline polymers that will be relevant for our analysis.

Creep fracture of a medium density ethylene-butene copolymer was studied by Ben Hadj Hamouda [23]. Based on SEM observations, he noted that intraspherulitic creep damage was similar to craze structure and perpendicular to the principal stress, thus often localized in the equatorial plane of the spherulite (fig. 1.28(a)).

More recently, Selles *et al.* [22; 103] studied the influence of the spherulitic structure on the damage mechanisms for the creep failure of PA6. Using magnified synchrotron radiation holotomography with a spatial resolution of 50 nm, they showed extensive damage taking place both in the polar regions of the spherulites and in the

equatorial plane (fig. 1.28(b)). Very little, if any, damage was observed at the center of the spherulite.



(a) Inter-lamellar creep damage. From Ben Hadj Hamouda [23].

(b) Void arrangements within a deformed spherulite. From Selles [22].

Figure 1.28: Spherulitic creep damage mechanisms.

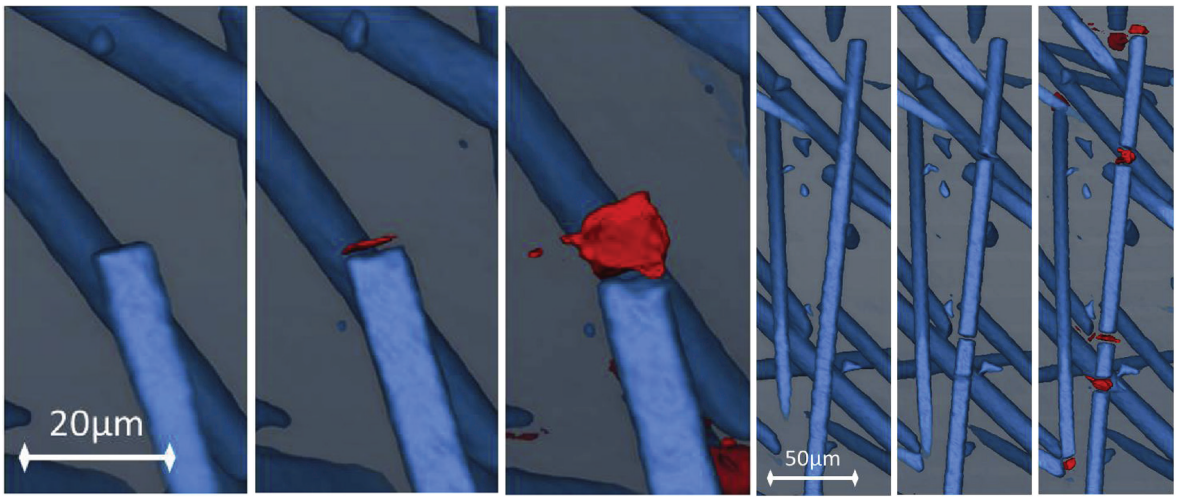
1.4.3 Damage mechanisms in the composite material

1.4.3.1 Quasi-static tensile tests

During quasi-static uniaxial tensile loading, voiding and damage in the material can be observed using in-situ tomography testing.

Four main mechanisms have been described in the literature [104]:

- **damage at fiber tip** is the main type of damage (figs. 1.29(a) to 1.29(c)). It is explained by both the lack of proper adhesion between the polymer and the glass, and by the fiber acting as a local stress concentrator. This results in the early and continuous growth of damage in these areas, until final failure.
- **fiber failure** is also a major type of damage during quasi-static loading (figs. 1.29(d) to 1.29(f)). Around two third of the fibers will eventually break during loading. Failure occurs preferentially at points of crossing between fibers, where stress concentrations are important. It is worth noting that 90° fibers can even fail transversely to the tensile loading direction, along their whole length.
- **debonding** at the fiber-matrix interface occurs rather late during testing. It is likely triggered by a local stress concentration due to the confinement of the polymer matrix. Debonding can later progress along the interface.
- **matrix damage** in the bulk of the material initiates from the other damage mechanisms mentioned above and can reach large volumes, mostly with a spherical shape, until the failure of the specimen.



(a) $\varepsilon_1 = 0.0\%$ (b) $\varepsilon_1 = 2.1\%$ (c) $\varepsilon_1 = 4.2\%$ (d) $\varepsilon_1 = 0\%$ (e) $\varepsilon_1 = 2.1\%$ (f) $\varepsilon_1 = 4.2\%$

Figure 1.29: Damage at fiber tip and fiber failure as observed during in situ microtomography tensile testing. From Rolland [104]

1.4.3.2 Fatigue tensile tests

Damage mechanisms caused by fatigue loading of reinforced PA66 have long been described using post-mortem SEM observations. This allowed Sato [105] and later Horst [37] to identify a first damage scenario (fig. 1.30):

- Damage initiates at the fiber ends (1).
- Microfailure progresses along the fiber-matrix interface (2).
- Plastic deformation bands appear in the polymer matrix (3).
- Crack opens and progresses slowly (4).
- Fast crack propagation leading to complete failure.

Nouri [106][12] reported that damage initiation is a combination of micro-cracks forming at the fiber-matrix interface and cavitation in the polymer matrix. Cavitation damage begins early in the material life, after a *low number* of loading cycles.

These observations were more recently backed and completed by tomographic (fig. 1.31) data [39; 43], giving access to quantitative data in the bulk of the material. The elementary mechanisms occurring during the fatigue lifetime of the short glass fiber reinforced PA6.6 haveare evidenced: fiber failure, debonding or damage at fiber ends and matrix damages (cavitation, fibrillation and cracks formation).

[12]The damage scenario suggested by based Nouri is based on the work of Toubal [107] on the fatigue damage of carbon/epoxy composite laminates, assessed by thermography measurements. It remains qualitative and transposition to thermoplastics as done by Nouri should be done with some caution.

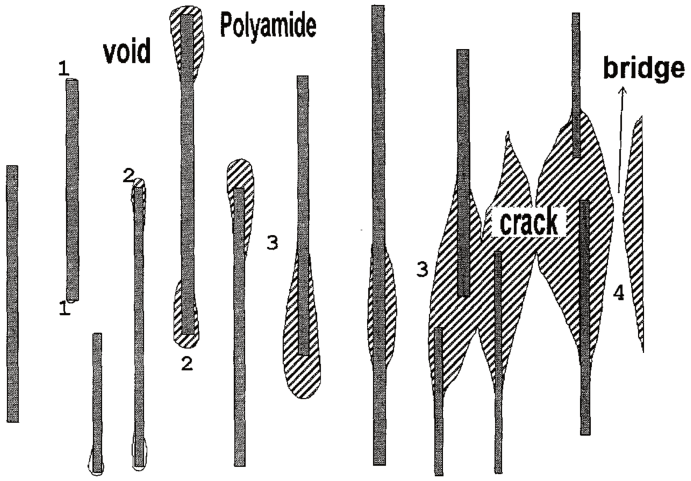


Figure 1.30: Failure mechanisms in fatigue. From Horst [37]

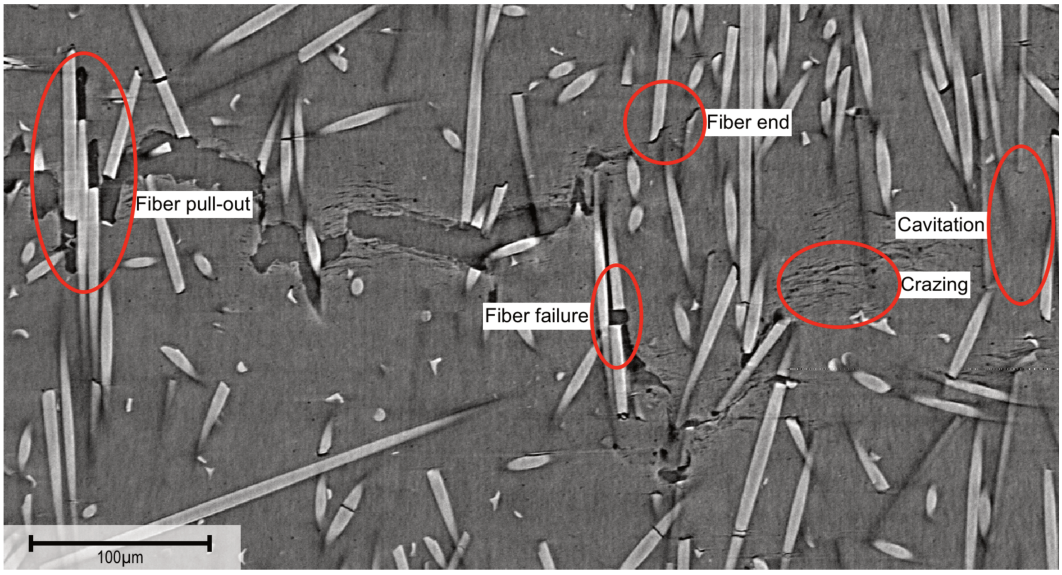


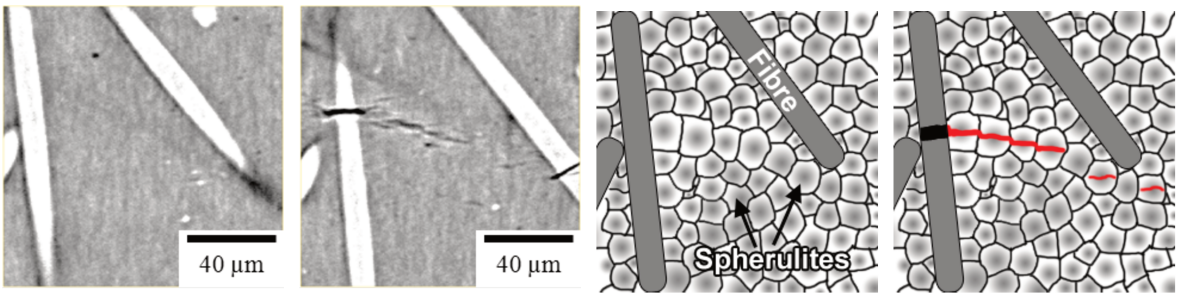
Figure 1.31: Fatigue damage mechanisms as observed by synchrotron tomography.

In-situ testing using high resolution synchrotron X-ray tomography [26] was especially useful in studying the very early stages of fatigue damage and establish the complete sequence leading to the final failure. In particular, matrix cavitation was found to play a major role in the onset of fatigue damage in the bulk of the material. The cavitation process develops in two types of regions:

- highly reinforced areas where the presence of packed fibers induces highly triaxial stress fields.
- poorly reinforced areas where strain levels can be higher, allowing for increased matrix deformation.

It was concluded that controlling the cavitation behavior of the polymer may lead to significantly enhanced fatigue properties of the composite material.

It was also shown that subsequent short fatigue cracks in SFRP propagate with a characteristic length. These microscopic cracks/crazing structures exhibits length of about $25\mu m$ and progress in well defined steps (figs. 1.32(a) and 1.32(b)). Hypothesis was thus made that fatigue damage in the matrix is intra-spherulitic and that cracks advance by opening spherulites in their equatorial planes (figs. 1.32(c) and 1.32(d)), this spherulite opening being triggered by cavitation.



(a) $N/N_f = 0.0\%$ (b) $N/N_f = 60.8\%$ (c) $N/N_f = 0.0\%$ (d) $N/N_f = 60.8\%$

Figure 1.32: Microcracks observed by micro-tomography and proposed damage mechanism as a function of spherulite organization - RH50 - 0° specimen - $N_f = 2468$ cycles. From Rolland [26].

1.5 Numerical modeling

In this part we will give and overview various approaches for the numerical modeling at different scales and with different application. We will first introduce through process modeling for injection molded parts. We will then focus on the mechanical simulation of macroscopic specimens and detail some aspects of constitutive modeling. Finally we will focus on the microscopic scale both in terms of micro-mechanical modeling, microstructure calculations and spherulitic modeling.

1.5.1 Through process modeling

Through Process Modeling (TPM) is a methodology to compute the local mechanical properties of a part, in our case a short-fiber reinforced polymer. It is based on an homogenization process similar to what was introduced above and can be used as an intermediary step before mechanical simulation and the use of a fatigue criterion as presented below.

The first step of TPM is the simulation of the injection process. This yields the local fiber orientation in the part.

The second step is the homogenization process in order to compute the mechanical properties based on the known orientation tensor of the fibers. This yields the local effective mechanical properties in the part.

Finally, classical Finite Element Modeling (FEM) calculations can be performed on the part from which the necessary information can then be extracted to apply the chosen durability criterion.

1.5.2 Macroscopic mechanical modeling

1.5.2.1 Constitutive modeling

The approach for constitutive modeling detailed below is the one used by Boisot [108] for the study of PA11.

The material is assumed to be elasto-visco-plastic, yielding the usual partition of the total strain $\underline{\underline{\varepsilon}}$ tensor:

$$\underline{\underline{\varepsilon}} = \underline{\underline{\varepsilon}}^{e} + \underline{\underline{\varepsilon}}^{vp} \tag{1.21}$$

with $\underline{\underline{\varepsilon}}^{e}$ the elastic strain and $\underline{\underline{\varepsilon}}^{vp}$ the visco-platic strain. Visco-elastic strain is neglected as an independent contribution to the total strain (otherwise a fourth term would be added to eq. (1.21)).

Plastic strain rate is defined using a Norton law:

$$\dot{p} = \dot{\varepsilon}_0 \left(\frac{\phi}{K} \right)^n \tag{1.22}$$

with $\dot{\varepsilon}_0 = 1s^{-1}$. Parameter K (MPa) controls the intensity of the plastic strain rate, n controls the non-linearity of the visco-plastic behavior and ϕ is the yield surface defined by:

$$\phi = \sigma_* - \sigma_y(p) \tag{1.23}$$

with σ_* the effective stress (dependent of the void fraction in the material, and equal to the von Mises stress if there is no porosity - see eq. (1.25)) and $\sigma_y(p)$ the yield stress of the material.

$\sigma_y(p)$ is defined using an isotropic hardening model given by:

$$\sigma_y(p) = \sigma_0 + Q\,(1 - \exp(-bp)) \tag{1.24}$$

Several parameters thus need to be identified:

- parameters for the linear elastic behavior: the Young modulus E and Poisson ratio ν.
- parameters of the Norton law for the viscous behavior: K and n.
- parameters of the isotropic hardening model for the plastic behavior : σ_0, Q and b.

It can be noted that in some studies, including the most recent modeling works of creep behavior of polymers, the authors used a *two-mechanisms, two-criteria* model [109; 110]. This model is mostly similar to the one presented above but all set of equations are doubled to account for the two mechanisms.

The use of such model comes from the bi-linearity of the strain-rate *vs.* stress curves during creep tests (fig. 1.33). Authors commonly relate these two mechanisms to the two phases (crystalline and amorphous) of the polymer, even though experimental support for such claim seems to be lacking.

However, for the fatigue loading conditions studied in this work no bilinear behavior were found. A simpler *one-mechanism, one-criterion* was thus used in our study.

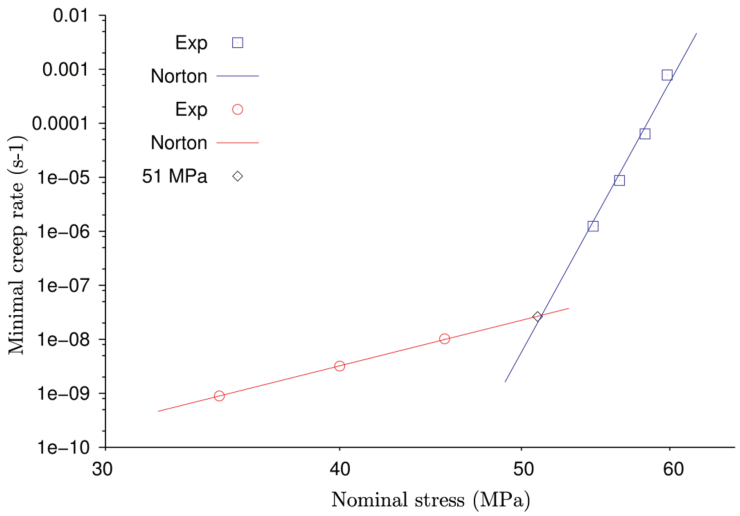


Figure 1.33: Creep rate vs. Applied stress. Adapted from Selles [103].

1.5.2.2 The GTN damage model

In order to model the loss of mechanical properties under mechanical loading, a damage model can be added to the numerical simulation. Several such models and variants exist in the literature and Boisot [108] provided a detailed analysis of the progressive development of these works since the end of the 1960s.

The GTN model is based on the original work of Gurson [111] on a single spherical void in a plastic matrix. The original criterion was later modified by Tvergaard and Needleman [112] in order to account for the interaction between several voids and the growth of those voids.

This yields the following criterion, as implemented in the Finite-Elements code ZeBuLoN [113] :

$$\Phi(\underline{\underline{\Sigma}}, f_*, \sigma_*) = \frac{\Sigma_{eq}^2}{\sigma_*^2} + 2q_1 f \cosh\left(\frac{q_2 \Sigma_{kk}}{2\sigma_*}\right) - 1 - q_1^2 f^2 = 0 \tag{1.25}$$

With Σ_{eq} the macroscopic equivalent von Mises stress, Σ_{kk} the trace of the macroscopic stress tensor, and f the porosity. Identification of the parameters q_1 and q_2 is fully empirical and varies between authors. The aims is to determines the best parameters following various criteria:

- Tvergaard [114] showed that $q_1 = 1.5$ and $q_2 = 1$ yielded an improved overall estimation of the strain evolution and shear band orientation.
- Lafarge [115] performed a more detailed sensitivity analysis and showed that $q_1 = 0.8$ and a variable q_2 as a function of the maximal principal strain would yield better estimation of the bulk damage kinetics.
- Selles [103] adjusted the parameters value at $q_1 = 1.62$ and $q_2 = 1.25$ based on the creep strain evolution and the agreement with damage localization observed by synchrotron radiation tomography.

Equation eq. (1.25) defines σ_*, the scalar effective stress, as a function of the porosity and the macroscopic stress.

This gives the expression for the plastic potential ϕ as a function of σ_*, and the matrix yield stress σ_y:

$$\phi = \sigma_* - \sigma_y \tag{1.26}$$

The plastic strain rate is thus determined using the normality rule:

$$\underline{\underline{\varepsilon}}^{vp} = (1-f)\dot{p}\frac{\partial \sigma_*}{\partial \underline{\underline{\sigma}}} \tag{1.27}$$

And supposing the matrix to be incompressible, the growth of the cavities is controlled by:

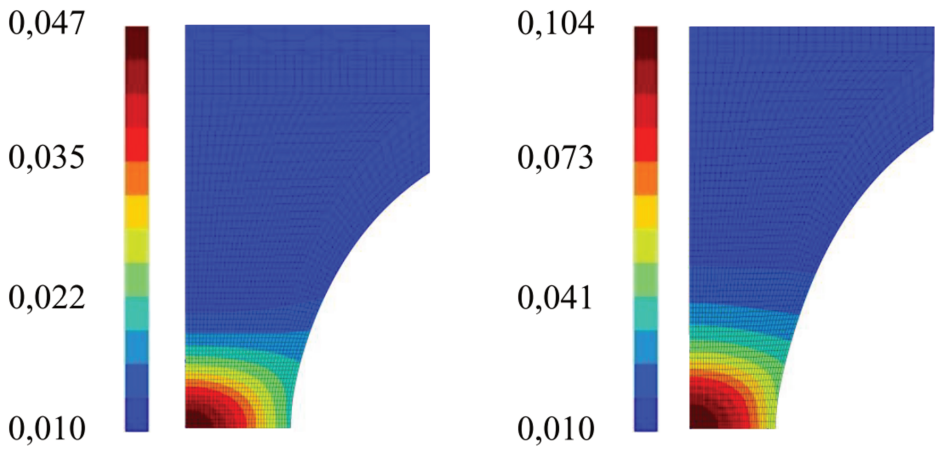
$$\dot{f} = (1-f)\mathrm{tr}[\underline{\underline{\dot{\varepsilon}}}^{vp}] \tag{1.28}$$

Modeling can also account for nucleation and coalescence of voids. This was notably implemented by Besson [116] based on the models of Chu and Needleman [117] for nucleation, and the models of Thomason [118] and subsequent adaptations by Tvergaard and Needleman [112] for coalescence.

However Selles [103] noted that void nucleation has not been evidenced experimentally and that porosity evolution is only resulting from the growth of pre-existing voids. This raises questions about what is a cavity in its initial stage and adds to the discussion regarding the earliest stages of damage, but helps justify that models can be simplified to only account for the initial presence of a void fraction and for subsequent cavity growth in the polymer.

Moreover the coalescence of voids is considered to be really fast in semi-crystalline polymers, as noted by Poulet. It occurs in the very last instant before final failure, and can be neglected in some modeling works [103] depending on the aim of the numerical analysis.

Examples of computed void volume fraction under quasi-static and creep loading are given in fig. 1.34.



(a) Quasi-static loading. At maximal nominal stress

(b) Creep loading. At the end of the secondary stage

Figure 1.34: Computed void volume fraction for PA6 axisymmetric specimens. From Selles [103]

1.5.3 Modeling at the microscopic scale

1.5.4 Micro-mechanical modeling

Micro-mechanical modeling aims at representing the mechanical behavior of the composite material by considering the behavior of its different phases.

The effective behavior is computed by studying the mechanical response of an heterogeneous unit cell and performing an homogeneization in order to obtain an equivalent homogeneous material. This unit cell that needs to be representative of the whole material is called a Representative Elementary Volume (REV).

Two main type of calculations can be performed:

- Full-field methods aim at the explicit calculation of the local mechanical fields in the REV. They are time consuming but yield important information for the understanding of local phenomena. It is similar to the microstructure modeling detailed below.
- Mean-field methods rely on a partial description of the microstructure and yield an average value of the mechanical fields for each phase. They provide faster results, as often required for industrial applications.

Carrere [119] introduced a model for the prediction of failure of laminates composite under triaxial loadings. It introduces micro-mechanical aspects (e.g. the effect of the local debonding) at the mesoscopic scale. It is also sensitive to the various modes of failure for fibers (fiber tension, fiber compression) and inter-fiber (matrix or fiber/matrix failure modes).

The model proposed by Despringre [120] is based on SEM and tomographic observations. The modified Mori-Tanaka method includes damage evolution laws for three different damage mechanisms: fiber failure, matrix micro-cracking and damage at the interface.

1.5.4.1 Microstructure modeling: context and methods

Microstructure modeling is an efficient approach to model the behavior of heterogenous materials at the local scale. It has the potential to yield precious insight on the local mechanical fields that trigger the initiation of the different damage mechanisms observed in the material.

Microstructure modeling of short-fiber reinforced thermoplastic can be performed using a conventional Finite Element (FE) approach or a Fast Fourier Transform (FFT) based method.

FE microstructure modeling was performed by Horst [37] and Klimkeit [121] on 2D artificial microstructures in order to study respectively damage at fiber end and stress along fibers. Belmonte [122] performed 3D micro-modeling on a small microstructure based on tomographic data of a notched specimen.

FFT based microstructure modeling has been proposed for complex microstructures [123] such as poly-crystals, reinforced concrete [124] or short fiber reinforced thermoplastics [125]. This method is based on the exact expression of the Green function for a homogeneous linear elastic reference material. A Lippman-Schwinger equation is solved in the Fourier domain iteratively until convergence is reached. For non-linear materials the method is performed step by step in time.

Details on the mathematical formalism of the method are quite out of the scope of this work and can be found in the original paper by Moulinec and Suquet [123], as well as in the many works based on this method [124; 125].

The use of the FFT method relies on a grid description of the microstructure, each *voxel* being affected to a given material. It thus allows for a simulation of a given

region of interest directly from tomographic data. This gives the FFT method two main advantages:

- the need to mesh the microstructure disappears as the FFT algorithm relies solely on a binary description of the phases inside the volume.
- computed local mechanical fields can easily be compared to the observed damage on tomography images.

1.5.4.2 Microstructure modeling: results

Klimkeit and El Habib [121] performed calculations on a 2D model of fibers all oriented in the loading direction of a tensile test. The matrix is considered elastic, and perfectly bonded to the fibers. Although simplistic, this model allowed to highlight the stress concentrations at fiber tip especially when adjacent to other fibers (fig. 1.35), in area that are known to be prone to damage experimentally.

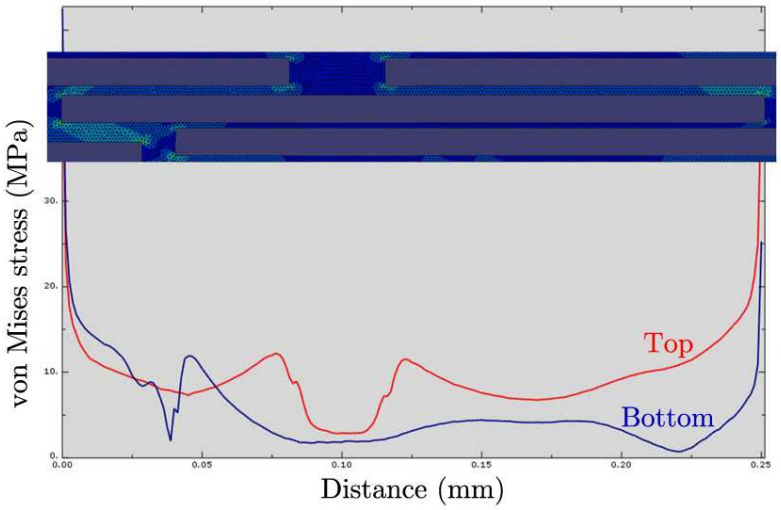


Figure 1.35: Plot of the von Mises stress along a fiber. From Klimkeit [121].

The 2D model of Horst [37] is focused on the tip of a single fiber in an elasto-plastic matrix. The matrix is not bonded to the end of the fiber (at the tip and along the fiber near the tip), to model the lack of sizing (see section 1.1.3.3). As strain increases, the model shows the void growth at fiber tip (fig. 1.36). A consequence of this opening is a change in the direction of the maximal principal stress towards a direction more perpendicular to the fiber axis. The point of highest shear stress along thus moves farther from the debonded area. Tensile stress is always maximal near the debonded area and decreases along the fiber.

Belmonte [122] reconstructed a 3D mesh from tomographic data of a small microstructure. He showed that the fatigue crack initiated close to the notch tip, in a densely reinforced volume subjected to significant stress concentration (fig. 1.37).

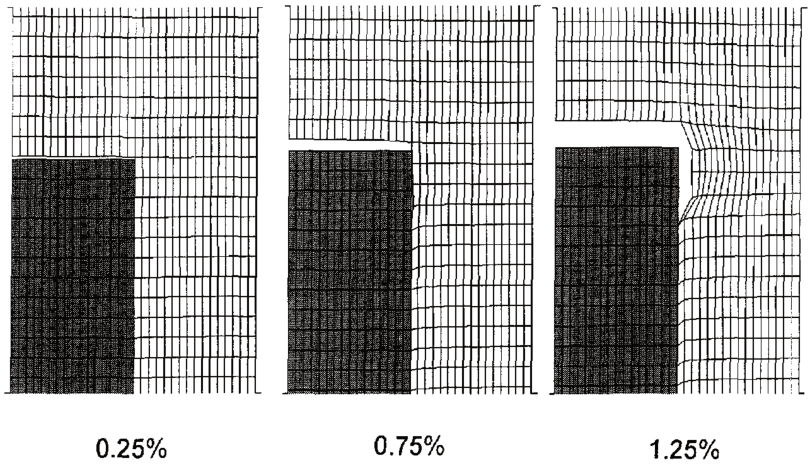


Figure 1.36: Deformations at the fiber end. Overall imposed strain are indicated. From Horst [37].

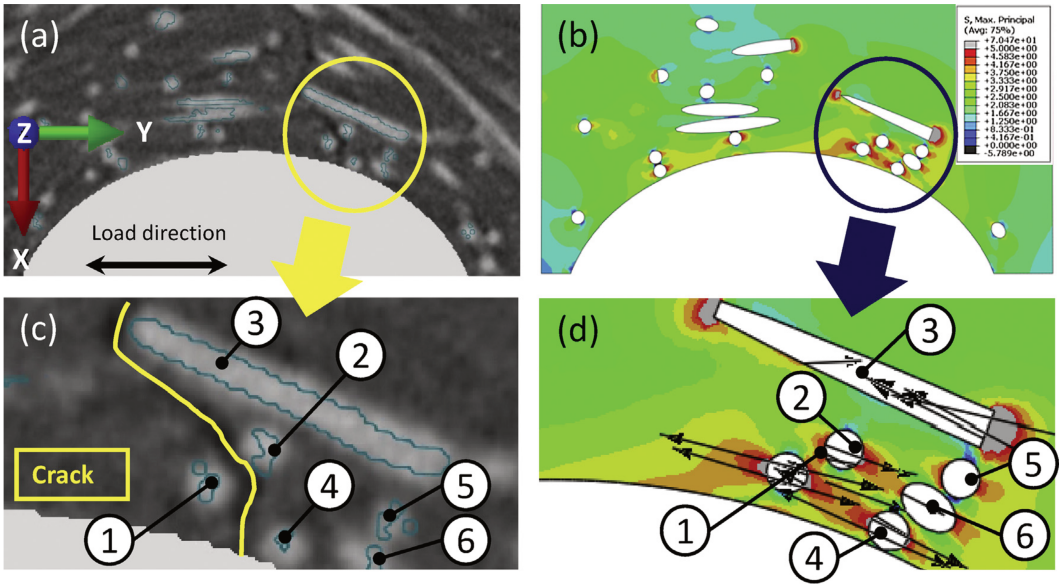
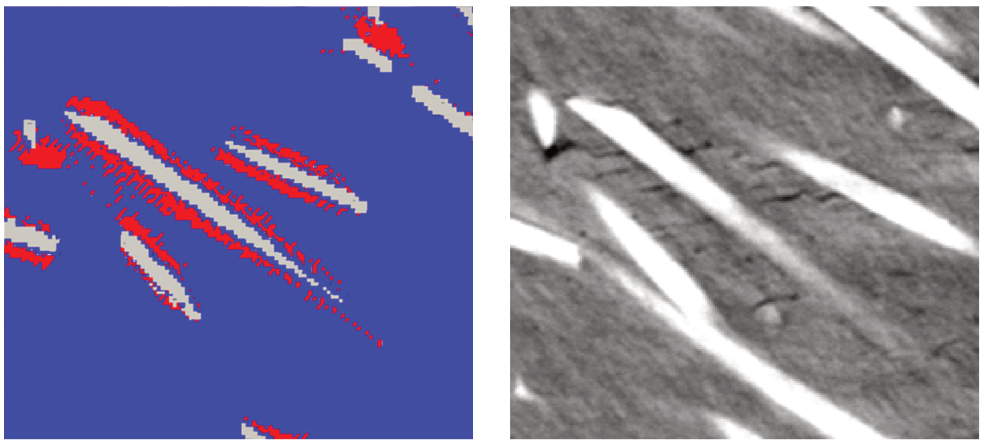


Figure 1.37: Comparison between X-Ray CT micrograph (a-c) and reconstructed model in the FEM code (b-d). Arrows indicate the direction of maximum principal stress during tensile loading.
From Belmonte [122].

Using the FFT method Rolland [42] performed calculations on microstructures segmented from tomographic data. Fibers are assumed elastic and perfectly bonded to an elasto-visco-plastic matrix. Analysis of the stress distribution in the volumes shows that for higher relative humidity of the matrix, stress reached in the polymer are lower. Results also show the importance of the fiber orientation on the triaxiality field in the matrix: microstructures with fibers at 0° have the most dispersed distributions while those with fibers at 45° exhibit limited dispersion.

Results from Rolland confirm the stress concentrations at fiber tips and in densely packed regions. They also demonstrate that the criterion proposed by Argon and Hannoosh [126] proved effective in showing the areas prone to crazing damage (fig. 1.38).

Results obtained by numerical computation on the different microstructures completed the observations made by micro-tomography. It showed that local orientation of the fibers has an impact on the stresses they undergo but also on the stress distribution in the matrix. Fibers oriented in the direction of loading are subjected to a higher stress, promoting fibre failure and damage at the fiber end. Microstructures oriented at 45° and 90° promote decohesion at the matrix interface and fibrillation due to a high shear component in the matrix coupled with highly confined areas. A ductile behaviour of the matrix promotes the localization of stresses and thus favours the initiation of multiple damage mechanisms.



(a) Crazing criterion (b) Tomographic slice

Figure 1.38: Comparison of the crazing criterion with the damage observed by tomography. Tensile test on a 45° RH50 specimen. From Rolland [43].

Current limitations of microstructure modeling mainly stems from the limited size of the computed ROI. Moreover these calculations are only performed under monotonic loading, this also limits the duration of computations and make for an easier identification of constitutive models.

Several outlooks can thus be envisioned from the existing works on microstructure modeling. More analysis on the different types of damage mechanisms could be made, focusing on those observed during fatigue loading. This would require larger

microstructures to be computed under a cyclic loading. Moreover a damage model could be used for the matrix so as to include the loss of mechanical properties in the calculation and not just as a post-processing criterion.

1.5.4.3 Spherulite modeling

Spherulite modeling is rarely covered in works regarding the modeling of composite material. The topic is addressed here for two reasons: first it is closely linked to the understanding of intra-spherulitic damage mechanisms in the polymer matrix and second it is also linked to our understanding of the spherulite as a complex structure.

Two types of studies can be found regarding the numerical modeling of spherulites. The first deals with the modeling of the growth during crystallization, whereas the second deals with the mechanical modeling of the fully grown spherulites.

Growth modeling The modeling of the spherulite growth aims at the prediction of the shape and structure of the spherulites formed in various thermal situations. As the crystallinity (as well as possibly the spherulite size) has an impact on the mechanical properties of the polymer (see section 1.2.4), being able to model the spherulite growth is of major interest.

These simulations are performed in 2D [127–129], allowing for direct comparison with crystallization experiments on thin films. The latest research on the topic made use of phase-field models [5; 129; 130] and yielded promising results (fig. 1.39).

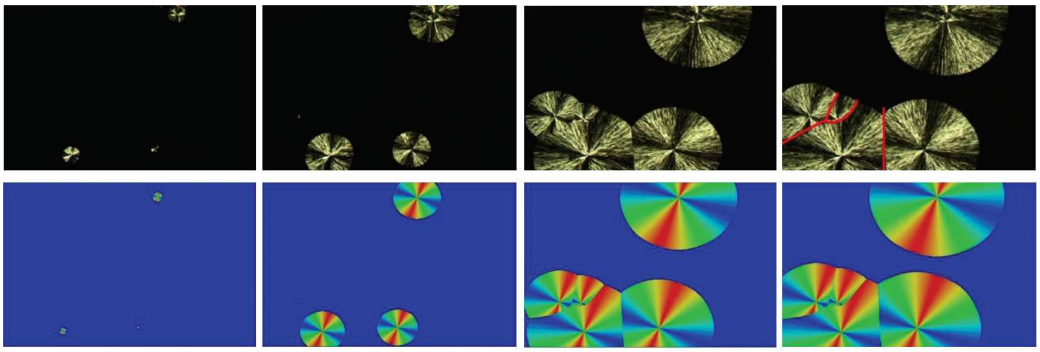


Figure 1.39: Snapshot during an crystallization of a polymer (upper row) and numerical simulation of the crystallization process using the multi-phase field method (lower row). In the simulation initial germs are located identically to the the experimentation. From Gong [130].

Mechanical modeling As with microstructure calculations including grains in metals, it would be interesting to be able to include the spherulites to enhance current the microstructure calculations of polymer composites as most of them do not account for this semi-crystalline organization of the matrix [43; 121; 125]. This approach is far from being developed but a few studies are worth mentioning regarding mechanical modeling of spherulites and spherulitic assemblies.

Multiscale modeling work by VAN DOMMELEN [131] focused on the intraspherulitic deformation of high-density polyethylene. The anisotropic constitutive behavior of the intraspherulitic material was modeled at the micro-scale by an aggregate of elasto-viscoplastic two-phase composite inclusions, each consisting of a crystalline and an amorphous phase.

The elastic part of the deformation in the crystalline phase was characterized by an anisotropic fourth-order elastic modulus tensor, coupled with the crystallographic directions. For the viscoplastic behavior of this phase, a rate-dependent crystal plasticity model was used with 8 distinct slip systems.

For the amorphous part, the polymer chain are in a rubbery state[13] and the phase was modeled by a neo-Hookean relationship to account for the large elastic strains.

VAN DOMMELEN concluded that deformations are initiated in the center of the spherulite, spreading out in the equatorial region under uniaxial loading and in inclined directions for plane strain loading. Furthermore, higher deviatoric stress were found in the center and near the polar boundary and triaxial stresses were largest near the radial boundary of the spherulite.

UCHIDA [132] studied the deformation behavior of a multi-spherulitic 2D meso-structure. Constitutive modeling was also based on crystal plasticity for the crystalline phase and on the nonaffine molecular chain network theory[14] for the amorphous phase. Similarly, early strain and stress are localized at the center of the spherulite. He noted that subsequent deformation occurs in oblique directions to the loading axis and that polar and equatorial regions tends to exhibit larger stress.

More recently OKTAY [134] propose an idealized FEM model of a single spherulite with 4, 8, 16 and 32 slices. These structures were submitted to simple tension loadings at different strain rates, compression and shear.

The authors investigated in detail the activation of different slip systems in the crystalline lamellae, in several region of the spherulitic structure.

On a modeling strategy point of view, it was also noted that the 32 slices model - despite having "many orders of magnitudes thicker crystalline and amorphous phase layers compared to the actual spherulite" - still yielded a *reasonable* spherulite idealization. It provided comparable stress–strain curves and crystallographic slip distributions with experimental studies, and was thus considered a valid model to capture "important spherulite deformation mechanisms".

It is important to note that in all these models the spherulite nucleus is seen as a point at the center of the structure. Spherulitic morphology is thus seen and modeled

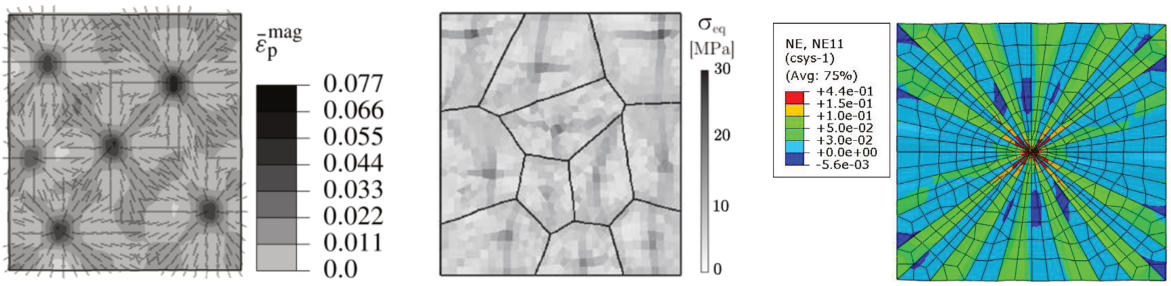
[13] For HDPE, $T_g = -70°$. For other polymers with a higer T_g, such as PA66, the amorphous phase would need to be modeled as elasto-viscoplasic.

[14] The microstructure of a glassy polymer is assumed to consist of long molecular randomly distributed chains. This results in a structure similar to rubber network, but with the chemical crosslinking replaced by physical entanglements between chains. Nonaffine models account for the change in the number of these entanglement points during deformation that induce a change in extensibility and stiffness in the material. Much more detail, as well as the proper formalism, can be found in the work of TOMITA [133].

by these authors as a "radial assembly of crystalline lamellae" [131; 132] grown out from a "common central nucleus" [134].

With such a singularity in the model, it is no wonder that stress and strain are localized at the center. While spherulites crystallized from a still melt might have fully radial structures, we will show that it is not the case in injected semi-crystalline polymers. In any case, more effort should be put in describing what constitutes the nucleus as better understanding will lead to better modeling.

Recent modeling work by Laiarinandrasana [135] included the nucleus of the spherulite. This approach is much more representative of the reality and showed that stresses are mainly localized in the equatorial plan as well as at the junction between the lamellae and the nucleus, giving further insight on the formation of polar-fan damage.



(a) Plastic strain at $\varepsilon = 0.05$, overlayed with the local material orientations. From van Dommelen [131].

(b) Equivalent stress distribution at $\varepsilon = 0.05$. From Uchida [132].

(c) Axial strain in loading direction at $\varepsilon = 0.03$. From Oktay [134].

Figure 1.40: Different spherulite models, loading direction is vertical.

1.6 Bibliography

[1] ACS, "The first nylon plant," 1995. 7

[2] du Pont de Nemours & Company, "DuPont Announces for the World of Tomorrow... a new world and a new material NYLON," 1939. 8

[3] P. Matthies and W. F. Seydl, "History and Development of Nylon 6," in *High Performance Polymers: Their Origin and Development* (R. B. Seymour and G. S. Kirshenbaum, eds.), pp. 39–53, Dordrecht: Springer Netherlands, 1986. 8

[4] G. N. Patel and R. D. Patel, "Growth mechanism of polymer hedrites," *European Polymer Journal*, vol. 6, no. 5, 1970. 10, 11

[5] L. Gránásy, T. Pusztai, G. Tegze, J. A. Warren, and J. F. Douglas, "Growth and form of spherulites," *Physical Review E - Statistical, Nonlinear, and Soft Matter Physics*, vol. 72, no. 1, pp. 1–15, 2005. 10, 53

[6] F. Khoury and E. Passaglia, "The Morphology of Crystalline Synthetic Polymers," in *Treatise on Solid State Chemistry* (N. B. Hannay, ed.), ch. 6, pp. 335–496, New York: Springer, 1976. 10, 11

[7] L. Gránásy, T. Pusztai, T. Börzsönyi, G. I. Tóth, G. Tegze, J. A. Warren, and J. F. Douglas, "Polycrystalline patterns in far-from-equilibrium freezing: A phase field study," *Philosophical Magazine*, vol. 86, no. 24, pp. 3757–3778, 2006. 10

[8] B. Crist and J. M. Schultz, "Progress in Polymer Science Polymer spherulites : A critical review," *Progress in Polymer Science*, vol. 56, pp. 1–63, 2016. 10, 11

[9] P. J. Flory, "On the Morphology of the Crystalline State in Polymers," *Journal of the American Chemical Society*, vol. 84, no. 15, pp. 2857–2867, 1962. 10

[10] S. Balijepalli and G. C. Rutledge, "Conformational statistics of polymer chains in the interphase of semi-crystalline polymers," *Computational and Theoretical Polymer Science*, vol. 10, no. 1-2, pp. 103–113, 2000. 10

[11] A. Keller and J. R. S. Waring, "The spherulitic structure of crystalline polymers. Part III. Geometrical factors in spherulitic growth and the fine-structure," *Journal of Polymer Science*, vol. 17, no. 86, pp. 447–472, 1955. 11, 12

[12] N. Tien, Y. Nishikawa, M. Hashimoto, M. Tosaka, S. Sasaki, and S. Sakurai, "Three-dimensional analyses of spherulite morphology in poly(oxyethylene) and its blends with amorphous poly(d,l-lactic acid) using X-ray computerized tomography," *Polymer Journal*, vol. 47, no. 1, pp. 37–44, 2015. 11

[13] A. S. Vaughan, "On morphology and polymer blends: polystyrene and polyethylene," *Polymer*, vol. 33, no. 12, pp. 2513–2521, 1992. 11

[14] A. King, P. Reischig, S. Martin, J. Fonseca, M. Preuss, and W. Ludwig, "Grain mapping by diffraction contrast tomography: extending the technique to sub-grain information," in *Risø International Symposium on Materials Science*, 2010. 11

[15] F. P. Price, "The Structure of High Polymer Spherulites," *Journal of Polymer Science*, vol. XXXVII, no. April 1958, pp. 71–89, 1959. 11

[16] L. Laiarinandrasana, N. Selles, O. Klinkova, T. Morgeneyer, H. Proudhon, and L. Helfen, "Structural versus microstructural evolution of semi-crystalline polymers during necking under tension: Influence of the skin-core effects, the relative humidity and the strain rate," *Polymer Testing*, vol. 55, pp. 297–309, Oct. 2016. 11

[17] V. Ferreiro and G. Coulon, "Shear banding in strained semicrystalline polyamide 6 films as revealed by atomic force microscopy: Role of the amorphous phase," *Journal of Polymer Science Part B: Polymer Physics*, vol. 42, no. 4, pp. 687–701, 2004. 12, 38

[18] F. Detrez, S. Cantournet, and R. Seguela, "Plasticity/damage coupling in semi-crystalline polymers prior to yielding: Micromechanisms and damage law identification," *Polymer*, vol. 52, no. 9, pp. 1998–2008, 2011. 12, 37, 38, 39

[19] F. Zok, "Environmental fatigue crack growth in spherulitic polyethylene," *Journals of Mateilas science Letters*, vol. 3, pp. 940–943, 1994. 12

[20] M. Aboulfaraj, C. G'Sell, B. Ulrich, and A. Dahoun, "In situ observation of the plastic deformation of polypropylene spherulites under uniaxial tension and simple shear in the scanning electron microscope," *Polymer*, vol. 36, no. 4, pp. 731–742, 1995. 12

[21] C. Regrain, L. Laiarinandrasana, S. Toillon, and K. Saï, "Multi-mechanism models for semi-crystalline polymer: Constitutive relations and finite element implementation," *International Journal of Plasticity*, vol. 25, no. 7, pp. 1253–1279, 2009. 12

[22] N. Selles, P. Cloetens, H. Proudhon, T. Morgeneyer, O. Klinkova, N. Saintier, and L. Laiarinandrasana, "Voiding Mechanisms in Deformed Polyamide 6 Observed at the Nanometric Scale," *Macromolecules*, vol. 50, no. 11, pp. 4372–4383, 2017. 12, 40, 41

[23] H. B. H. Hamouda, L. Laiarinandrasana, and R. Piques, "A local approach to creep fracture by slow crack growth in an MDPE : Damage modelling," *International Journal of Pressure Vessels and Piping*, vol. 86, no. 2-3, pp. 228–238, 2009. 12, 40, 41

[24] C. Devilliers, *Chemical degradation of PE and its influence on the creep response, damage and failure: application to lifetime assessment on pipes subjected to internal pressure*. Theses, École Nationale Supérieure des Mines de Paris, Dec. 2011. 12

[25] X. Lefebvre, *Fissuration fragile lente du polyamide 11 : mécanismes et durées de vie en fluage*. Theses, École Nationale Supérieure des Mines de Paris, Dec. 2002. 12

[26] H. Rolland, N. Saintier, I. Raphael, N. Lenoir, A. King, and G. Robert, "In-situ fatigue damage mechanisms in short fibre reinforced PA66 as observed by synchrotron X-ray microtomography," *Composites Part B: Engineering*, vol. 143, no. December 2017, pp. 217–229, 2018. 12, 44, XIV

[27] A. Keller, "The spherulitic structure of crystalline polymers. Part II. The problem of molecular orientation in polymer spherulites," *Journal of Polymer Science*, vol. 17, no. 85, pp. 351–364, 1955. 12

[28] J. Mann and L. Roldan-Gonzalez, "Orientation in nylon spherulites: A study by X-ray diffraction," *Journal of Polymer Science*, vol. 60, no. 169, pp. 1–20, 1962. 12

[29] J. H. Magill, "Formation of spherulites in polyamide melts: Part III. Even-even polyamides," *Journal of Polymer Science Part A-2: Polymer Physics*, vol. 4, no. 2, pp. 243–265, 1966. 12, XIII

[30] A. Keller and M. J. Machin, "Oriented Crystallization in Polymers," *Journal of Macromolecular Science, Part B*, vol. 1, no. 1, pp. 41–91, 1967. 13

[31] P. H. Lindenmeyer, "A molecular theory of polymer chain folding," *Journal of Polymer Science Part C: Polymer Symposia*, vol. 20, no. 1, pp. 145–158, 1967. 13

[32] A. J. Pennings, J. M. A. A. van der Mark, and A. M. Kiel, "Hydrodynamically induced crystallization of polymers from solution," *Kolloid-Zeitschrift & Zeitschrift für Polymere*, vol. 238, no. 1-2, p. 544, 1970. 13

[33] D. M. Huong, M. Drechsler, M. Möller, and H. J. Cantow, "Electron spectroscopic imaging of the morphology of in situ polyethylene 'shish kebabs'," *Journal of Microscopy*, vol. 166, no. 3, pp. 317–328, 1992. 13

[34] H. Zuidema, *Flow Induced Crystallization of Polymers Application to Injection Moulding*. PhD thesis, Technische Universiteit Eindhoven, 2000. 13

[35] J. D. Menczel and M. Jaffe, "How did we find the rigid amorphous phase?," *Journal of Thermal Analysis and Calorimetry*, vol. 89, no. 2, pp. 357–362, 2007. 13

[36] E. Parodi, L. E. Govaert, and G. W. Peters, "Glass transition temperature versus structure of polyamide 6: A flash-DSC study," *Thermochimica Acta*, vol. 657, no. September, pp. 110–122, 2017. 13, 14

[37] J. J. Horst, *Influence of fibre orientation on fatigue of short glassfibre reinforced Polyamide*. PhD thesis, TU Delft, 1997. 15, 20, 21, 28, 35, 42, 43, 49, 50, 51, XIV

[38] A. Bernasconi, F. Cosmi, and D. Dreossi, "Local anisotropy analysis of injection moulded fibre reinforced polymer composites," *Composites Science and Technology*, vol. 68, no. 12, pp. 2574–2581, 2008. 15, 27

[39] M. F. Arif, *Damage mechanisms in short glass fiber reinforced polyamide-66 under monotonic and fatigue loading : Effect of relative humidity and injection molding induced microstructure*. PhD thesis, ENSAM, 2014. 15, 42

[40] M. F. Arif, N. Saintier, F. Meraghni, J. Fitoussi, Y. Chemisky, and G. Robert, "Multiscale fatigue damage characterization in short glass fiber reinforced polyamide-66," *Composites Part B: Engineering*, vol. 61, pp. 55–65, 2014. 15

[41] A. Ayadi, *Modélisation et analyses expérimentales basées sur la caractérisation microstructurale par imageries a rayons X : application aux composites thermoplastiques renforcés par des fibres de verre courtes*. PhD thesis, Université de Lille 1, 2016. 15

[42] H. Rolland, N. Saintier, P. Wilson, J. Merzeau, and G. Robert, "In situ X-ray tomography investigation on damage mechanisms in short glass fi bre reinforced thermoplastics : Effects of fibre orientation and relative humidity," *Composites Part B*, vol. 109, pp. 170–186, 2017. 15, 52

[43] H. Rolland, *Comportement en fatigue et mécanismes d'endommagement du polyamide 6,6 renforcé de fibres courtes*. PhD thesis, ENSAM, 2017. 15, 35, 36, 42, 52, 53, XIII, XIV

[44] K. Noda, M. Tsuji, A. Takahara, and T. Kajiyama, "Aggregation structure and molecular motion of (glass-fiber/matrix nylon 66) interface in short glass-fiber reinforced nylon 66 composites," *Polymer*, vol. 43, no. 14, pp. 4055–4062, 2002. 16

[45] A. Bergeret, L. Ferry, and P. Ienny, "Influence of the fibre/matrix interface on ageing mechanisms of glass fibre reinforced thermoplastic composites (PA-6,6, PET, PBT) in a hygrothermal environment," *Polymer Degradation and Stability*, vol. 94, no. 9, pp. 1315–1324, 2009. 16, 24

[46] S. Rudzinski, L. Häussler, C. H. Harnisch, E. Mäder, and G. Heinrich, "Glass fibre reinforced polyamide composites: Thermal behaviour of sizings," *Composites Part A: Applied Science and Manufacturing*, vol. 42, no. 2, pp. 157–164, 2011. 16

[47] Y. Gabet, *Étude et optimisation des interfaces fibre-matrice polymère de composites structuraux à base thermoplastique*. PhD thesis, Université Claude Bernard Lyon 1, 2019. 16

[48] E. Mourglia Seignobos, *Compréhension des mécanismes physiques de fatigue dans le polyamide vierge et renforcé de fibres de verre*. PhD thesis, INSA Lyon, 2009. 16, 28, 35, 38, 39

[49] M. L. Shiao, S. V. Nair, P. D. Garrett, and R. E. Pollard, "Effect of glass-fibre reinforcement and annealing on microstructure and mechanical behaviour of nylon 6,6 - Part I Microstructure and morphology," *Journal of Materials Science*, vol. 29, no. 7, pp. 1973 – 1981, 1994. 16

[50] A. Bernasconi, P. Davoli, A. Basile, and A. Filippi, "Effect of fibre orientation on the fatigue behaviour of a short glass fibre reinforced polyamide-6," *International Journal of Fatigue*, vol. 29, no. 2, pp. 199–208, 2007. 17, 18, 19, 32, XIII

[51] K. Tanaka, T. Kitano, and N. Egami, "Fatigue Crack Propagation in Short-Fiber Reinforced Plastics," *The 10th International Conference on Multiaxial Fatigue & Fracture*, vol. 34, no. 0, pp. 309–317, 2015. 18, 19, 38, XIII

[52] P. K. Mallick and Y. Zhou, "Effect of mean stress on the stress-controlled fatigue of a short E-glass fiber reinforced polyamide-6,6," *International Journal of Fatigue*, vol. 26, no. 9, pp. 941–946, 2004. 20, 21, XIII

[53] H. Oka, R. Narita, Y. Akiniwa, and K. Tanaka, "Effect of Mean Stress on Fatigue Strength of Short Glass Fiber Reinforced Polybuthyleneterephthalate," *Key Engineering Materials Vols.*, vol. 341, pp. 537–542, 2007. 20, 28

[54] M. Eftekhari and A. Fatemi, "Creep-fatigue interaction and thermo-mechanical fatigue behaviors of thermoplastics and their composites," *International Journal of Fatigue*, vol. 91, pp. 136–148, 2016. 20

[55] G. Robert, O. Moulinjeune, and M. Houba, "Fatigue of glass fibers reinforced polyamides: Mean stress effects as a function of glass fibers orientation," *ICCM International Conferences on Composite Materials*, pp. 19–24, 2015. 20

[56] A. Fatemi, S. Mortazavian, and A. Khosrovaneh, "Fatigue Behavior and Predictive Modeling of Short Fiber Thermoplastic Composites," *Procedia Engineering*, vol. 133, pp. 5–20, 2015. 21, 32, 33, XIV

[57] A. Bernasconi and R. M. Kulin, "Effect of Frequency Upon Fatigue Strength of a Short Glass Fiber Reinforced Polyamide 6: A Superposition Method Based on Cyclic Creep Parameters," *Polymers and Polymer Composites*, 2009. 21, 28, 35

[58] Y. Zhou and P. K. Mallick, "Fatigue Performance of an Injection-Molded Short E-Glass Fiber-Reinforced Polyamide 6,6.," *Polymers and Polymer Composites*, pp. 230–237, 2006. 21, XIII

[59] B. Mouhmid, A. Imad, N. Benseddiq, S. Benmedakhène, and A. Maazouz, "A study of the mechanical behaviour of a glass fibre reinforced polyamide 6,6: Experimental investigation," *Polymer Testing*, vol. 25, no. 4, pp. 544–552, 2006. 22

[60] K. Handa, A. Kato, and I. Narisawa, "Fatigue characteristics of a glass-fiber-reinforced polyamide," *Journal of Applied Polymer Science*, vol. 72, no. 13, pp. 1783–1793, 1999. 22, XIII

[61] L. P. Razumovskii, V. S. Markin, and G. Y. Zaikov, "Sorption of water by aliphatic polyamides. Review," *Polymer Science U.S.S.R.*, vol. 27, no. 4, pp. 751–768, 1985. 23

[62] R. Puffr and J. Šebenda, "On the Structure and Properties of Polyamides. XXVII. The Mechanism of Water Sorption in Polyamides," *Journal of Polymer Science Part C: Polymer Symposia*, vol. 16, no. 1, pp. 79–93, 1967. 23, XIII

[63] J. Karger-Kocsis and K. Friedrich, "Skin-core morphology and humidity effects on the fatigue crack propagation of pa-6.6," *Plastics, Rubber and Composites*, vol. 12, no. 1, pp. 63–68, 1989. 23

[64] D. Ferreño, I. Carrascal, E. Ruiz, and J. A. Casado, "Characterisation by means of a finite element model of the influence of moisture content on the mechanical and fracture properties of the polyamide 6 reinforced with short glass fibre," *Polymer Testing*, vol. 30, no. 4, pp. 420–428, 2011. 23

[65] P. E. Bretz, R. W. Hertzberg, and J. A. Manson, "Influence of absorbed moisture on fatigue crack propagation behaviour in polyamides - Part 1 Macroscopic response," *Journal of Materials Science*, vol. 16, no. 8, pp. 2061–2069, 1981. 23, 39

[66] S. Barbouchi, V. Bellenger, A. Tcharkhtchi, P. Castaing, and T. Jollivet, "Effect of water on the fatigue behaviour of a pa66/glass fibers composite material," *Journal of Materials Science*, vol. 42, no. 6, pp. 2181–2188, 2007. 23, XIII

[67] E. H. Boasson, B. Kamerbeek, A. Algera, and G. H. Kroes, "The photooxidation of nylon 6 and 66," *Recueil*, vol. 81, pp. 624–634, 1962. 24

[68] I. Ksouri, O. De Almeida, and N. Haddar, "Long term ageing of polyamide 6 and polyamide 6 reinforced with 30% of glass fibers: physicochemical, mechanical and morphological characterization," *Journal of Polymer Research*, vol. 24, no. 8, 2017. 24

[69] O. Okamba Diogo, *Thermo-oxydation des polyamides*. PhD thesis, ENSAM, 2015. 24

[70] J. Karger-Kocsis, "Effects of processing induced microstructure on the fatigue crack propagation of unfilled and short fibre-reinforced PA-6," *Composites*, vol. 21, no. 3, pp. 243–254, 1990. 24, 26

[71] J. L. Way, J. R. Atkinson, and J. Nutting, "The effect of spherulite size on the fracture morphology of polypropylene," *Journal of Materials Science*, vol. 9, no. 2, pp. 293–299, 1974. 24, 25, 26

[72] H. W. Starkweather and R. E. Brooks, "Effect of spherulites on the mechanical properties of nylon 66," *Journal of Applied Polymer Science*, vol. 1, no. 2, pp. 236–239, 1959. 25, 26

[73] D. Taylor, "Geometrical effects in fatigue: a unifying theoretical model," *International Journal of Fatigue*, vol. 21, no. 5, pp. 413–420, 1999. 25

[74] P. Luo, W. Yao, L. Susmel, and P. Li, "Prediction methods of fatigue critical point for notched components under multiaxial fatigue loading," *Fatigue & Fracture of Engineering Materials & Structures*, no. August, pp. 1–12, 2019. 27, XIV

[75] C. M. Sonsino and E. Moosbrugger, "Fatigue design of highly loaded short-glass-fibre reinforced polyamide parts in engine compartments," *International Journal of Fatigue*, vol. 30, no. 7, pp. 1279–1288, 2008. 27, 28, XIV

[76] A. Bernasconi, F. Cosmi, and E. Zappa, "Combined effect of notches and fibre orientation on fatigue behaviour of short fibre reinforced polyamide," *Strain*, vol. 46, no. 5, pp. 435–445, 2010. 27

[77] S. Castagnet, C. Nadot-Martin, A. Bernasconi, E. Lainé, E. Conrado, and P. Caton-Rose, "Through process modeling for the fatigue life assessment of notched injection-molded specimens," *16th European Conference on Composite Materials, ECCM 2014*, no. June, pp. 1–4, 2014. 27

[78] L. Laiarinandrasana, T. F. Morgeneyer, Y. Cheng, L. Helfen, V. Le Saux, and Y. Marco, "Microstructural observations supporting thermography measurements for short glass fibre thermoplastic composites under fatigue loading," *Continuum Mechanics and Thermodynamics*, 2019. 28

[79] E. Andrews and B. Walker, "Fatigue fracture in polyethylene," in *Royal Society London*, vol. 79, pp. 57–79, 1971. 28, 38, 39, 40, XIV

[80] E. Macha and C. M. Sonsino, "Energy criteria of multiaxial fatigue failure," *Fatigue and Fracture of Engineering Materials and Structures*, vol. 22, no. 12, pp. 1053–1070, 1999. 30

[81] A. Benaarbia, *Analyse énergétique du comportement thermomécanique du PA6.6 renforcé de fibres de verre*. PhD thesis, Université Montpellier 2, 2014. 31

[82] A. Benaarbia, A. Chrysochoos, and G. Robert, "Thermomechanical behavior of PA6.6 composites subjected to low cycle fatigue," *Composites Part B: Engineering*, vol. 76, pp. 52–64, 2015. 31

[83] B. Klimkeit, Y. Nadot, S. Castagnet, C. Nadot-Martin, C. Dumas, S. Bergamo, C. M. Sonsino, and A. Büter, "Multiaxial fatigue life assessment for reinforced polymers," *International Journal of Fatigue*, vol. 33, no. 6, pp. 766–780, 2011. 31, 32, 33, 34, XIV

[84] F. Ellyin, "Cyclic strain energy density as a criterion for multiaxial fatigue failure," *Icbmff2*, p. 13, 2013.

[85] N. Fouchier, *Approche intégrée pour estimer la durée de vie en fatigue de pièces thermoplastiques renforcés fibres courtes dans un cadre viscoélastique haute température*. PhD thesis, ENSMA, 2019. 31, 34

[86] A. Launay, M. H. Maitournam, Y. Marco, and I. Raoult, "Multiaxial fatigue models for short glass fibre reinforced polyamide. Part II: Fatigue life estimation," *International Journal of Fatigue*, vol. 47, pp. 390–406, 2013. 31, 32, 34, 35, XIV

[87] J. Morrow, "Cyclic plastic strain enetgy and fatigue of metals," *Internal Friction*, pp. 45–87., 1965. 34

[88] D. Kujawski and F. Ellyin, "A unified approach to mean stress effect on fatigue threshold conditions," *International Journal of Fatigue*, vol. 17, no. 2, pp. 101–106, 1995. 34, 35

[89] B. Klimkeit, S. Castagnet, Y. Nadot, A. E. Habib, G. Benoit, S. Bergamo, C. Dumas, and S. Achard, "Fatigue damage mechanisms in short fiber reinforced PBT+PET GF30," *Materials Science and Engineering A*, vol. 528, no. 3, pp. 1577–1588, 2011. 35

[90] E. C. Monkman and N. J. Grant, "An empirical relationship between rupture life and minimum creep rate in creep– rupture test," *Proc. Am. Soc. Test. Mater.*, p. 593, 1956. 35

[91] A. Pawlak and A. Galeski, "Plastic deformation of crystalline polymers: The role of cavitation and crystal plasticity," *Macromolecules*, vol. 38, no. 23, pp. 9688–9697, 2005. 37

[92] A. Pawlak, "Plastic deformation and cavitation in semicrystalline polymers studied by X-ray methods," *Polimery/Polymers*, vol. 59, no. 7-8, pp. 533–541, 2014. 37, 39

[93] Z. Bartczak and A. Galeski, "Plasticity of semicrystalline polymers," *Macromolecular Symposia*, vol. 294, no. 1, pp. 67–90, 2010. 37, 39

[94] S. Huguet, N. Godin, R. Gaertner, L. Salmon, and D. Villard, "Use of acoustic emission to identify damage modes in glass fibre reinforced polyester," *Composites Science and Technology (UK). Vol. 62, tner, R; Salmon, L; Villard, D*, vol. 62, pp. 1433–1444, 2002. 38

[95] B. Mouhmid, *Etude de l'endommagement et de la rupture d'un polyamide 66 chargé en fibres de verre courtes*. PhD thesis, 2007. 38

[96] C. Thomas, V. Ferreiro, G. Coulon, and R. Seguela, "In situ AFM investigation of crazing in polybutene spherulites under tensile drawing," *Polymer*, vol. 48, no. 20, pp. 6041–6048, 2007. 38

[97] C. Thomas, R. Seguela, F. Detrez, V. Miri, and C. Vanmansart, "Plastic deformation of spherulitic semi-crystalline polymers: An in situ AFM study of polybutene under tensile drawing," *Polymer*, vol. 50, no. 15, pp. 3714–3723, 2009. 38

[98] A. Galeski, A. S. Argon, and R. E. Cohen, "Changes in the morphology of bulk spherulitic nylon-6 due to plastic-deformation," *Macromolecules*, vol. 21, no. 9, pp. 2761–2770, 1988. 38

[99] H. Kausch, R. Gensler, C. Grein, C. J. G. Plummer, and P. Scaramuzzino, "Crazing in semicrystalline thermoplastics Crazing in Semicrystalline Thermoplastics," *Journal of Macromolecular Science, Part B: Physics*, vol. 38, pp. 803–815, 1999. 39

[100] E. Raphaël and P. G. De Gennes, "Rubber-rubber adhesion with connector molecules," *Journal of Physical Chemistry*, vol. 96, no. 10, pp. 4002–4007, 1992. 39

[101] T. C. McLeish, C. J. Plummer, and A. M. Donald, "Crazing by disentanglement: non-diffusive reptation," *Polymer*, vol. 30, no. 9, pp. 1651–1655, 1989. 39

[102] P. Bretz, J. Manson, and R. Hertzberg, "The Effect of Molecular Weight on Fatigue Crack Propagation in Nylon 66 and Polyacetal," *Journal of Applied Polymer Science*, vol. 27, pp. 1707–1717, 1982. 39

[103] N. Selles, *Cavitation et rupture du Polyamide 6 sous état de contrainte multiaxial en traction monotone, fluage et fatigue. Dialogue entre imagerie 3D et modélisation par éléments finis.* PhD thesis, PSL, 2018. 40, 46, 47, 48, XIV

[104] H. Rolland, N. Saintier, and G. Robert, "Damage mechanisms in short glass fibre reinforced thermoplastic during in situ microtomography tensile tests," *Composites Part B: Engineering*, vol. 90, pp. 365–377, 2016. 41, 42, XIV

[105] N. Sato, T. Kurauchi, S. Sato, and O. Kamigaito, "Microfailure behaviour of randomly dispersed short fibre reinforced thermoplastic composites obtained by direct SEM observation," *Journal of Materials Science*, vol. 26, no. 14, pp. 3891–3898, 1991. 42

[106] H. Nouri, F. Meraghni, and P. Lory, "Fatigue damage model for injection-molded short glass fibre reinforced thermoplastics," *International Journal of Fatigue*, vol. 31, no. 5, pp. 934–942, 2009. 42

[107] L. Toubal, M. Karama, and B. Lorrain, "Damage evolution and infrared thermography in woven composite laminates under fatigue loading," *International Journal of Fatigue*, vol. 28, no. 12, pp. 1867–1872, 2006. 42

[108] G. Boisot, *Mécanismes et modélisation mécanique de la déformation, de l'endommagement et de la rupture du PolyAmide 11 pur et renforcé choc.* PhD thesis, Ecole Nationale Supérieure des Mines Paris, 2009. 45, 47

[109] S. Nikolov and I. Doghri, "A micro/macro constitutive model for the small-deformation behavior of polyethylene," *Polymer*, vol. 41, no. 5, pp. 1883–1891, 2000. 46

[110] N. Selles, N. Saintier, and L. Laiarinandrasana, "Voiding mechanisms in semi-crystalline polyamide 6 during creep tests assessed by damage based constitutive relationships and finite elements calculations," *International Journal of Plasticity*, vol. 86, pp. 112–127, 2016. 46

[111] A. L. Gurson, "Continuum theory of ductile rupture by void nucleation and growth," *Journal of Engineering Materials and Technology*, vol. 99, no. 76, pp. 2–15, 1977. 47

[112] V. Tvergaard and A. Needleman, "Analysis of the cup-cone fracture in a round tensile bar," *Acta Metallurgica*, vol. 32, no. 1, pp. 157–169, 1984. 47, 48

[113] J. Besson, D. Steglich, and W. Brocks, "Modeling of crack growth in round bars and plane strain specimens," *International Journal of Solids and Structures*, vol. 38, no. 46-47, pp. 8259–8284, 2001. 47

[114] V. Tvergaard, "Influence of voids on shear band instabilities under plane strain conditions," *International Journal of Fracture*, vol. 17, no. 4, pp. 389–407, 1981. 47

[115] M. Lafarge, *Modélisation couplée comportment endommagement et critère de rupture dans le domaine de la transition vitreuse du {PVDF}.* PhD thesis, Ecole Nationale Supérieure des Mines de Paris, 2004. 47

[116] J. Besson, "Damage of ductile materials deforming under multiple plastic or viscoplastic mechanisms," *International Journal of Plasticity*, vol. 25, no. 11, pp. 2204–2221, 2009. 48

[117] C. C. Chu and A. Needleman, "Void Nucleation Effects in Biaxially Stretched Sheets," *Journal of Engineering Materials and Technology*, vol. 102, no. 3, p. 249, 1980. 48

[118] P. F. Thomason, "A three-dimensional model for ductile fracture by the growth and coalescence of microvoids," *Acta Metallurgica*, vol. 33, no. 6, pp. 1087–1095, 1985. 48

[119] N. Carrere, F. Laurin, and J. F. Maire, "Micromechanical-based hybrid mesoscopic 3D approach for non-linear progressive failure analysis of composite structures," *Journal of Composite Materials*, vol. 46, no. 19-20, pp. 2389–2415, 2012. 49

[120] N. Despringre, Y. Chemisky, F. Meraghni, J. Fitoussi, G. Robert, and S. E. Plastics, "Fatigue Damage in Short Glass Fiber Reinforced Pa66 : Micromechanical Modeling and Multiscale," *20th International Conference on Composite Materials*, no. July, pp. 19–24, 2015. 49

[121] B. Klimkeit, *Etude experimentale et modélisation du comportement en fatigue multiaxiale d'un polymère renforcé pour application automobile*. PhD thesis, ENSMA, 2009. 49, 50, 53, XIV

[122] E. Belmonte, M. De Monte, T. Riedel, and M. Quaresimin, "Local microstructure and stress distributions at the crack initiation site in a short fiber reinforced polyamide under fatigue loading," *Polymer Testing*, vol. 54, pp. 250–259, 2016. 49, 50, 51, XIV

[123] H. Moulinec and P. Suquet, "A numerical method for computing the overall response of nonlinear composites with complex microstructure," *Computer Methods in Applied Mechanics and Engineering*, vol. 157, no. 1-2, pp. 69–94, 1998. 49

[124] C. Moos, *An Algorithm for Damage Mechanics Based on the Fast Fourier Transform*. PhD thesis, Ruhr-Universität Bochum, 2013. 49

[125] J. Spahn, *An Efficient Multiscale Method for Modeling Progressive Damage in Composite Materials*. PhD thesis, TU Kaiserslautern, 2015. 49, 53

[126] A. S. Argon and J. G. Hannoosh, "Initiation of crazes in polystyrene," *Philosophical Magazine*, vol. 36, no. 5, pp. 1195–1216, 1977. 52

[127] S. Swaminarayan and C. Charbon, "A Multiscale Model for Polymer Crystallization. I: Growth of Individual Spherulites," *Polymer Engineering & Science*, vol. 38, no. 4, 1998. 53

[128] C. Charbon and S. Swaminarayan, "A Multiscale Model for Polymer Crystallization. II: Solidification of a Macroscopic Part," *Polymer Engineering & Science*, vol. 38, no. 4, 1998.

[129] M. Asanishi, T. Takaki, and Y. Tomita, "Polymer Spherulite Growth Simulation during Crystallization by Phase-Field Method," *International Conference on Advances and Trends in Engineering Materials and their Applications, AES - ATEMA 2007*, pp. 195–203, 2007. 53

[130] Y. H. Gong, F. Detrez, Y. M. Luo, and L. Chevalier, "Simulation of polymer crystallization induced by temperature using the phase field method: Focus on the Avrami rate constant," in *AIP Conference Proceedings*, vol. 1896, 2017. 53, XIV

[131] J. A. W. V. Dommelen, D. M. Parks, M. C. Boyce, W. A. M. Brekelmans, and F. P. T. Baaijens, "Micromechanical modeling of intraspherulitic deformation of semicrystalline polymers," *Polymer*, vol. 44, pp. 6089–6101, 2003. 54, 55

[132] M. Uchida, T. Tokuda, and N. Tada, "Finite element simulation of deformation behavior of semi-crystalline polymers with multi-spherulitic mesostructure," *International Journal of Mechanical Sciences*, vol. 52, no. 2, pp. 158–167, 2010. 54, 55

[133] Y. Tomita and T. Adachi, "Network models for glassy polymer and prediction of instability propagation.," *Materials Science Research International*, vol. 3, no. 3, pp. 125–136, 1997. 54

[134] H. E. Oktay and E. Gürses, "Modeling of spherulite microstructures in semicrystalline polymers," *Mechanics of Materials*, vol. 90, pp. 83–101, 2015. 54, 55

[135] L. Laiarinandrasana, "Stress Heterogeneity Leading to Void Nucleation within Spherulites for Semi-Crystalline Polymers," *Crystals*, 2019. 55

Chapter 2

Materials and methods

In magic, today as always, the effect is what counts. The method or methods used are always purely secondary.

Dai Vernon

Magician and scientist both need to produce engaging results, with the difference that in science you have to explain (almost...) all the tricks! This traditional "Materials and methods" chapter thus introduces the material used in this study, as a brief addition to the information provided in the literature review of chapter 1. A description of the experimental set-ups is then given before an overview of the different observation techniques used for this research.

2.1 Testing specimens

2.1.1 Material

Both unreinforced and reinforced polyamide 6,6 (PA66) were studied in this work. They are supplied in the form of injection-molded plates by Solvay Performance Polyamides.

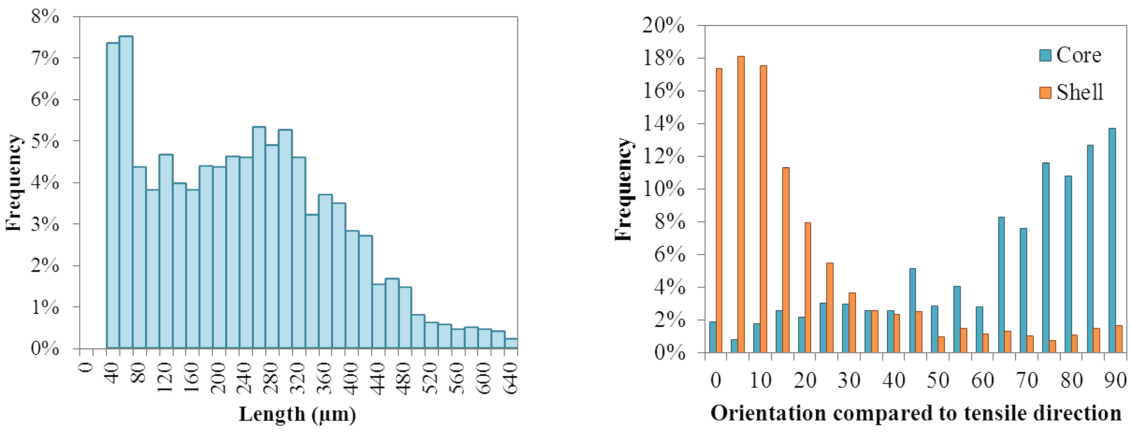
The composite material studied is a PA66 reinforced with 30wt% short glass fibers. Fibers are made of E-type glass. Length distribution ranges from $20\mu m$ to $800\mu m$, as shown on fig. 2.1(a). Fiber diameter has an average value of $11\mu m$, and shows little scatter.

2.1.2 Microstructure of the composite

As introduced in section 1.1.3.2, the composite material exhibits a skin-shell-core microstructure induced by the injection molding process.

In our case, the thickness of these layers can be measured using micro-tomography, giving:

- a core layer $300\mu m$ thick.



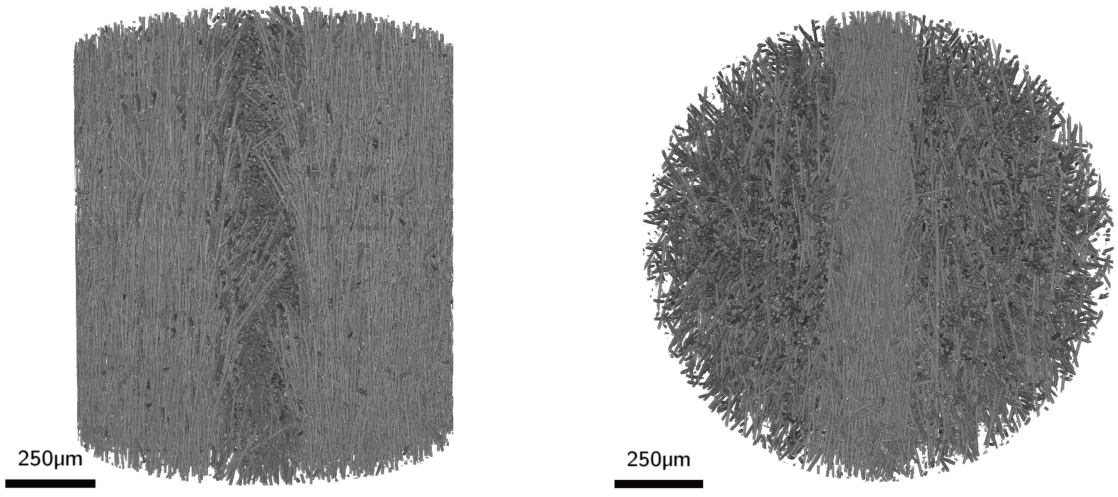
(a) Length distribution

(b) Orientation distribution in a 0° specimen

Figure 2.1: Fiber length and orientation distribution in the composite material. From Rolland [1].

- two shell layers, both about $1.4mm$ thick.
- two thin skin layers, about $50\mu m$ thick, at the surface of the specimen.

Figure 2.1(b) show quantitatively this evolution of fiber orientation throughout the microstructure in a 0° specimen. Figure 2.2(a) illustrates this microstructure as segmented from tomography data. The core layer is visible at the center but only part of the shells can be seen in the field of view.



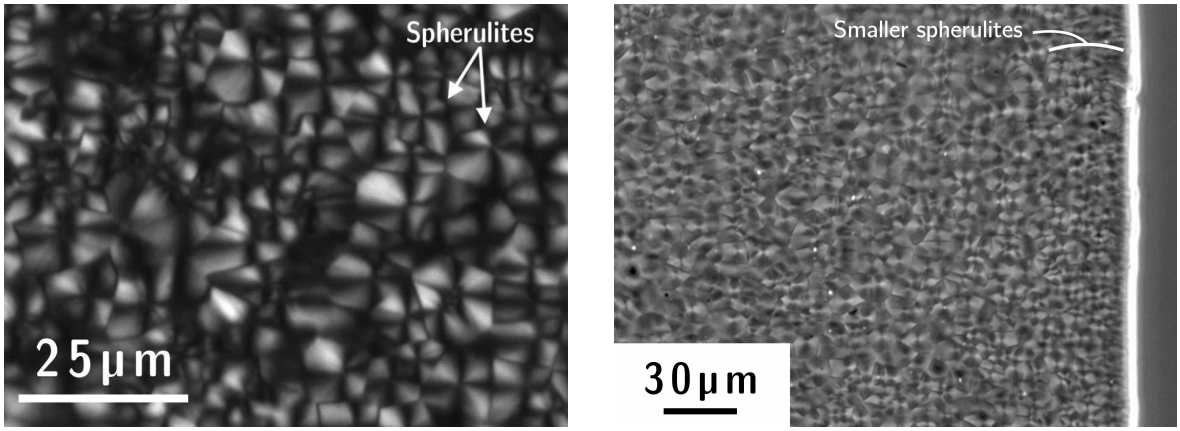
(a) Side view

(b) Top view

Figure 2.2: Segmented fibers at the center of a 0° specimen as observed using synchrotron tomography. The core layer is visible, but only part of the shells can be seen in the field of view.

2.1.3 Spherulitic microstructure

Figure 2.3(a) illustrates the spherulitic microstructure of the pure PA66 as observed by polarized light microscopy. Spherulites diameters are in the range of $15 - 30\mu m$. However this size varies throughout the thickness of the specimen, especially on a $30\mu m$ distance from the surface of the specimen where spherulites are notably smaller: average measured diameter on thin slices[1] is twice as small than in the bulk with $7\mu m$ against $13\mu m$ (fig. 2.3(b)).



(a) Core of the specimen (b) Surface of the specimen

Figure 2.3: Spherulites in PA66 observed using polarized light microscopy on thin slices obtained by microtomy.

Figure 2.4 illustrates the spherulitic microstructure in the composite material. Slicing was performed in a longitudinal direction compared to fibers, which gives better view of the microstructure but is more challenging than cutting perpendicularly to the fiber orientation, as usually performed for bulk composite material.

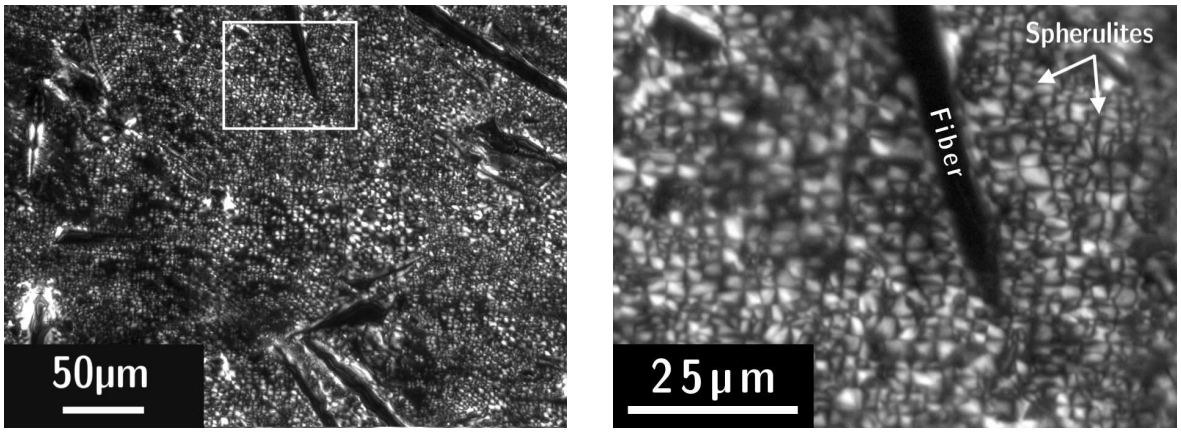
These observations clearly indicate that the spherulite size depends on the local microstructure. Close to the fibers, spherulites are smaller and more difficult to observe. In poorly reinforced areas, although a bit smaller, spherulite morphology is similar to the one observed in pure PA66. This smaller spherulite size can be explained by the increased number of sites for potential nucleation on the surface of fibers or fiber glass *dust* resulting from the manufacturing process, and heterogeneous cooling rates at the microstructural level.

2.1.4 Smooth specimen geometry

All specimens are water-jet cut from 3.2 mm thick[2] rectangular plates 360x100mm in dimensions obtained by injection molding (fig. 2.5). Samples were cut from the plates

[1] Direct measurement of the spherulite diameter on the thin slices tends to yield smaller diameters, as the spherulites are not necessarily cut in their center. Precise evaluation of the distribution in bulk spherulite sizes remains a challenge.

[2] Exact thickness of every specimen was measured prior to testing.



(a) General view (b) Detail at fiber tip

Figure 2.4: Spherulites observed using polarized light microscopy on thin slices of reinforced PA66 obtained by microtomy.

along three directions with respect to the MFD: 0°, 45° and 90° for both pure and reinforced polymer.

Geometry for standard smooth specimen is given in fig. 2.6.

2.1.5 Notched specimens

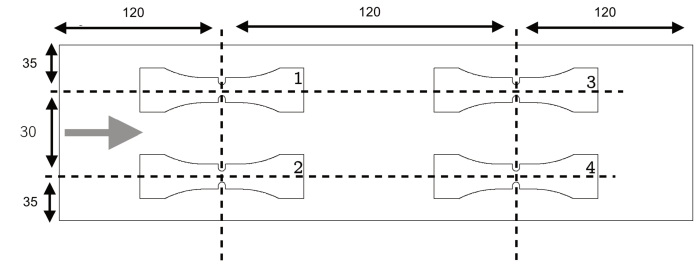
Two U-shaped notch geometries with radii of 0.5 and 2 mm are mainly studied (figs. 2.7(a) to 2.7(c)). Two complementary geometries were also used, a 2 mm notch with larger net section (fig. 2.7(d)) and a smaller specimen for in-situ tomography testing (fig. 2.7(e)).

It should be noted that in this work notched specimens were water-jet cut from the injected plates, so that the local orientation of fibers at the notch is similar to the one in the plates. This allows to separate the effect of the geometrical defect as a stress concentrator form its role in modifying the local microstructure when introduced during the molding process.

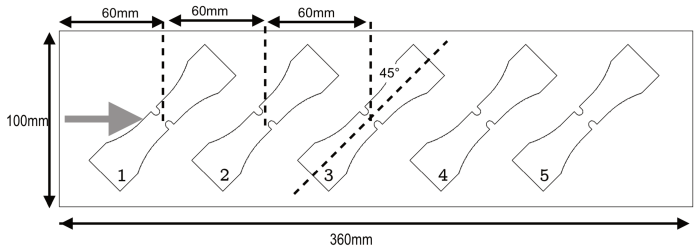
2.1.6 Specimen conditioning

As mechanical behavior and fatigue damage of PA66 is humidity dependent, all specimens were conditioned at a given relative humidity (RH) prior to testing:

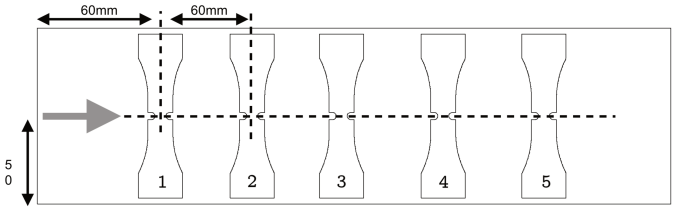
- RH0 specimens are *dry as moulded*. They were sealed directly after manufacturing.
- RH50 specimens are placed at RH=62% and 70° C until stabilization in the water uptake. They are then placed at RH 50% and 23° C for two weeks.
- Similar protocol was followed for RH80 specimens that were placed at RH=80% and 70° C until complete water uptake, then placed at RH 80% and 30°C for two weeks.



(a) 0° specimens



(b) 45° specimens



(c) 90° specimens

Figure 2.5: Position of the specimens in the plates. Note that they are the same for smooth and notched specimens.

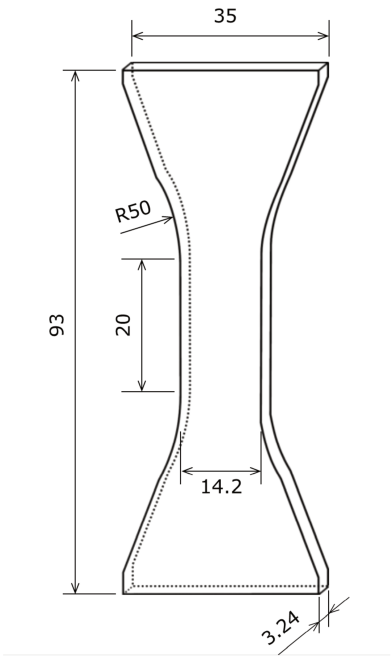
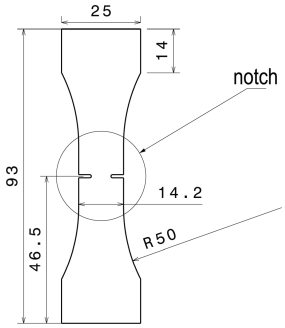


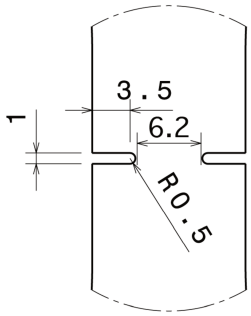
Figure 2.6: Geometry for smooth specimens.

These water uptakes are reversible and the protocol does not modify the position of the fibers, nor the semi-crystalline structure of the material [1].

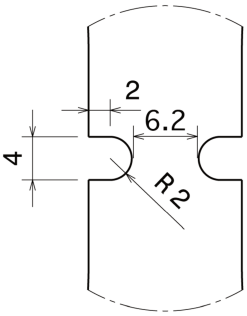
After conditioning all specimens were sealed in dedicated packages. These packages were protected for high temperatures and were only opened just prior to testing.



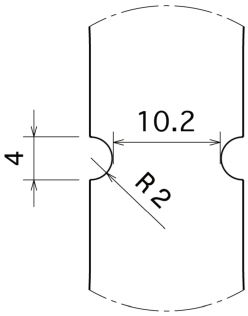
(a) Global view



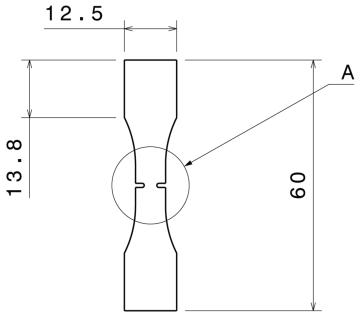
(b) U05 notch - $K_T = 3.1$ $\eta = 2.2$

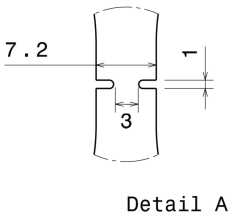


(c) U2 notch - $K_T = 1.8$ $\eta = 1.2$

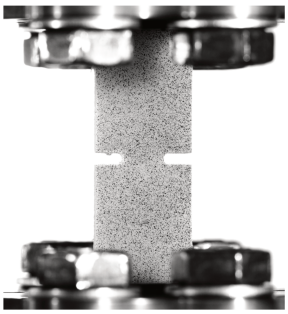


(d) O2 notch - $K_T = 2.0$ $\eta = 1.5$





(e) Notched specimen for tomography - $K_T = 2.3$ - $\eta = 1.6$



(f) U0.5 notched specimen with speckle pattern for DIC strain measurement.

Figure 2.7: Dimensions of notched specimens, stress concentration factor K_T and stress triaxiality ratio η (see definitions given in section 2.2.1.4).

2.2 Experimental set-up

2.2.1 In-lab testing

2.2.1.1 Quasi-static testing

Quasi-static loading was performed on an electro-mechanical 50kN Instron machine. Tests were conducted by controlling the crosshead speed. A speckle pattern was sprayed at the surface of the specimen using black paint (fig. 2.7(f)). Local strain evolution was monitored using Digital Image Correlation (DIC)[3].

2.2.1.2 Fatigue testing

Fatigue testing was performed under load control, and strain evolution was monitored using timed Digital Image Correlation (see section 2.2.1.3 below).

An electro-mechanical Bose Electroforce testing machine (fig. 2.8) was used to load the specimens at a frequency of 0.5Hz. Contrarily to hydraulic machines, the electro-mechanical loading machine does not heat up and the thus do not require special water-cooled grips to hold the specimen. Thanks to this "cold" technology and low cycling frequency, no air cooling was needed to prevent heating of the specimens.

However it should be noted that the low testing frequency will mostly limit the scope of this work to the Low Cycle Fatigue regime. The number of cycles to failure N_f for the different specimens will be given with the results and observations.

Testing was performed at a constant temperature (23°C ± 0.5°C) and the overall experiment duration was sufficiently short to minimize any change in the water uptake (RH50) of the specimen.

A photo camera was used to performed DIC measurement on notched specimens.

A FLIR thermal imaging camera was also used to check for the limited heat build-up in the specimens.

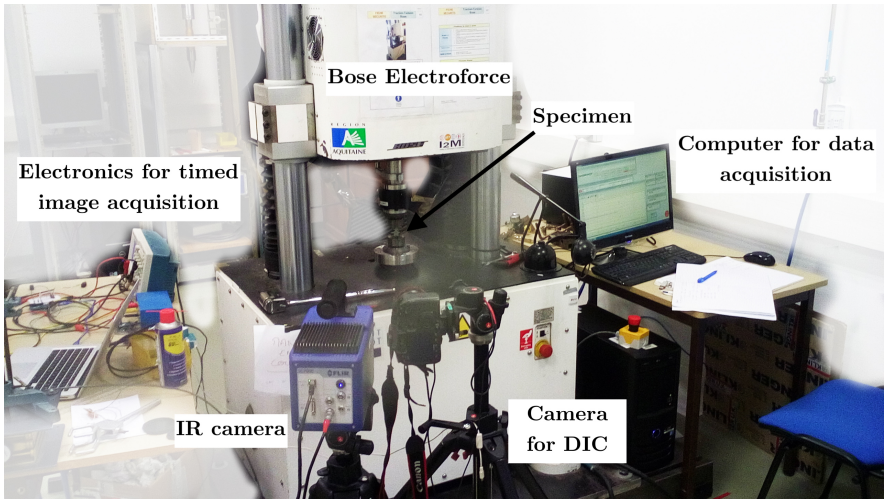


Figure 2.8: Experimental setup for fatigue testing.

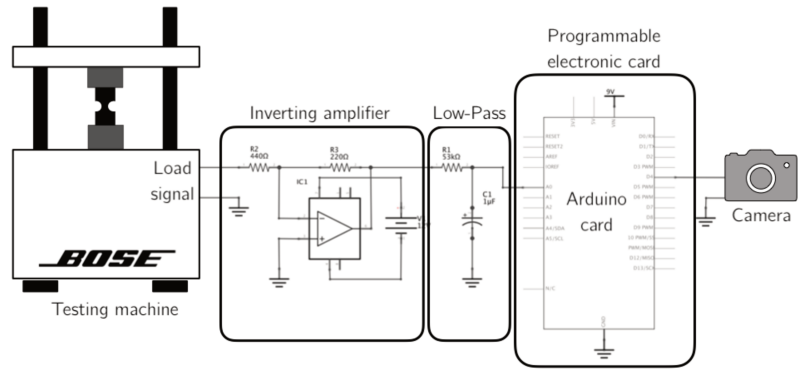
[3]More details on the DIC method will given in section 2.3.5

Note that part of the experimental database was provided by Solvay Performance Polyamides. For these tests a servo-hydraulic MTS fatigue machine was used to load the specimens. Air cooling of the specimen was used to prevent heating (indicated as *forced convection* in the results). This machine was used to performed testing at multiple load ratios (R=-0.5 to R=0.7). A climate chamber allowed for the medium to be kept at a constant temperature (23°C ± 0.5°C) and humidity (50% RH). This testing was performed at a frequency of 3Hz.

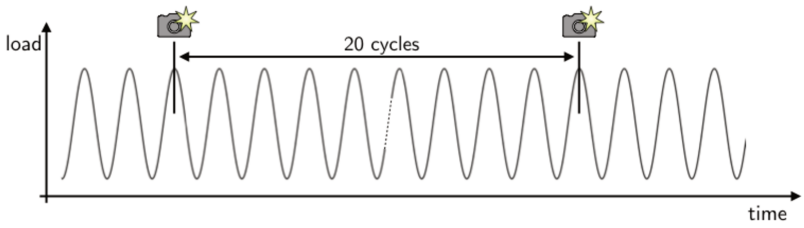
2.2.1.3 Local strain measurements using DIC

In order to monitor the local cyclic strain fields on the surface of the specimens during fatigue loading, a timed Digital Image Correlation (DIC) system was set-up.

A simple electronic assembly was used to collect and analyze the load signal from the testing machine (fig. 2.9(a)). This was used to count the cycles and trigger the camera every 20 cycles, at the time of maximum loading (fig. 2.9(b)). Such a protocol ensured that the strain later computed by DIC was due to cyclic creep and not variations in the timing of the image acquisition during a cycle.



(a) Electronics for timed image acquisition



(b) Image acquisition every 20 cycles at peak loading

Figure 2.9: Timed image acquisition with fatigue loading.

Lighting of the specimen was insured using LED spots which provided sufficient light without heating the material. This made possible to set a high enough shutter speed (1/50s) compared to the loading frequency (0.5Hz) and thus ensure minimal blur of the images.

Images collected were processed using the DIC software Vic2D to compute cyclic strain fields.

DIC data was also used to measure the Notch Opening Displacement (NOD) by placing *virtual* extensometers. These were placed between two points on either side of the notch, 1 mm from the specimen edges (see fig. 2.10).

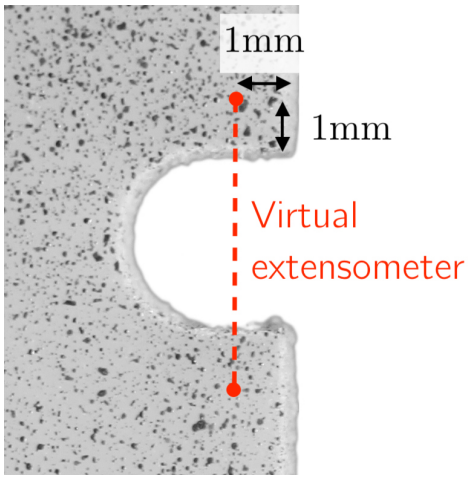


Figure 2.10: Position of the virtual extensometer on a notched U2 specimen for NOD measurement.

2.2.1.4 Definitions

In this short paragraph some definitions will be given so as to avoid any future confusion or misunderstanding.

We will call nominal stress σ the value given by :

$$\sigma = \frac{F}{S_{net}} \tag{2.1}$$

with F the applied force and S_{net} the net section of the specimen, measured between notch roots for notched specimens.

This is also sometimes referred to as the *net* stress in the literature.

For load controlled fatigue testing we will sometimes refer to the maximal nominal stress σ_{max}. This refers to the maximal stress imposed during one loading cycle.

Note that all stress values have been normalized by an arbitrary value for confidentiality reasons.

The stress triaxiality ratio η is the ratio between the hydrostatic pressure and the von Mises equivalent stress as defined by eq. (2.2).

$$\eta = \frac{\frac{1}{3}(\sigma_I + \sigma_{II} + \sigma_{III})}{\frac{1}{\sqrt{2}}\sqrt{(\sigma_I - \sigma_{II})^2 + (\sigma_{II} - \sigma_{III})^2 + (\sigma_{III} - \sigma_I)^2}} \tag{2.2}$$

We thus have $\eta = 1/3$ for uniaxial loading and $\eta = 0$ for pure shear[4].

[4]Damage models based on the triaxiality ratio (e.g. the GTN model, see section 1.5.2.2) will thus not account for cavitation growth in a specimen under pure macroscopic shear. However, at

Global triaxiality can be induced by a multiaxial loading. Local triaxiality can be induced during uniaxial loading due to the presence of local stress concentration (caused by notches, holes, etc).

For flat specimens the triaxiality ratio can be determined using the Bridgman formula:

$$\eta = \frac{\sqrt{3}}{3}\left[1 + 2\ln\left(1 + \frac{d}{4r}\right)\right] \tag{2.3}$$

with d the inter-notch distance and r the notch radius.

Evaluation of the cyclic-creep phenomenon is based on the *cyclic strain* parameter. It can be evaluated in a number of way, by considering the maximum, minimum on mean value of the strain for each loading cycle (fig. 2.11). In our case we will use the mean strain per cycle as the cyclic strain, except for experimental measurements where the maximum strain is used. This choice is merely conventional as there is very little -if any- difference between the three measurements when later considering the cyclic strain *rate*.

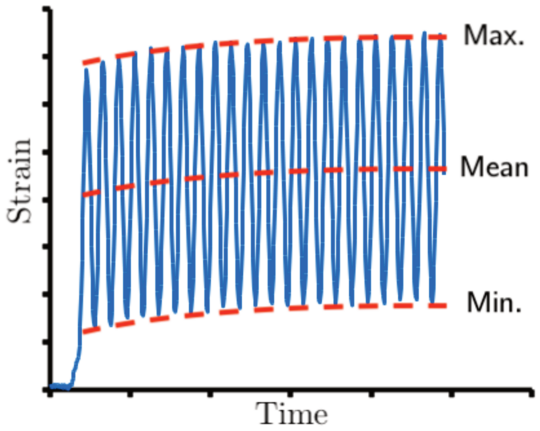


Figure 2.11: Example of the *cyclic strain* measurement for cyclic-creep evaluation during fatigue loading.

2.2.2 In-situ synchrotron testing

In-situ testing on a synchrotron tomography beamline requires a compact and lightweight experimental set-up capable of loading the specimen in the desired condition while fitting in the reduced space of the experimental hutch.

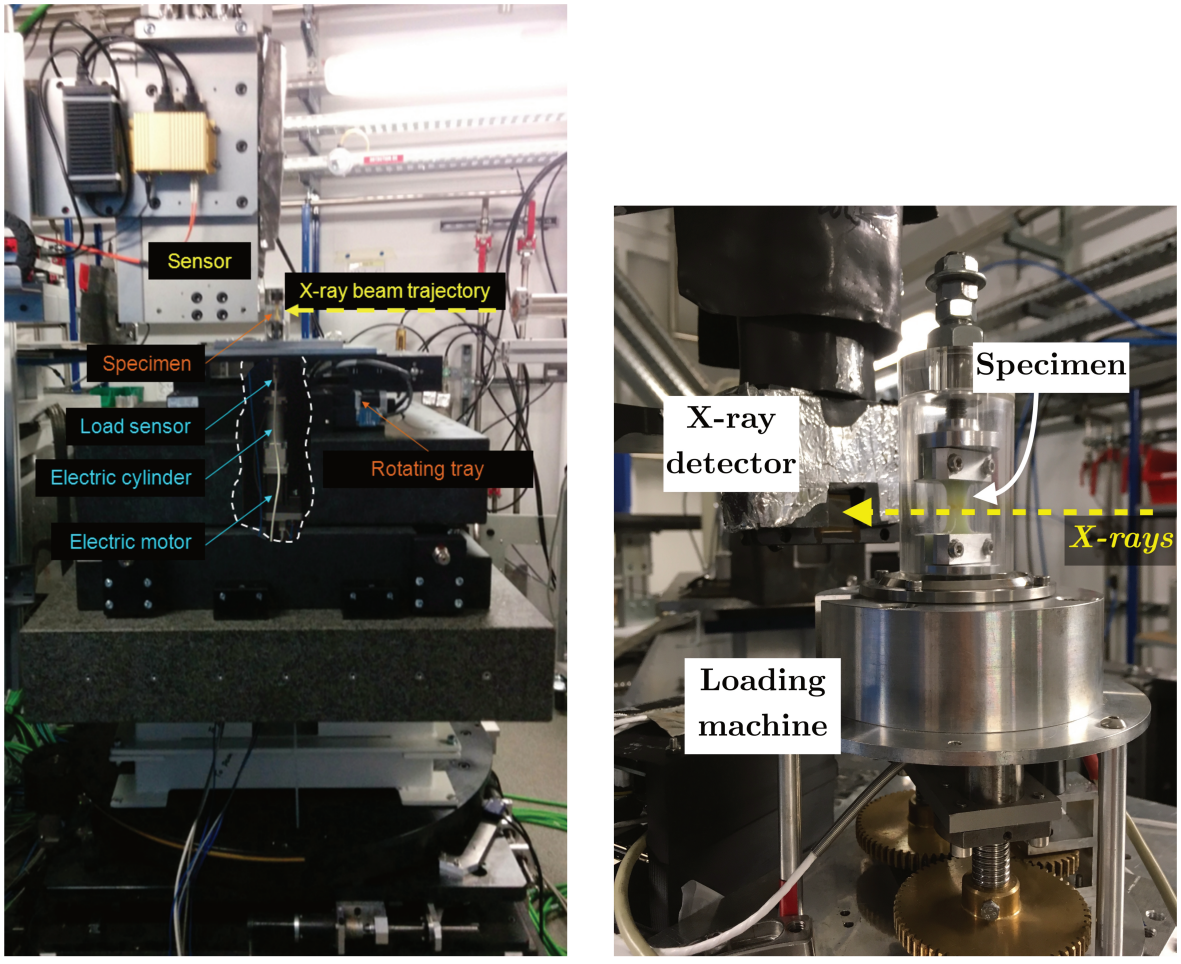
A compact machine allows for the detector to be brought closer to the sample and thus improving the resolution of the image. The apparatus must also be stable and balanced around the rotation axis of the tomographic platform to avoid any unwanted movement during scanning. The machine must not reduce the beam too much, and

the spherulitic level where damage initiates, the stress state is not pure shear (even probably quite multiaxial) due to the two-phases organization at the local scale, and triaxiality in not null.

make use of a PMMA tube serving as a window to let the X-rays through with little absorption. Finally a good set-up should allow for an efficient change between samples in order to minimize the time *lost*.

Several machine were developed at the lab during the PhD work of Rolland [1]. The final set-up was conceived for the PSICHE beamline at the SOLEIL synchrotron (fig. 2.12(a)). It allowed for a load controlled fatigue loading of the specimens at a frequency up to 1Hz. Part of the tomographic data used in this study was acquired using this machine.

Another machine, seen on fig. 2.12(b), was provided by Novitom and used on the PSICHE beamline (SOLEIL synchrotron) and the ID19 beamline (ESRF). It also allowed for a load controlled cyclic loading of the specimen but at lower frequencies (up to 1Hz). This machine was used for a faster access to a synchrotron beamline, but proved less effective than the home-made design.



(a) Home-made machine [1]

(b) Machine provided by Novitom

Figure 2.12: Experimental setups for in-situ testing, on the PSICHE beamline.

At SOLEIL the filtered X-ray beam (2 mrad mirror, 0.5 mm aluminum and 0.25 mm silver) had an energy of about 26 keV. The CMOS detector with 6.5 micron pixels, was associated to a x10 objective, leading to a voxel edge size of $0.65\mu m$, on the acquired image. Specimen-sensor distance was 35 mm. 1500 projections were recorded per scan during a 180 degrees rotation of around 5 min, with 31 references pictures before and after scanning.

At the ESRF a fast-scan setup was used. This allowed for the scans to be performed without interrupting the quasi-static tensile tests, without having image-blur. Scan duration was of about 2s and one scan was made every 20s while performing tensile testing at $1\mu m/s$.

2.3 Observation techniques

Whether it is to investigate the damage distribution in a sample, to image a microstructure, to determine a damage scenario or to examine the organization of matter at the smallest of scales, multiple observation techniques are required. Most are classical methods or instruments in materials science and the aim of this section is only to make a quick tour of the different techniques that will be used in the present work.

2.3.1 Transmission cross-polarized light microscopy

As introduced in section 1.1.2.3, transmission cross-polarized light microscopy is the traditional way used to observe spherulites in thin polymer films.

The incident light is polarized by a first linear filter, and hits the thin sample (fig. 2.13). The transmitted light beam is no longer polarized, the local change in polarization direction being a function of the local birefringence of the sample.

The beam then encounters an analyzer, a second filter that lets pass only one direction of polarized light. By rotating the analyzer we can thus adjust the final image.

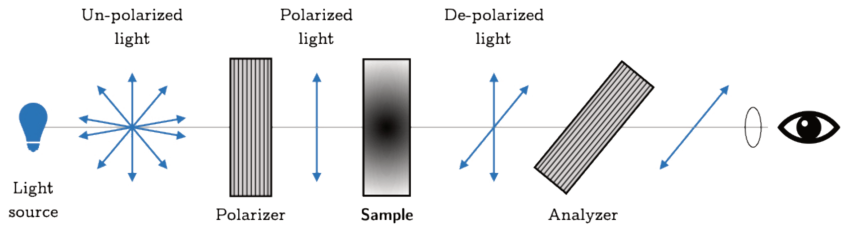


Figure 2.13: Transmission polarized light microscopy.

Note that the same method can be used for all birefringent materials, and is most commonly used in mineralogy. It also works in reflection on shiny surfaces (e.g. for polished metallic microstructures).

2.3.2 Scanning Electron Microscopy

Scanning Electron Microscopy (SEM) is one of the most commonly used type of microscopy in materials science. Since its invention in 1937, the technology has evolved allowing for nanometric resolutions.

The image is produced by bombarding the sample with electrons and collecting the signals back from the sample. A lot of different signals can be analyzed with the proper detectors: secondary, backscattered and Auger electrons, characteristic and continuum X-rays, cathodoluminescence, etc. All these signals yield different types of information on the sample morphology and chemical composition.

In the case of secondary electrons, the most common imagery mode (see fig. 2.14), the detector is place off to the side and collects low-energy electrons ejected from the atoms of the near surface of the material (up to a depth of a few nanometers). The intensity of the collected beam depends of the volume impacted and thus on the local orientation of the surface compared to the incident electron beam. Secondary electron imagery thus gives good images of the surface topology.

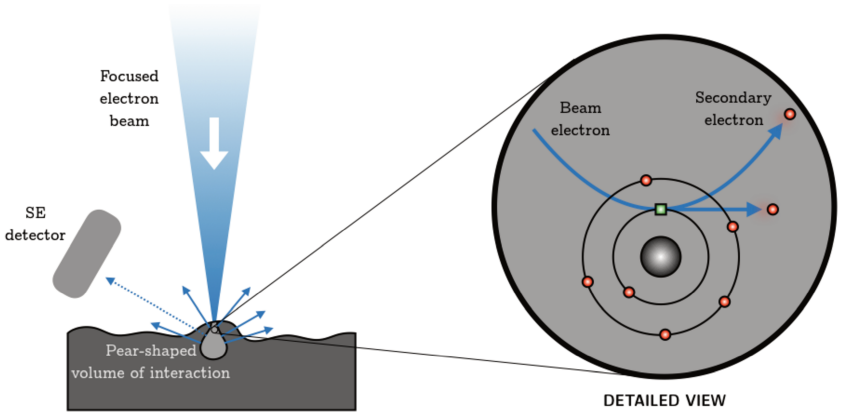


Figure 2.14: Secondary electron imagery in SEM.

For a simple SEM in a typical set-up, the sample needs to be able to conduct the electrons. Non-conductive materials such as polymers are thus often coated using sputter-deposition with a nanometric layer of gold or carbon.

2.3.3 Micro-tomography

Tomography allows for the 3D imaging of bulk specimens. It is commonly used in the medical domain as CT scans, and micro-tomography works on a similar principle but with higher beam energies allowing for an improved resolution.

During the tomographic scan, the sample is placed on a rotating plateform (fig. 2.15(a)). The X-ray beam is sent through the specimen and on to a detector on the other side. As the beam encounters the specimen, the X-ray photons interact with the matter. The intensity I of the transmitted signal depends on the absorption μ of the different media encountered along a given trajectory s. This can be expressed by the Beer-Lambert law of attenuation in its line integral form:

$$-\log \frac{I}{I_0} = \int_s \mu(s) ds \tag{2.4}$$

For a given angular position of the rotating platform, the image obtained is a radiography (here called a *projection*). The contrast on the image thus depends of the width and composition of the specimen.

Multiple projections, typically 1500, are recorded at different angular positions for a half or full rotation of the specimen (fig. 2.15(b)).

Reconstruction of the image consists in determining the local value of the absorption coefficient μ at every "point" in the specimen. The size of these "points" depends on the quality of the material used and the set-up. They form volumetric pixels or *voxels*. On a standard tomograph voxel size is of a few microns, while sychrotron tomography currently allows to reach sub-micron voxel size even reaching a few tens of nanometer in some cases.

The mathematical basis of the reconstruction is found in the work of Radon [2] in 1917 when he showed that an object can be reconstructed perfectly from a full set of line integrals. In practice, various reconstruction algorithms have been developed in order to obtain a 3D image from the projections (fig. 2.15(c)). While detailed explanations of the different reconstruction algorithms is out of the scope of this work, much more information can be found in the specialized book by Herman [3].

Once the 3D image has been reconstructed, the data can be visualized (fig. 2.15(d)) and analyzed. Gray level for a given voxel depends on the local absorption of the material and on the various imaging artifacts and noise (see appendix A for more details).

While often considered a non-destructive imaging technique, it is worth reminding that the basic principle of X-ray tomography relies on the interaction of the beam with the matter. This interaction can indeed have some effects on the material, as will be discussed later in section 6.1.2.4.

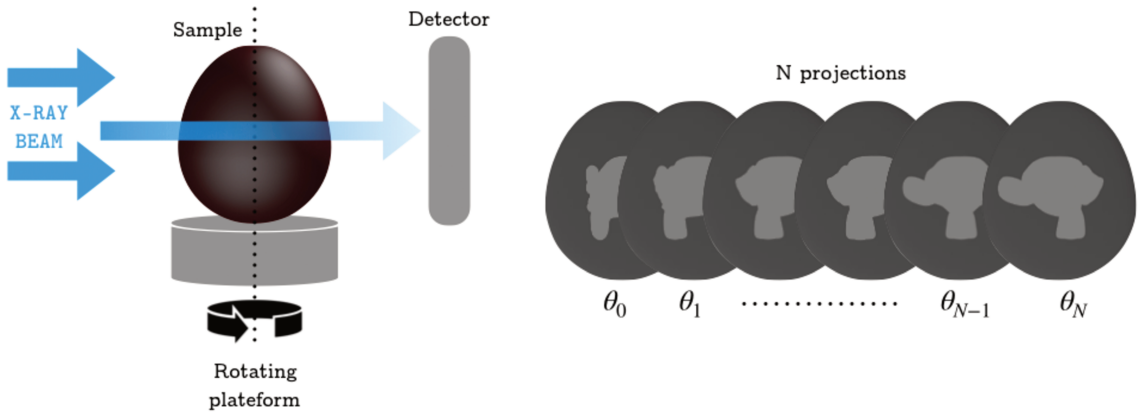
2.3.4 Atomic Force Microscopy

Atomic Force Microscopy (AFM) was invented in 1982, and quickly became one of the best tool to image and probe matter at the nano-scale. In its simplest configuration it is used to map the sample topography, but can also yield data on much more properties such as visco-elasticity, conductivity, capacitance, magnetic forces, etc. depending on the imaging mode being used.

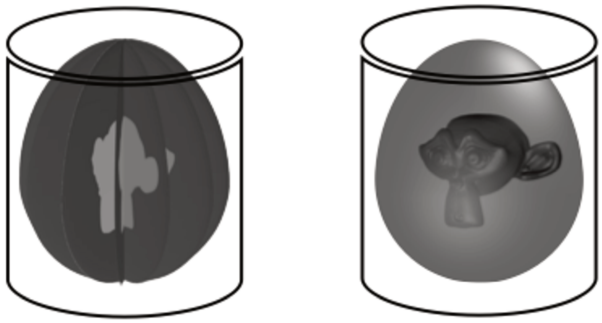
The basic principle of AFM is that a tip at the end of a cantilever probes the surface of the specimen (fig. 2.16). The attractive or repulsive forces between the tip and the sample make the cantilever move and deflect the laser beam. The vertical position of the tip can thus be measured and plotted as an image.

2.3.5 Digital Image Correlation

Using cross-correlation to measure shifts in datasets has been applied to digital images since at least the early 1970s. More specifically, Digital Image Correlation (or "DIC")



(a) Acquisition (b) Projections



(c) Reconstruction (d) Visualization

Figure 2.15: Micro-tomography.

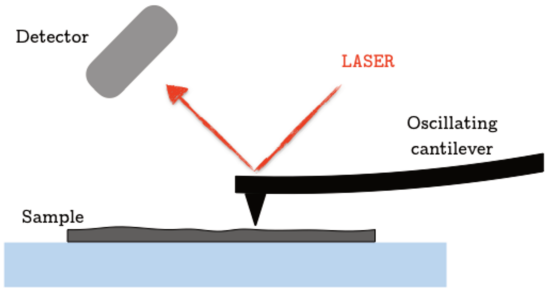


Figure 2.16: Atomic Force Microscopy.

is an optical method which measures surface strain fields. Using a *non-repetitive*, *isotropic*, *high-contrast* speckle pattern on an object's surface, the method tracks the changes in grey value pattern in small neighborhoods called subsets during deformation.

Using a dedicated correlation algorithm, it is thus possible to obtain a full-field surface strain measurements.

More recent extensions of such methods can be found in Digital Volume Correlation (DVC), for example used on X-ray tomographic data, which gives access to bulk 3D strains.

2.4 Bibliography

[1] H. Rolland, *Comportement en fatigue et mécanismes d'endommagement du polyamide 6,6 renforcé de fibres courtes.* PhD thesis, ENSAM, 2017. 68, 72, 78, XIV

[2] J. Radon, "Uber die bestimmung von funktionen durch ihre integralwerte langs gewisser mannigfaltigkeiten," *Journal of Mathematical Physics*, vol. 69, pp. 262–277, 1917. 81

[3] G. T. Herman, *Fundamentals of Computerized Tomography.* Springer, London, 2009. 81

Chapter 3

Voiding mechanisms at the micro-scale

By the help of microscopes, there is nothing so small, as to escape our inquiry; hence there is a new visible world discovered to the understanding.

Robert Hooke

When Robert Hooke published his book *Micrographia* in January 1665, it was the first major publication to illustrate the world as seen through microscopes. As true as it was more than three centuries ago for insects, plants and small objects, observations and analysis at the micro-scale remain an essential way of improving our understanding of the structure and deformation mechanisms of materials.

This chapter provides an in depth analysis of the fatigue damage mechanisms[1] of reinforced semi-crystalline polymers and gives a new insight on the organization of matter for those materials and its evolution during deformation.

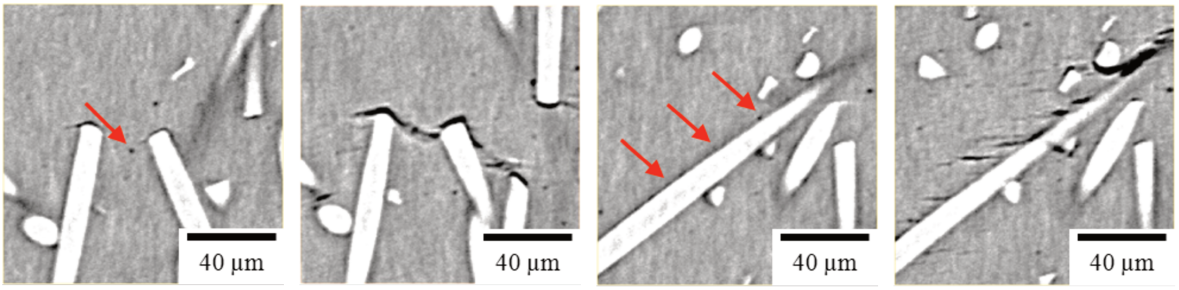
3.1 Further study of the usual damage mechanisms

The usual fatigue damage mechanisms as well as the more recent insights gained by tomographic analysis has be developed in section 1.4.3.2.

Microtomography is a good tool to observe the diversity of the bulk damage mechanisms and can yield valuable information both qualitative and quantitative. In particular it showed that fiber confinement played a major role in triggering fiber failure and that cavitation in the matrix was a precursor of many other usual fatigue damage mechanisms (fig. 3.1).

Yet the this description can be further completed by new observations. These were based first on tomographic data, both with a new analysis of the large database from

[1]The term *damage* used also includes voiding mechanisms at small scales, these do not necessarily induce a loss of mechanical properties nor compromise the integrity of the part. Only the growth, coalescence and accumulation of these damages can eventually lead to the failure of the material.



(a) $N/N_f = 40.5\%$ (b) $N/N_f = 99.7\%$ (c) $N/N_f = 40.5\%$ (d) $N/N_f = 99.7\%$

Figure 3.1: Damage at fiber ends and crazing - RH50 - 0° specimen - $N_f = 2468$ cycles. Cavitation is evidenced by arrows. From ROLLAND [1].

the work of ROLLAND, and with a series of new imaging campaigns especially on neat polymer.

Furthermore, to complete this analysis of the mechanisms, a large number of SEM fractography observations were performed, allowing for a higher resolution. These SEM observations were key to make a detailed analysis of the damage mechanisms as these take place at scales close to the resolution limit of the tomographic data used in this work.

3.1.1 Fiber failure

The importance of fiber failure has been evidenced by tomographic data. Two factors were proposed to explain the failure of fibers even at low levels of macroscopic stress. First, fibers crossing each other can induced local stress concentrations and trigger a failure. Second, surface defects in fibers resulting from the manufacturing process or caused by the injection could also explain the observed damage.

The fiber failure induced by neighboring crossing fibers can clearly be seen by fractography analysis as shown on fig. 3.2. It is clear that failure was due to the proximity of the fibers, inducing a stress concentration in the polymer and the reinforcements.

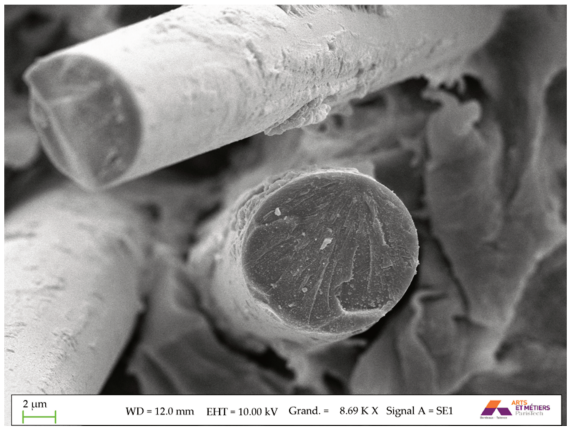
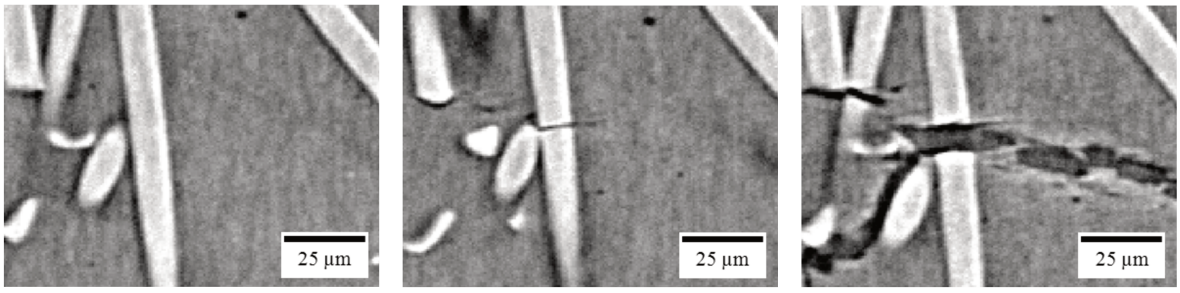


Figure 3.2: Fiber failure induced by the proximity of a crossing fiber in the shell - U2 0° specimen - RH50 - f=0.5Hz - R=0.1 - Normalized $\sigma_{max} = 0.54$ - $N_f = 6206$.

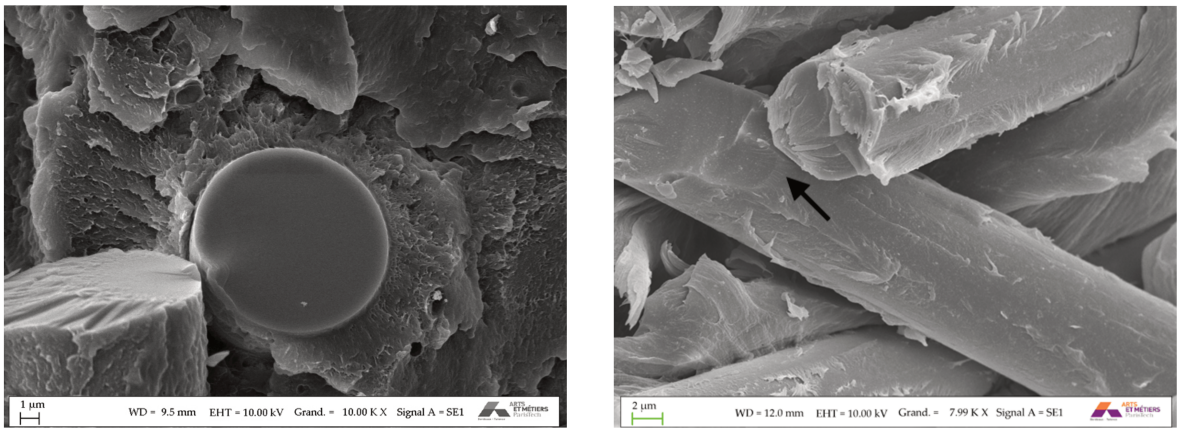
Moreover, on tomographic data, it is relatively hard to know if fibers are close or actually touching each other in some cases (fig. 3.3). Complementary fractography observations clearly indicate that contact can occur between fibers (fig. 3.4). This contact can induce some indentation or could even induce some fretting-fatigue phenomenon.

To our knowledge it is the first time that fiber failure triggered by contact between crossing fibers has been reported for short-fiber reinforced thermoplastics.



(a) Initial state - $N/N_f = 0.0\%$ (b) fibre failure under cyclic loading - $N/N_f = 40.5\%$ (c) Damage evolution under cyclic loading - $N/N_f = 99.7\%$

Figure 3.3: Sequence of fibre failure as observed by microtomography. Note how difficult it can be to determine if, where and when adjacent fibers are actually in contact.



(a) Indentation. Observation in the shell (b) Surface damage. Observation in the core

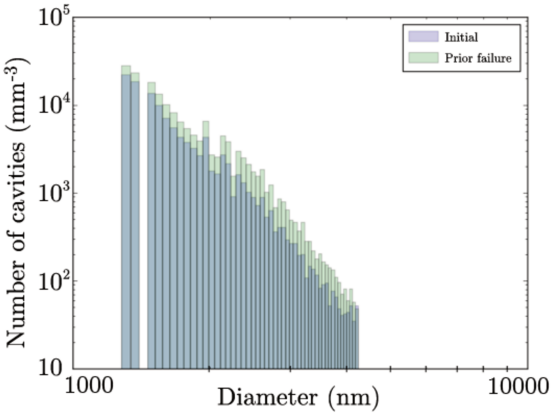
Figure 3.4: Evidences of contact inducing damage and failure of fibers during fatigue loading - U2 0° specimen - RH50 - f=0.5Hz - R=0.1 - Normalized $\sigma_{max} = 0.54$ - $N_f = 6206$.

3.1.2 Cavitation

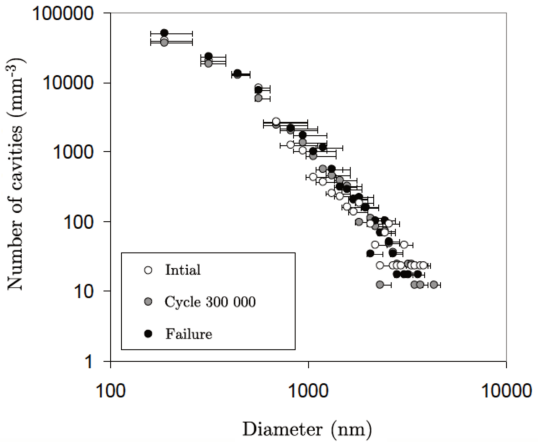
As previously mentioned, cavitation is a major type of early damage in semi-crystalline polymers.

Cavities can be observed and analyzed on tomographic data in which they appear as spheres 1 to $5\mu m$ in diameter (fig. 3.5(a)). They do not grow significantly during the fatigue lifetime, but their number strongly increases with the applied loading. This is true regardless of fiber orientation.

The size distribution of the cavities can be qualitatively compared to the one obtained by Mourglia-Seignobos [2] using a SEM in transmission mode on $1\mu m$ thick slices of the neat polymer (fig. 3.5(b))



(a) As obtained by tomography in a 90° reinforced PA66 specimen



(b) As obtained from microscopy in a PA66 specimen. From Mourglia-Seignobos [2]

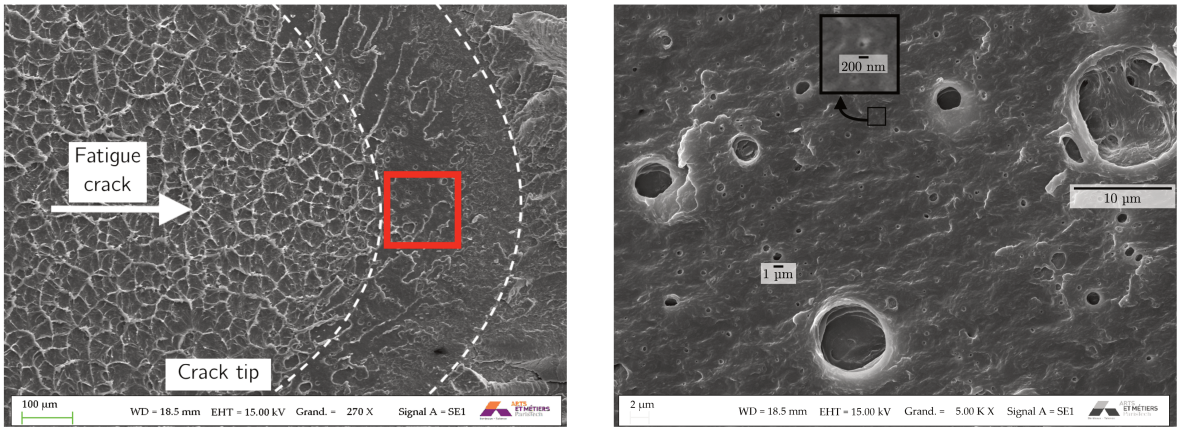
Figure 3.5: Cavity distribution by diameter as obtained by various methods.

Similar tendencies are obtained with the two methods. However two remarks should be made:

- Tomography, with the technology used, only allows for the analysis of cavities above the micron size. Yet much smaller diameters up to $100nm$ can be measured using electron microscopy.
- More cavities are observed using tomography, this could be explained by the different loading conditions as well as by the higher local stress levels in the reinforced specimen in fig. 3.5(a), with the fibers acting as stress concentrators.

This can be further illustrated by performing fractography SEM observations of the cavitation process at the fatigue crack tip in a PA66 specimen (fig. 3.6). This region is a transition zone between the fatigue crack and the brittle finale failure of the specimen. It is prone to an intense cavitation phenomenon during fatigue loading, as clearly shown on fig. 3.6(b).

Such observations confirm the vast range of cavities sizes, even in a same area. Diameters range from around $100nm$ and up to $10\mu m$ for the largest cavities. However even the smallest voids observed here are one order of magnitude larger than the lamellae and amorphous phases in the spherulites. A whole range of nanometric voids that are thus not yet observed and will be key to gain a better understanding of the nucleation process and the earliest stages of cavitation growth. This will in particular shed light on the issue of the stability of small cavities (less than a few tens of nanometers in diameter) and help define the transition from polymer chain mobility to a stable cavity.



(a) View of the fatigue crack tip

(b) Intense cavitation ahead of fatigue crack tip

Figure 3.6: Detail view of cavitation ahead of crack tip in neat PA66 - U0.5 specimen - RH50 - f=0.5Hz - R=0.1 - Normalized $\sigma_{max} = 0.30$ - $N_f = 2123$.

3.1.3 Debonding

The initiation of debonding in fatigue in difficult to observe experimentally. Indeed the fiber-matrix interface is hard to analyze on tomographic data, even with sub-micrometric resolution, in part due to the phase contrast at the boundary between the phases (fig. 3.7).

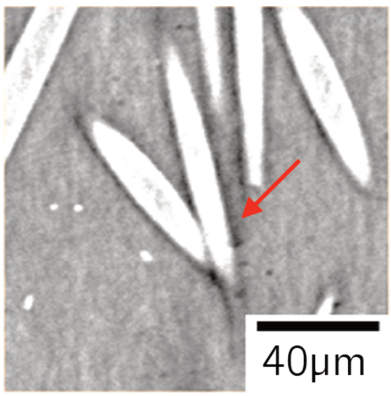


Figure 3.7: Early stage of debonding at the interface, seen here at $N/N_f = 20.3\%$ in a RH50 0° specimen - $N_f = 2468$. Note how difficult it can be to distinguish debonding from the phase contrast at the fiber-matix interface.

Debonding is usually described to initiate from the fiber tips, where adhesion is poor. Failure then propagates along the interface.

Figure 3.8 evidences such mechanism on a longitudinally broken fiber. It also yields an insight on the importance of cavitation, as it had been suggested by tomographic observations. Indeed cavitation is seen to occur near or even at the interface. This could induce the beginning of a debonding process, even far from a fiber tip.

Adhesive and cohesive failure modes can be observed. This can be observed along debonded fibers or at the interface of broken fibers (fig. 3.9).

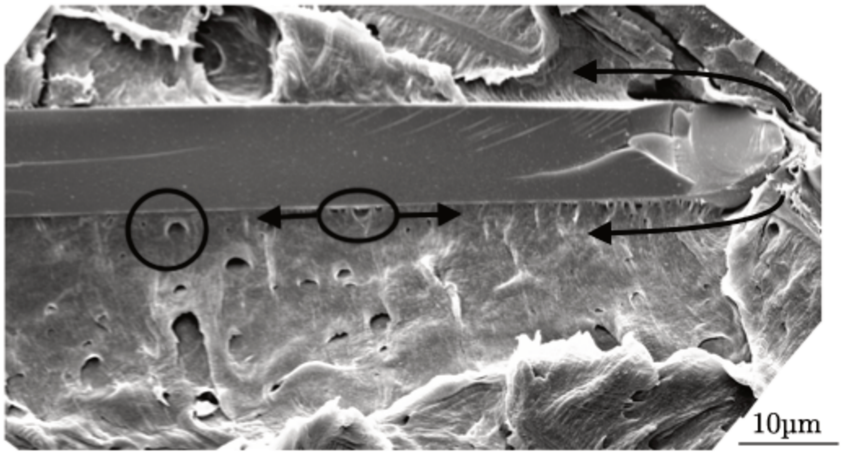
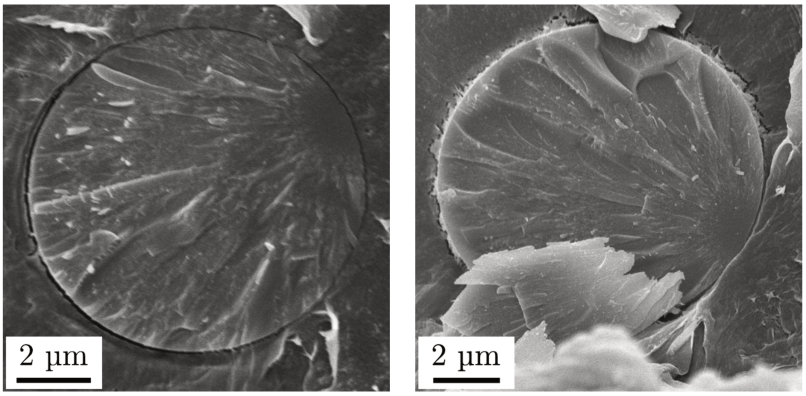


Figure 3.8: Damage at the interface along a transversely broken fiber after fatigue loading - 0° specimen.



(a) Adhesive damage (b) Cohesive near-interface damage

Figure 3.9: Damage at the interface around broken fibers after fatigue loading - 0° specimen.

3.2 Spherulitic damage

Focus on the spherulitic damage was set after extensive tomographic observation of crazing and short cracks in bulk material. These first observations on the composite material revealed that damage structures had a characteristic size, close to the diameter of the spherulites in the material (fig. 3.10).

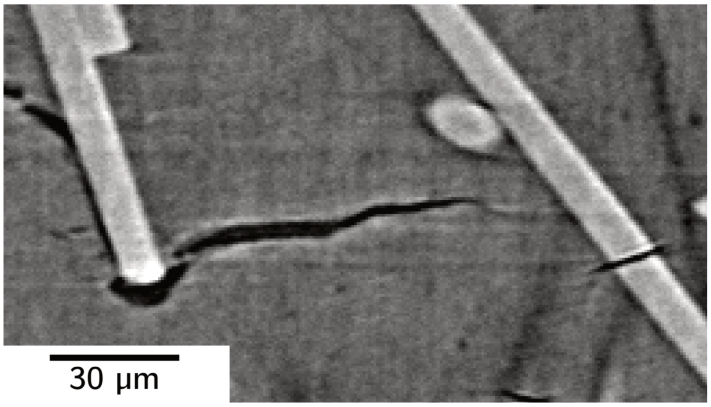


Figure 3.10: Crack tip in a 0° PA66GF30 specimen as observed by microtomography - f=3Hz - RH50 - Normalized $\sigma_{max} = 0.69$ - $N = 2462$.

Further investigation was thus necessary. Additional analysis and observations were performed with the focus of gaining a better understanding of the link between matrix damage and the spherulitic microstructure. These observations were not limited to composite specimens, and neat PA66 specimens were also investigated as spherulitic damage is a matrix-related phenomenon.

3.2.1 Specimens geometry and loading conditions

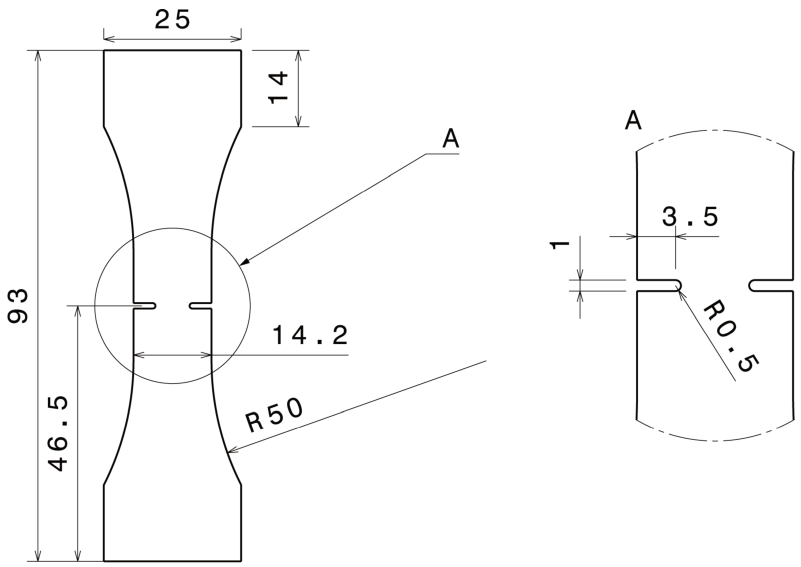
The use of notched specimens allows for the localization of the damage to make the observation of fatigue damage by tomography easier. The notched geometry that was considered here is a symmetric "U" notch of $0.5mm$ in radius (fig. 3.11(a)).

All specimens were conditioned at a relative humidity (RH) of 50% and 23°C. For these conditions, the polymer and associated composite are tested in their ductile regime i.e. above the glass transition temperature.

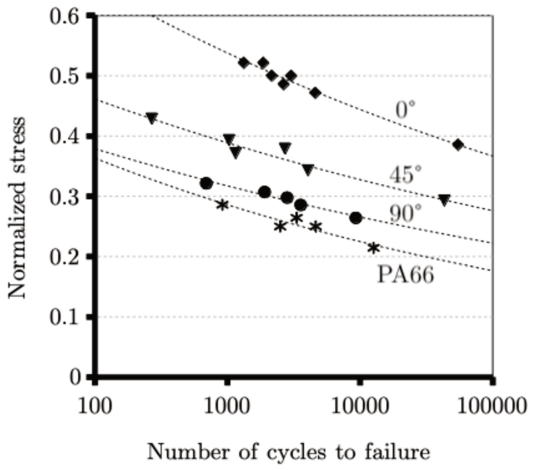
Fatigue tests were performed under load control, at a loading ratio of R=0.1 and a frequency of 0.5Hz (a sufficiently low frequency to ensure a low heat build-up during fatigue tests). Testing at R=0.1 means that this study focuses on what will latter be referred to as the cyclic creep regime (by opposition to the dissipative regime at R<0, see chapter 4).

3.2.2 Tomographic observations on short fatigue cracks

Interrupted fatigue specimens were observed using tomography after the initiation of a macroscopic crack. Typical example of a fatigue crack as observed on pure PA66 is given on fig. 3.12. Figure 3.12(a) and fig. 3.12(b) represent respectively the 2D view



(a) U0.5 notched geometry



(b) Normalized S-N curves

Figure 3.11: Geometries and S-N curves for the notched specimens.

and segmented view of the fatigue crack initiation. Several short fatigue cracks can be identified at the notch indicating simultaneous initiation at different locations in the notch area. Once initiated from the notch root, fatigue crack then propagates with a slightly irregular trajectory, as observed on fig. 3.12(a). By close examination of tomographic slices, it is possible to identify a characteristic length of 20-30μm along the crack propagation direction. In addition, these observations evidence the presence of damage ahead the crack tip.

Indeed, both small cavities of a few microns and micro-cracks can clearly be observed ahead the crack tip. It is worth noticing that the characteristic size of the micro-crack and of the crack propagation pattern is of the order of magnitude of the spherulites. These observations confirm also that cavitation very near the crack tip seems to play a major role in the fatigue crack propagation process.

On the shorter crack visible on fig. 3.12(a), it can clearly be seen that the same damage processes are taking place: irregular path with a characteristic length and cavitation at the crack tip. This tends to support that those processes are not limited to long fatigue cracks.

Figures 3.12(c) and 3.12(d) give additional information on these damage precursors. First, the top view of crack front indicates a very irregular crack front with significant diffuse damage ahead of the crack front. Considering the size (in the micrometer range) and aspect ratio of these damage markers they most probably correspond to the cavitation process identified on fig. 3.12(a). In addition to this cavitation process, some larger damaged area can be clearly identified. Once segmented, they appear as flat, penny shape like volumes about 20μm in diameter (see fig. 3.13(c)). This size and shape strongly suggest that these penny shaped damage zones correspond to intraspherulitic damage developing ahead the crack tip.

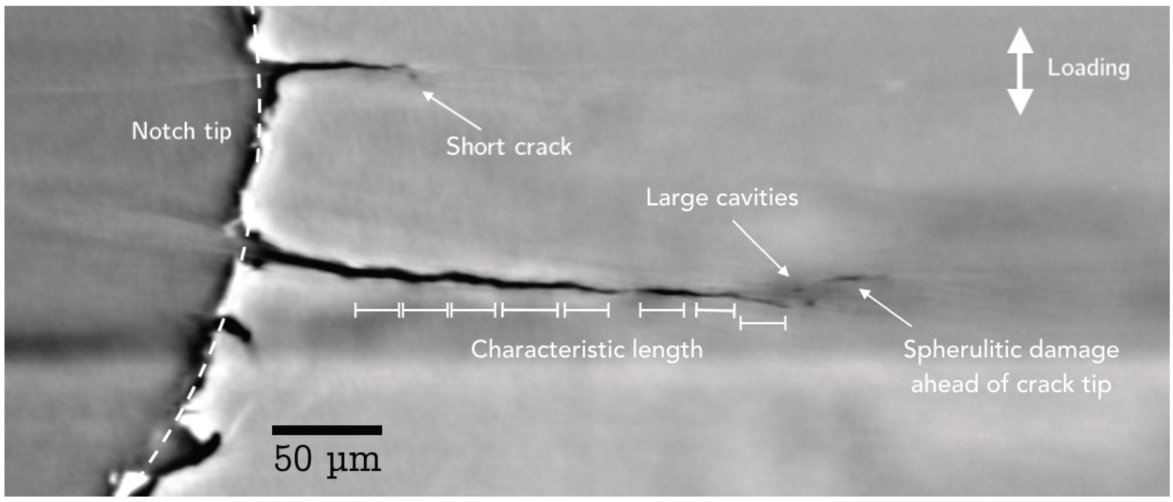
In the case of reinforced polymer, another example of fatigue microcracks is given fig. 3.14(b). The top view clearly confirms the presence of a multiplicity of penny shape damaged zones that combined constitute the short fatigue crack. These are crazing structures along a fiber, which is a common fatigue damage mechanism in 45° specimens. The damage structures can clearly be seen as having a characteristic disk-shaped morphology.

Moreover fig. 3.15 confirms that the opening of a new damage region also occurs in a very distinctive manner in the polymer matrix. The crack progresses with this distinct disk-shaped morphology of the crack tip. This damage occurs relatively quickly[2], ahead of the main crack tip.

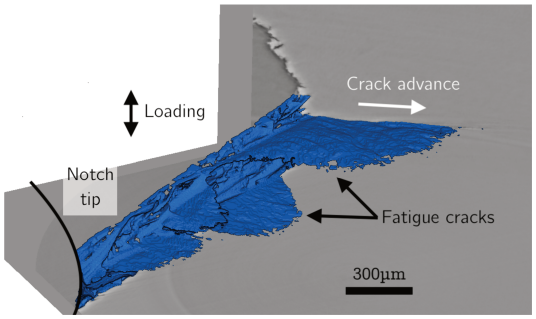
These complementary observations on the composite material, along with the one presented on fig. 3.10, appear very similar to those made on pure PA66: damage is shown as having a penny shape structure 20μm in diameter. The same mechanisms are thus proposed for both reinforced and neat polymer.

Based on these observations a scenario is proposed in which the damage is localized

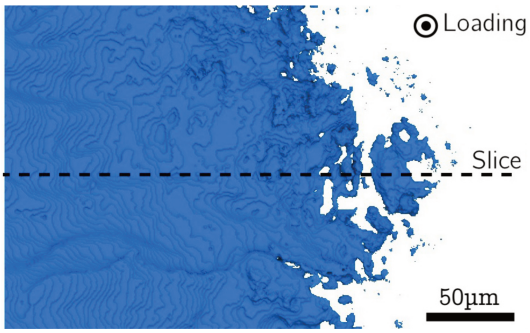
[2]Smaller damage was probably already present in fig. 3.15(a), but not large enough on the tomographic data to be properly seen and segmented.



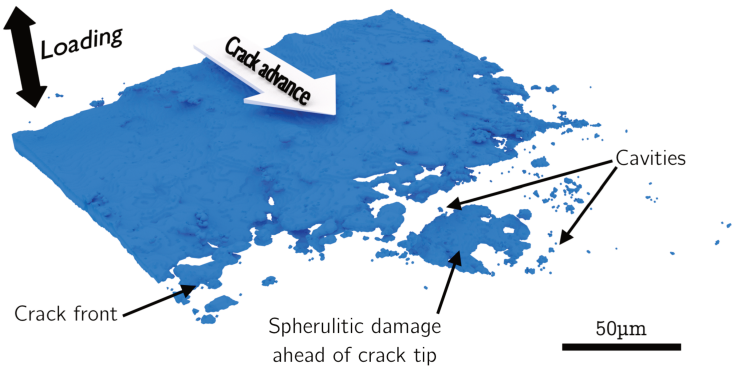
(a) 2D slice



(b) Segmented view of the fatigue cracks



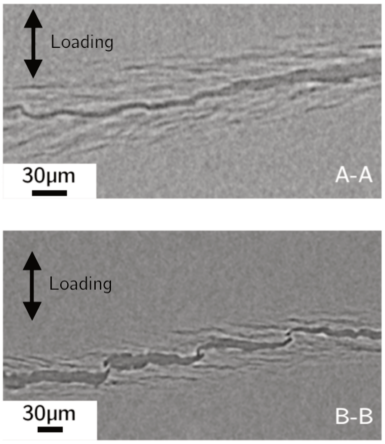
(c) Detailed top view of the segmented crack tip and position of the 2D slice from fig. 3.12(a)



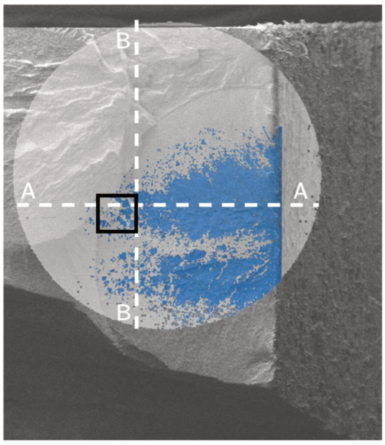
(d) Segmented view of the crack tip

(e) QR code to access the 3D render of fig. 3.12(d). Try scan it or go to: https://skfb.ly/6MNGY

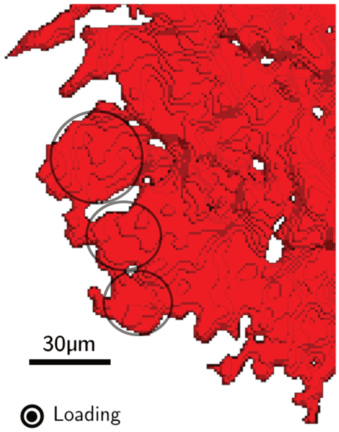
Figure 3.12: Tomographic observation and segmentation of the crack tip in a PA66 notched specimen, test interrupted at 4221 cycles and 90% of estimated fatigue life.



(a) 2D views

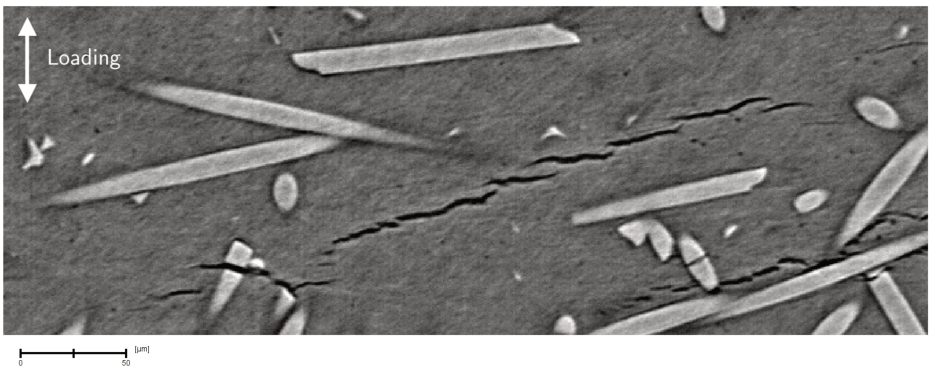


(b) Fracture surface with the segmented crack ovelayed

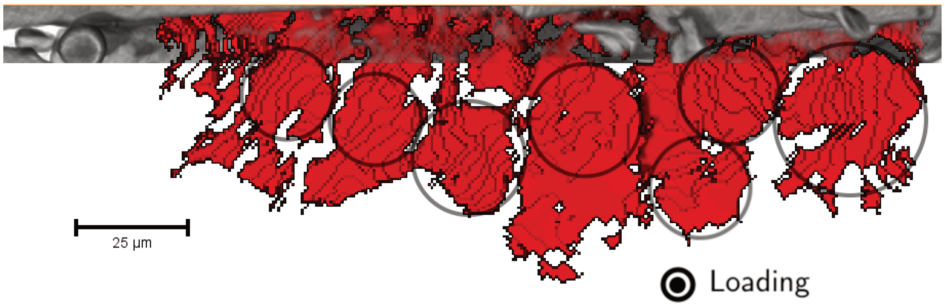


(c) Detailed view of the segmented crack tip (black square area in figure 3.13(b))

Figure 3.13: Crack tip in a PA66 notched specimen as observed by microtomography, test interrupted at 2531 cycles and 95% of estimated fatigue life.

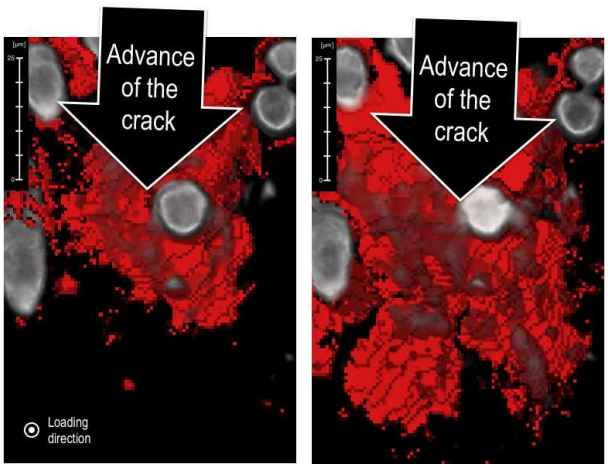


(a) 2D slice



(b) Top view of the segmented damage

Figure 3.14: Short cracks in a 45° PA66GF30 smooth specimen as observed by microtomography, test interrupted at 1500 cycles and 98% of estimated fatigue life.



(a) After 2460 loading cycles (b) After 2462 loading cycles

Figure 3.15: Advance of the crack tip, segmented in a RH50 0° specimen and viewed in the plane orthogonal to the loading direction.

in the equatorial plane of the spherulites. The distinctive structures observed by tomography both for crazing and crack propagation can be associated to an intra-spherulitic fatigue crack propagation process in the equatorial plane, resulting in spherulites being *cut in half*.

However, because spherulites in PA66 are not visible using tomography, these observations and damage scenario need to be completed by other observation techniques in order to confirm the nature of the spherulitic damage.

3.2.3 Fractography analysis of fatigued PA66 specimens

3.2.3.1 Spherulite observation

The idea behind the observations presented hereafter is that if the fatigue crack results from the opening of the spherulites in their equatorial planes, half of the spherulite should be observable on the fracture surface.

Fracture surfaces obtained after fatigue loading on notched PA66 specimens can be divided into several regions: the main and secondary fatigue crack area starting from the notches on both sides, the final failure surface and a transition zone in between the two (fig. 3.16).

The final failure surface, at the center of the specimen, exhibits a patchy irregular surface (fig. 3.17(a)). Some authors suggested that the patches are related to the spherulites [3], although possible, this seems far from being evident just by looking at the fracture surface.

The transition zone, between the fatigue crack path and the final fracture surface, is rather smooth (fig. 3.17(b)). An important number of cavities can be observed in this region as shown earlier on fig. 3.6.

In the fatigue crack paths on both sides, one can observe parabolic fatigue striations on the outer layers of the specimen (fig. 3.17(c)). On the center, a layer of rough aspect can be observed compared to the surrounding matrix. This rough layer could

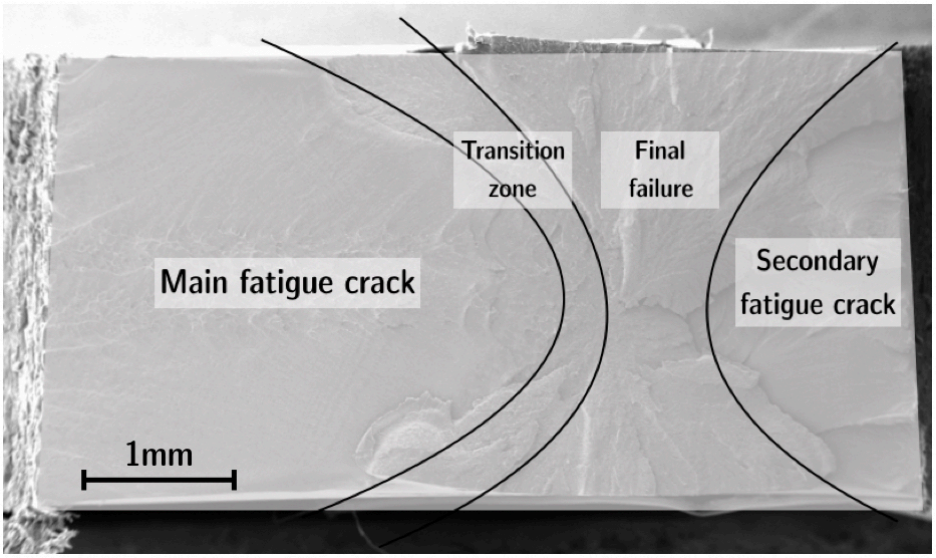


Figure 3.16: Fracture surface of a notched PA66 specimen after fatigue testing - Normalized $\sigma_{max} = 0.29$ - $N_f = 917$.

be explained by greater strain levels at the center of the specimen or, although less likely based on our observations[3], by a gradient in the material properties [4]. By taking a closer look in this region, we can unambiguously observe the spherulites (figs. 3.17(d) and 3.17(e)). Fracture surface roughness appears to be induced by the interaction of the crack with the spherulitic microstructure and clearly indicate that the crack has followed the equatorial planes of the different spherulites on its path.

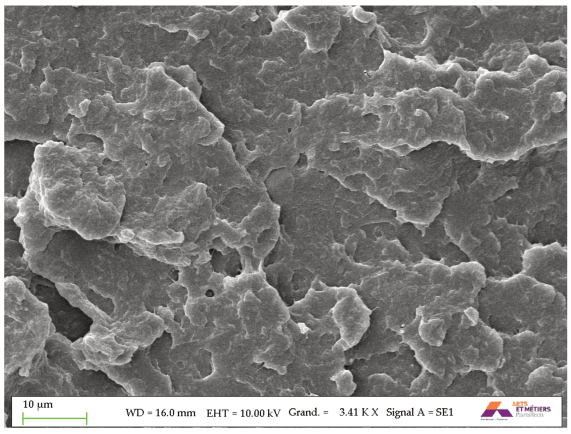
Observations of a specimen submitted to interrupted fatigue loading followed by cryofractography in traction help further explicit the damage scenario. Figure 3.18 illustrates the spherulite damage ahead of the crack tip. At the time where cryo-fractography was performed, the spherulite was already damaged and opened in half by the fatigue loading (figs. 3.18(c) and 3.18(d)). The spherulite is thus perfectly visible against the brittle failure region caused by cryo-fracture. Several sites of spherulitic damage can be observed ahead of the crack front (fig. 3.18(e)). This observation, together with fig. 3.12(a), definitively confirm that spherulitic damage occurs ahead of the main fatigue crack front.

Furthermore, as the nuclei of the spherulites can be seen on the fatigue fracture surface of the different specimens, this confirm the scenario of an intra-spherulitic failure in the equatorial plane. The importance of the nucleus in the intra-spherulitic damage process will be detailed in section 3.2.4.

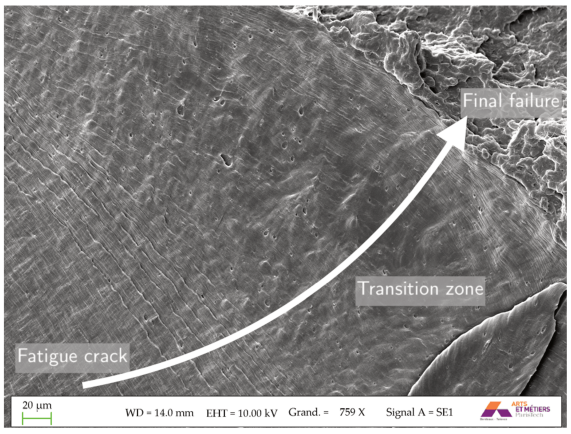
The 2D tomographic observations of a characteristic damage length and the 3D observations of disk-like structures allow to propose a damage propagation scenario as illustrated figure 3.19. Locally, the crack takes a path that depends on the spatial spherulitic arrangement.

It can be noted that the crack propagates either perpendicularly (region 1 on

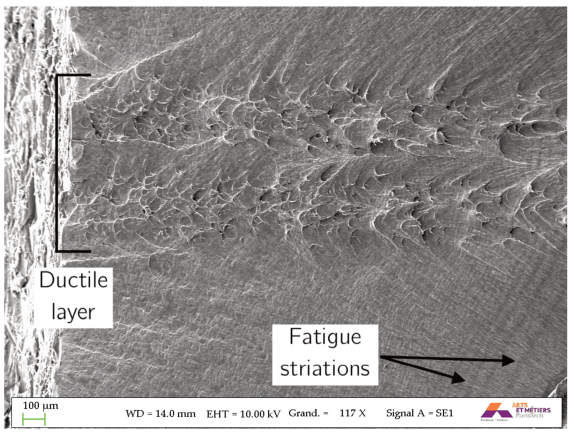
[3]Based on the observations we performed using cross-polarized microscopy, smaller spherulites are only observed in a $30\mu m$ layer under the surface of the material (see section 2.1.3).



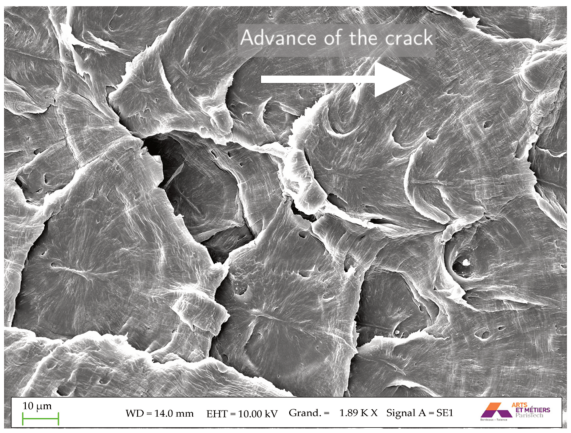
(a) Final failure surface



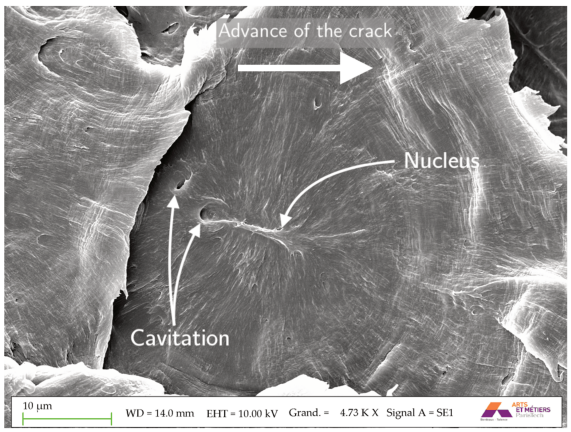
(b) Transition zone



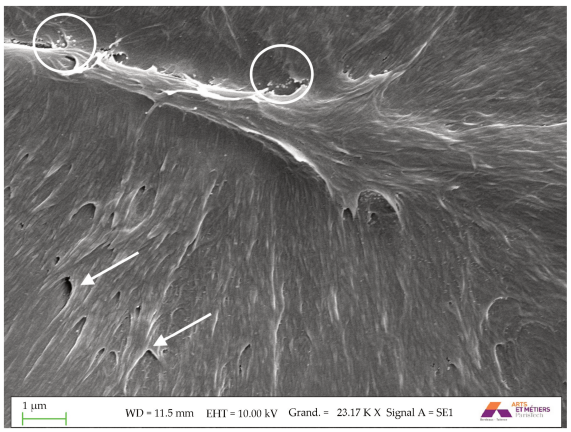
(c) Fatigue crack path



(d) Spherulites on the fracture surface

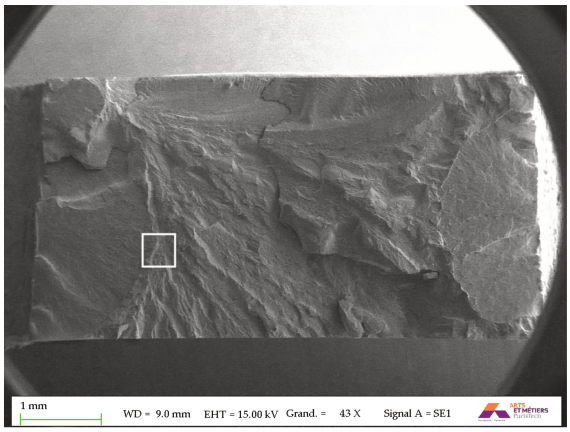


(e) Detail of a spherulite

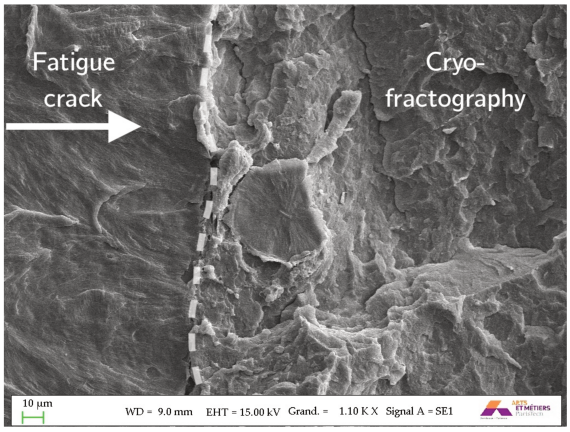


(f) Detail of the nucleus from fig. 3.17(e)

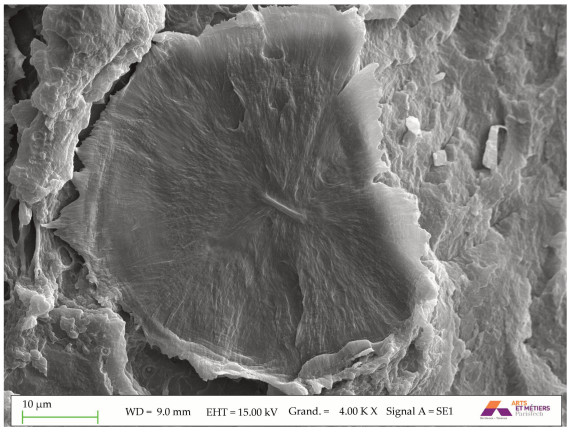
Figure 3.17: SEM fractography of a notched PA66 specimen ($N_f = 917$).



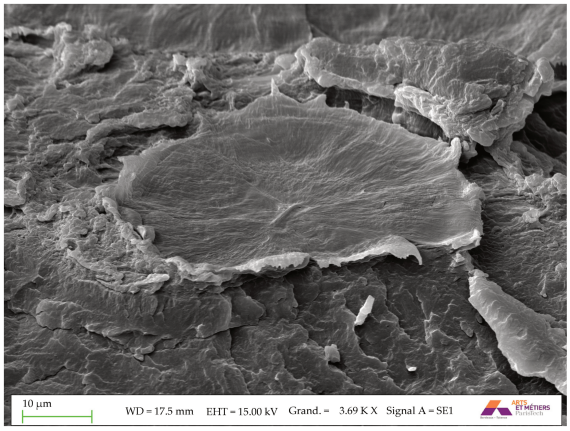
(a) Global view of the fracture surface



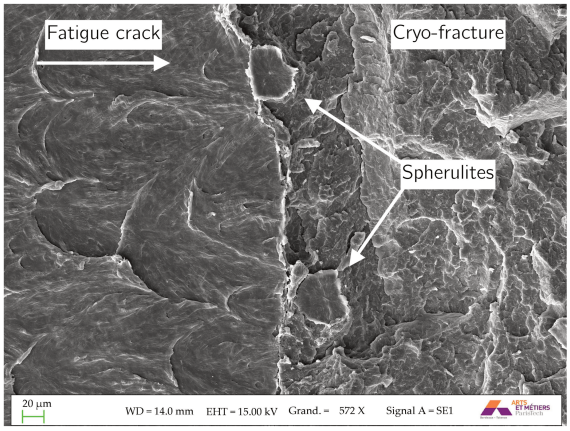
(b) Limit between fatigue crack and cryofractography



(c) Top view of the spherulite



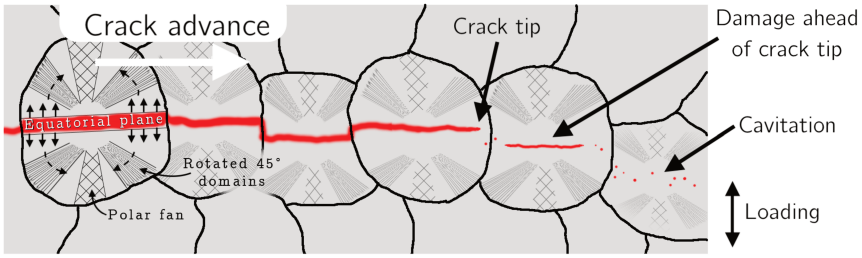
(d) Tilted view of the spherulite



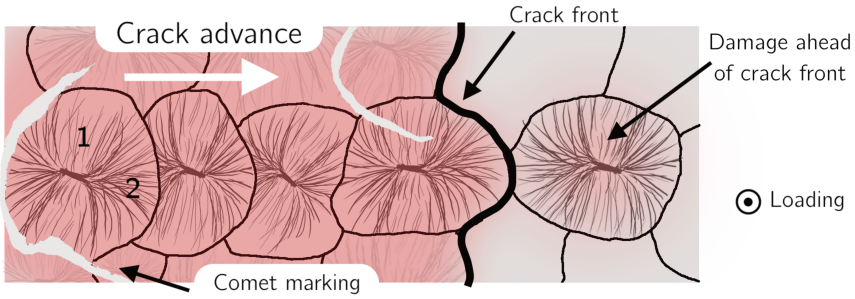
(e) Global view of the crack front

Figure 3.18: Spherulitic damage ahead of the fatigue crack in a notched U0.5 PA66 specimen after cryofractography, test interrupted at 4221 cycles and 90% of estimated fatigue life.

fig. 3.19(b)) or parallel (region 2 on fig. 3.19(b)) to the lamellae in the equatorial plane. More diffuse damage might also develop in other regions of the spherulite (see fig. 3.19(a)) for longer cracks, as suggested by fig. 3.13(a). However more precise tomographic (nano-tomography) data would be required to fully assess the nature of this secondary damage.



(a) Side view of the crack advance



(b) Top view of the crack advance

Figure 3.19: Schematic of the influence of the spherulitic structure of the polymer on fatigue crack advance.

3.2.3.2 Spherulite orientation

The orientation of the nuclei with respect to the horizontal can be measured on the images (fig. 3.20). As they seem to be preferentially oriented in a given direction, it is likely that the orientation of the nuclei is induced by the injection process. All nuclei would then be aligned because the specimens were all cut at 90° with respect to the MFD.

Pure PA66 samples were thus cut at 0° and 45° for further analysis. After fatigue loading and observation of the fracture surface, the nucleus clearly appears as a disc on the fracture surface of 0° specimens (fig. 3.21(a)). For 45° specimens the nucleus can have a slightly elliptical shape, although being harder to observe (fig. 3.21(b)). Conversely, for the 90° specimen, the nucleus appears as an elongated cylinder with high aspect ratio (figs. 3.17(e) and 3.21(c)). This confirms the observations of Selles [5], for creep of PA6 90° specimens, showing an undamaged *harder* cylindrical volume at the center of the spherulite.

These observations could be explained by a phenomenon of flow-induced crystallization whereby nucleation is in part triggered by the local organization of the polymer chains induced by the flow. Although the strain in the flow is not important enough to obtain crystallization as a shish-kebab structure [6], is might be sufficient to induce a preferential direction at the onset of crystallization. Some polymer chains extend in the molten polymer and organize themselves resulting in a crystalline structure, oriented in the flow direction, that will form the future nucleus. Subsequent crystalline lamellae growth continues radially from this structure during cooling, thus forming an overall *spherical* arrangement around the oriented nucleus. The semi-crystalline organisation in our injection-molded thermoplastic is therefore an intermediate between purely radial spherulites and strongly oriented shish-kebab structures (fig. 3.22).

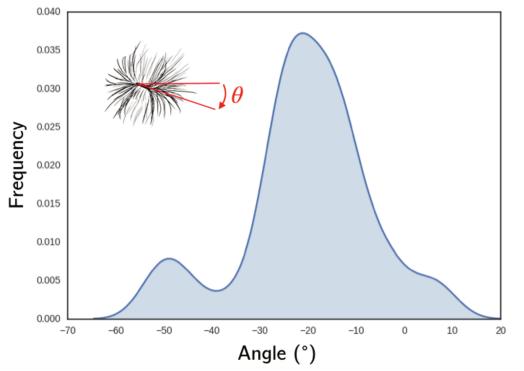
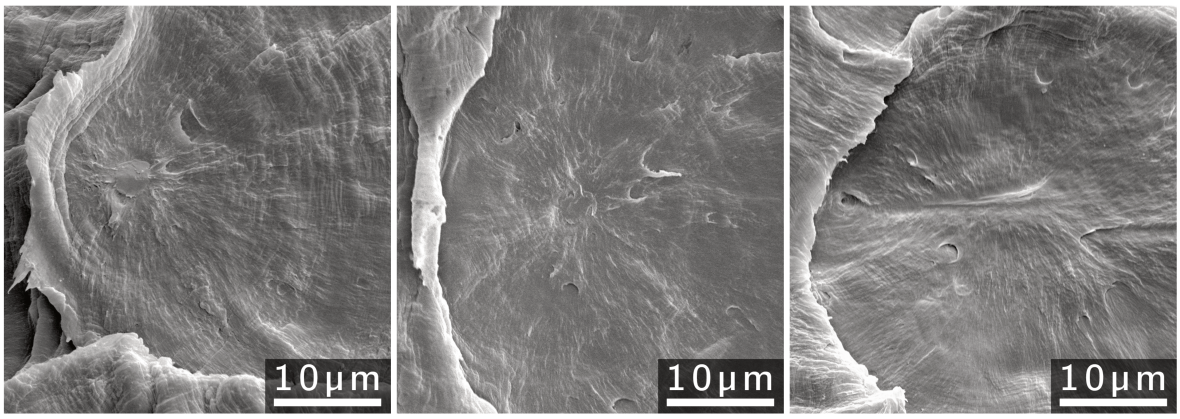


Figure 3.20: Orientation of the 40 nuclei observed on 3 different PA66 specimens after fatigue testing.



(a) 0° specimen (b) 45° specimen (c) 90° specimen

Figure 3.21: SEM observations of the nuclei for three different specimens orientation ($N_f \approx 1500$).

3.2.4 On the importance of the spherulite nucleus

As seen on the previous images, the nuclei of the spherulites can be easily be observed on fatigue fracture surfaces. It has a cylindrical shape about $3-5\mu m$ in diameter and

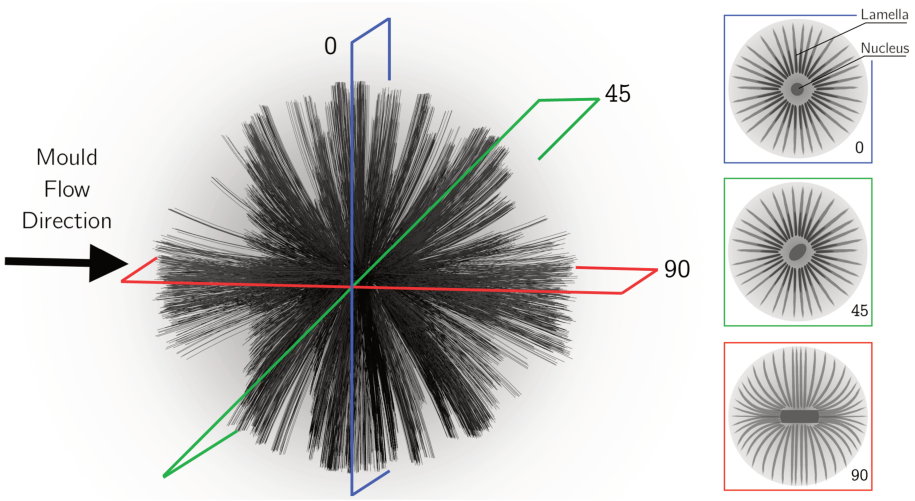


Figure 3.22: Oriented spherulitic structure induced by the injection molding.

$7 - 10\mu m$ in length, although it is probable these dimensions depend on the injection conditions of the material.

The nucleus seems harder and denser[4] than the surrounding lamellae and may act as damage precursor. As shown on fig. 3.17(f) small cavities that can be found close to the nucleus confirm this point as well as small white spheres that could be nucleating agents introduced during the manufacturing process.

We can take a more precise look at how fatigue damage initiates in the equatorial plane of the oriented-spherulite, close to te nucleus.

Fractography of interrupted specimens yields more interesting details. In front of the main fatigue crack, spherulitic damage can be observed (fig. 3.23(a)). But unlike images presented above, the current observation reveals in one image the whole damage sequence occurring in the spherulite (fig. 3.23(b)).

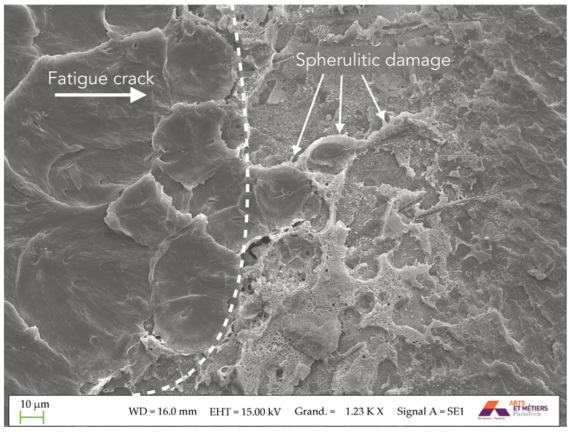
In front of the main fatigue crack tip, extensive spherulitic damage can already be seen. This damage is localized around the nuclei of the spherulites and indicates the progressive opening of the structure in the equatorial plane.

Similar observations can be made in other places along the crack front (fig. 3.24) supporting the argument for a damage scenario (and not just an isolated case).

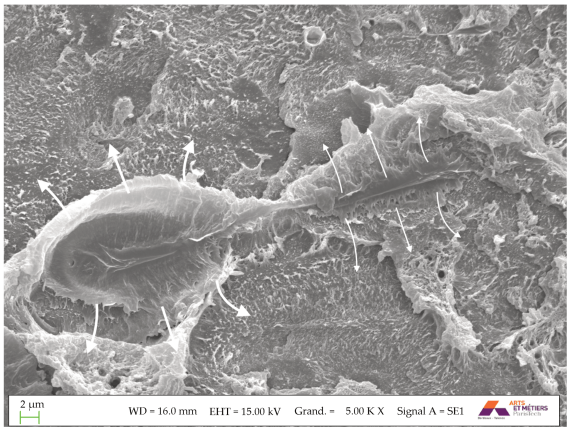
A damage sequence for the oriented spherulite can thus be put forward (fig. 3.25). Damage initiates along nucleus, which is more rigid than the surrounding matter. It then grows outwards in the equatorial plan, progressively taking a circular shape, until complete spherulitic failure occurs.

We therefore have a full scenario of the intra-spherulitic fatigue damage growth, from the preferential localization of damage initiation along the oriented nucleus to the complete opening in the equatorial plane. This would support the hypothesis made by Mourglia-Seignobos [2] that fatigue failure was "very probably localized at the spherulite's equator" against the claim from Andrews [7] that it occurred "frequently

[4]This could be verified using AFM measurement, and will be discussed in section 6.1.2.2.



(a) Fatigue crack front in a PA66 specimen



(b) Detailed view showing damage initiating from the nucleus

Figure 3.23: SEM fractography a notched "tomo" PA66 specimen - $N/N_f = 73\%$ - f=0.5Hz - Normalized $\sigma_{max} = 0.36$.

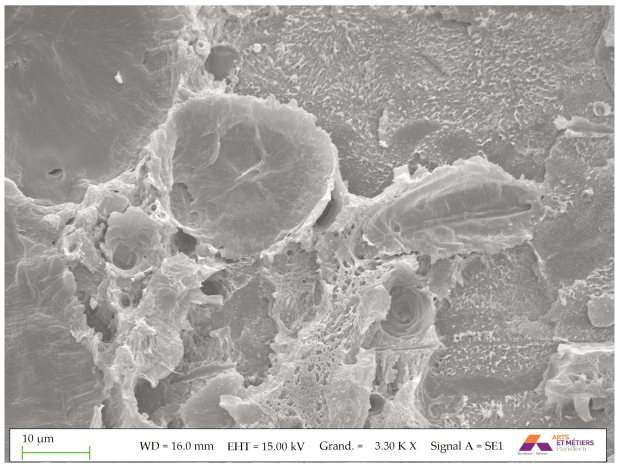


Figure 3.24: Complementary SEM fractography of a notched "tomo" PA66 specimen showing damage initiating from the nucleus - $N/N_f = 73\%$ - f=0.5Hz - Normalized $\sigma_{max} = 0.36$.

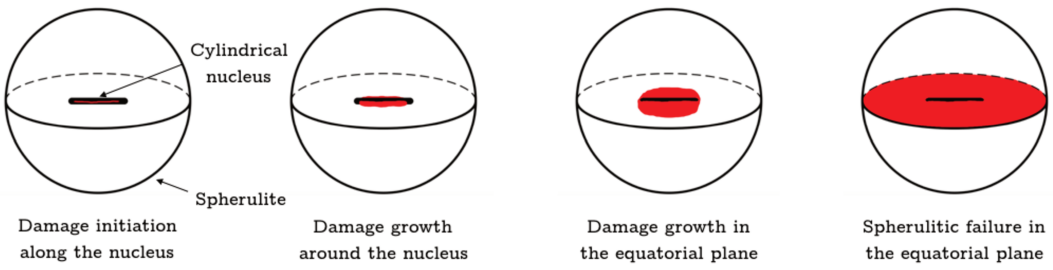


Figure 3.25: Fatigue damage progress in oriented spherulite.

along the inter-spherulitic boundaries"[5].

3.2.5 Fractography analysis of fatigued composite specimens

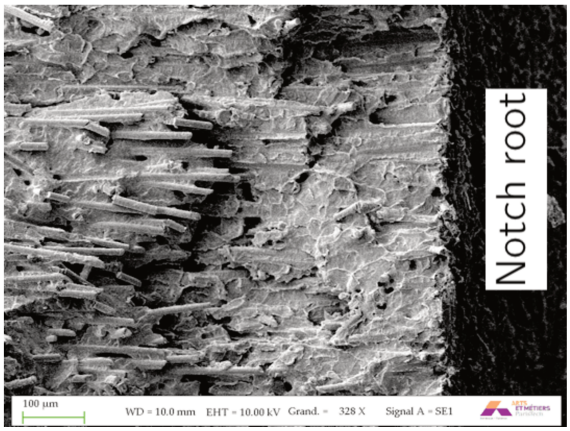
Observation of the spherulites, around $25\mu m$ in diameter, on the fracture surface of PA66GF30 specimens is made more difficult by the presence of the glass fibers, $10\mu m$ in diameter. However careful examination of the fracture surface (fig. 3.26(a)), in the fatigue crack path close to the notch, also allows for the observation of spherulites (fig. 3.26(b)).

In particular observations on fig. 3.26(d) shows the spherulites opened along a fiber, on a configuration very similar to what was observed using tomography (fig. 3.14)

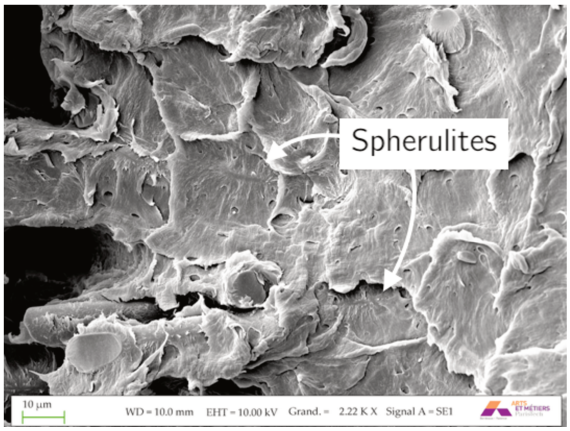
This confirms the scenario based on the tomographic data of fatigued composite material. Fatigue damage is closely linked to the advance of short cracks in the equatorial plane of the spherulites.

Finally, it can be noted that cavities are much more present than on the unreinforced material. This is caused by the much higher local stress triaxiality ratios induced by the presence of glass fibers, confining the matrix.

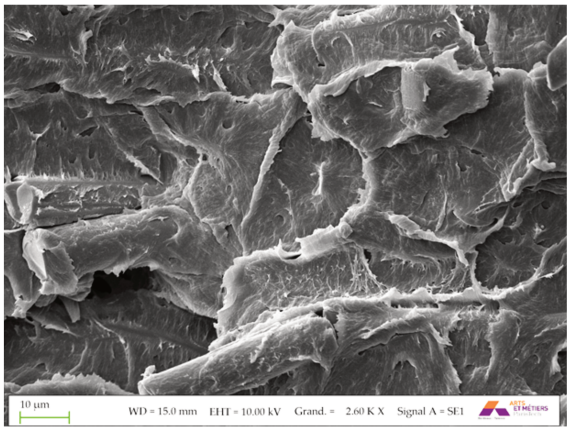
[5] As explained in section 1.2.4, it should be reminded that increasing the spherulite size might cause the failure mode to shift from intra- to inter-spherulitic, as shown by Way [8]. This might explain the different observations made by the aforementioned authors and would require further detailed experimental analysis to definitively asses the effect of increased spherulite size.



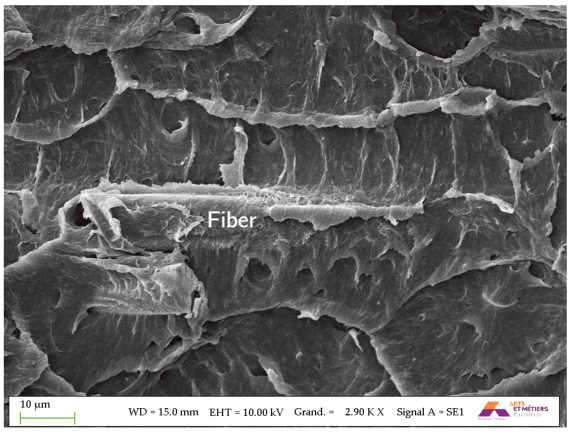
(a) Fatigue crack path in the shell of the specimen



(b) Spherulites and fibers on the fracture surface



(c) Spherulites and fibers on the fracture surface



(d) Spherulites along a fiber

Figure 3.26: SEM fractography a notched U0.5 90° PA66GF30 specimen - f=0.5Hz - Normalized $\sigma_{max} = 0.34$ - $N_f = 24565$.

Main conclusions of the chapter

- Fiber failure can be triggered by **contact between crossing fibers**, a phenomenon that had not been reported in the literature.
- The injection process **strongly orients the pre-spherulitc structure** that will eventually form the nucleus of the fully grown spherulite.
- This oriented nucleus is a **preferential site of fatigue damage initiation** within the spherulite, in the polymer matrix.
- Fatigue damage then progresses outwards in the **equatorial plane** of the spherulite, until complete opening.
- This spherulitic damage occurs **ahead of the main crack front**.

Fatigue damage mechanisms of the thermoplastic polymer exhibit strong similarities with the observations made for creep loading.

3.3 Bibliography

[1] H. Rolland, N. Saintier, I. Raphael, N. Lenoir, A. King, and G. Robert, "In-situ fatigue damage mechanisms in short fibre reinforced PA66 as observed by synchrotron X-ray microtomography," *Composites Part B: Engineering*, vol. 143, no. December 2017, pp. 217–229, 2018. 86, XV

[2] E. Mourglia Seignobos, *Compréhension des mécanismes physiques de fatigue dans le polyamide vierge et renforcé de fibres de verre*. PhD thesis, INSA Lyon, 2009. 88, 102

[3] P. Bretz, J. Manson, and R. Hertzberg, "The Effect of Molecular Weight on Fatigue Crack Propagation in Nylon 66 and Polyacetal," *Journal of Applied Polymer Science*, vol. 27, pp. 1707–1717, 1982. 96

[4] R. Pantani, V. Speranza, and G. Titomanlio, "Effect of flow-induced crystallization on the distribution of spherulite dimensions along cross section of injection molded parts," *European Polymer Journal*, vol. 97, no. July, pp. 220–229, 2017. 97

[5] N. Selles, P. Cloetens, H. Proudhon, T. Morgeneyer, O. Klinkova, N. Saintier, and L. Laiarinandrasana, "Voiding Mechanisms in Deformed Polyamide 6 Observed at the Nanometric Scale," *Macromolecules*, vol. 50, no. 11, pp. 4372–4383, 2017. 100

[6] H. Zuidema, *Flow Induced Crystallization of Polymers Application to Injection Moulding*. PhD thesis, Technische Universiteit Eindhoven, 2000. 101

[7] E. Andrews and B. Walker, "Fatigue fracture in polyethylene," in *Royal Society London*, vol. 79, pp. 57–79, 1971. 102

[8] J. L. Way, J. R. Atkinson, and J. Nutting, "The effect of spherulite size on the fracture morphology of polypropylene," *Journal of Materials Science*, vol. 9, no. 2, pp. 293–299, 1974. 104

Chapter 4

Fatigue behavior at the macro-scale

Successful engineering is all about understanding how things break or fail.

Henry Petroski

The study of the material's mechanical response at the macro-scale helps to identify models and establish durability criteria that can be used in an industrial context on larger parts and structures. As shown in chapter 3, damage mechanisms observed in fatigue are very similar to those observed for creep loading, where strain rate is known to drive the durability of the material. The idea is thus to investigate the use of the cyclic strain rate as appropriate indicator for the fatigue life under cyclic loading.

In the first part of this chapter we will first try to test a cyclic strain rate based fatigue criterion for various relative humidity contents and for the unreinforced polymer. Then we will introduce a mixed criterion that yields more accurate results especially for negative load ratios.

In the second and third parts of this chapter, we will present an experimental and numerical work on notched specimens to investigate the effect of local triaxiality. The extension of the durability criterion to notched components is crucial in order to be used on real parts that often exhibit complex geometries with structural heterogeneities[1].

4.1 Durability criteria for smooth specimens

4.1.1 A cyclic strain rate based criterion

Under cyclic loading with controlled load the mean strain increases throughout the test. Similar evolution of the mean strain can be observed even for negative ones, as shown on fig. 4.1 (note that the abscissa is in logarithmic scale for this graph, to show

[1]These structural heterogeneities induce a local stress triaxiality that is added to both a possible global multiaxial loading and the very local stress triaxialities induced in the microstructure by the presence of fibers.

the mean strain evolution for both low and high N_f. Primary cyclic creep stage is not visible.).

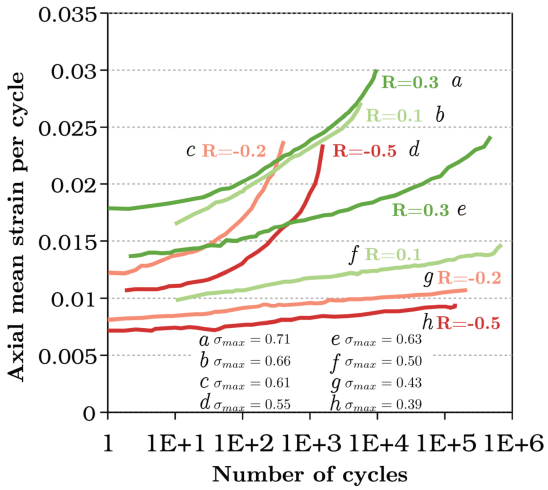


Figure 4.1: Evolution of the mean strain for several load ratios and fatigue lives on smooth 0° PA66GF30 specimens - RH50 - f = 3Hz - forced convection.

This effect exists regardless of the lifetime range or fiber orientation. A cyclic strain rate-based criterion proved to be effective in unifying fatigue results to a certain extent as presented in section 1.3.2.5.

The lifetime was estimated from the cyclic strain rate $\dot{\varepsilon}_{cycl}$ at mid-fatigue life using:

$$N_f = \left(\frac{\dot{\varepsilon}_{cycl}}{\dot{\varepsilon}_0}\right)^n \tag{4.1}$$

Such a criterion proved effective in unifying fatigue results for samples from different positions on an injection molded plate [1], for various testing temperatures [2], for various loading frequencies [3] and for all fiber orientations and a large range of positive load ratios [4; 5].

4.1.2 Effect of water-intake

As the water content of the material has a major impact on the properties of the material, the criterion (that was identified on RH50 specimens [4; 5]) was applied on smooth PA66GF30 45° specimens with RH going from 0 to 80.

Results on fig. 4.2 show that the criterion unifies results for the different humidity ratios.

4.1.3 Improving the strain-rate based durability criterion

Although yielding very good results for positive load ratios, this cyclic strain rate based criterion is much less precise when it comes to negative load ratios (as was presented on fig. 1.26(d)).

The aim of this section is to propose an enhanced version of the criterion in order to further improve the quality of its prediction.

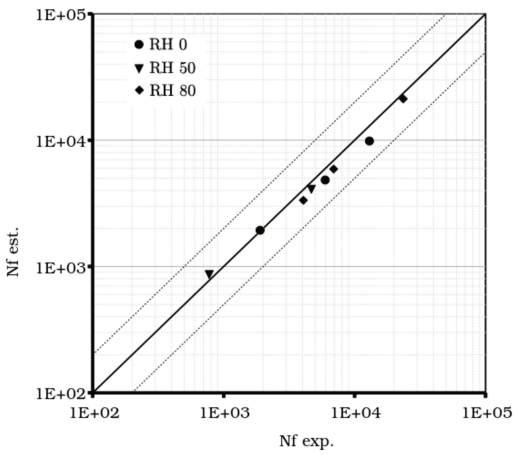


Figure 4.2: Estimated fatigue life using eq. (4.1) vs. experimental number of cycle to failure on smooth PA66GF30 45° specimens - f = 0.5Hz - free convection. Scatter band of factor 2 is marked in dashed lines.

4.1.3.1 Experimental method

The same experimental database as in ROLLAND [4] was used in order to have a direct comparison on the improvement of the criterion.

This database was provided by Solvay Perfomance Polyamide and consists of 207 fatigue tests included in this work.

All testing was performed under load control. Strain evolution was monitored using an extensometer and digital image correlation (DIC) as presented in section 2.2.1.3. A clip on extensometer (class 0.5) with a gage length of 12mm was used. DIC strain field is averaged over the same zone monitored with the extensometer. DIC and extensometer were both used systematically, and DIC data was used when the extensometer knives moved during the test due to cyclic loading, making the extensometer data inaccurate.

A servo-hydraulic MTS fatigue machine was used to load the specimens. Air cooling of the specimen was used to prevent heating (indicated as *forced convection*). This machine was used to performed testing at multiple load ratios (R=-0.5 to R=0.7). A climate chamber allowed for the medium to be kept at a constant temperature (23°C ± 0.5°C) and humidity (50% RH). Testing was performed at a frequency of 3Hz.

Surface temperature of the specimen was monitored using a FLIR thermal camera during testing. This allowed to ensure a limited heat build-up of the specimens.

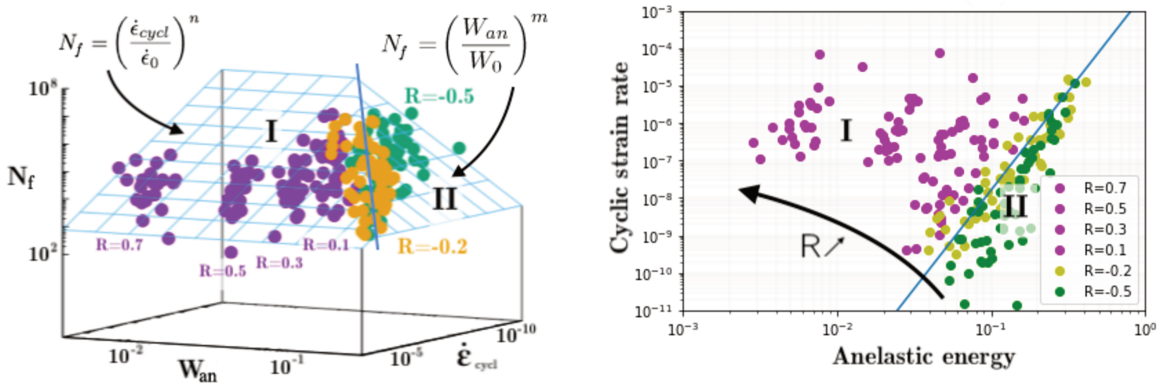
4.1.3.2 Mixed criterion: anelastic energy and cyclic strain rate

The cyclic strain rate based criterion in eq. (4.1) is less precise for negative load ratios. However it was shown that the anelastic[2] energy W_{an} is a parameter unifying results for these negative load ratios [4; 5].

A 3D diagram with the number of cycles to failure versus both the cyclic strain

[2]The anelastic energy was calculated as the area of the hysteresis loop as detailed in section 1.3.1 where the mechanical parameters are described.

rate and the anelastic energy is plotted in order to better illustrate the dependency on those two parameters (fig. 4.3(a)).



(a) 3D scatter plot of the N_f vs. W_{an} and $\dot{\varepsilon}_{cycl}$

(b) $\dot{\varepsilon}_{cycl}$ vs. W_{an}

Figure 4.3: Analysis to establish a relationship between the number of cycle to failure N_f, the anelastic energy W_{an} and the cyclic strain rate $\dot{\varepsilon}_{cycl}$ - RH50 specimens - f = 3Hz - forced convection - all fiber orientations.

Two regimes can be distinguished:

- for positive load ratios, the durability is mostly driven by the cyclic creep strain rate.
- for negative load ratios, because of the high stress amplitude, the dissipative behavior becomes dominant. The fatigue lifespan is then mostly driven by an energetic parameter.

It is worth noting that the present work deals with positive load ratios up to 0.7. A load ratio equal to 1 would correspond to a static creep test and is not addressed here.

As a first approach we consider each of these regimes to be driven by only one parameter ($\dot{\varepsilon}_{cycl}$ or W_{an} respectively). These two regimes are represented by two distinct surfaces in fig. 4.3(a) defined by:

$$N_f^I = \left(\frac{\dot{\varepsilon}_{cycl}}{\dot{\varepsilon}_0}\right)^n \tag{4.2}$$

$$N_f^{II} = \left(\frac{W_{an}}{W_0}\right)^m \tag{4.3}$$

Parameters $\dot{\varepsilon}_0$ and n (resp. W_0 and m) are determined by fitting experimental data for positive (resp. negative) load ratios:

$$\dot{\varepsilon}_0 = 0.842 \text{ and } n = -0.674 \text{ for domain I.}$$
$$W_0 = 3.59\ 10^{-7} \text{ and } m = -3.547 \text{ for domain II.}$$

A trivial, yet effective, approach would consist in estimating the number of cycles to failure as the minimum of eqs. (4.2) and (4.3):

$$N_f = \min\left[\left(\frac{\dot{\varepsilon}_{cycl}}{\dot{\varepsilon}_0}\right)^n, \left(\frac{W_{an}}{W_0}\right)^m\right] \tag{4.4}$$

This yields very good results for all load ratios and fiber orientations (fig. 4.4), with almost every estimated N_f being within a scatter band of factor 2 around the experimental values.

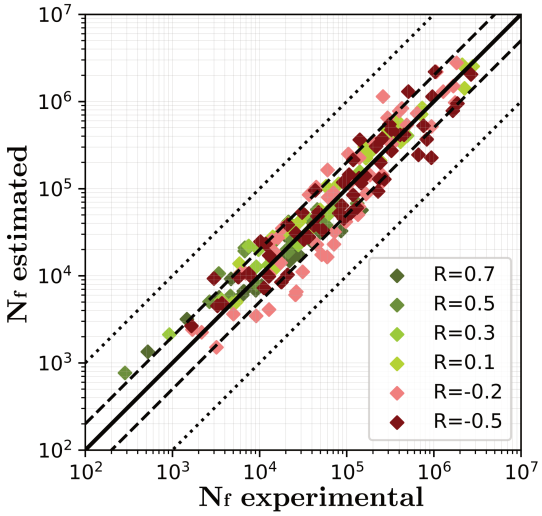


Figure 4.4: Estimated fatigue life using eq. (4.4) vs. experimental number of cycle to failure - RH50 specimens - f = 3Hz - forced convection - all fiber orientations. Scatter bands of factor 2 and 10 are marked in dashed and dotted lines respectively.

However it also possible to obtain a *continuous*[3] criterion by using a weight function to ensure the transition between the cyclic creep (I) and the dissipative regime (II).

Let f be the weight function defined by:

$$f = \frac{1}{2}\left\{1 + \tanh[\gamma(\alpha_0 - \alpha(\dot{\varepsilon}_{cycl}, W_{an}))]\right\} \tag{4.5}$$

with $\alpha_0 = \dot{\varepsilon}_0 W_0^{\frac{m}{n}}$ and:

$$\alpha(\dot{\varepsilon}_{cycl}, W_{an}) = \frac{\dot{\varepsilon}_{cycl}}{\dot{\varepsilon}_0}\left(\frac{W_{an}}{W_0}\right)^{-\frac{m}{n}} \tag{4.6}$$

The parameter α_0 indicates the boundary between the two regimes as illustrated in fig. 4.3(b). Values for m and n used in the calculation of α_0 and eq. (4.6) are subjected to an optimization process, as detailed below.

The parameter γ determines the *sharpness* of the transition between the two regimes (figs. 4.6(a) and 4.6(b)). The range for γ was chosen to have two extreme cases: 10

[3]This would mostly be useful for engineering practise. Giving a clear physical meaning to a transition function would require precise experimental evidence of a shift in damage mechanisms between the two regimes (type, kinetics, etc.).

for smooth transition between the two branches of the model while 10^4 provides with a sharp transition (see fig. 4.5).

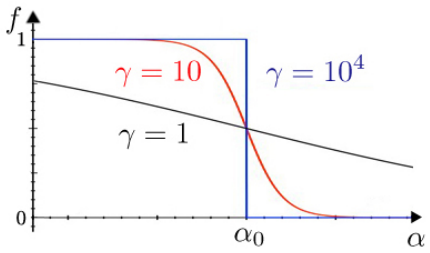


Figure 4.5: Weight function f for various values of the parameter γ.

We can then determine the number of cycles to failure as:

$$N_f = (1-f)\cdot\left(\frac{\dot{\varepsilon}_{cycl}}{\dot{\varepsilon}_0}\right)^n + f\cdot\left(\frac{W_{an}}{W_0}\right)^m \tag{4.7}$$

Parameters $\dot{\varepsilon}_0$, n, W_0 and m are optimized to minimize the discrepancy between the estimated and experimental N_f over the whole dataset. Note that the values of α_0 and α are updated during the optimization process with the correct values of parameters n and m. This yields, for $\gamma = 10^4$:

$$\dot{\varepsilon}_0 = 1.11,\ n = -0.660$$
$$W_0 = 1.60\ 10^{-7},\ m = -3.247$$

For low values of γ (e.g. $\gamma = 10$) not enough correction is applied and the results are not better than with a simple strain rate criterion (eq. (4.1)). However, larger values (e.g. $\gamma = 10^4$) yield very good results, even at high N_f and for negative load ratios R (fig. 4.6(d)).

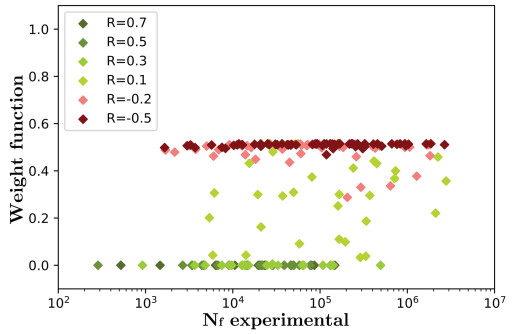
It should also be pointed that instead of being fixed prior to the optimization of the other parameters, the parameter γ can also be included in the optimization process. Optimized value is $\gamma_{opt} = 54390$, with very little change to the other parameters ($\dot{\varepsilon}_0 = 1.12$, $n = -0.661$, $W_0 = 1.75\ 10^{-7}$, $m = -3.263$) and a criterion that only yields minimal improvement as shown in fig. 4.7.

4.1.3.3 Identification on a smaller database

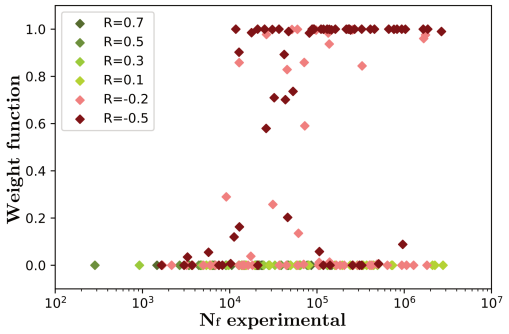
The criteria presented above (eq. (4.7)) has been identified on results from 207 fatigue tests. If a similar criterion was to be applied for a new material, obtaining such a large experimental database would be long and costly. The question thus arises of the accuracy of a criterion identified on a smaller set of experimental results.

In order to give an insight on these possibilities, various datasets for identification have been tested. Figure 4.7 gives the relative error made on the estimation of N_f based on the following datasets:

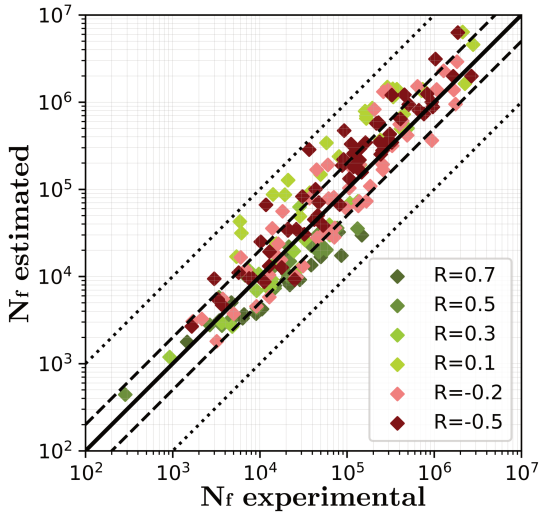
- Separate: all 207 specimens were used with parameters identified separately for each of the two regimes. Similar as obtained by eq. (4.4) and plotted on fig. 4.4.



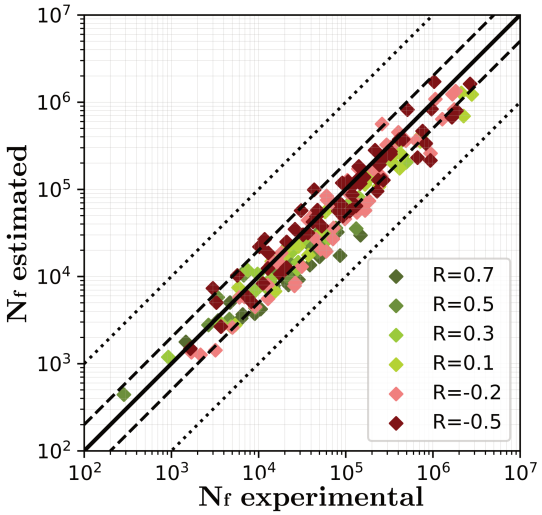
(a) Weight function vs. N_f - $\gamma = 10$



(b) Weight function vs. N_f - $\gamma = 10^4$



(c) Estimated fatigue life with $\gamma = 10$ vs. experimental number of cycles to failure



(d) Estimated fatigue life with $\gamma = 10^4$ vs. experimental number of cycles to failure

Figure 4.6: Weight function f and estimated fatigue life using the mixed criterion [eq. (4.7)] for all fiber orientations. Scatter bands of factor 2 and 10 are marked in dashed and dotted lines respectively.

- 0° - $\gamma = 10^4$: only results on 0° specimens were used for identification - 66 specimens in total. Value of γ was set to 10^4.
- All spc - $\gamma = 10$: all 207 specimens were used with parameters identified over the whole dataset. Value of γ was set to 10. Corresponds to results given on fig. 4.6(c).
- 27 spc - $\gamma = 10^4$: only 3 specimens per orientation (0°, 45°, 90°) for only three of the load ratios (R=$[-0.5; 0.1; 0.7]$) were used for identification - 27 specimens in total. For each configuration, the 3 specimens were chosen with N_f values around 10^3, 10^4, and 10^5 or above, to cover over the whole range of fatigue lives. Value of γ was set to 10^4.
- 106 spc - $\gamma = 10^4$: only specimens for three of the load ratios (R=$[-0.5; 0.1; 0.7]$) were used for identification - 106 specimens in total. Value of γ was set to 10^4.
- All spc - $\gamma = 10^4$: all 207 specimens were used with parameters identified over the whole dataset. Value of γ was set to 10^4. Corresponds to results given on fig. 4.6(d).
- All spc - $\gamma = 54390$: all 207 specimens were used with parameters identified over the whole dataset. Value of γ was also set as an optimization variable, yielding $\gamma = 54390$.

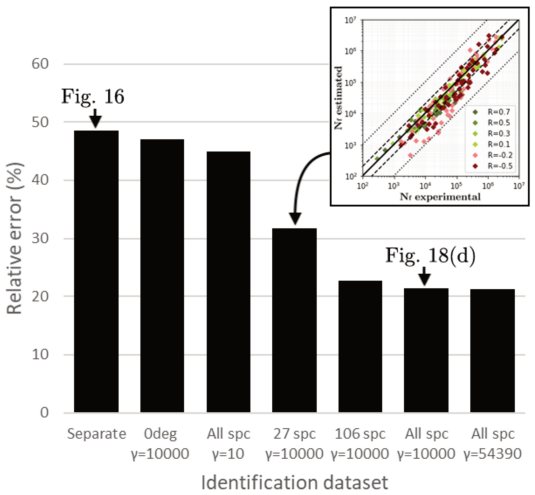


Figure 4.7: Relative error on N_f using the mixed criterion eq. (4.7) identified on various datasets.

Note that a relative error of 50% might seem important, but is in fact already very small compared to the usual fatigue predictions often spanning more than a decade.

Even though more analysis would be required to determine the minimal necessary experimental dataset to obtain the desired accuracy of the identified criterion, fig. 4.7 shows that relatively good results can be obtained with only a very reduced number of specimens compared to the 207 included in this study.

4.1.3.4 Further remarks on the mixed criterion

The criterion presented here was based on the anelastic energy W_{an} to account for the dissipative behavior of the material, however similar results can be obtained using the given strain energy W_g (see figs. 1.22(b), 1.26(a) and 4.8)

Based on the criterion presented here, SANTHARAM completed the analysis in a recently submitted paper [6]. Several comments can be made.

First, as noted by SANTHARAM the use of the weight function f might not be needed - and might even introduced some bias, as the non-linearity of the formulation is sufficient to account for the two regimes. The criterion could therefore be re-written in a simpler way as:

$$N_f = \left(\frac{\dot{\varepsilon}_{cycl}}{\dot{\varepsilon}_0}\right)^n + \left(\frac{W_{an}}{W_0}\right)^m \tag{4.8}$$

or using the given energy:

$$N_f = \left(\frac{\dot{\varepsilon}_{cycl}}{\dot{\varepsilon}_0}\right)^n + \left(\frac{W_g}{W_0}\right)^m \tag{4.9}$$

Second, SANTHARAM introduced a variant of the criterion proposed in this work, but based on the creep energy rather than on the cyclic strain rate:

$$\frac{1}{N_f} = \left(\frac{W_{cr}}{A}\right)^n + \left(\frac{W_{an}}{B}\right)^m \tag{4.10}$$

with the creep energy:

$$W_{cr} = \sigma_m \dot{\varepsilon}_{cycl} \tag{4.11}$$

This seems to slightly improve the quality of the prediction on the dataset considered by the authors. However on main remark can be made. As noted earlier using a stress-based approach has proven inefficient as it cannot properly unify results for such an anisotropic and load-ratio sensitive material. This was the original reason for which other parameters had to be found and the cyclic strain rate has proven to be extremely effective in unifying fatigue results for a wide variety of loading conditions. As such, using the creep energy is thus multiplying a parameter that *doesn't* unify results with a parameter that *does* unify results, and hoping it could further improve the predictions...

Results obtained by SANTHARAM still hold because of the large difference between the variations of the stress measurement (σ_m varies between no more than one order of magnitude) and those of the cyclic strain rate ($\dot{\varepsilon}_{cycl}$ varies between 5 to 7 orders of magnitude depending on the dataset).

Using the creep energy would then *at best* yield results as good as when using simply the cyclic strain rate (fig. 4.8). One could thus question the relevance of this choice.

It should therefore be further clarified if the small improvements reported by SANTHARAM are really due to the use of the creep energy or to some other factor (slightly different formulation, not using a weight function, etc).

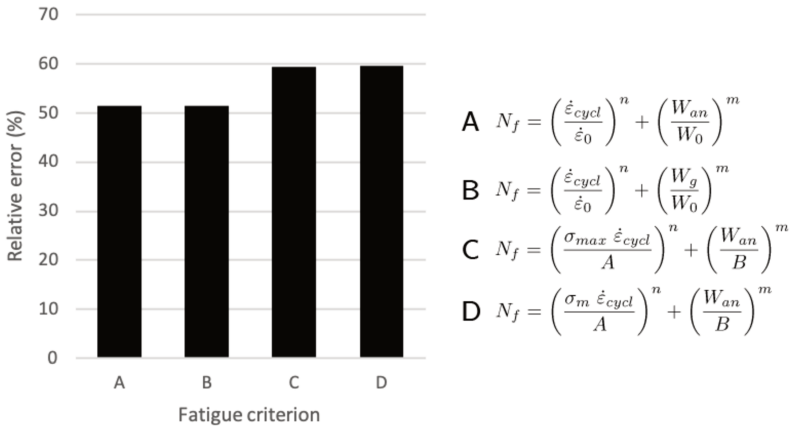


Figure 4.8: Relative error on N_f using several criteria.

4.1.3.5 Conclusion on the mixed criterion

Notable improvement of the prediction for all load ratios was possible with the mixed criterion, allowing to take into account the dissipative behavior of the material under high stress amplitudes. This criterion yields particularly good results when compared to experimental data. Although damage mechanisms for the cyclic creep regime are now well understood (see chapter 3), it would be interesting to study damage mechanisms in the dissipative regime. This would further support the use of a mixed - two mechanisms criterion.

4.2 Experimental study on notched specimens

4.2.1 Quasi-static testing

4.2.1.1 Unreinforced PA66

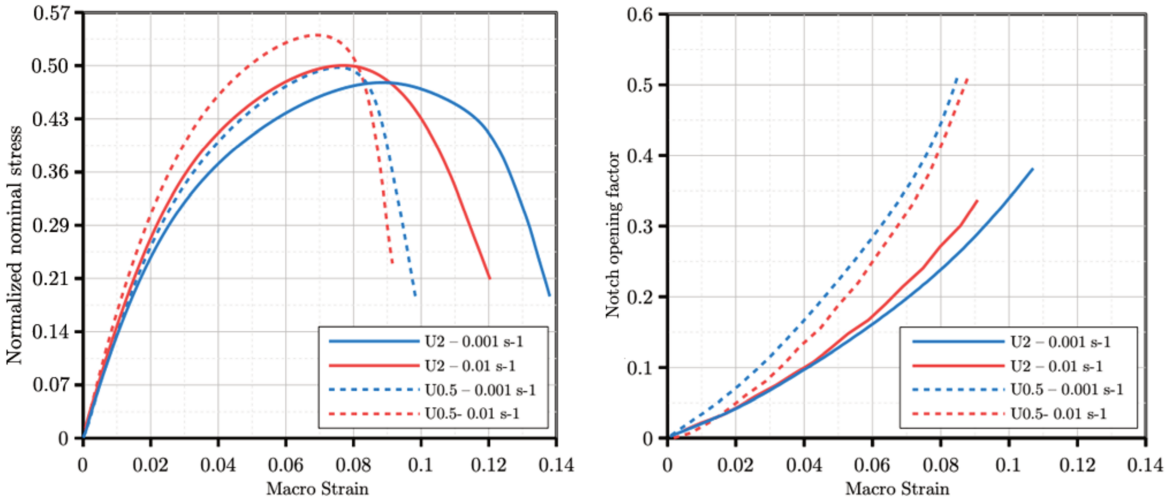
Quasi-static testing was first performed on unreinforced PA66.

Plotting the strain-stress curves (fig. 4.9(a)) shows that, at a given strain rate, a more severe notch reduces the strain at break and slightly increases the maximum stress reached during testing. For a given notch geometry, a lower strain rate increases the strain at break and reduces the maximum stress.

Notch opening was monitored using *virtual* extensometers placed on the DIC data (fig. 4.9(b)). For severe notches the strain rate does not influence the notch opening factor at break. For less severe notches, the notch is slightly less opened at break for higher strain rate.

The notch opening factor is a measure of the local strain, which is much higher than the global strain. An adapted stress-strain curve can therefore be plotted (fig. 4.10).

Damage process is observed by synchrotron tomography during in-situ testing. Observation of the initial notch root shows that water-jet cutting induces defects and roughness on the surface (fig. 4.11(a)). Very similar to what was reported by Cheng [7], damage progresses from theses defects (fig. 4.11(c)). This early localization means



(a) Stress-strain curves

(b) Notch opening factor

Figure 4.9: Quasi-static tensile tests for notched PA66 specimens. Note that U2 and U0.5 refers to the notch geometry as defined in fig. 2.7.

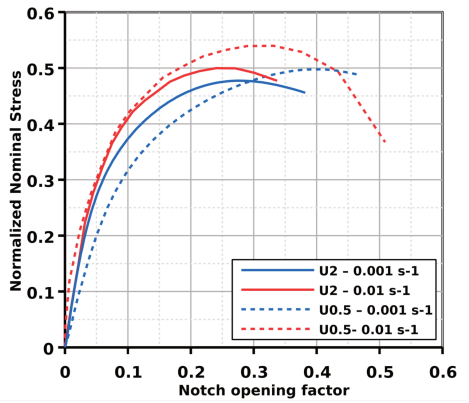
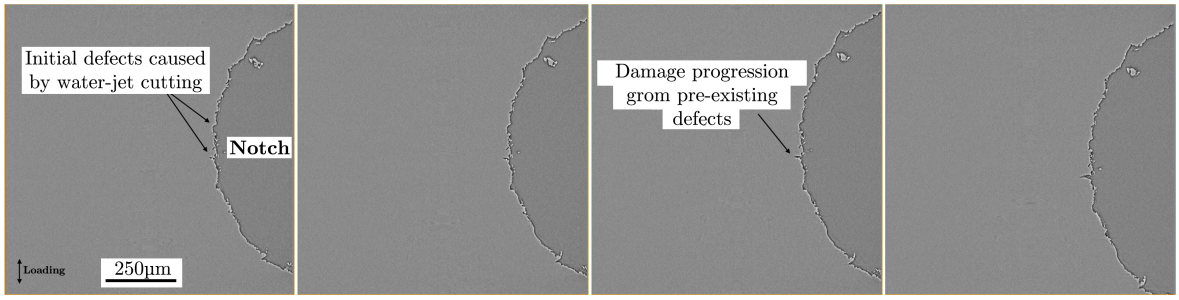
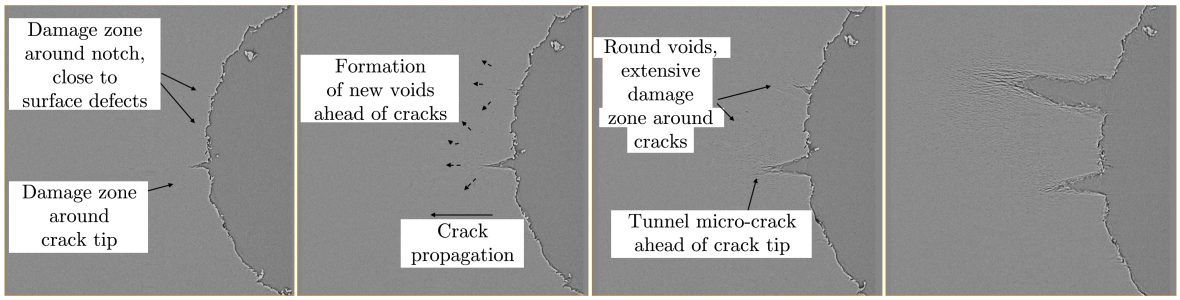


Figure 4.10: Nominal stress vs. notch opening factor

almost no damage is observed elsewhere around the notch root, as it was reported for defect-free notches. As the strain increases, the crack propagates by coalescence of micro-cracks and multiple round voids form in a large area the crack tips (figs. 4.11(e) to 4.11(g)). Finally extensive damage is observed in the specimen, leading to fast crack propagation and failure of the specimen (figs. 4.11(g) and 4.11(h)).



(a) $\varepsilon/\varepsilon_f = 0\%$ (b) $\varepsilon/\varepsilon_f = 12.5\%$ (c) $\varepsilon/\varepsilon_f = 25\%$ (d) $\varepsilon/\varepsilon_f = 37.5\%$



(e) $\varepsilon/\varepsilon_f = 50\%$ (f) $\varepsilon/\varepsilon_f = 62.5\%$ (g) $\varepsilon/\varepsilon_f = 75\%$ (h) $\varepsilon/\varepsilon_f = 82.5\%$

Figure 4.11: Tomographic slice of a notched "tomo" PA66 specimens during in-situ quasi-static tensile testing, at $\dot{\varepsilon} = 10^{-3}s^{-1}$.

4.2.1.2 Reinforced PA66

Tensile testing was performed on reinforced PA66 samples. As expected the 0° sample presents a higher stiffness, reaches a higher stress and a lower strain at break when compared to the 90° specimen (fig. 4.12).

Notch radius appears to have little influence when for 0° samples, but sharper notch reduces the strain at break for 90° specimens.

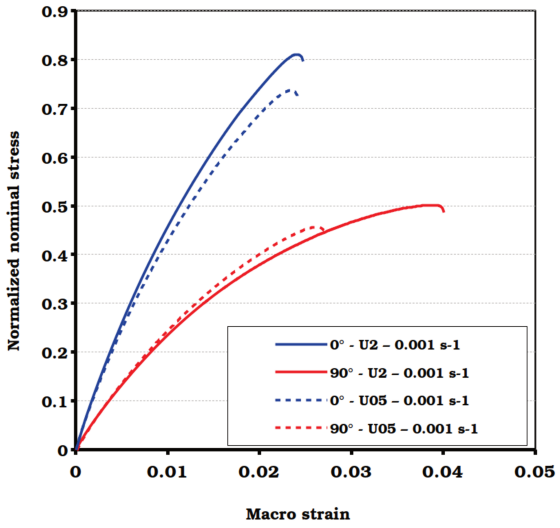


Figure 4.12: Tensile test on notched PA66GF30 specimens at $\dot{\varepsilon} = 10^{-3}s^{-1}$.

In the reinforced material, damage initiates close to the notch root as reported in the literature [8]. However local damage process are mostly influenced by the local micro-structure and are thus similar to the ones described for smooth specimens [9].

4.2.2 Fatigue testing

4.2.2.1 Unreinforced PA66

Figure 4.13 presents the S-N experimental data obtained for the two notch geometries on neat PA66. A more severe notch reduces the fatigue life but notch sharpness seems to have little influence on the slope of the curve.

Local cyclic strain fields on the surface of the specimen are measured by DIC. Evolution of the cyclic strain at notch root can be monitored. The two notches behave similarly until one starts to become the main site of damage, thus experiencing a faster strain increase (fig. 4.14(a)). Cyclic strain rate fields become progressively dissymmetric as the main crack begins to initiate on one side of the specimen, localizing most of the damage in this area (fig. 4.14(b)).

Tomography of damaged samples shows that damage initiates at the notch root in the core of the specimen (fig. 4.15(a)). Cavitation is limited, at least at the micrometric scale observed here. As strain levels are limited during fatigue loading it is possible that cavities remain too small to observe. Damage is clearly visible in the last

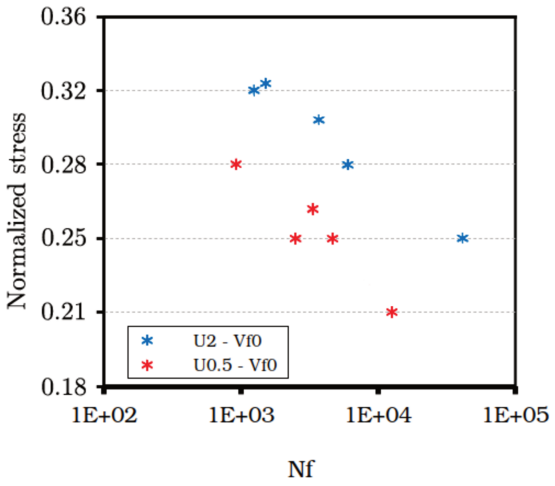
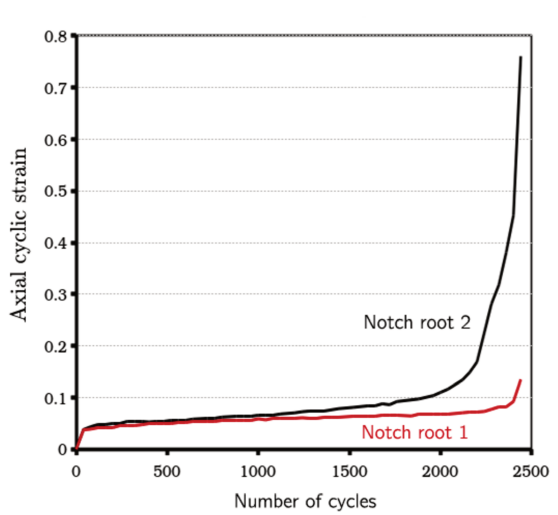
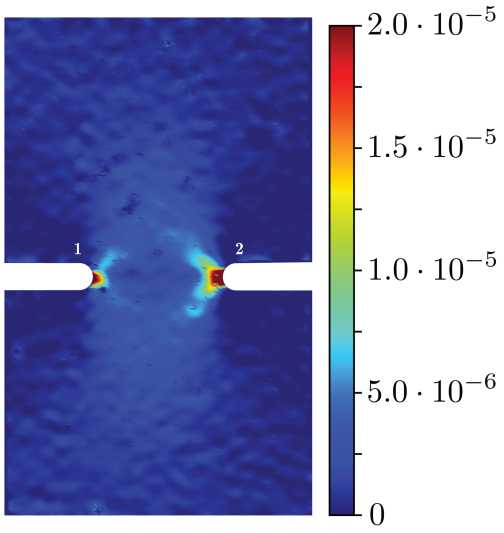


Figure 4.13: S-N curves for PA66 notched specimens.



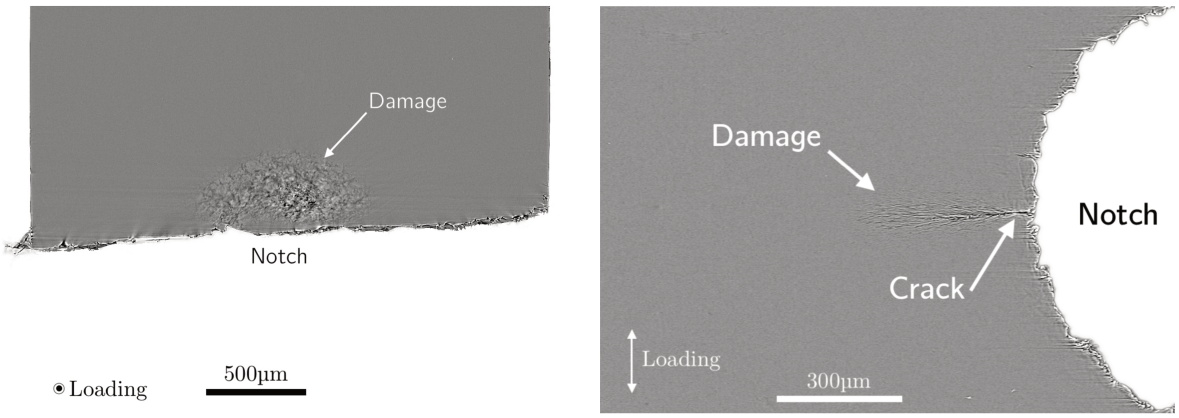
(a) Mean strain evolution at notch root



(b) Maximum principal cyclic strain rate field at mid-life

Figure 4.14: Cyclic strain evolution and local strain rate as measured by timed DIC in a PA66 specimen - U0.5 notch - Normalized $\sigma_{max} = 0.26$.

stages of fatigue loading as a crack initiates from the notch root and progresses forward (fig. 4.15(b)). The process zone is about $200\mu m$ long ahead of the crack tip and spans around $100\mu m$ in the loading direction. While clearly visible the damage remains very localized when compared to the observations made during creep loading [10].



(a) Transverse slice

(b) Longitudinal slice

Figure 4.15: Fatigue damage in a "tomo" notched PA66 specimen as observed by micro-tomography.

The fatigue crack can be segmented from tomographic scans of interrupted fatigue samples. Several cracks form at each of the two notch roots, but one crack finally becomes the main crack that will propagate faster and cause the failure of the specimen (fig. 4.16(a)).

By looking at the superimposed top views of the main fatigue cracks on fig. 4.16(b), it can be noted that cracks initiate at mid-thickness along the notch root.

However several short cracks can be seen initiating from the around the notch. Similar to quasi-static loading, this is probably due to the irregular surface of the notch root.

It can also be remarked that the crack tends to propagate faster on one side of the sample for some of the specimens. This might be caused by the slight taper angle caused by the water-jet cutting of the sample, resulting in a higher stress on one side of the sample, or to a slight specimen misalignment during loading.

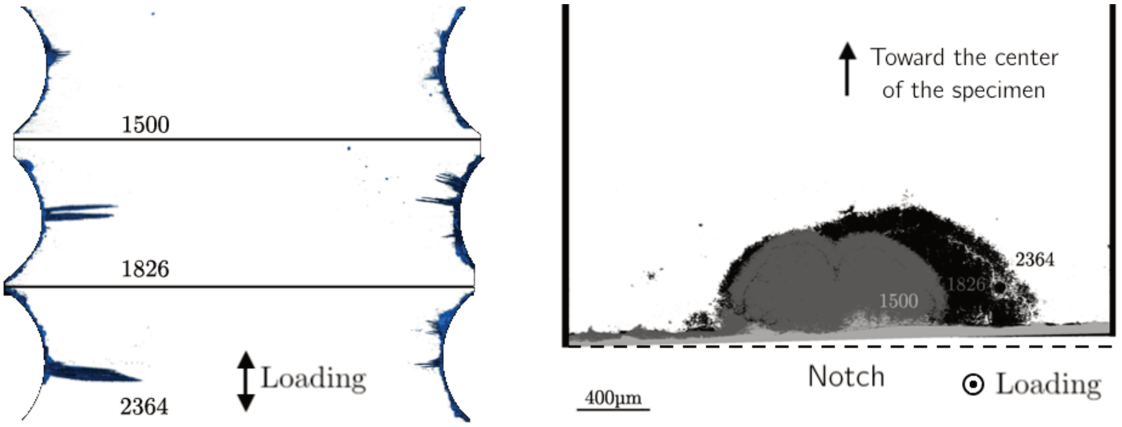
Fractography of a notch PA66 sample, presented on fig. 4.17, shows the crack path for the main and secondary fatigue cracks. The center of the fatigue crack path exhibits a ductile aspect, which can be linked to a spherulitic damage process (see chapter 3).

4.2.2.2 Reinforced PA66

Figure 4.18 presents the S-N curves obtained for the two notch geometry and three fiber orientations.

For a given fiber orientation, a more severe notch reduces the fatigue life (figs. 4.18(a) to 4.18(c)). The slope of the S-N curve is also very slightly reduced for sharper notches.

For a given notch geometry, fatigue life is reduced with increasing angle between the fibers and the loading direction (figs. 4.18(d) and 4.18(e)). The slope of the S-N



(a) Side views (b) Superimposed top views of the main cracks

Figure 4.16: Segmented fatigue cracks in 3 interrupted notched "tomo" PA66 specimens as observed by micro-tomography - Number corresponds on the number of applied loading cycles before the test was interrupted for tomographic imaging - Normalized $\sigma_{max} = 0.36$.

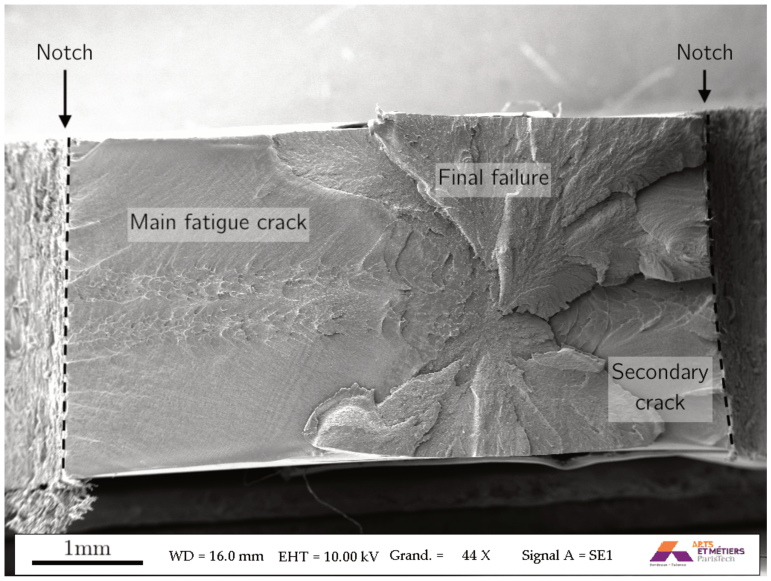
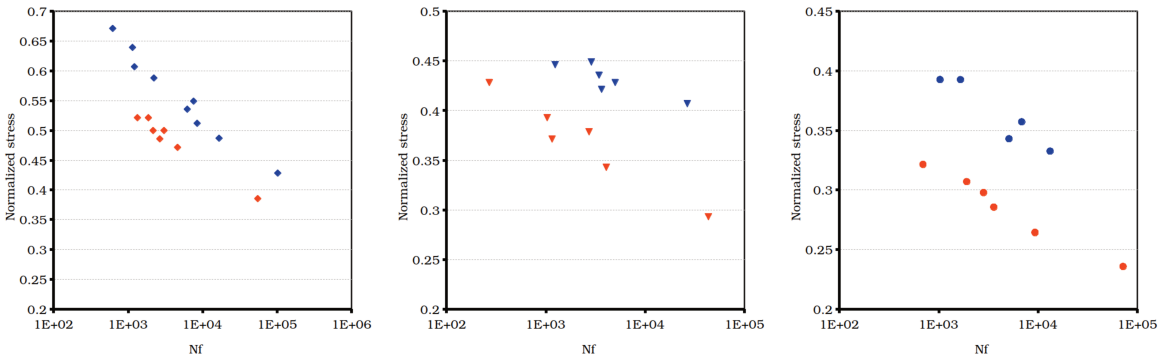
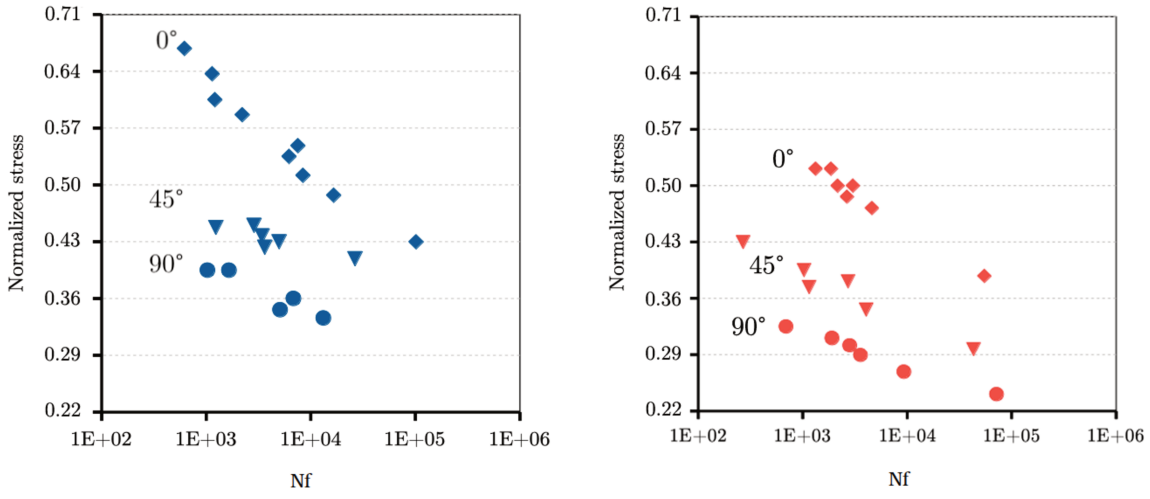


Figure 4.17: SEM fractography of a notched U0.5 PA66 specimen - $N_f = 917$.

curve is also reduced for 45° and 90° specimens.



(a) 0° specimens (b) 45° specimens (c) 90° specimens



(d) U2 notch (e) U0.5 notch

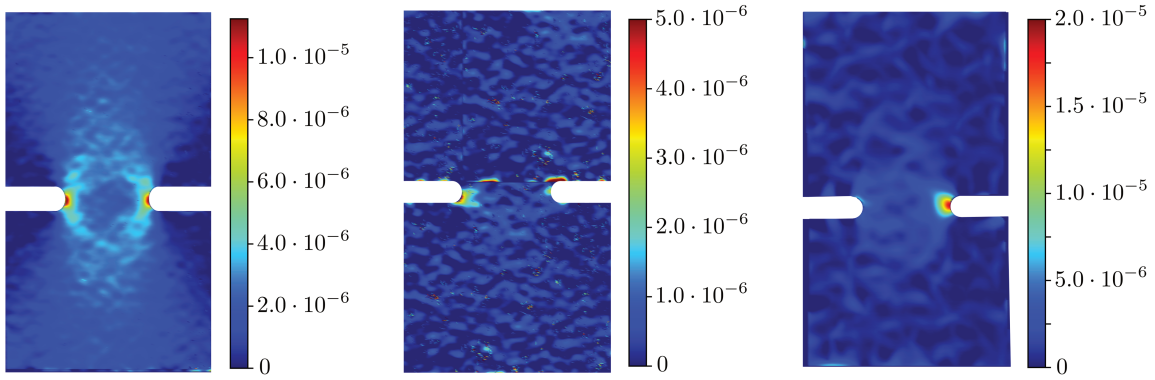
Figure 4.18: S-N curves for notched reinforced PA66 specimens.

Analysis of the cyclic strain rate profile between notches at mid-life (fig. 4.20) yields some more information:

- The length affected by cyclic creep is of about 1.5 mm from the notch root.
- Notch radius has little effect on this length (fig. 4.20(a)).
- Fiber orientation and loading have little effect on this length (figs. 4.20(b) and 4.20(c)).

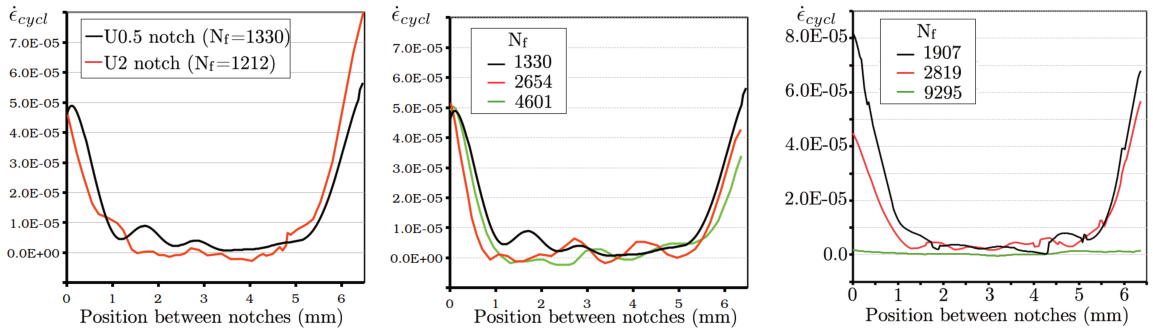
Fatigue damage mechanisms in smooth samples of short-fiber reinforced polyamide have been extensively described in the literature (see section 1.4). On notched specimens, the damage process is similar (fig. 4.21) but localized in the notch region.

As reported for smooth specimen [11], bulk damage is much more intense in the 0° layers (fig. 4.21(c)). There, the usual mechanisms can be observed: damage at fiber tip, fiber failure, debonding, crazing, etc. Even if bulk damage is much spread out, overall



(a) U0.5 - 0° (b) U0.5 - 45° (c) U0.5 - 90°

Figure 4.19: Maximum principal cyclic strain rate as measured on the surface of the specimens by timed DIC.



(a) Influence of notch geometry - 0° (b) Influence of loading - U0.5 - 0° (c) Influence of loading - U0.5 - 90°

Figure 4.20: Maximum principal cyclic strain rate between notched at $N_f/2$.

crack propagation is rather slow because the crack has to break or circumvent fibers (fig. 4.21(d)). Note that the circular morphology of the segmented damage observed on fig. 4.21(e) in the 0° layers is not *spherulitic* damage as described in the previous chapter. Instead, these circular shapes mostly come from damage at fiber tip and damage at the locations of fiber failures.

In the 90° layer the damage is less diffuse (fig. 4.21(e)). However once a crack is formed it quickly spreads, mostly along fibers, within the microstructure (fig. 4.21(f)). Crack advance along the fiber-matrix interface requires very little energy: fibers at 90° do not at as reinforcements but rather as guide for crack progression. This *tunneling* effect in the 90° core is consistent with what has been described for smooth specimens.

Much less diffuse damage can be observed farther from the notch root, in the rest of the microstructure. This is consistent with was has been reported in the literature for notched specimens [12].

4.2.3 Durability criteria

Similar to prior work on smooth specimens [5], the global axial cyclic strain rate $\dot{\varepsilon}_{cycl}$ determined from the crosshead displacement was plotted against the number of cycles prior to failure N_f in a Monkmann-Grant type curve adapted to fatigue (fig. 4.22(a)). The strain rate parameter unifies the fatigue dataset independently of the notch geometry and specimen orientation, within this dataset.

As a first approach a macroscopic criterion, based on the global axial cyclic strain rate during secondary *creep*[4], was thus identified:

$$N_f = A \left(\frac{\dot{\varepsilon}_{cycl}}{\dot{\varepsilon}_0} \right)^n \tag{4.12}$$

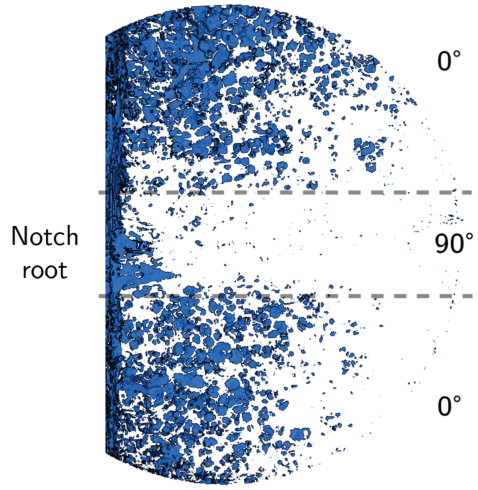
The parameter $\dot{\varepsilon}_0 = 1s^{-1}$ is introduced to obtain a dimensionless indicator and the parameters A and n are empirically evaluated from best fit of experimental results, by least-square method on the relative error:

$$A_{macro} = 0.220 \text{ and } n_{macro} = -0.81.$$

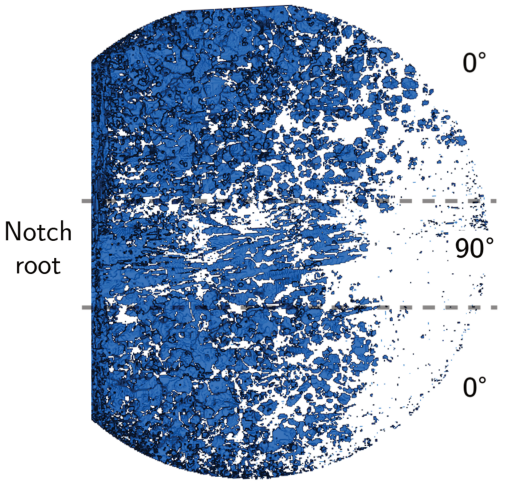
By plotting the estimated number of cycles to failure against the experimental values, it becomes apparent that this criterion yields very good results with all data points being included within a factor of two scatter band (fig. 4.22(b)).

However such a criterion based on a macroscopic experimental value of the cyclic strain rate cannot be applied for the analysis of critical geometrical defects in structures. Subsequently a second criterion can be introduced by identifying the parameters A and n based on a local value of the maximum principal cyclic strain rate $\dot{\varepsilon}^I_{loc}$ measured at the notch root during secondary creep. Note that these local values are measured

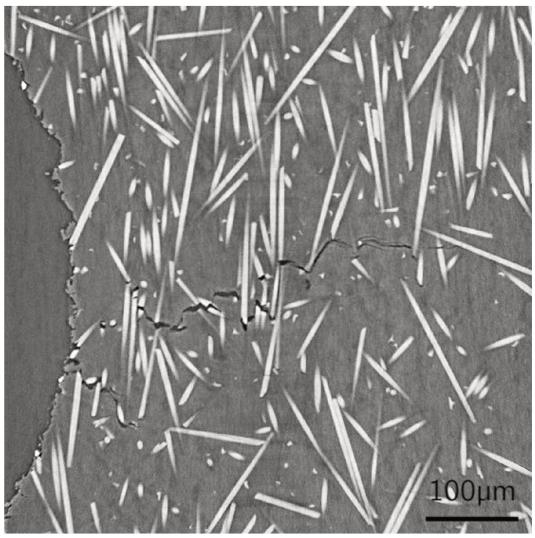
[4]Secondary creep here relates to the "second stage of cyclic creep", as introduced in section 1.2.6. It will be called "secondary creep" here for simplicity reasons and should not be confused with stationary creep.



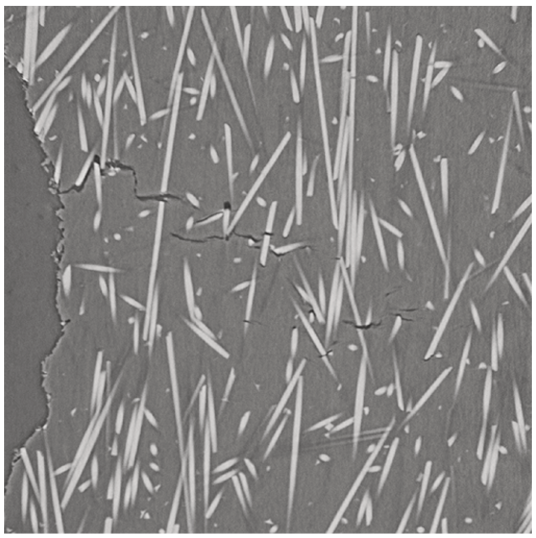
(a) Top view of the segmented damage - N=2516



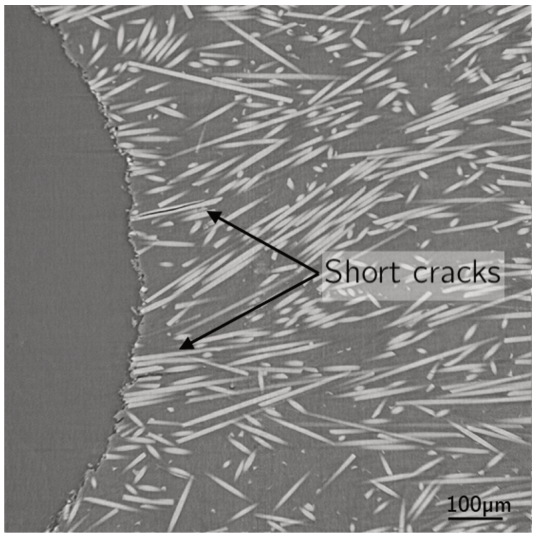
(b) Top view of the segmented damage - N=2531



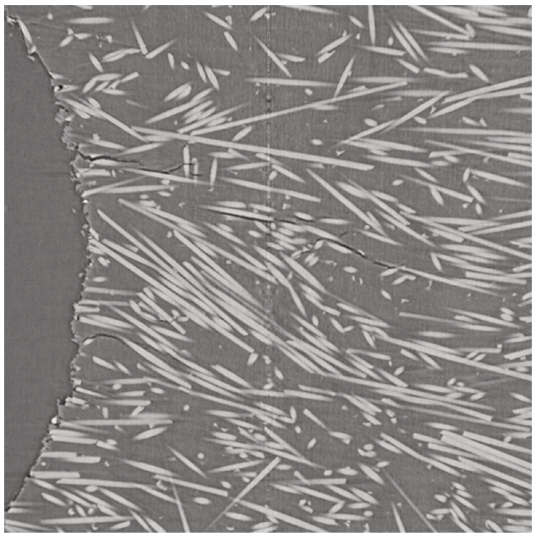
(c) In the 0° shell - N=2516



(d) In the 0° shell - N=2531



(e) In the 90° core - N=2516



(f) In the 90° core - N=2531

Figure 4.21: Tomographic evaluation of fatigue damage in a notched "tomo" 0° specimen - Normalized $\sigma_{max} = 0.60$.

experimentally using timed DIC on the surface of the specimens[5]. For each specimen we considered the highest of the two local values at notch root to be the most critical and used it for the local criterion.

This yielded a new set of parameters for the formula introduced in eq. (4.1):

$$A_{loc} = 19.55 \text{ and } n_{loc} = -0.42.$$

This local criterion gives good results for all fiber orientations and notch geometries (fig. 4.22(c)). It also proved effective in unifying results for unreinforced specimen - labeled as "Vf0" on fig. 4.22(c).

Finally, a third criterion is introduced with the aim of using the set of parameters values identified on smooth specimens:

$$N_f = A_{smooth} \left(\frac{\dot{\varepsilon}_{VMm}}{\dot{\varepsilon}_0} \right)^{n_{smooth}} \tag{4.13}$$

with the parameters values identified on smooth specimens [5]:

$$A_{smooth} = 1.29 \text{ and } n_{smooth} = -0.674$$

and with $\dot{\varepsilon}_{VMm}$ the non-local equivalent cyclic strain rate computed as:

$$\dot{\varepsilon}_{VMm} = \frac{1}{L} \int_0^L \dot{\varepsilon}_{VM}(s) ds \tag{4.14}$$

with the length $L = 1.5mm$ based on data from fig. 4.20, and:

$$\dot{\varepsilon}_{VM} = \frac{\partial \varepsilon_{VM}}{\partial N} \tag{4.15}$$

with the ε_{VM} the average cyclic value of the von Mises equivalent strain during secondary creep.

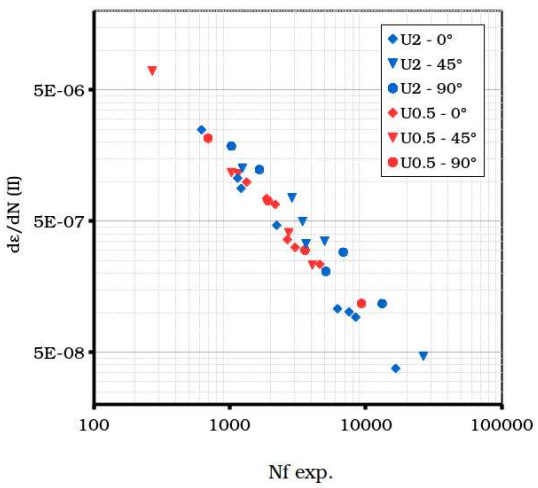
Once again, note that the experimental measurement of the cyclic strain rate is made on the surface of the specimens using DIC.

This criterion yielded good results with most data points being included within a factor of two scatter band (fig. 4.22(d)). Estimation was less precise (but conservative) for the two points at higher fatigue lives ($N_f \approx 10^5$). This could be explained by the very low cyclic strain making the experimental DIC measurement less accurate.

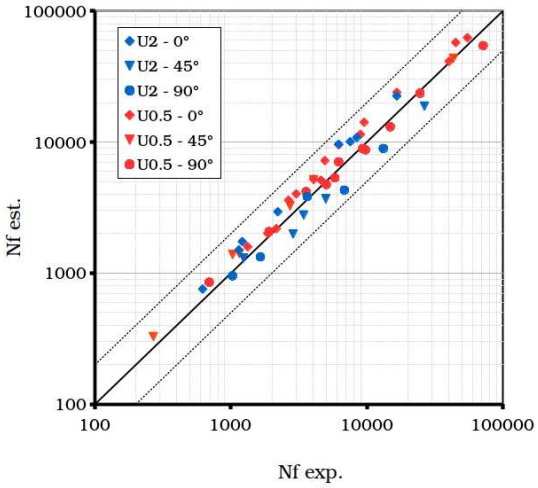
4.2.4 Further comments about the criteria

The different criteria introduced all rely on the measurement of the cyclic strain rate during secondary creep. It does not take into account the possible influence of the primary and tertiary creep stages on the durability of the specimens.

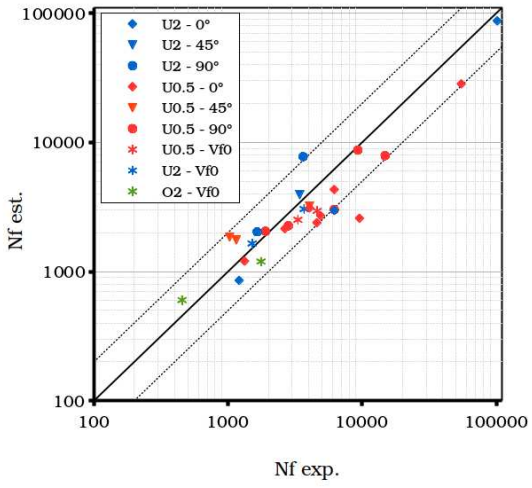
[5] Although we showed that damage preferentially at mid-thickness in the specimen, experimental evaluation of the cyclic strain rate in the bulk material is much more difficult, this will be discussed in section 4.2.4.



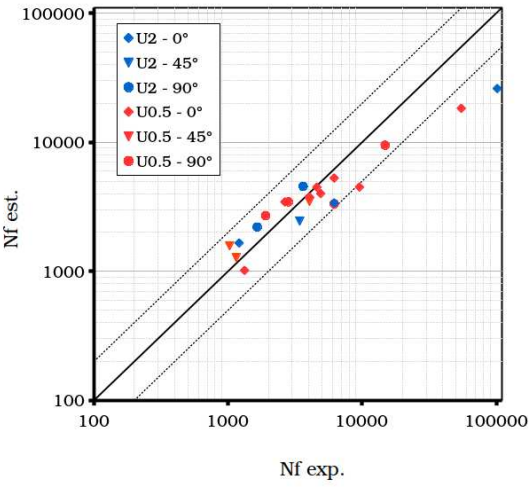
(a) Global strain rate vs. N_f



(b) Macroscopic criterion



(c) Local criterion



(d) Non-Local criterion

Figure 4.22: Identification of several fatigue criteria for notched PA66GF30 specimens - R=0.1 - 0.5 Hz. Scatter band of factor 2 is marked in dotted lines.

Furthermore these measurements are made using timed DIC and are thus surface measurements. Cyclic strain rate is higher in the bulk but its experimental is much more difficult and would for example require the use of DVC on in-situ tomographic data. Alternately the bulk cyclic strain rate can be evaluated using Finite Element analysis as it will be shown in the next chapter, although gaining confidence in the results of the calculation would still require experimental validation.

The criteria presented above are adaptations of the Monkman-Grant relationship to fatigue loading. As it yields good results, it means that:

$$\left(\frac{\Delta\varepsilon_{cycl}}{\Delta N}\right)^{\alpha} \cdot N_f = \varepsilon_c = \text{constant} \tag{4.16}$$

in which $\alpha = 1$ and ε_c is a Monkman-Grant ductility [13] for fatigue.

The exponent α in the Monkman-Grant relationship is generally close to 1 for most material[6] [13]. In our cases, we have a value of $\alpha < 1$ ($\alpha = -n$ from the criteria). A value of α inferior to 1 indicates that the contribution of the secondary cyclic creep strain decreases with an increased fatigue life, i.e. with decreased stress levels (see [15] for static creep).

The fact that a Monkman-Grant type criterion unifies results regardless of fiber orientation, load ratio, frequency, temperature, relative humidity, etc, would suggest that there is a fixed fatigue ductility ε_c for all configurations.

The sensitivity of the non-local criterion on the distance L in eq. (4.14) should also be investigated and the choice of this distance should be tested on other notch geometries. Given this is a millimetric length, it would seem unlikely to be directly related to some microstructural features of the material, but precise investigation remain to be done.

4.3 F.E. analyses

The numerical study presented in this work firstly aims at identifying a model capable of accurately estimating the cyclic strain rate for notched specimens, so as to apply the durability criterion identified experimentally to the numerical cyclic strain fields. All modeling was performed for conditioned samples at RH50, 23°C. The chosen approach for constitutive modeling is the one used by Boisot [16] for the study of PA11 and was introduced in section 1.5.2.1.

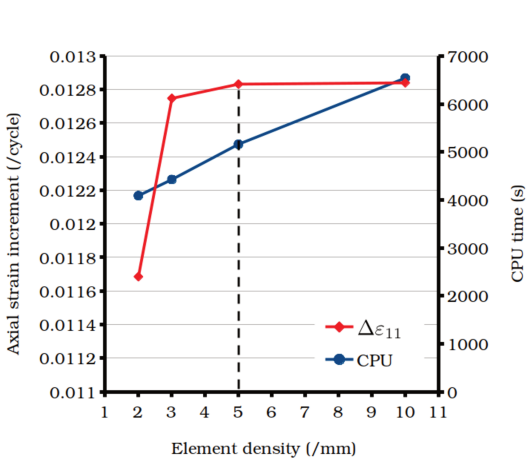
4.3.1 F.E. models

Finite-element 3D models for a quarter of each notched geometries were meshed by c3d20 quadratic brick elements. Refinement near the notch root was a balance between a too coarse imprecise mesh and a too refined one leading to increased computation time, all the more so as hundreds of loading cycles would have to be computed for

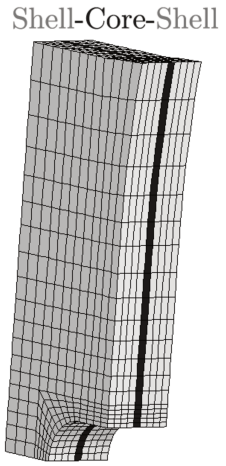
[6] Brinkman [14] noted that for ceramics α is usually slightly greater than 1 and that for metals it is often slightly less than 1.

the modeling of fatigue loading. Chosen density was 5 elements/mm, yielding good estimation of the strain rate with reasonable computational resources (fig. 4.23(a)).

For the composite material, simple *three layers* geometry was used to represent the Shell-Core-Shell microstructure (fig. 4.23(b)). Nine c3d20 brick elements were placed in the thickness of the specimen: four were used for each of the two shell layers and the center row is assigned the properties of the core layer.



(a) Computed strain rate at the notch root and CPU time required for the first 5 loading cycles in a U0.5 PA66 specimen - Normalized $\sigma_{max} = 0.29$



(b) Shell-Core-Shell geometry

Figure 4.23: Finite-element model.

4.3.2 Parametric identification for constitutive models

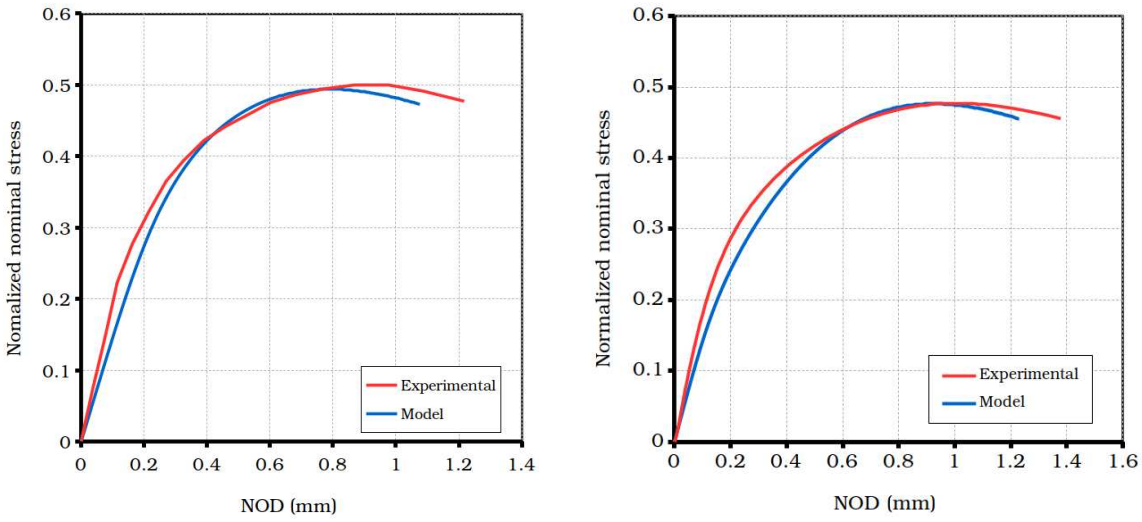
4.3.2.1 Parameters' identification for quasi-static tensile test

Parameter identification is first performed for neat PA66 samples using a genetic algorithm on quasi-static tests at $\dot{\varepsilon} = 10^{-2}s^{-1}$ and $\dot{\varepsilon} = 10^{-3}s^{-1}$ in order to match the stress-strain curves and the evolution of the Notch Opening Displacement (NOD) during loading. Resulting curves of the normalized stress versus the NOD for a U2 notch are given in fig. 4.24 and parameters for PA66 are given in Table 4.1.

Similar protocol was followed for the composite material. Parameters were considered identical for a given phase (e.g. the 0° phase) regardless of it being the shell or the core of the specimen.

An orthotropic stiffness tensor was used to describe the anisotropic linear elastic behavior for each of the two phases.

Normalized stiffness tensor is here given for the 0° phase at RH50, 23° C:



(a) $\dot{\varepsilon} = 10^{-2}s^{-1}$ (b) $\dot{\varepsilon} = 10^{-3}s^{-1}$

Figure 4.24: Normalized stress vs. NOD for a U2 notched PA66 specimen during tensile testing.

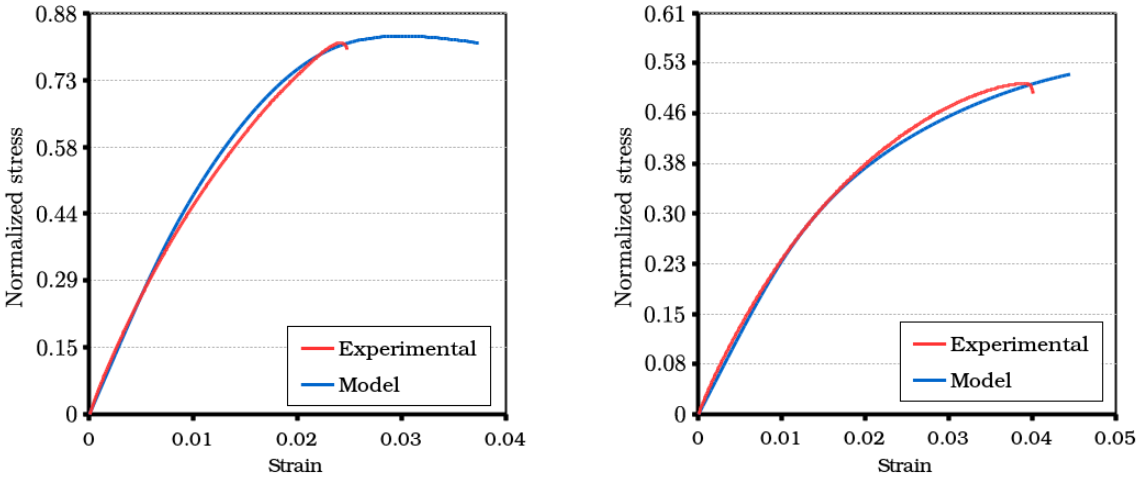
Parameters	**Quasi static**	**Fatigue**
E (Norm.)	7.8	7.8
ν	0.38	0.38
K (Norm.)	1.8	0.7
n	2.74	4.2
σ_0 (Norm.)	0.026	0.026
Q (Norm.)	0.24	0.26
b	37.3	40

Table 4.1: Parameters identified for unreinforced PA66 (RH50, 23°C) under quasi-static loading and adapted for fatigue loading at f=0.5Hz. All stress values are normalized.

$$\underline{\underline{C_{0^\circ}}} = \begin{pmatrix} 77.4 & 33.6 & 31.8 & 0 & 0 & 0 \\ 33.6 & 43.5 & 32.5 & 0 & 0 & 0 \\ 31.8 & 32.5 & 41.1 & 0 & 0 & 0 \\ 0 & 0 & 0 & 6.8 & 0 & 0 \\ 0 & 0 & 0 & 0 & 4.5 & 0 \\ 0 & 0 & 0 & 0 & 0 & 4.9 \end{pmatrix} \tag{4.17}$$

Other parameters for the 0° phase were first identified using experimental tests conducted on a 0° specimen (thus containing a 90° core). The mechanical contribution of the 90° core of the specimen was neglected. Parameters for the 90° phase were subsequently identified using experimental tests conducted on a 90° specimen (thus containing a 0° core).

This yields satisfactory results in both cases (figs. 4.25(a) and 4.25(b)).



(a) 0° specimen

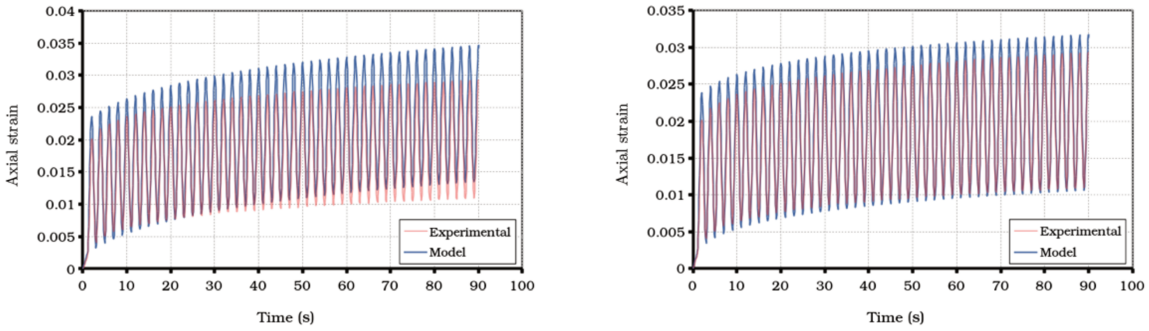
(b) 90° specimen

Figure 4.25: Shell-Core geometry and stress-strain curves for U2 notched PA66GF30 specimens during tensile testing at $\dot{\varepsilon} = 10^{-3}s^{-1}$.

4.3.2.2 Adjustments for fatigue loading

The aim is to identify a model that could yield an accurate value for the overall axial cyclic strain rate. Computed optimization would have require for an extensive number of calculations to be performed. As each of those would last several days in order to apply the necessary number of loading cycles to reach a secondary cyclic creep state before comparison of the computed cyclic strain rate with the experimental value, this would in total require a huge amount of time.

It was therefore decided that the parameters identified for the quasi-static loading would be manually readjusted for the cyclic loading in order to obtain a consistent value for the overall axial cyclic strain rate. This proved quite effective (fig. 4.26).



(a) With the parameters from quasi-static loading

(b) With readjusted parameters

Figure 4.26: Cyclic loading of a notched U2 PA66 specimen with parameters from the quasi-static loading identification and the readjusted parameters for improved cyclic strain rate calculation - f=0.5Hz - R=0.1 - Normalized σ_{max}=0.36.

4.3.3 Cyclic strain rate

As cyclic creep is driving fatigue life in these testing conditions, we will compare experimental and numerical results for the global strain rate (determined from the crosshead displacement) and for the local strain rate (determined from timed DIC measurements).

4.3.3.1 Global strain rate

Unreinforced PA66 On neat PA66 the identified numerical model yields accurate result for the global axial cyclic strain rate during fatigue loading. Calculated values are slightly underestimated for the first few cycles of loading (fig. 4.27(a)) but the subsequent evolution is well predicted by the model.

Without a damage model, the final stage leading to the failure cannot be numerically achieved. Discrepancies thus appear in the last tens of loading cycles as the experimental value of the cyclic strain rate increases rapidly (fig. 4.27(b)).

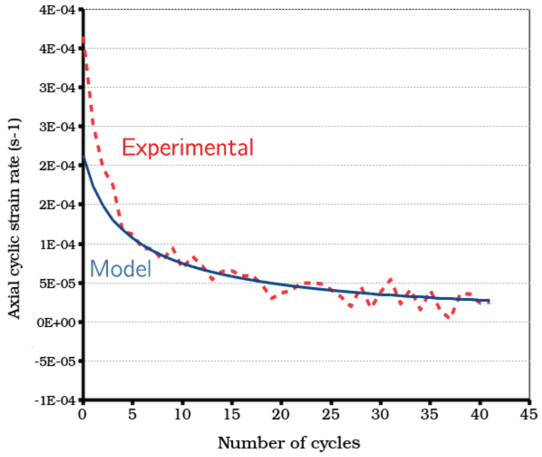
Overall agreement between the experimental and numerical values of the axial cyclic strain rate during secondary creep is good (fig. 4.27(c)).

Reinforced PA66 On reinforced PA66, although experimental data is quite noisy, the three-layer numerical model presented above well predicts the overall evolution of the global axial cyclic strain rate during fatigue loading for both 0° (fig. 4.28(a)) and 90° specimens (fig. 4.28(b)).

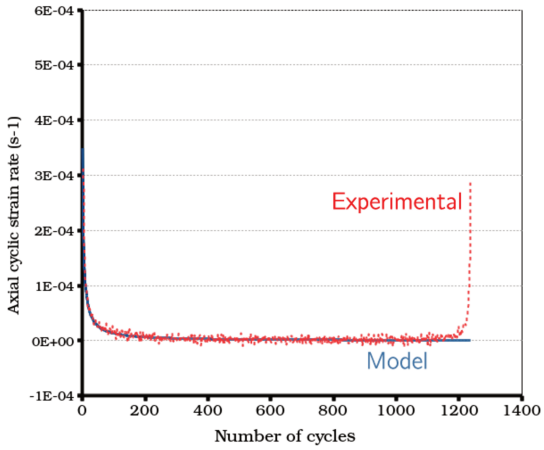
As described for the neat PA66, without a damage model, the final stage leading to the failure cannot be numerically achieved.

4.3.3.2 Local cyclic strain rate

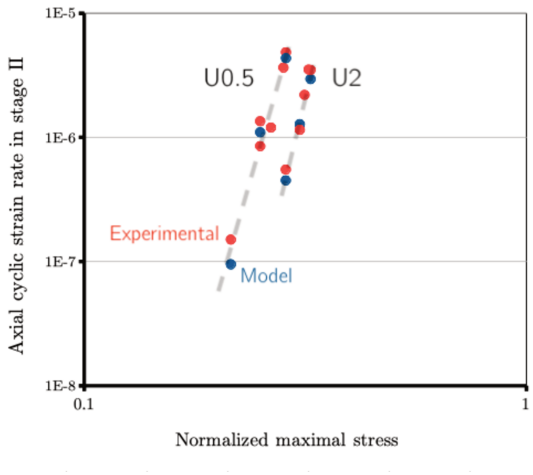
In order to obtain a strain rate based durability criterion that can be used for complex structures, our model need to yield accurate values for the local cyclic strain rate during secondary cyclic creep.



(a) U2 specimen - Normalized $\sigma_{max} = 0.30$

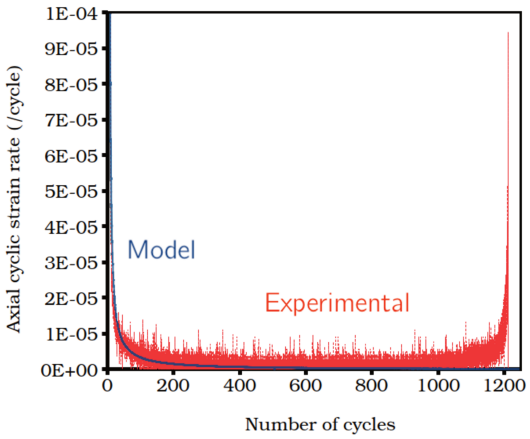


(b) U2 specimen - Normalized $\sigma_{max} = 0.32$

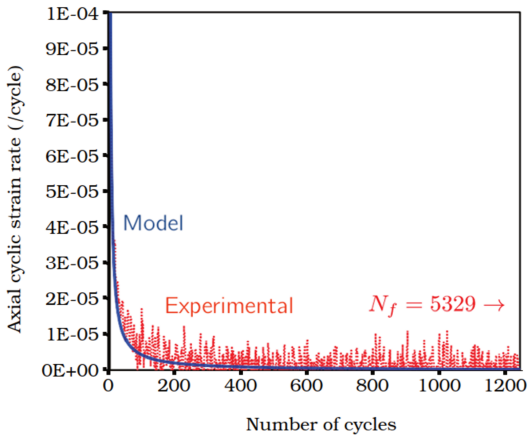


(c) Cyclic strain rate vs. nominal stress

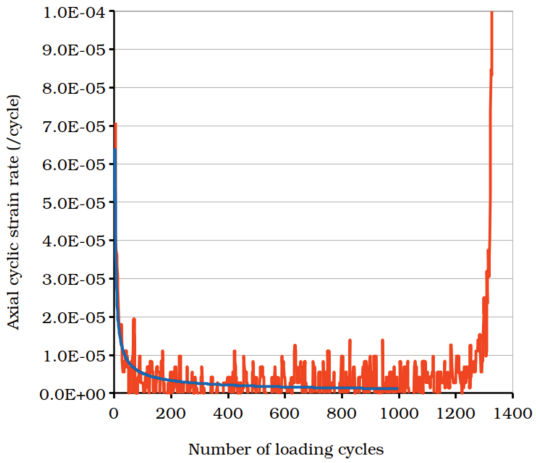
Figure 4.27: Global axial cyclic strain rate for notched PA66 specimens (R=0.1 - f=0.5Hz), determined experimentally from the crosshead displacement and the top surface displacement in the numerical model.



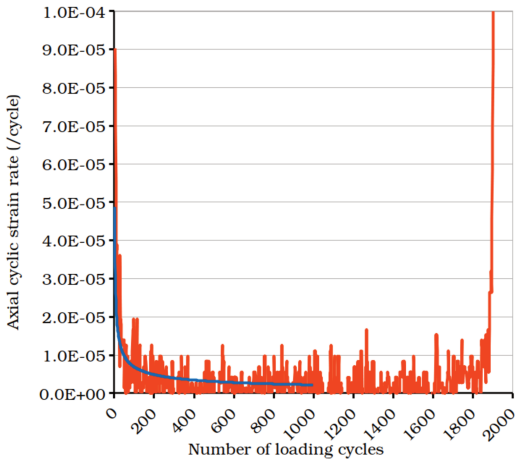
(a) 0° U2 specimen - Normalized $\sigma_{max} = 0.6$



(b) 90° U2 specimen - Normalized $\sigma_{max} = 0.4$



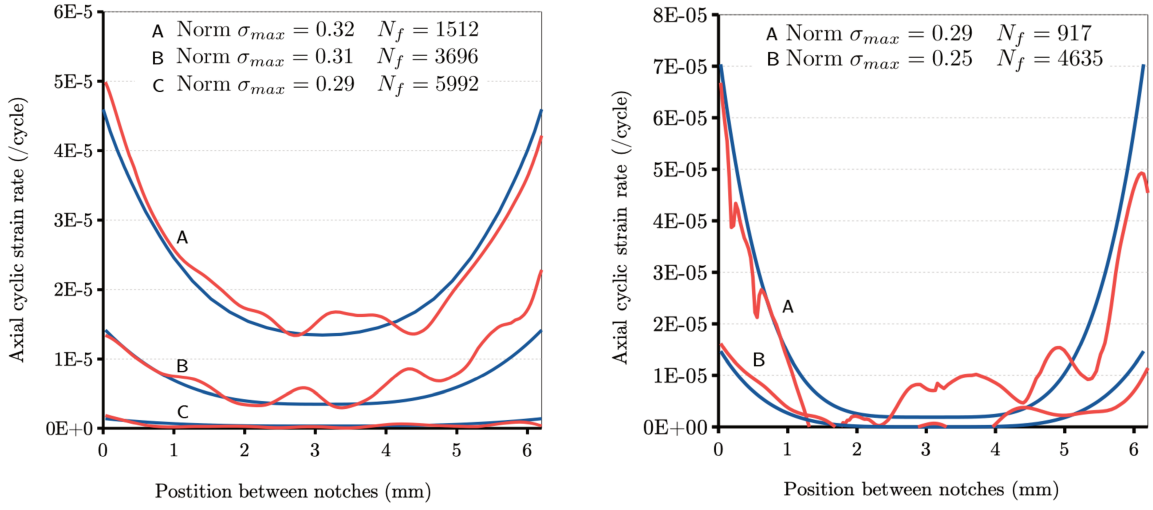
(c) 0° U05 specimen - Normalized $\sigma_{max} = 0.52$



(d) 90° U05 specimen - Normalized $\sigma_{max} = 0.31$

Figure 4.28: Global axial cyclic strain rate for notched PA66GF30 specimens.

Unreinforced PA66 As a first approach, the values of the axial cyclic strain rate can be plotted along the profile between the two notch roots. The model accurately estimates the values and spatial evolution in this critical region of the specimen during the secondary creep both for U2 (fig. 4.29(a)) and U0.5 specimens (fig. 4.29(b)).

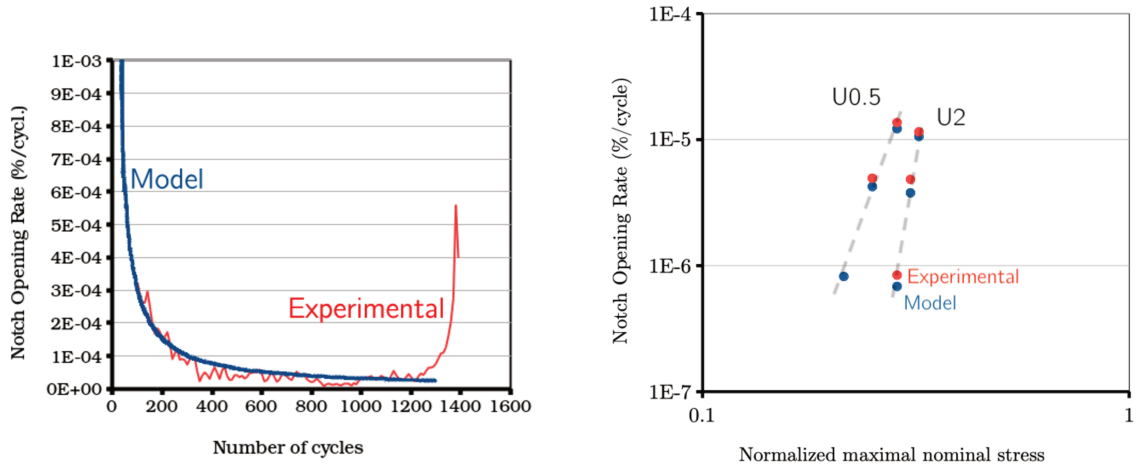


(a) U2 specimens

(b) U0.5 specimens

Figure 4.29: Profile of the axial cyclic strain rate between notches during at $N = N_f/2$.

Moreover the model yields good results in estimating the evolution of the Notch Opening Rate (NOR) until the final stage of loading (fig. 4.30(a)). The measured NOR at mid-life is compared to the computed value after 1000 loading cycles (fig. 4.30(b)) and gives good results.



(a) Typical evolution of the NOR during fatigue loading. Here for a PA66 specimen - U2 notch - Normalized $\sigma_{max} = 0.32$.

(b) NOR at $N = N_f/2$ vs. nominal stress

Figure 4.30: Notch opening rate for notched PA66 specimens.

The axial cyclic strain rate field can be plotted both for the experimental values (from timed DIC) and FE modeling. As the experimental measurements can be quite noisy, the cyclic strain rate is calculated for each pixel over a period of 200 cycles, centered on $N = N_f/2$, during secondary creep (fig. 4.31).

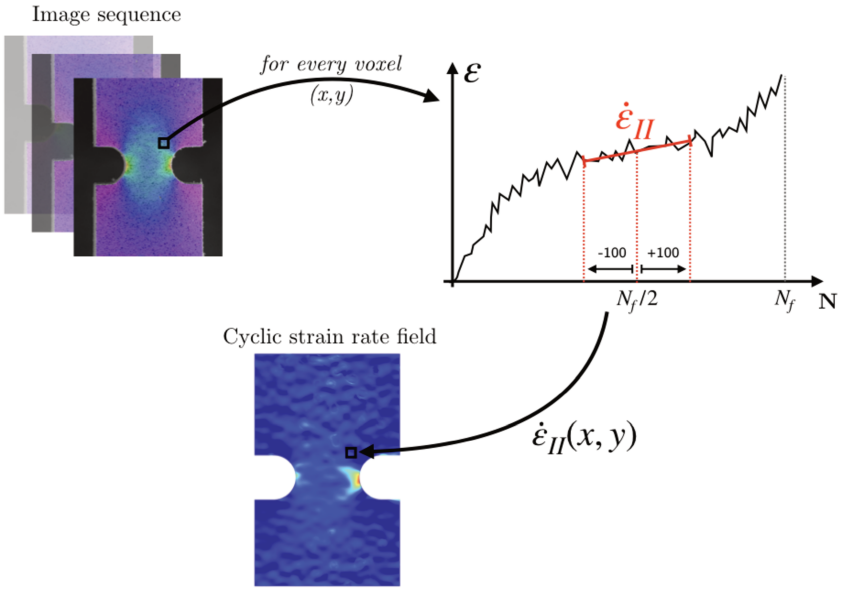


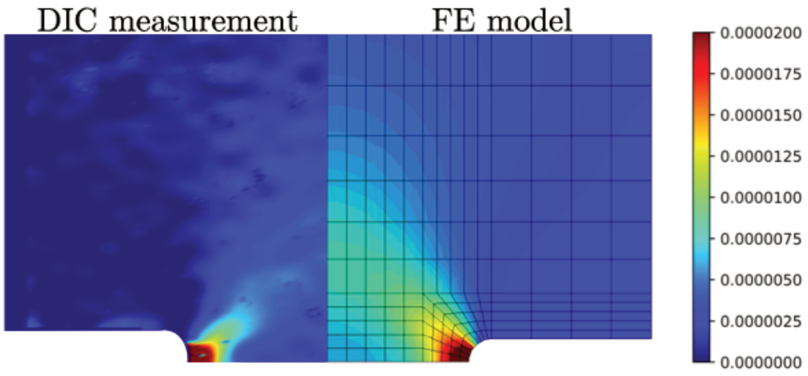
Figure 4.31: Process to plot local cyclic strain rate maps, here on a U2 specimen.

Figure 4.32 gives the example of both U0.5 and U2 notched PA66 specimens, showing that the model yields accurate estimations over the whole surface of the specimen.

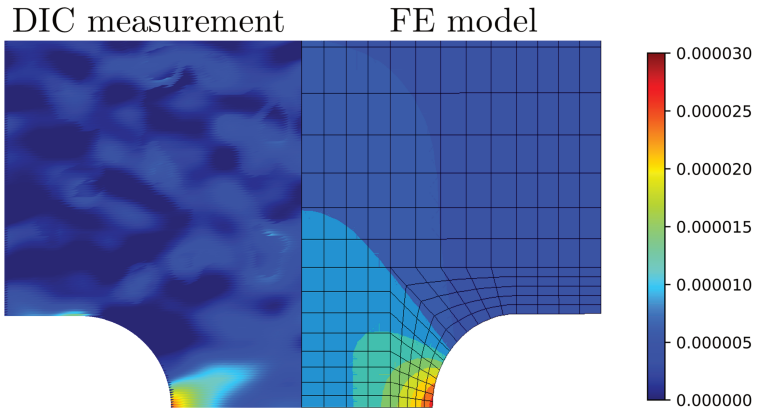
Reinforced PA66 Using the three layers model for the composite material, the computed cyclic strain rate fields can be plotted on fig. 4.33 and compared to the DIC experimental measurements presented on fig. 4.19.

Numerical results properly model the much more localized cyclic creep in 90° specimens, whereas in 0° specimens this phenomenon in not restricted to the volume between the notch roots.

Moreover the use of a numerical model gives an insight on the mechanical fields within the bulk of the specimen (fig. 4.34(a)). To which extent these estimations of the bulk cyclic strain rate are precise for the three layer composite model is hard to determine. This would require local experimental evaluation of the cyclic creep phenomenon. This might be done by performing full in-situ fatigue testing on a tomography beamline, although performing Digital Volume Correlation (DVC) on fatigue data is probably quite challenging...

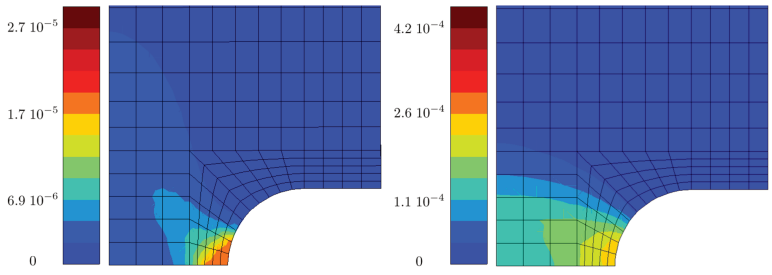


(a) U0.5 notch - Normalized $\sigma_{max} = 0.26$



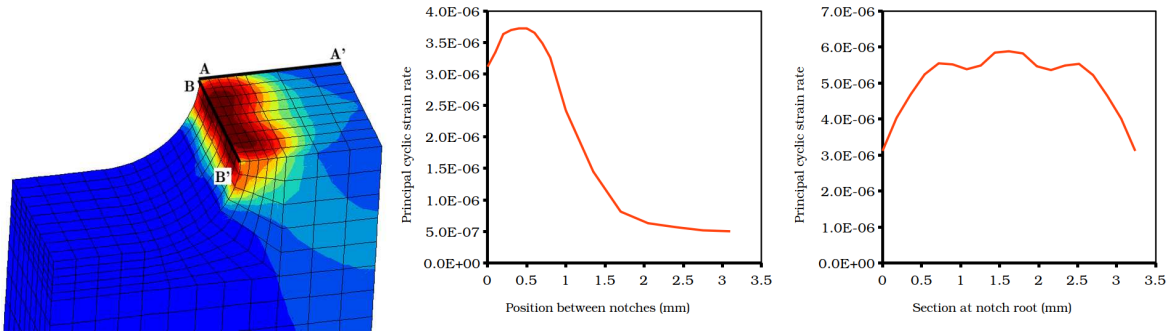
(b) U2 notch - Normalized $\sigma_{max} = 0.32$

Figure 4.32: Axial cyclic strain rate fields measured at $N = N_f/2$ and calculated at the corresponding number of computed cycles.



(a) 0° (b) 90°

Figure 4.33: Principal cyclic strain rate in composite specimens - U2 notch - Normalized $\sigma_{max} = 0.36$.



(a) Global view (b) Profiles A-A' (c) Profiles B-B'

Figure 4.34: Principal cyclic strain rate in a 0° specimen during the secondary stage of cyclic creep - U2 notch - Normalized $\sigma_{max} = 0.36$.

4.3.4 GTN model and void growth

4.3.4.1 Parameters GTN model

Formalism of the GTN damage model was introduced in section 1.5.2.2. Values for the two parameters were set at $q_1 = 1.4$ and $q_2 = 2$. This yielded, as a first approach, good correlation between the computed damage growth and experimental observations for the two notch geometries.

More precise identification of q_1 and q_2 would require tomographic data at a resolution sufficient for fatigue damage evaluation at the early stages of loading[7].

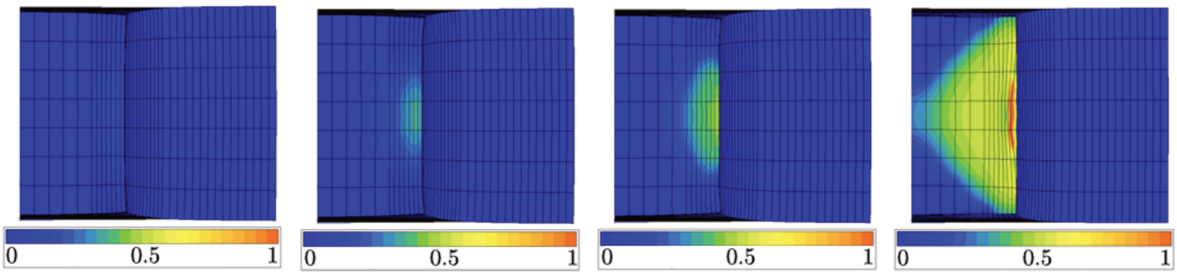
4.3.4.2 Damage growth

Unreinforced PA66 For pure polyamide 6,6 submitted to fatigue loading, void grows from the center of the specimen, where the triaxiality ratio is maximal (figs. 4.35(a) and 4.35(b)). Damage then quickly progresses forward in the center of the specimen (figs. 4.35(c) and 4.35(d)).

Computed void growth induced by fatigue loading is located in a small region between notches. This is consistent with the tomographic data, showing that fatigue damage is very localized (fig. 4.36).

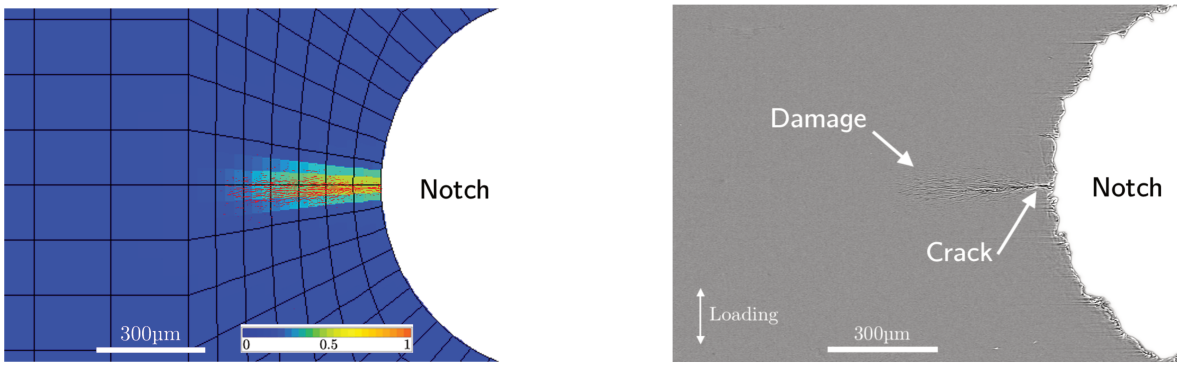
It should be noted that cavities induced by fatigue loading are mainly of submicrometric size and are thus difficult to properly segment and quantify with the current tomographic data (voxel size of $0.6\mu m$). Direct comparison between the computed void volume fraction and the measured cavitation was successfully performed for creep loading, where voids are more open [17]. Similar quantitative analysis for early fatigue induced cavitation will thus requires more precise tomographic data.

[7]Fatigue involves much lower strain levels than for quasi-static or creep tests and damage is thus is much harder to observe. The use of synchrotron tomography at a sufficient resolution will be discussed as an outlook in section 6.1.1.5



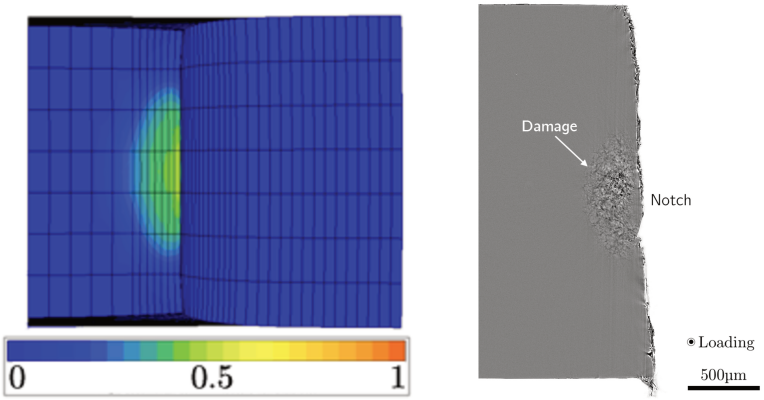
(a) 400 cycles (b) 600 cycles (c) 700 cycles (d) 800 cycles

Figure 4.35: Computed void volume fraction f in a notched PA66 "tomo" specimen - Normalized $\sigma_{max} = 0.36$.



(a) Computed void volume fraction f and, overlaid in red, the damage segmented on the corresponding tomographic slice from fig. 4.36(b)

(b) Tomographic slice



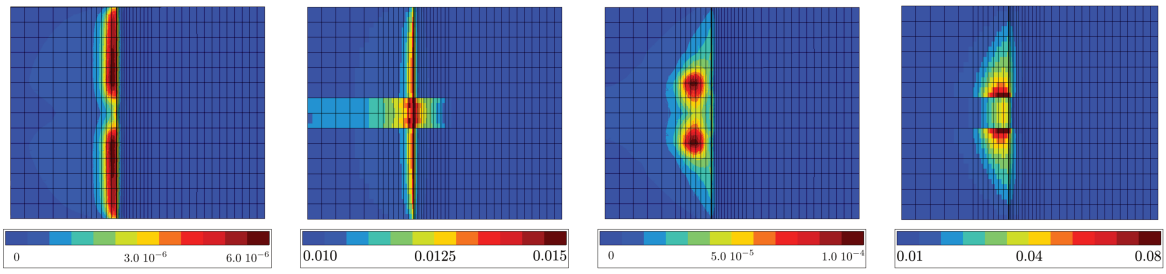
(c) Computed void volume fraction f

(d) Tomographic slice

Figure 4.36: Computed void volume fraction f and corresponding tomographic slice. Notched PA66 "tomo" specimen - Normalized $\sigma_{max} = 0.36$.

Reinforced PA66 For the composite material in the case of the 0° specimen, computed void growth mainly occurs close to the notch root in the shell, and is more important in the 90° core (fig. 4.37(b)).

For the 90° specimen, the computed voiding is mainly localized in the shell, but especially close to the 0° core, in a region of high cyclic creep (figs. 4.37(c) and 4.37(d)).



(a) Cyclic strain rate. 0° specimen (b) Void fraction. 0° specimen (c) Cyclic strain rate. 90° specimen (d) Void fraction. 90° specimen

Figure 4.37: Cyclic strain rate and computed void volume fraction after 500 loading cycles in notched "tomo" specimens - Normalized $\sigma_{max} = 0.36$.

It is worth mentioning that experimental evaluation of fatigue damage tends to show that damage in the 0° specimen is more diffuse than in the 90° specimen where transition from micro-damage to meso-crack is much more sudden, as was already reported in the literature [11]. Diffuse damage in the 0° layers occurs mainly at notch tip. This strong effect of the local microstructure on the damage process is not properly accounted for in our three layers homogenized model.

However in 0° specimens the crack propagates faster than in the 90° core. Conversely in 90° specimens the crack mainly propagates in the shell. This would be coherent with the computed void fractions (figs. 4.37(b) and 4.37(d)).

4.3.5 Application of the criterion

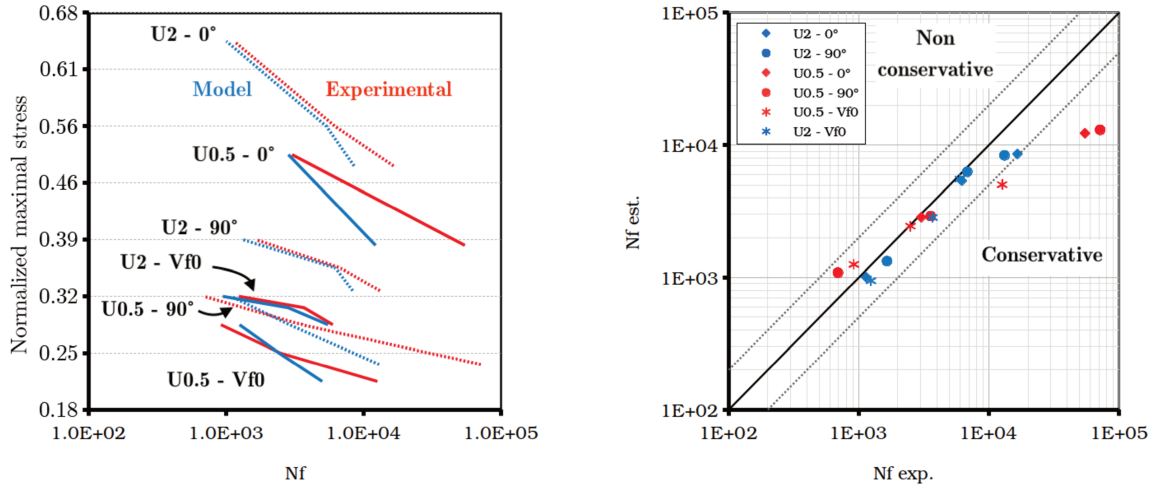
The non-local fatigue criterion introduced in eq. (4.13) and identified on experimental data can be applied on the results from finite element modeling.

Non-local von Mises cyclic strain rate was determined on the surface of the specimen after 1000 computed loading cycles. The estimated number of cycles to failure N_f was then calculated using the criterion from eq. (4.13). This yielded the S-N curves that can be compared to the experimental curves as presented on fig. 4.38(a).

At lower N_f the prediction are very accurate and within a factor 2 scatter band of the experimental data (fig. 4.38).

However for longer fatigue life (e.g. $N_f > 10^4$) the prediction becomes much less precise as the model underestimates the number of cycles to failure. This might be due to the fact that the criterion was applied after 1000 computed loading cycles, which might be to early in the fatigue life for those specimens. The cyclic strain rate is much higher after 1000 cycles than at mid-life and the estimated N_f based on this higher cyclic strain rate is thus too low.

The same explanation could be given for the model overestimating the durability for low N_f (e.g. for U0.5 unreinforced specimens). In this case, after 1000 computed cycles the strain rate might be lower than at mid-life, yielding an estimated value of N_f higher than expected.



(a) S-N curves

(b) Durability prediction

Figure 4.38: Comparison between computed N_f and experimental values.

Two approaches could lead to better results. First, the study of the cyclic strain rate during the first stage of fatigue loading could lead to a durability criterion established from the first few cycles of loading. This would however require to properly model the cyclic strain rate during the transient regime. Second, the behavior of the material could be identified on the stabilized secondary regime. The use of this stabilized behavior could directly give access to the secondary cyclic strain rate without actually computing all the loading cycles. These two possible outlooks could ultimately greatly reduce computing time and thus make this such cyclic-strain rate base criterion more convenient for larger industrial parts.

Main conclusions of the chapter

- A mixed criterion based on the **cyclic strain rate and anelastic energy** can accurately estimate the durability of smooth specimens, even at negative loading ratios.
- For notched specimens, both a local and a non-local criterion based on the **cyclic creep behavior** were introduced and yielded good results.
- Cyclic strain rate is **a parameter driving durability at the macro-scale**.
- Finite-Element modeling of the elasto-visco-plastic specimens yielded a **proper estimation the cyclic creep phenomenon**.
- The criterion identified experimentally was applied on the local values of the computed cyclic strain rate and yielded **promising results**.

4.4 Bibliography

[1] J. J. Horst, *Influence of fibre orientation on fatigue of short glassfibre reinforced Polyamide*. PhD thesis, TU Delft, 1997. 108

[2] E. Mourglia Seignobos, *Compréhension des mécanismes physiques de fatigue dans le polyamide vierge et renforcé de fibres de verre*. PhD thesis, INSA Lyon, 2009. 108

[3] A. Bernasconi and R. M. Kulin, "Effect of Frequency Upon Fatigue Strength of a Short Glass Fiber Reinforced Polyamide 6: A Superposition Method Based on Cyclic Creep Parameters," *Polymer Composites*, 2009. 108

[4] H. Rolland, *Comportement en fatigue et mécanismes d'endommagement du polyamide 6,6 renforcé de fibres courtes*. PhD thesis, ENSAM, 2017. 108, 109

[5] I. Raphael, N. Saintier, H. Rolland, G. Robert, and L. Laiarinandrasana, "A mixed strain rate and energy based fatigue criterion for short fiber reinforced thermoplastics," *International Journal of Fatigue*, vol. 127, pp. 131–143, 2019. 108, 109, 125, 127

[6] P. Santharam, Y. Marco, V. L. Saux, M. L. Saux, G. Robert, I. Raoult, C. Guévenoux, D. Taveau, and P. Charrier, "Fatigue criteria for short fiber-reinforced thermoplastic validated over various fiber orientations , load ratios and environment conditions," 115

[7] Y. Cheng, L. Laiarinandrasana, L. Helfen, H. Proudhon, O. Klinkova, T. Baumbach, and T. F. Morgeneyer, "3D Damage Micromechanisms in Polyamide 6 Ahead of a Severe Notch Studied by in Situ Synchrotron Laminography," *Macromolecular Chemistry and Physics*, vol. 217, no. 5, pp. 701–715, 2016. 116

[8] E. Belmonte, M. De Monte, T. Riedel, and M. Quaresimin, "Local microstructure and stress distributions at the crack initiation site in a short fiber reinforced polyamide under fatigue loading," *Polymer Testing*, vol. 54, pp. 250–259, 2016. 119

[9] H. Rolland, N. Saintier, and G. Robert, "Damage mechanisms in short glass fibre reinforced thermoplastic during in situ microtomography tensile tests," *Composites Part B: Engineering*, vol. 90, pp. 365–377, 2016. 119

[10] N. Selles, F. Nguyen, T. F. Morgeneyer, H. Proudhon, W. Ludwig, and L. Laiarinandrasana, "Comparison of voiding mechanisms in semi-crystalline polyamide 6 during tensile and creep tests," *Polymer Testing*, vol. 49, pp. 137–146, 2016. 121

[11] H. Rolland, N. Saintier, I. Raphael, N. Lenoir, A. King, and G. Robert, "In-situ fatigue damage mechanisms in short fibre reinforced PA66 as observed by synchrotron X-ray microtomography," *Composites Part B: Engineering*, vol. 143, no. December 2017, pp. 217–229, 2018. 123, 141

[12] E. Belmonte, M. De Monte, C.-J. Hoffmann, and M. Quaresimin, "Damage mechanisms in a short glass fiber reinforced polyamide under fatigue loading," *International Journal of Fatigue*, vol. 94, pp. 145–157, 2017. 125

[13] C. Phaniraj, B. K. Choudhary, K. Bhanu Sankara Rao, and B. Raj, "Relationship between time to reach Monkman-Grant ductility and rupture life," *Scripta Materialia*, vol. 48, no. 9, pp. 1313–1318, 2003. 129

[14] C. Brinkman and S. Duffy, "Life prediction methodologies and data for ceramic materials," ASTM West Conshohocken, PA, 1994. 129

[15] E. Isaac Samuel, B. K. Choudhary, D. P. Rao Palaparti, and M. D. Mathew, "Creep deformation and rupture behaviour of P92 steel at 923 K," *Procedia Engineering*, vol. 55, pp. 64–69, 2013. 129

[16] G. Boisot, *Mécanismes et modélisation mécanique de la déformation, de l'endommagement et de la rupture du PolyAmide 11 pur et renforcé choc.* PhD thesis, Ecole National Supérieure des Mines ParisTech, 2009. 129

[17] N. Selles, N. Saintier, and L. Laiarinandrasana, "Voiding mechanisms in semi-crystalline polyamide 6 during creep tests assessed by damage based constitutive relationships and finite elements calculations," *International Journal of Plasticity*, vol. 86, pp. 112–127, 2016. 139

Chapter 5

Microstructure modeling

Nothing is to be feared, it is only to be understood.

Marie Curie

Linking the observed damage mechanisms with local mechanical fields can appear as an ambitious endeavour, especially in the complex microstructure of injected short-fiber reinforced composites.

This chapter will complete the picture by confronting the experimental evaluation of local damage with computed local mechanical fields and durability criteria. In order to do so micro-modeling will be performed on *real* microstructures segmented from tomographic data. This data was acquired during full in-situ fatigue testing on smooth RH50 specimens, and we thus have the full damage sequence. This allows for the direct comparison of the actual damage mechanisms with the computed local mechanical fields. We will especially focus on the link between the cyclic strain rate computed locally with the onset of cavitation in the material.

5.1 FFT modeling

5.1.1 Method

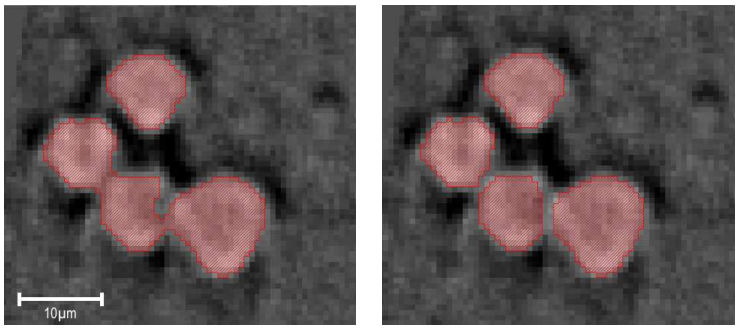
5.1.1.1 Microstructure segmentation

In order to perform FFT modeling, the microstructure must be properly segmented within a given volume of the tomographic data. For this segmentation, the tomographic data is first re-sampled from a voxel resolution of 0.65 μm to 1.1 μm or 1.3 μm. As FFT modeling directly relies on a voxel-based description of the volume, this allows for a larger volume to be later computed with reasonable resources, while at the same time still ensuring a good spatial resolution.

A first rough segmentation of the fibers was performed by applying sequentially a 3D median filter, three times, in order smooth the sometimes noisy image, and a

threshold of 35000 on the gray levels, keeping only the high values corresponding to the denser glass fibers.

The final step was to ensure each fiber was accurately segmented. This was done by manually separating the fibers picture by picture in the regions were they were touching or too close to be separated by the threshold value (section 5.1.1.1). While time consuming (there are around 500 slices to analyze and manually correct for a given volume), this step was necessary to obtain a representative microstructure in regions where fiber confinement is the highest, all the more so as these regions are the ones most prone to damage initiation.



(a) Fiber bundle

(b) Properly segmented fibers for micro-mechanical modeling.

Figure 5.1: Fiber segmentation from micro-tomography data. Slicing is made perpendicularly to the fiber direction.

5.1.1.2 Considered volume

The choice of a given region of interest (ROI) to perform micro-mechanical modeling is dictated by several factors. First, damage must be seen inside the ROI on the microtomography scan performed during fatigue life. Moreover the segmented ROI must be large enough to be representative of the local microstructure that induced the observed damage. Finally the volume must be small enough so that simulations could be performed using reasonable computational resources and in a reasonable timeframe.

As a consequence, each segmented volume was a cube of side 119 to 140 voxels, containing around 100 fibers segments (fig. 5.2). Calculations each took around 40 hours to complete.

5.1.1.3 Periodic microstructure

In order to compute the local mechanical fields using an FFT-based algorithm the volume needs to be periodic. As a raw segmented microstructure is non-periodic, the volume is enclosed in a larger box by adding an extra layer, 20 voxels thick[1], on the

[1]This thickness was chosen as a good compromise between a 30 voxels thick layer leading to an increased calculation time up to 6 days and a 10 voxels thick layer yielding poorer quality results. This was demonstrated by Refai [1].

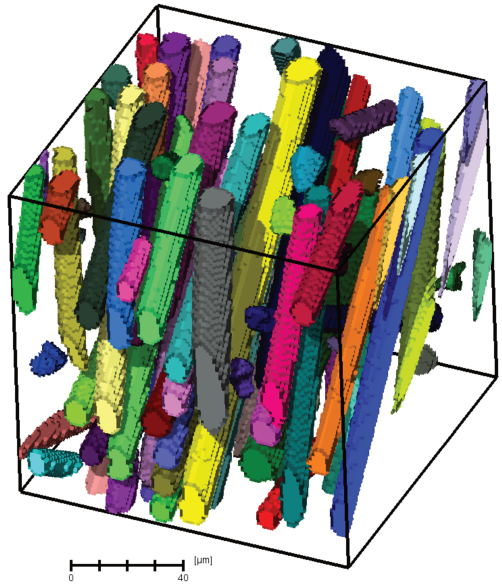


Figure 5.2: Example of segmented microstructure for FFT micro-modeling.

six sides of the segmented cube. This extra buffer layer is homogeneous and isotropic. This yielded a total cubic volume of side 154 μm to 208 μm, containing up to 4 096 000 voxels.

5.1.1.4 Material model

In the present model the glass fibers are assumed to be elastic and isotropic. Both the matrix and the homogeneous layer are given elasto-viscoplastic isotropic behaviors.

Material behavior is modeled in the small perturbations formalism. Total strain $\underline{\underline{\varepsilon}}$ is the sum of an elastic $\underline{\underline{\varepsilon_e}}$ and a plastic $\underline{\underline{\varepsilon_p}}$ contribution. Thermal effects are neglected in our study, thought they could be taken into account by the algorithm. We thus have:

$$\underline{\underline{\varepsilon}} = \underline{\underline{\varepsilon_e}} + \underline{\underline{\varepsilon_p}} \tag{5.1}$$

For a given time t, elastic strain is calculated as:

$$\underline{\underline{\varepsilon_e}} = \underline{\underline{s}} : \underline{\underline{\sigma}} \tag{5.2}$$

where $\underline{\underline{s}}$ is the compliance tensor and $\underline{\underline{\sigma}}$ is the stress tensor.

In order to calculate $\underline{\underline{\varepsilon_p}}$, the material is assumed to be viscoplatic. A yield function ϕ is introduced as a function of the stress $\underline{\underline{\sigma}}$ as well as of the kinematic and isotropic hardening variables, $\underline{\underline{x}}$ and r:

$$\phi = \sqrt{\frac{3}{2}\left(\underline{\underline{\sigma'}} - \underline{\underline{x}}\right) : \left(\underline{\underline{\sigma'}} - \underline{\underline{x}}\right)} - r - \sigma_0 \tag{5.3}$$

where $\underline{\underline{\sigma'}}$ is the deviatoric part of $\underline{\underline{\sigma}}$ and σ_0 the initial yield stress. The plastic multiplier is then computed as:

$$\dot{p} = \begin{cases} 0, & \phi < 0 \\ (\phi/K)^n, & \phi \geq 0 \end{cases} \tag{5.4}$$

where K and n are parameter for viscous properties. Finally we get the plastic strain rate:

$$\underline{\underline{\dot{\varepsilon}_p}} = \frac{3}{2}\dot{p}\frac{\left(\underline{\underline{\sigma'}} - \underline{\underline{x}}\right)}{\sqrt{\frac{3}{2}\left(\underline{\underline{\sigma'}} - \underline{\underline{x}}\right) : \left(\underline{\underline{\sigma'}} - \underline{\underline{x}}\right)}} \tag{5.5}$$

Hardening variables evolution is given by:

$$\dot{r} = Q\left(1 - \frac{B}{Q}r\right)\dot{p} \tag{5.6}$$

$$\underline{\underline{\dot{x}}} = -\underline{\underline{x}}\dot{p} \tag{5.7}$$

In eq. (5.6), B and Q are parameters describing the evolution of the different contributions to the strain hardening.

5.1.1.5 Parameter identification

The parameters are identified using quasi-static tensile tests on smooth specimens at a constant strain rate $\dot{\varepsilon} = 10^{-4}s^{-1}$. These tests are performed on an electromechanical Instron 50 kN machine. Hypothesis is thus made that the parameters identified at the macro-scale on a full specimen were still valid at the micro-scale.

The identification is accomplished in a direct manner. Parameters for each phase (i.e. fiber, matrix and homogeneous layer) are identified independently. It is worth noting that an identification using an inverse method on the composite material is also theoretically possible. However, it would require for several microstructure calculations to be performed for every iteration in the optimization loop. But as each microstructure calculation takes at least 30 hours to complete, the inverse method is hardly appropriate in our case.

Values obtained are summarized in table 5.1 for the PA66 matrix and in table 5.2 for the homogeneous layer.

RH	E (Norm.)	ν	σ_0	K (Norm.)	n	Q	B
RH0	43	0.4	0	0.43	23	11200	400
RH50	29	0.4	0	0.14	8	2920	73
RH80	15	0.4	0	0.14	12	1960	70

Table 5.1: Parameters for the PA66 matrix at different humidity ratios. All stress values are normalized.

5.1.1.6 Fiber-matrix interface

Before being put in the injection-molding machine, glass fibers are covered with a chemical agent that insures a better bonding between the glass and the polymer matrix. Yet this bonding is not perfect and debonding occurring at the fiber-matrix interface is a typical damage mechanism in fiber reinforced materials. Moreover fiber ends are very poorly bonded to the matrix leading to voiding and deformation of the surroundings matrix during tensile tests.

RH	Angle	E (Norm.)	ν	σ_0	K (Norm.)	n	Q	B
RH0	0	83	0.4	0	0.71	8	11500	95
RH0	45	33	0.4	0	0.85	8	9500	100
RH0	90	19	0.4	0	0.50	8	6000	400
RH50	0	47	0.4	0	1.57	8	10000	150
RH50	45	29	0.4	0	0.14	8	2920	73
RH50	90	26	0.4	0	0.71	8	5300	100
RH80	0	25	0.4	0	0.36	8	6500	57
RH80	45	12	0.4	0	0.14	8	4500	70
RH80	90	11	0.4	0	0.14	8	3900	70

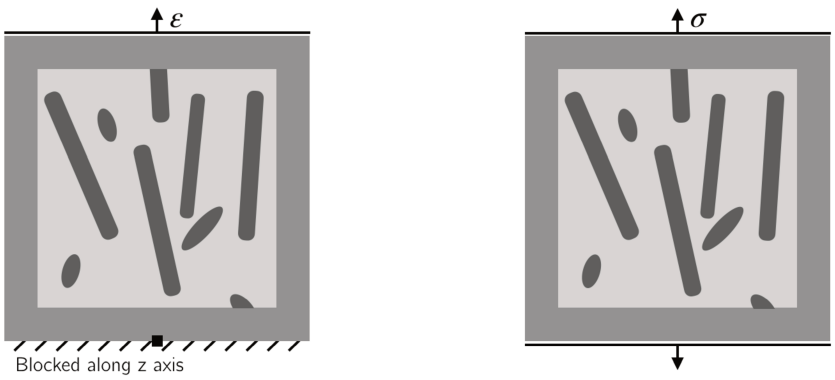
Table 5.2: Parameters for the homogeneous layer at different orientations and humidity ratios. All stress values are normalized.

One of the main limitation of the current micro-mechanical modeling is to consider the fiber-matrix interface as perfect. This assumption was also made by most of the authors whether using FFT based algorithms [2] or FE models [3; 4]. Only Horst [5] made a 2D FE model with the fiber end not bonded to the matrix in order to study voiding and matrix deformation.

For our calculations, perfect bonding is assumed. As the goal is to link the local mechanical fields to the very early stages of fatigue damage (cavitation, crazing) where voiding at fiber tip is still very limited, this assumption might have a smaller impact. However, the possibility of modeling this poor adhesion at fiber tip will be investigated and discussed on a simple case in section 5.1.2.2.

5.1.1.7 Loadings

Two types of loadings are considered for FFT modeling. Monotonic tensile loadings are performed at a constant strain rate of $\dot{\varepsilon} = 10^{-4}s^{-1}$ until a global strain of 8% is reached (fig. 5.3(a)). Cyclic tensile loadings are performed by imposing a repeated loading-unloading sequence on the global strain, at a frequency of 0.5Hz.



(a) Imposed global axial strain rate (b) Imposed axial stress

Figure 5.3: Boundary conditions for FFT and FE modeling.

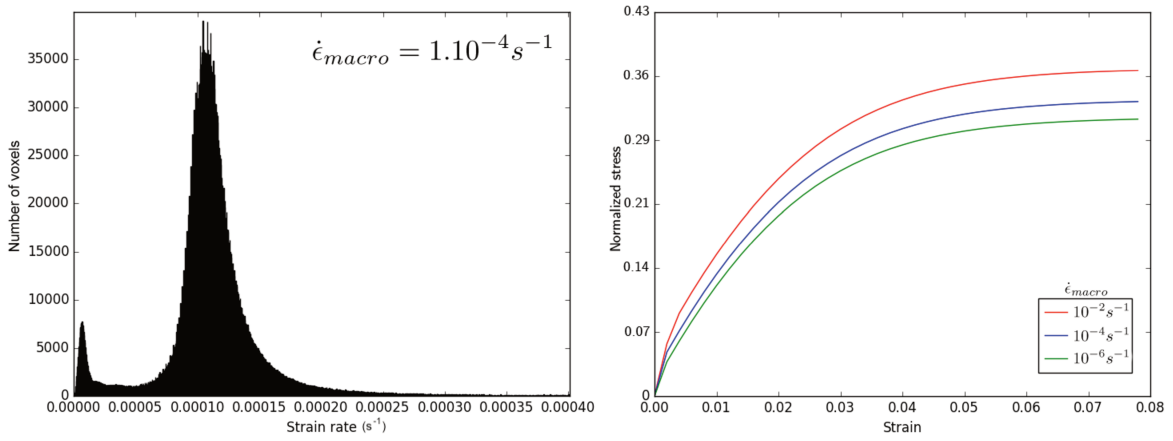
5.1.2 FFT modeling, results and analysis

The first part (section 5.1.2.1) will focus of the mechanical response of matrix. This study was performed as a verification of the study conducted by ROLLAND [6] in which the homogenized layer was always given the properties of a RH50-45° material, regardless of the actual microstructure computed.

The second part (section 5.1.2.2) presents the results focusing on damage mechanisms and in particular on cyclic microstructure calculations in order to link the computed mechanical fields with cavitation observations.

5.1.2.1 Material behavior

Strain rate in the matrix Due to the heterogeneous microstructure, local strain rates can differ from the macroscopic strain rate. In order to evaluate this dispersion, we plotted the distribution of the maximal strain rate for every voxel in the matrix during a tensile test at a constant macroscopic strain rate $\dot{\varepsilon} = 10^{-4}s^{-1}$ (fig. 5.4(a)). All the values are within a range where our model for the polyamide matrix behavior was checked to be consistent (fig. 5.4(b)).



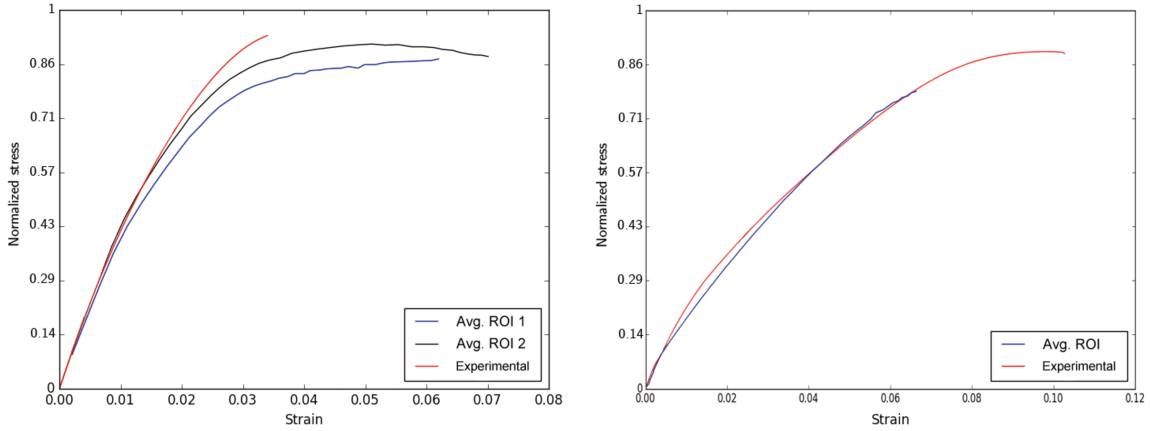
(a) Strain rate distribution

(b) Stress-Strain curves computed for various strain rates

Figure 5.4: Strain rate distribution in the matrix and sensitivity of the matrix model to the imposed macroscopic strain rate - FFT modeling.

Comparison with the composite material By averaging respectively the stress and strain fields over all the voxels within our ROI (matrix and fiber voxels) at different steps ouf our loading, we can plot a homogenized (averaged) stress-strain curve for the microstructure. This curve can be compared to the experimental data obtained on the composite material (fig. 5.5).

Agreement between the homogenized material from the micro-modeling and the composite material is satisfactory. Discrepancies in some of the cases studied, can be explained by a number of factors :



(a) RH 50 - 0° specimen

(b) RH 80 - 0° specimen

Figure 5.5: Experimental stress-strain curves *vs.* microstructure calculation - FFT modeling.

- ROI are chosen for the damage observed within the volume. They are therefore not necessarily Representative Elementary Volumes in the sense of the composite macroscopic behavior.
- Parameter identification was performed in a simple, direct manner for each phase individually. Using an inverse method on the whole microstructure would have yielded better results, although this process has also considerable drawbacks in term of the computational resources needed (as discussed in section 5.1.1.5).

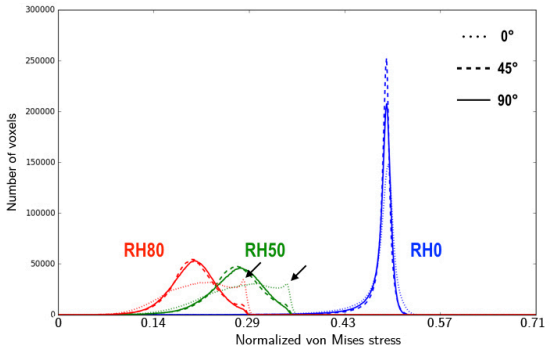
Distribution of the local mechanical fields in the matrix Local mechanical fields distributions in the matrix have been investigated for different fiber orientations and RH.

At a given imposed macroscopic strain, the von Mises stress distribution is directly influenced by the RH (fig. 5.6(a)). The lower the RH, the lower the standard deviation and the higher the mean value are. Influence of the fiber orientation is minimal, except at 0° where the distribution is flatter and more spread out. In the latter case, for 0° microstructure at RH50 and RH80, a small peak at the upper bound of the distribution can be noticed, as indicated by arrows on fig. 5.6(a). The voxels here are located close to fiber tips. At a given macro-strain these voxels are already loaded at the maximum value. This *saturation* value is directly linked to the constitutive model of the matrix.

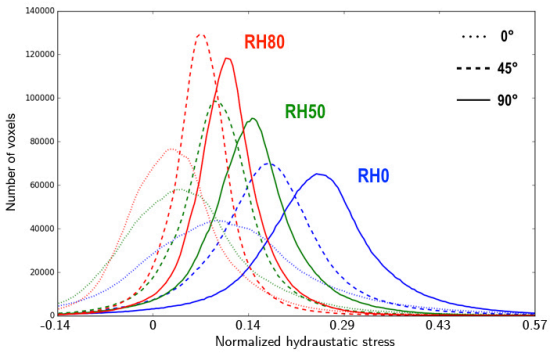
The hydrostatic stress distribution is influenced by both the RH and fiber orientation (fig. 5.6(b)). For a given fiber orientation, the lower the RH, the lower the standard deviation and the higher the mean hydrostatic stress are. At a given RH, the mean value is higher for 90° than for 45° and 0° specimens. However distributions are far more dispersed for 0° specimens.

Unlike for the von Mises stress, the triaxility ratio distribution is mostly influenced by the fiber orientation (fig. 5.6(c)). For 90° specimens, the standard deviation is lower and the mean value is higher than for 45° and 0° specimens. Influence of the RH

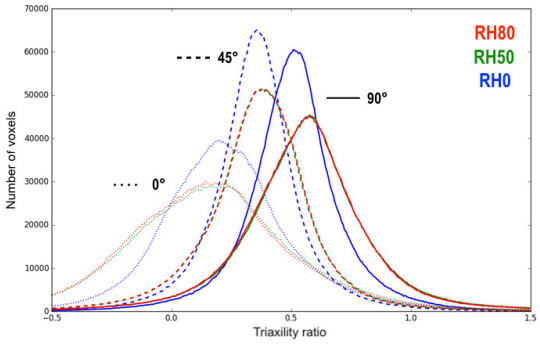
is minimal between RH50 and RH80 specimens. For RH0 specimens, the standard deviation is lower. However no clear trend can be noticed for the mean value.



(a) von Mises stress distribution



(b) Hydrostatic stress distribution



(c) Triaxiality ratio distribution

Figure 5.6: Local mechanical fields distribution in the matrix for different RH and fiber orientation at iso-macroscopic axial strain $\varepsilon = 3.6\%$ after loading at $\dot{\varepsilon} = 10^{-4}s^{-1}$ - FFT modeling.

Overall the distributions found with the appropriate homogeneous layer parameters (correct orientation and correct RH) do not significantly defer from the results by Rolland [6] using a RH50-45° layer in every case. Local mechanical fields are thus much more dependent on the local complex microstructure than sensitive to the surrounding buffer layer. An immediate consequence (and a good news) is thus that the much detailed analysis of the local mechanical fields distributions provided by Rolland remains correct.

5.1.2.2 Main damage mechanisms

While performing micro-mechanical modeling on an artificially generated microstructure can also provide an insight on the influence of fiber orientation and matrix RH on the mechanical field distributions, the direct comparison between those fields and actual damage is only made possible by the study of a real microstructure submitted to in-situ fatigue loading. In this part, tomographic slices of fatigue damaged material are compared to the calculated mechanical fields in order to gain a better understanding of the different damage mechanisms.

Fiber failure Fiber failure has long been overlooked as a damage mechanism occurring before the final stages of fatigue failure. However recent studies based on tomographic data suggest that some fibers break early in the material life [6]. Gaining a better understanding of why and where fibers break is therefore important.

The maximal principal stress is plotted along the centerline of a fiber almost aligned with the loading direction. The gray levels along its centerline on the tomographic picture are also plotted in order to obtain the position of the fiber breakage marked by a sharp drop in gray levels (fig. 5.7). By comparing these to curves, it is observed that the fiber failure occurred in an area of maximal stress. The presence of the fiber $n°2$ crossing the fiber $n°1$ induces a stress concentration in the polymer matrix and in the fiber. Two main information can be inferred from these results:

- micro-mechanical modeling can simulate stress concentration occurring in the fibers and leading to fiber failure.
- stress concentration in a fiber is induced by the proximity of surrounding fibers. This emphasize the importance of taking into account a representative volume when modeling a microstructure.

However it can also be noted on the tomographic slice that the fibers are actually in contact. Fiber failure could therefore also be initiated by the wear at the contact point. Fretting-fatigue induced fiber failure in reinforced thermoplastics has never been mentioned in the literature to our knowledge. However SEM fractography of the specimens seem to indicate that this mechanisms could actually be occurring in the material as presented in section 3.1.1.

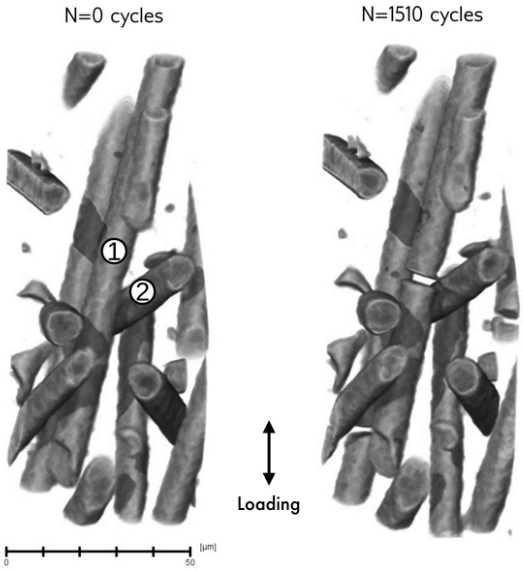
Damage at fiber end As mentioned previously, perfect bonding at the fiber-matrix interface is assumed in our model (fig. 5.8(a)). It is likely that in reality this regions have a poor adhesion.

This poor adhesion at the fiber-matrix interface at crack tip (fig. 5.9(a)) is explained by the manufacturing process: as the fibers break during the injection, their ends are not covered by the sizing agent (for chemical bonding) sprayed onto the fibers prior to molding.

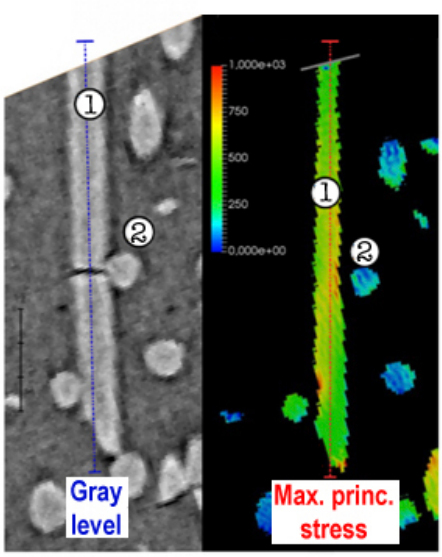
FFT simulations show that the matrix around a fiber end is subjected to a significant stress concentration, this confirms results previously obtained on an artificial 2D microstructure by FE calculations that can be found in the literature [7]. Furthermore this volume around a fiber end is subjected to a high hydrostatic stress (fig. 5.9(b)) and high triaxiality ratio (fig. 5.9(c)).

Note that fibers oriented perpendicularly to the loading direction (e.g. in a 90° specimen) are much less subject to over-stresses at fiber tip compared to fibers aligned at 0° (fig. 5.10).

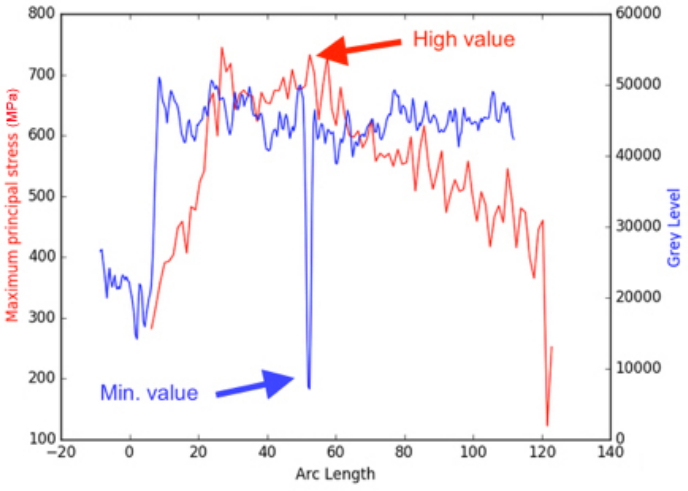
A test was performed on a single fiber tip, using an extra phase with degraded mechanical properties in order to model the void. Although the stress levels reached at a given imposed strain are lower, results did not evidenced a significant stress redistribution (fig. 5.8(b)) induced by taking into account the poor bonding at fiber tip.



(a) Fiber failure after fatigue loading of a RH50 - 45° specimen observed by in-situ microtomography

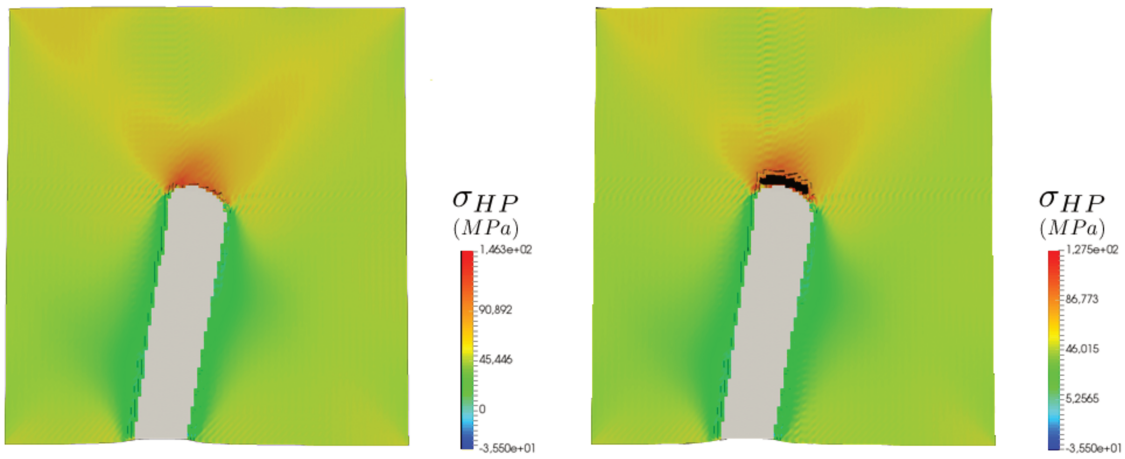


(b) Sliced view of the tomographic data and computed maximal principal stress inside the short glass fiber after quasi-static loading at $\dot{\varepsilon} = 10^{-4}s^{-1}$ until a global strain of $\varepsilon = 3.6\%$



(c) von Mises and gray levels plotted along the center line

Figure 5.7: Study of a short glass fiber failure - FFT modeling.



(a) Perfect bonding at fiber tip

(b) Poor bonding at fiber tip

Figure 5.8: Modeling voiding at fiber end by an extra phase with degraded properties - FFT modeling. Small oscillations in the computed fields come from an aliasing effect as the conditions of the Nyquist-Shannon are not formally respected (high contrast between the phases).

Crazing Crazing in amorphous thermoplastics is observed to develop perpendicularly to the highest normal strain. Many crazing criteria can be found in the literature [8].

The one used in this study was calculated as proposed by ARGON and HANNOOSH [9]. It is a simplified local stress criterion:

$$S_0 = \frac{\alpha_1}{\alpha_2 + \frac{3\sigma_{HP}}{2Q\sigma_Y}} \tag{5.8}$$

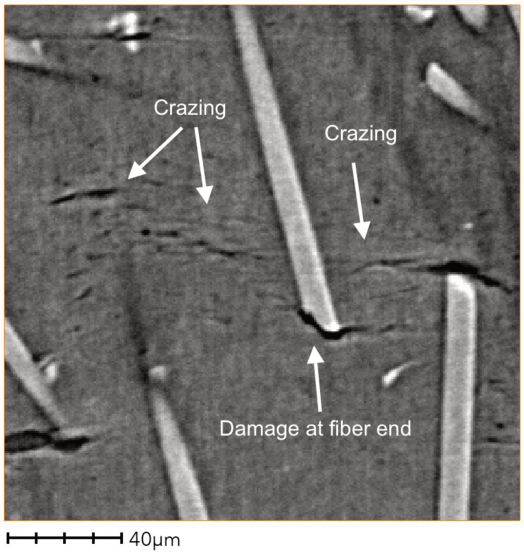
with $S_0 = \sigma_I - \sigma_{III}$ the global deviatoric stress, $\sigma_{HP} = \frac{1}{3}\text{tr}(\underline{\underline{\sigma}})$ the hydrostatic stress, $\sigma_Y = 60MPa$ the material yield stress, $Q = 0.133$ is a factor giving the effective decrease in cavitation resistance of a porous region when a large deviatoric stress near the yield stress is present, $\alpha_1 = 2000$ and $\alpha_2 = 12$ are parameters tuned to adjust the model.

The most craze-prone areas are in green and red on the fig. 5.9(d). One can observe the good correlation between the craze criteria and the actual damage observed.

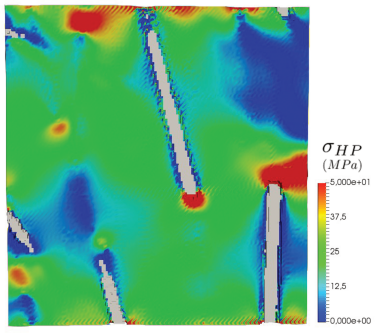
Cavitation Cavitation in the thermoplastic matrix in one of the first sign of damage occurring in the material during fatigue loading. These small voids can be detected in our tomographic data if they have a diameter larger than a micron.

Cavities are known to form in the amorphous phase, between crystalline lamellae, on the equatorial plane of the spherulites [10]. Volumes prone to cavity formation are usually separated into two categories:

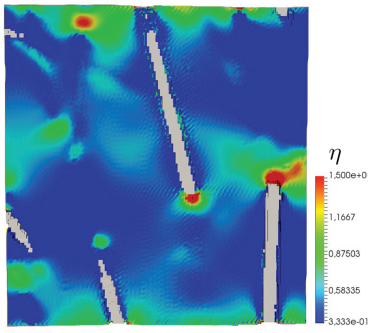
- In highly confined volumes and along glass fibers, where the stress triaxiality ratio is higher.
- In poorly reinforced volumes, where the matrix deformation is greater.



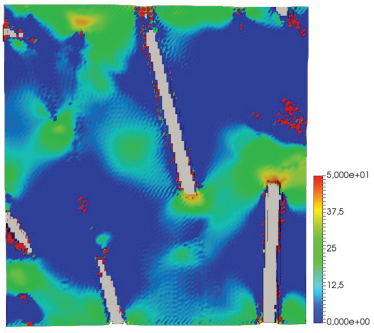
(a) Sliced view of the tomographic data



(b) Hydrostatic stress

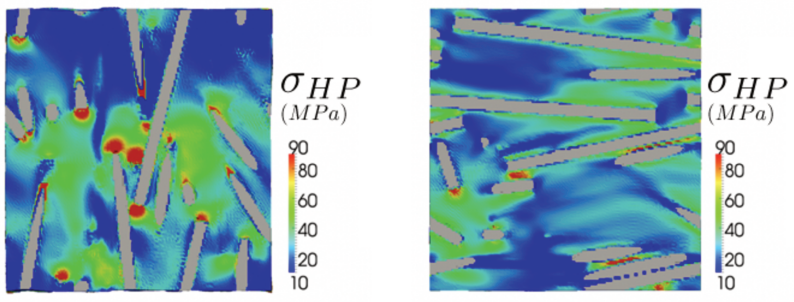


(c) Stress triaxiality ratio



(d) Argon and Hannoosh crazing criterion

Figure 5.9: Results for monotonic tensile loading of a RH 50 - 0° specimen at $\dot{\varepsilon} = 10^{-4}s^{-1}$ until a global strain of $\varepsilon = 3.6\%$- FFT modeling.



(a) RH 50 - 0° - Normalized $\sigma_{11} = 0.72$ (b) RH 50 - 90° - Normalized $\sigma_{11} = 0.43$

Figure 5.10: Hydrostatic stress in two microstructures after quasi-static loading at $\dot{\varepsilon} = 10^{-4}s^{-1}$ until a global strain of $\varepsilon = 3.6\%$. At this imposed strain, different stresses are reached depending on the fiber orientation.

Cavities are often described to form under high triaxial stresses. Calculating the local stress triaxiality in the microstructure show that this is indeed the case for some configurations (figs. 5.11(a) and 5.11(b)), mostly in confined areas. However in other cases, intense cavitation can be observed without a highly triaxial stress field (figs. 5.11(c) and 5.11(d)), these are in region where fiber density is low and would therefore correspond to the second type of cavitation describe above.

Based on the results presented in chapter 4, we also calculated the cyclic strain increment $\frac{\Delta\varepsilon_{11}}{\Delta N}$ at every cycle and for every voxel of the volume (fig. 5.12), a parameter which we have shown to be key in the evaluation of the fatigue lifetime at the macro scale.

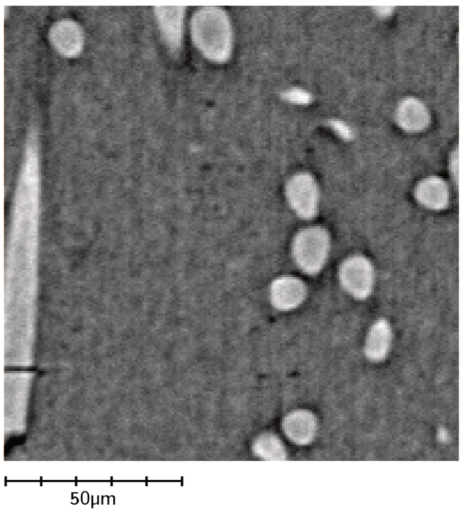
Plotting the maximum value $\frac{\Delta\varepsilon_{11}}{\Delta N}_{max}$ reached by every voxel during the cyclic loading we get maps such as the ones presented on fig. 5.13. On the same image we can mark the positions of the cavities observed in the material after fatigue loading. Those positions were registered on the tomographic slice by a blind investigator to reduce the potential bias during this operation.

Cavities appear to form mainly in areas where the maximal cyclic strain increment is the highest, whether close to a fiber or in a poorly reinforced region.

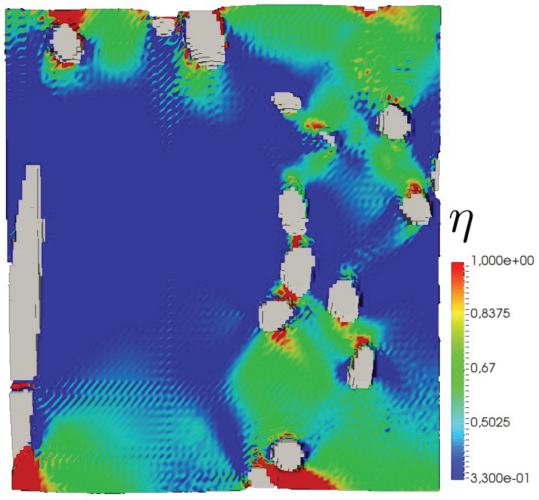
However a few cavities seem no to obey this rule, they might be cavities formed during the injection process and already present in the virgin material or they might have formed on defects in the matrix not taken into account in our micro-modeling.

Overall, this would support the fact that the cyclic strain rate is an important mechanical parameter driving the formation of cavities in the material at the local scale.

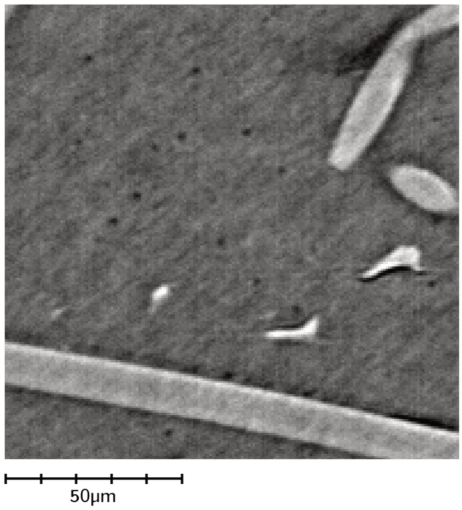
In order to have a more statistical approach we tried to register the computed volume and the tomographic scan. This proved more difficult than expected, and slight errors in the registration process induced incoherences in the results (e.g. only a few voxel of error resulted in cavitations being registered on positions were there was a fiber in the model, and thus completely different mechanical fields).



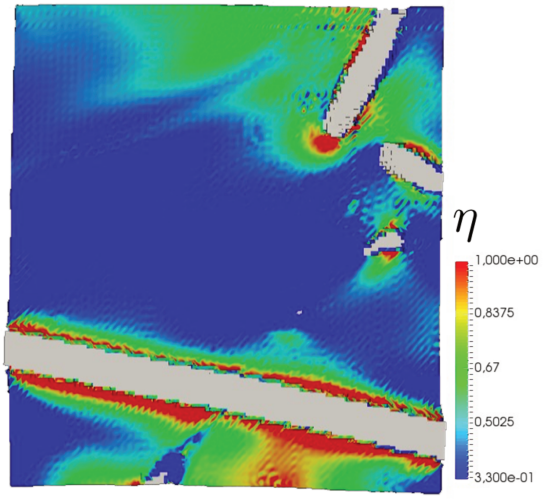
(a) Tomographic slice



(b) Stress triaxiality



(c) Tomographic slice



(d) Stress triaxiality

Figure 5.11: Cavitation in a RH50 90° specimen after 2500 loading cycles - 3Hz - R=0.1 - Normalized $\sigma_{max} = 0.37$, and computed stress triaxiality ratio.

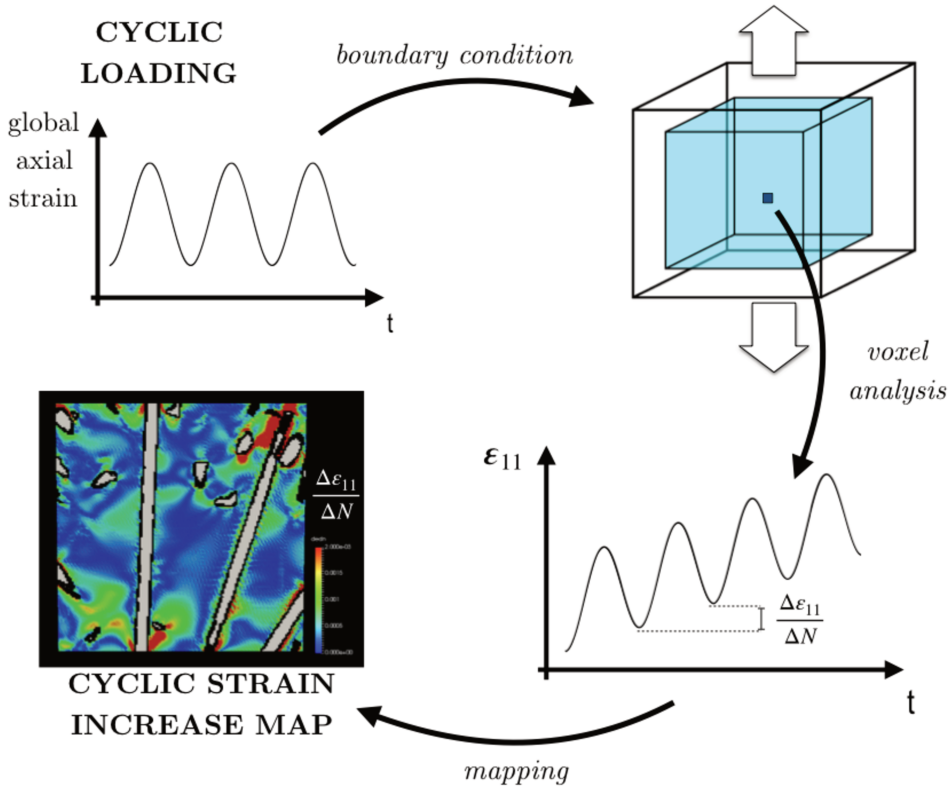
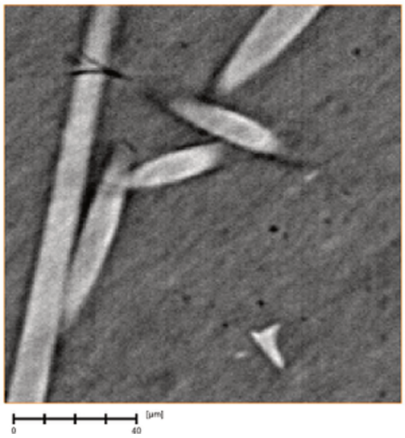
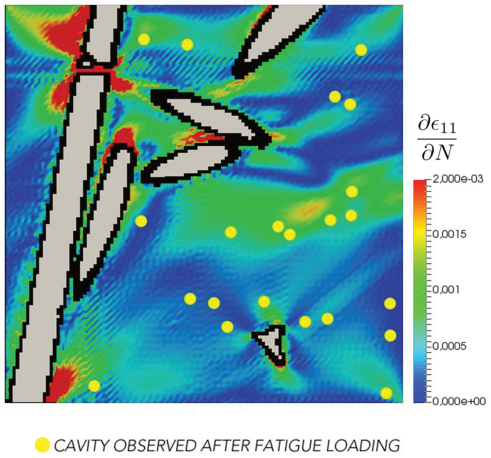


Figure 5.12: Calculation of the local cyclic strain rate.



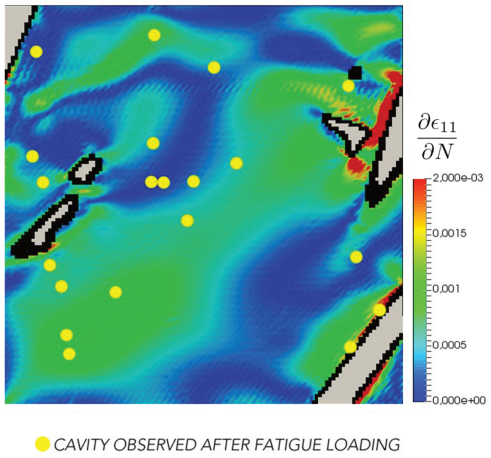
(a) Tomographic slice



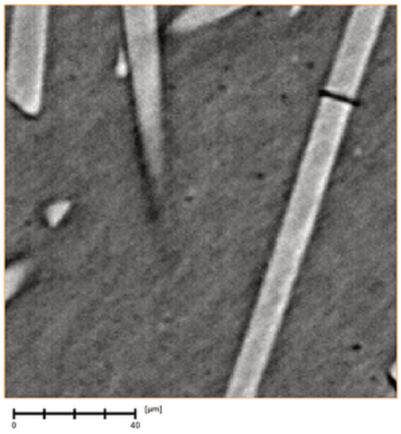
(b) Calculated strain increment



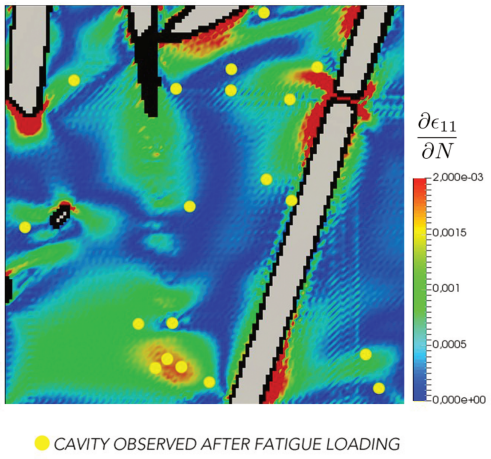
(c) Tomographic slice



(d) Calculated strain increment



(e) Tomographic slice



(f) Calculated strain increment

Figure 5.13: Cartography of $\frac{\Delta \varepsilon_{11}}{\Delta N}_{max}$, with the locations of the cavities observed on the corresponding tomographic slice, in a RH 50 - 45° specimen - FFT modeling.

5.2 FE modeling

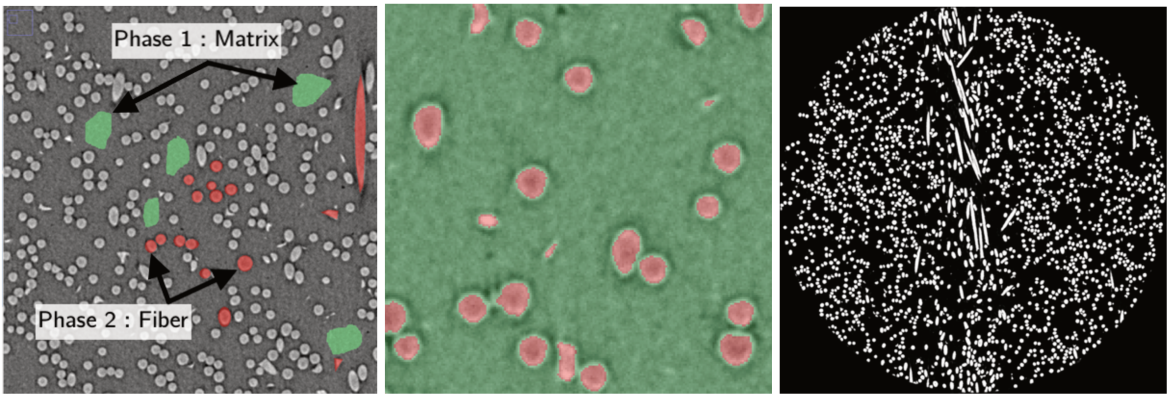
FE modeling was performed to provide additional insight on the results provided by FFT calculation, mainly with the use of a mechanics of porous media model for the polymer matrix.

5.2.1 Method

5.2.1.1 Microstructure segmentation and meshing

Segmentation protocol was a bit different than the one described for FFT (section 5.1.1.1). The Weka machine learning algorithm [11] was trained to efficiently separate the fibers: training is performed by manually indicating the different phases[2] on the images (fig. 5.14(a)). As the algorithm *learns* to segment the phases, corrections can be manually made to adjust for the errors and perform a novel training phase. More training generally yields better results... but not always. When results are satisfactory, the *knowledge* can be saved as a classifier. This classifier can latter be used to segment all similar images, without further manual operation (fig. 5.14(b)).

This yields results comparable to what would have been obtained by semi-automatic segmentation but in much less time and/or on much larger volumes (fig. 5.14(c)).



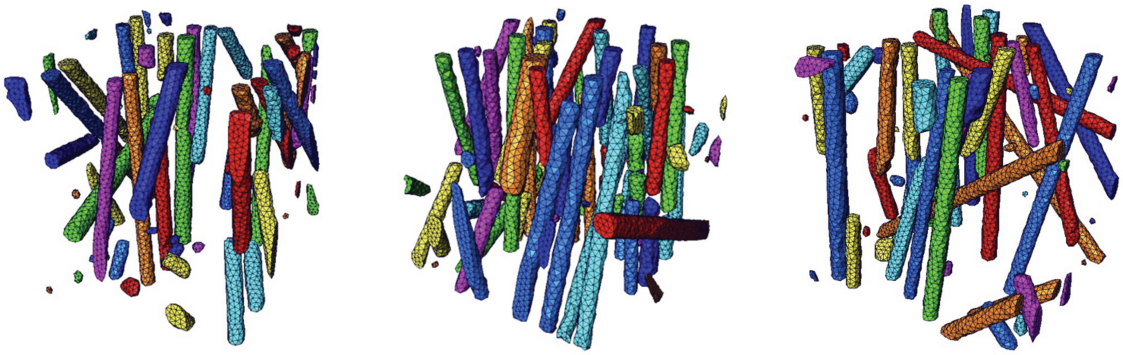
(a) Training (b) Results on a small volume (c) Results on large volume

Figure 5.14: Example of segmentation using the Weka machine learning algorithm.

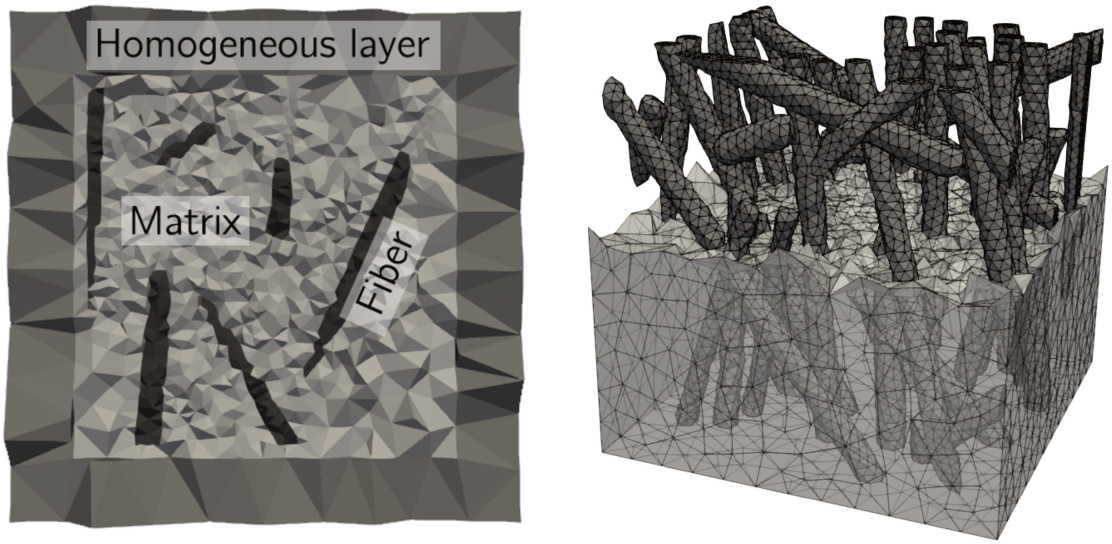
An homogeneous layer is also used around the volume of interest in order to reduce edge-effects. Once segmented the 3D mesh is constructed using Gmsh [12].

Complete meshes are cubes, $120\mu m$ by side, each containing around 150.10^3 four-nodes linear tetrahedral elements (c3d4). Although this yields a rather coarse mesh (fig. 5.15), it allows for cyclic calculation to be performed within a reasonable time frame (e.g. about two computed load cycles per hour).

[2]Note that the best strategy that I found for our case was to actually use 3 phases in the training. The first and second one are for the matrix and fibers. The third one is to teach the algorithm to recognize the usually problematic areas where the matrix is confined between very close fibers. This third phase can latter be recognized as matrix for analysis or calculation, allowing for proper segmentation of the fibers.



(a) Mesh of segmented fibers (b) Mesh of segmented fibers (c) Mesh of segmented fibers



(d) Slice along elements surfaces (e) ROI with only part of the matrix visible

Figure 5.15: Example of meshed microstructures for FE modeling.

5.2.1.2 Constitutive model

Similar to what is done for FFT, hypothesis is made that the parameters identified at the macro-scale on full specimens are valid at the micro-scale. The elasto-visco-plastic behavior model and the GTN damage model used here are thus the same than identified for PA66 in section 4.3.

5.2.1.3 Loading

For FE modeling sinusoidal cyclic tensile loading is imposed on the microstructure (fig. 5.3(b)). However the loading is here performed under load control. Loading frequency is 0.5Hz and load ratio is set at R=0.1. Maximum stress level is fixed at a normalized value of $\sigma_{max} = 0.21$ to limit issues with the solver convergence.

Performing the calculation under load control allows for the cyclic creep to occur without being constrained by an imposed global strain.

5.2.2 FE modeling, results and analysis

5.2.2.1 Cyclic loading

Under load-control fatigue loading at R=0.1, the microstructure exhibits a cyclic creep behavior. In the context of this work, we will study the formation and growth of damage after 10, 25 and 50 loading cycles. As shown on fig. 5.16, the cyclic strain rate reaches a stationary state (i.e. constant slope) after only 15-20 loading cycles.

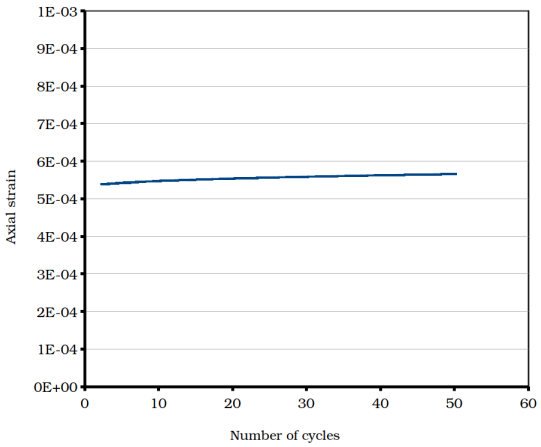


Figure 5.16: Cyclic strain evolution for FE microstructure modeling - 0° - RH50 - R=0.1 - f=0.5Hz - Normalized $\sigma_{max} = 0.21$.

It is worth noting that the experimental tomographic data used for comparison correspond to tests performed at 3Hz under a maximum normalized loading stress of $\sigma_{max} = 0.69$ (R=0.1). Tomographic images shown here were taken after 1500 loading cycles, close to the failure of the specimen. Damage is therefore much more developed experimentally than in our calculations after a few tens of loading cycles at lower stress levels. However the main goal of this micro-modeling is to test the efficiency of a

damage model in estimating the localization of damage in the microstructure. Results are thus more qualitative than quantitative regarding the exact void volume fraction.

5.2.2.2 Matrix damage growth

Note on the damage model Rather than being determined using a criterion during post-processing, damage is included within the calculation. The damage variable (i.e. the calculated void volume fraction) can be superimposed to the tomographic slices.

It is worth noting that in the GTN damage model used in this work [13], the evolution of the void volume fraction f is controlled by the visco-plastic strain rate:

$$\dot{f} = (1 - f)\mathrm{tr}[\underline{\underline{\dot{\varepsilon}}}^{vp}] \tag{5.9}$$

The use of such a model is thus in line with the results presented in section 5.1.2.2 on the influence of the cyclic strain rate on the local void growth.

Localization and growth of damage Figure 5.17 represents the calculated void volume fraction after 10 loading cycles overlaid on the corresponding tomographic slice. Only the values above the initial porosity value of 10^{-2} are plotted.

Calculated void growth preferentially initiates at fiber tips (figs. 5.17(b) and 5.17(d)). Apart from the edge effects, the localization of the calculated damage is consistent with the experimental observations.

However our modeling does not take into account the spherulitic organization of the matrix that plays a major role in fatigue damage of semi-crystalline polymer as demonstrated in section 3.2. This might also explain why, besides the low stress levels and low number of loading cycles, some matrix voiding features characteristic of spherulitic damage seem not properly modeled (see the arrow on fig. 5.17(f)).

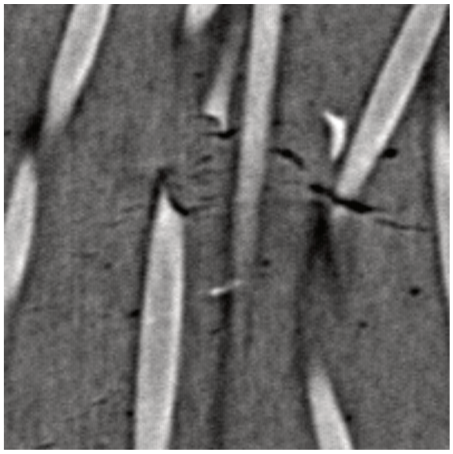
Damage growth progress in the polymer is followed during 50 loading cycles (fig. 5.18). Initial damage grows as expected from fiber tips (fig. 5.18(a)). Subsequent growth occurs joining the already damaged areas and then extending to the whole volume (figs. 5.18(b) and 5.18(c)).

The good agreement between the computed and observed damage locations confirms the hypothesis that the strain rate drives the damage initiation at the local scale and that a model based on this parameter yields promising results.

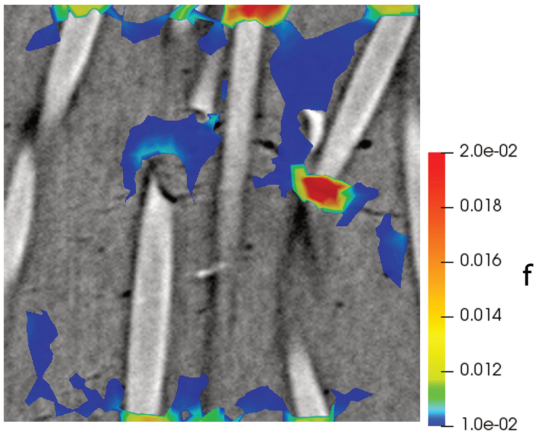
Further analysis would require a larger number of microstructures, with various fiber orientations, to be segmented and (properly) meshed. While extremely time consuming this would allow for a more statistical and quantitative approach.

Tomographic observations of the damage growth sequence for various matrix RH would also give more reference data.

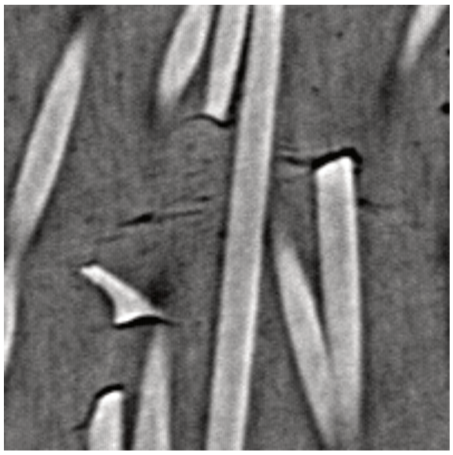
Finally as only the damage related to the direct effect of the fibers is properly accounted for in our modeling, a -challenging- outlook would be to take into account the presence, structure and behavior of the spherulites in the matrix.



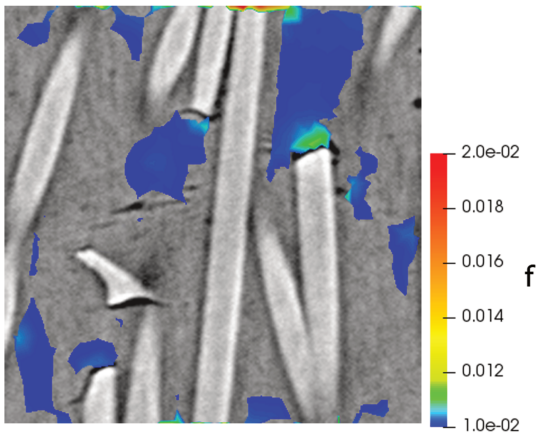
(a) Tomographic slice



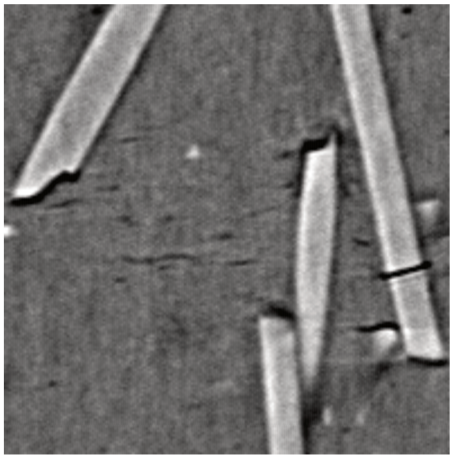
(b) Calculated porosity



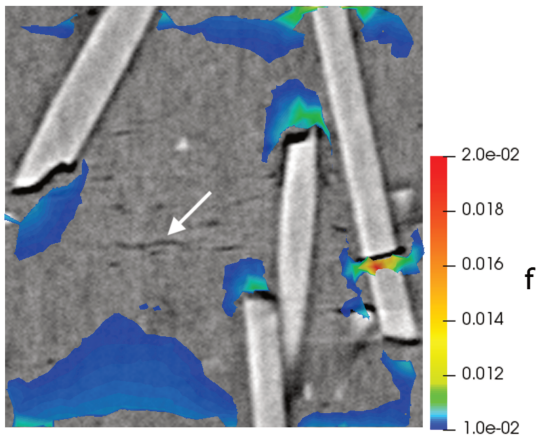
(c) Tomographic slice



(d) Calculated porosity

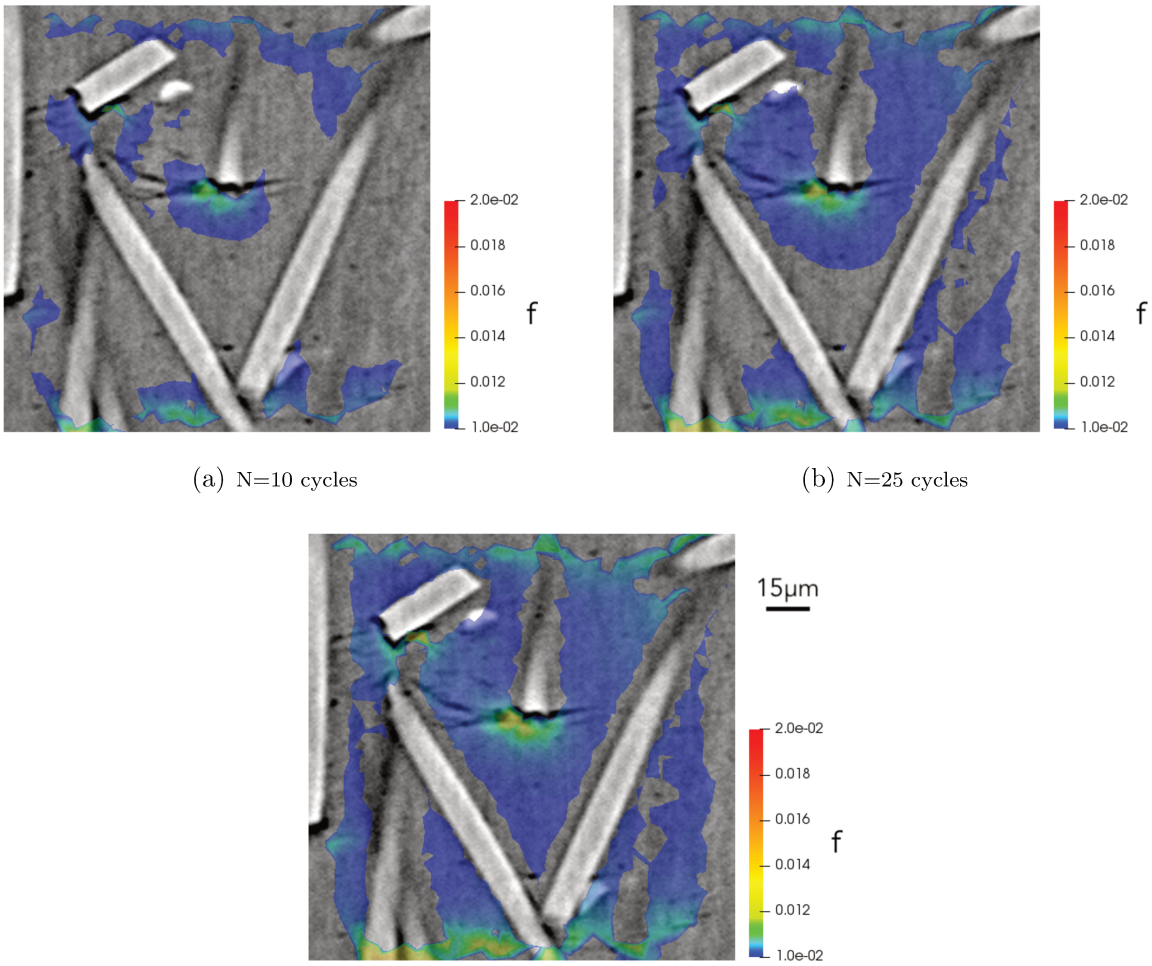


(e) Tomographic slice



(f) Calculated porosity

Figure 5.17: Calculated void volume fraction after 10 loading cycles at a normalized $\sigma_{max} = 0.21$ overlaid on the corresponding tomographic slice, in a RH50 - 0° specimen after 1500 loading cycles at a normalized $\sigma_{max} = 0.69$ - FEM modeling.



(a) N=10 cycles

(b) N=25 cycles

(c) N=50 cycles

Figure 5.18: Calculated void volume fraction at a normalized $\sigma_{max} = 0.21$ overlaid on the corresponding tomographic slice, in a RH 50 - 0° specimen after 1500 loading cycles at a normalized $\sigma_{max} = 0.69$ - FEM modeling.

Main conclusions of the chapter

- Microstructure modeling confirms that cavitation and damage occur in areas with **high cyclic strain rate**.
- The use of the GTN damage model yields **promising results at the local scale**, although the spherulitic microstructure is not accounted for.
- Cyclic strain rate is **a parameter driving damage growth at the micro-scale**.

5.3 Bibliography

[1] K. Refai, "Mécanismes d'endommagement au sein d'un composite à matrice thermoplastique," tech. rep., I2M Bordeaux, 2016. 146

[2] J. Spahn, *An Efficient Multiscale Method for Modeling Progressive Damage in Composite Materials*. PhD thesis, TU Kaiserslautern, 2015. 149

[3] E. Belmonte, M. De Monte, C.-J. Hoffmann, and M. Quaresimin, "Damage mechanisms in a short glass fiber reinforced polyamide under fatigue loading," *International Journal of Fatigue*, vol. 94, pp. 145–157, 2017. 149

[4] S. Fliegener, T. Kennerknecht, and M. Kabel, "Simulation of the damage mechanisms of glass fiber reinforced polypropylene based on micro specimens and 1/1 models of their microstructure," in *ECCM17*, no. June, 2016. 149

[5] J. J. Horst, *Influence of fibre orientation on fatigue of short glassfibre reinforced Polyamide*. PhD thesis, TU Delft, 1997. 149

[6] H. Rolland, *Comportement en fatigue et mécanismes d'endommagement du polyamide 6,6 renforcé de fibres courtes*. PhD thesis, ENSAM, 2017. 150, 152, 153

[7] B. Klimkeit, *Etude experimentale et modélisation du comportement en fatigue multiaxiale d'un polymère renforcé pour application automobile*. PhD thesis, ENSMA, 2009. 153

[8] R. Estevez and E. Van der Giessen, "Modeling and Computational Analysis of Fracture of Glassy Polymers," *Advanced Polymer Science*, vol. 188, no. September, pp. 195–234, 2005. 155

[9] A. S. Argon and J. G. Hannoosh, "Initiation of crazes in polystyrene," *Philosophical Magazine*, vol. 36, no. 5, pp. 1195–1216, 1977. 155

[10] E. Mourglia Seignobos, *Compréhension des mécanismes physiques de fatigue dans le polyamide vierge et renforcé de fibres de verre*. PhD thesis, INSA Lyon, 2009. 155

[11] I. Arganda-Carreras, V. Kaynig, C. Rueden, K. W. Eliceiri, J. Schindelin, A. Cardona, and H. S. Seung, "Trainable Weka Segmentation : a machine learning tool for microscopy pixel classification," *Bioinformatics,*, vol. 33, no. 15, pp. 2424–2426, 2017. 161

[12] C. Geuzaine, "Gmsh : A 3-D finite element mesh generator with built-in pre- and post-processing facilities," *Int. J. Numer. Meth. Engng*, vol. 79, pp. 1309–1331, 2009. 161

[13] J. Besson, D. Steglich, and W. Brocks, "Modeling of crack growth in round bars and plane strain specimens," *International Journal of Solids and Structures*, vol. 38, no. 46-47, pp. 8259–8284, 2001. 164

Chapter 6

Outlooks and conclusion

The future interests me - I'm going to spend the rest of my life there.

Mark Twain

In this work we presented a number of new results regarding cyclic creep of PA66 under fatigue loading, at both macro and micro scales. Yet, as it answered some questions, it also underlined new challenges for the years to come.

In this short final chapter we will review some of the possible outlooks to the present study before making a general conclusion.

6.1 Outlooks

6.1.1 At the macro-scale

6.1.1.1 Notched specimens

The study on notched specimens could be completed by testing more notched geometries to probe the validity of the proposed criterion, and make the necessary adjustments. More interestingly, various machining techniques resulting in various surface states could be investigated, as well as the behavior of molded notches.

For molded notches the local microstructure is modified and the validity of the criterion should be checked. However as it has been demonstrated that a cyclic-strain rate based criterion is able to unify fatigue results for various fiber orientations, one can be hopeful that it will still hold for molded structural heterogeneities.

6.1.1.2 Multi-axial loading

The mechanical response of reinforced PA66 specimens under multi-axial fatigue loading is at the core of the current PhD work of Caroline Goutal. In her study the focus is set on establishing an energetic criterion for multi-axial loadings, in line with previous work performed at the Pprime Institute (as introduced in section 1.3.2.3).

However as for uniaxial testing at positive loading ratio, the cyclic strain rate based criterion proved more effective than the energetic approach, a major outlook and complementary to the study by Goutal, the cyclic strain rate based criterion should be evaluated and adapted for multi-axial loadings.

6.1.1.3 Towards other materials

It would also be worth testing the validity of the criterion on PA66 composite with other weight fractions of fibers. As for fiber orientation, humidity ratio and temperature, the cyclic-creep phenomenon probably accounts for the fraction of reinforcements.

Proving this would be interesting in that it would show that the criterion holds for larger industrial parts where the exact fraction of reinforcements might differs for different points in the structure.

It would also be interesting to test a similar approach for other polymers, especially in various conditions with respect to the glass transition temperature, where cyclic-creep might be very limited or very important.

6.1.1.4 Adaptation for industrial use

For large industrial components the numerical calculation requires large amount of resources and is thus limited to a very low number of cycles.

The proposed criterion based on the cyclic-creep during the secondary regime could be adapted to be based on the initial evolution of the cyclic strain rate. Efforts in that regards are currently being made by Prashanth Santharam in his PhD work, and seem to yield promising results.

6.1.1.5 Calibration of the damage model

In this work we used the GTN damage model. The damage variable is the void volume fraction and the model thus require precise observation and measurement of cavitation in order to calibrate the model.

This is usually done using tomographic data, but as noted above, voiding induced by fatigue loading is small in size and therefore harder to observe than for quasi-static or creep loading. The use of synchrotron-radiation tomography is necessary and even then the usual[1] resolution of $0.5 - 0.7\mu m$ is not enough.

Most advance imaging techniques reach resolution of around $50nm$ and is due to improve in the coming years. This might yield the quantitative data necessary to properly and confidently calibrate the chosen damage model. Future work might focus on getting this experimental data, although this would require access to a synchrotron facility[2].

[1] *Usual* as of 2019, it improves so fast...!

[2] Access to beamline is either very expensive or quite hard to obtain. On all the academic proposals submitted during the time of my PhD, none were accepted due to "insufficient beam time available". Hopefully with the upgrade of the ESRF in 2020 and the opening of new beamlines, the access protocol will be less restrictive.

6.1.2 At the micro-scale

6.1.2.1 Measuring local strains

As an outlook to the micro-modelling presented in this work and in order to compare the computed local strains with an experimental reference, Digital Volume Correlation (DVC) could be used.

The use of DVC during in-situ tensile test would provide valuable local information at the micro-structural level. The transition to fatigue loading is probably more complex but would yield a local measurement of the cyclic-creep phenomenon.

The current PhD work of Yacine Nait Abdelaziz on the generation and homogenization of RVE will possibly include DVC and help gain a better understanding on local mechanisms of deformation and damage.

6.1.2.2 Influence of the spherulite morphology

As we obtain obtain more precise data on micro-damage mechanism, it will become possible to engineer polymer materials at the spherulite scale, just as the microstructure of metallic alloys is now well controlled in the industry.

Based on the existing literature, and on few preliminary fatigue tests of our own (fig. 6.1), it would seem that inducing spherulite nucleation increases the durability of the material under fatigue loading (see fig. 6.1).

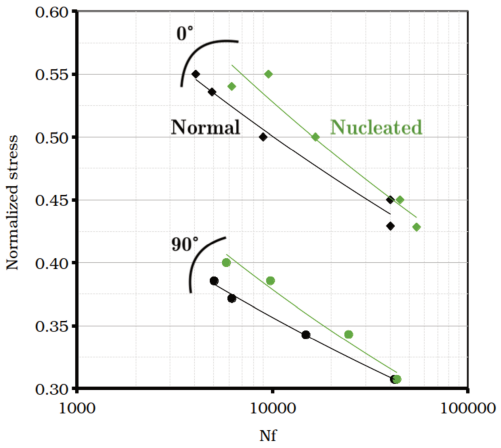


Figure 6.1: S-N curves for normal and nucleated matrix in composite material specimens.

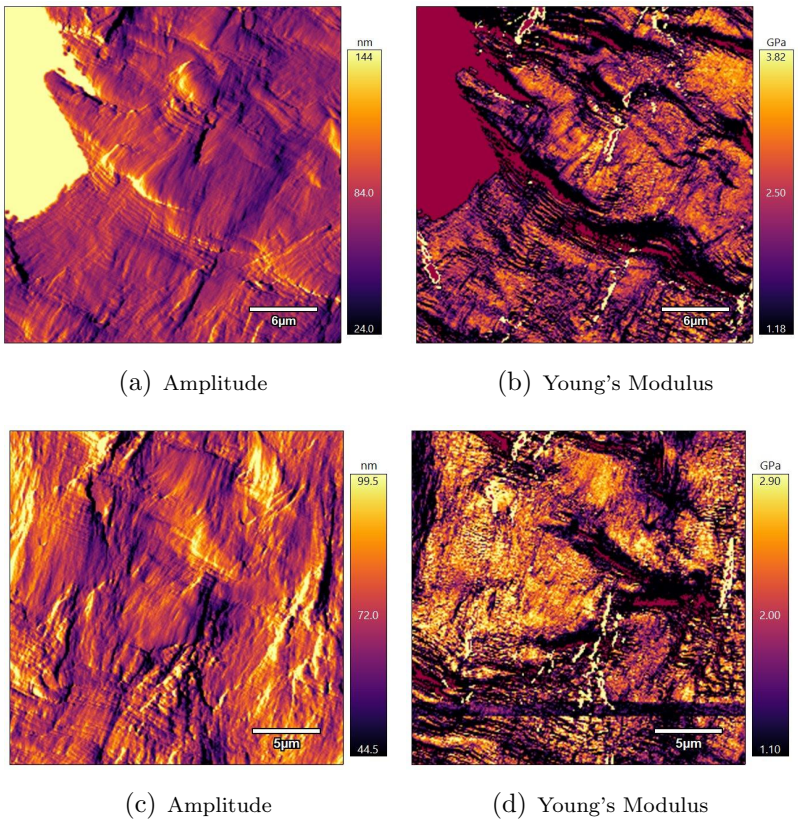
More detailed investigation on nucleation protocol and resulting spherulite size and crystallinity could lead for a significant increase in the mechanical properties of the polymer.

However the size of the spherulite is not everything. As we still have a rather poor understanding of the tri-dimensional organization of a spherulite, efforts should also be put on describing and controlling this morphology.

We have shown the major role played by the nucleus in damage initiation. This nucleus seems to experience little damage, as was also reported for creep by Selles [1].

In order to gain a better understanding of the mechanical properties of this nucleus, one solution would be to performed local properties measurements using an AFM, benefiting from the fact that fatigue failures open the spherulite in half, exposing the nucleus.

Preliminary AFM observations were performed in collaboration with Bogdan Donose from the University of Queensland, Australia. These observations (fig. 6.2) demonstrated the potential to use fatigue fracture surface to gain access to the spherulitic structure. More efforts should be put in precisely imaging a well defined spherulite in order to observe its structure and measure the properties in different areas including the nucleus.



(a) Amplitude (b) Young's Modulus

(c) Amplitude (d) Young's Modulus

Figure 6.2: AFM imaging of a fatigue fracture surface in PA66.

With further study, we could probably gain a good understanding of the spherulitic structure and optimize it in order to improve the durability of the polymer.

6.1.2.3 Microstructure modeling

The loadings applied for microstructure modeling in this work are uniaxial, which is a first approach and would probably not be the case in a real part or structure. One way to apply more relevant boundary conditions, especially for notched specimens, would

be to pinpoint the location of the ROI studied in the specimen. Using a FE calculation, local stress state could be determined and used as boundary condition for the micro-modeling. This kind of approach was used by POULET [2] on artificially generated RVE of PA11 reinforced by unidirectional glass fibers. Performing the same analysis but on real microstructures -segmented from tomographic data and more complex- could technically be achieved but would required supplementary effort.

As we have shown that the nucleus of the spherulite is a cylindrical oriented structure and not a point in injected materials, the microstructure of one (and later an assembly...) of spherulite could be modeled, as shown in the recent work of LAIARINANDRASANA [3]. Taking into account the nucleus region in the simulation could explain intra-spherulitic damage mechanisms (polar fan and equatorial plane damage).

Coupled with a good description of the morphology and local properties, this would be the first step towards micro-modeling similar to what is performed for the crystal plasticity of metals.

6.1.2.4 Tomography, a non-destructive tool?

Tomography is branded as a non-destructive imaging tool, but is it really? Given that it is a more controversial issue (almost a taboo subject!) in the community, I will only try to give my opinion on the matter.

In recent years many studies began using X-ray tomography to investigate microstructures and damage in various materials. This is fine, in most cases.

However, for delicate materials such as polymers, X-ray tomography could be more destructive than commonly acknowledged. A number of facts, gathered during my PhD, back up such a possibility:

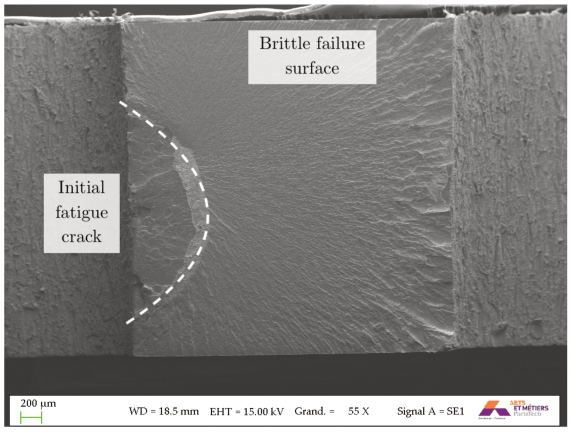
- the polymer changes color under the X-ray beam. The local *yellowing* of the matter is well know by experimentalists. It is often said to be temporary, but some of my samples still have this characteristic brownish-burnt tint more than 10 months after having been exposed to a synchrotron light source...

- the beam induces intense wear in exposed polymer. This observation was not made on samples that are usually exposed for a relatively short period of time but on the PMMA widows of tensile machines used on the beamlines. Not only the polymer changes of color at the level of the X-ray beam passage, but in some points the cylindrical PMMA part loses some matters and begins to exhibits flat spots. This is observed on a virgin part of PMMA, after only a few minutes of being exposed to the X-ray radiation.

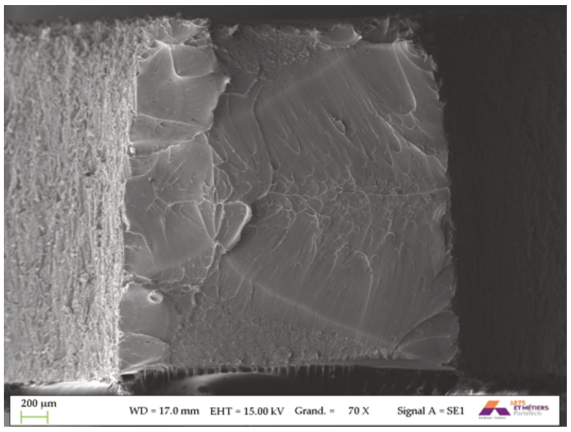
- polymer specimens regularly failed in a brittle manner after being imaged on a synchrotron beamline. When two similar PA66 pre-cracked specimen were tested under fatigue loading at the same conditions on an in-situ testing apparatus on the ID19 beamline at ESRF, the one that was regularly imaged using tomography failed in a brittle manner (fig. 6.3(a)) whereas the other that was not imaged failed in a conventional way with extensive fatigue crack propagation (fig. 6.3(b)).

In my opinion, possible damage induced by the X-ray beam can really become an issue for in-situ testing of unreinforced polymers, and should be properly addressed especially as the focus shifts towards very local damage mechanisms.

A complete study on the potential effects of this *non-destructive* tool is required. It should not only be based on macroscopic testing but also on the investigation of the chemical structure of the polymer (using Raman spectroscopy for example). This would give the community the confidence, or the necessary recommendations, in order to properly use a powerful imaging tool at ever-finer scales.



(a) Brittle failure of a pre-cracked PA66 specimen after being exposed to synchrotron radiation



(b) Classic fatigue failure of a pre-cracked PA66 specimen without exposition to synchrotron radiation.

Figure 6.3: Influence of the exposition to synchrotron radiation on the failure mode of PA66 under cyclic loading.

6.1.3 Towards the nano-scale

6.1.3.1 Molecular dynamics, a quick review

Transitioning between the micro to the nano-scale is a complicated step. A number of works have been performed on the molecular dynamics (MD) of polymers - almost exclusively on poly-ethylene for simplicity reasons.

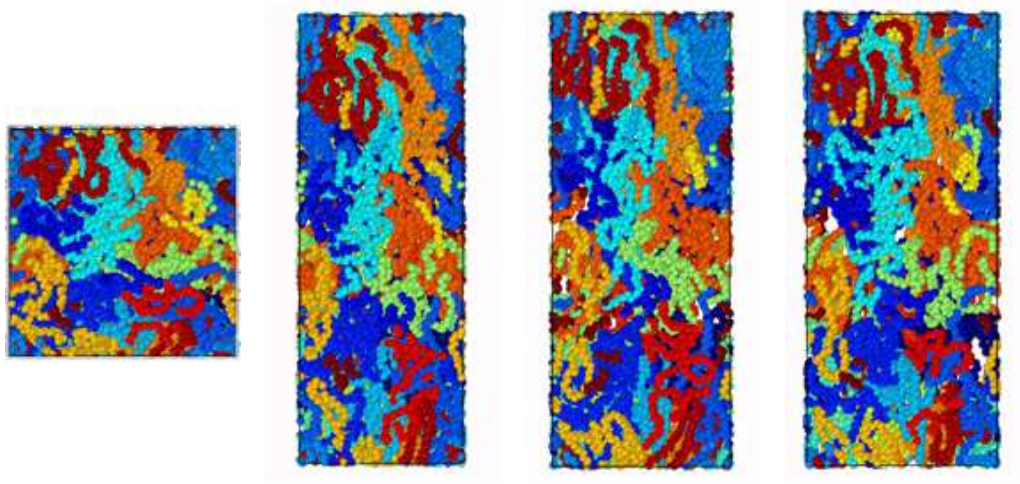
MD calculations were first performed on amorphous polymer chains, under quasi-static [4; 5] and cyclic [6] loading.

Modeling of a semi-crystalline assembly is possible but still the focus of current research activities in the community [7–9].

6.1.3.2 Why it matters...

This is where damage is initiated - at the level of polymer chains, as they move, deform or break. Proper modeling of the physics at this nano-scale can yield major insights on the initiation of damage, a help bridge the gap between the discrete matter and the continuous material.

Simple quasi-static MD calculations on a cube of amorphous PE were performed using LAMMPS[3] at three different strain rates.



(a) Initial (b) $5.10^{-6} fs^{-1}$ (c) $5.10^{-5}\ fs^{-1}$ (d) $5.10^{-4} fs^{-1}$

Figure 6.4: Molecular dynamics tensile test on amorphous PE at different imposed strain rates. 10 polymer chains, 1000 atoms per chain.

As the imposed strain rate is increased, polymer chain no longer have the time to reorganize to accommodate the deformation and *cavitation* occurs. This can easily be seen as for higher strain rate the Poisson effect is limited, thus traducing an increase in volume.

This small example on the origin of the viscous nature of polymers at the nano-scale might explain why strain rate is such a good indicator of damage and durability at the micro and macro scales.

6.1.3.3 ... And what it could bring

One could envision the use of MD calculation to identify a damage model (GTN or other) at the nano-scale. It would even then be possible to identify (rigorously) constitutive and damage parameters for the amorphous and crystalline phases. These would then feed a spherulite damage model at the micro-scale, that could in-turn be used at the macro-scale in a multi-scale homogenization process.

6.2 General conclusion

In this work we have first shown the need for a better understanding and a better modeling of the fatigue behavior of short-glass fiber reinforced polyamide 6,6. The chosen approach was based on the many similarities between fatigue and creep loading. Indeed, under repeated loading with a positive mean stress the mean strain progressively increases, a phenomenon called *cyclic creep*. Similar to the approaches developed for

[3]See appendix B for more details.

creep loading, the focus was set on the strain rate during the secondary stage. In the case of fatigue loading, we decided to call it *cyclic* strain rate.

At the macroscopic scale we first aimed at improving a durability criterion for smooth specimen by extending it for negative load ratios. In this case a mixed cyclic strain rate and anelastic energy based criterion was introduced. It proved very effective in unifying results for all three specimen orientations, in a wide range of load ratios (-0.5 to $+0.7$).

Focus was then set on machined notched specimens, as industrial parts often exhibit complex geometries. A non-local fatigue criterion was proposed based on experimental DIC measurements of the local cyclic strain rate. It proved effective for the three specimen orientations and two notch geometries that were tested. Parameters for an elasto-visco-plastic behavior model were identified so as top properly capture the rate of the cyclic creep phenomenon. This allowed for the durability criterion to be applied on FE models and yielded promising results.

At the microscopic scale we investigated the local damage mechanisms in the material and their similarities with earlier observations made for creep loading. Based on detailed tomography and microscopy analyses we established a damage scenario for injected thermoplastics under fatigue loading. Damage initiates along the oriented nucleus, at the center of the spherulitic structure. It then progresses outwards in the equatorial plane, until complete opening of the spherulite and advance of the microcrack.

Micro-mechanical modeling was performed using FFT and FE methods on real micro-structures segmented from tomographic data. Calculations helped study the influence of fiber orientation and humidity ratio on the mechanical fields in the microstructure. They also show good agreement between the computed and observed damage locations which confirms the hypothesis that the strain rate drives the damage initiation at the local scale and that a model based on this parameter is effective.

Throughout this work we therefore showed that spherulitic damage mechanisms under fatigue loading have strong similarities with creep damage. Moreover we demonstrated that a single parameter -the cyclic strain rate- is relevant for the description of fatigue damage and durability at the macroscopic and microscopic scales. The explanation can probably be found at the nanoscopic scale, at the origin of the viscous nature of the polymer, whereby the strain rate is directly responsible for the initiation of damage when polymer chains can no longer reorganize to accommodate the deformation.

As we close this final chapter, it is worth reminding of the necessity for future works not to omit the study of the material and its microstructure. Far too many studies settle for a purely macroscopic mechanical approach, but the key to a good understanding and modeling of such a complex material can only be found in an in-depth knowledge of the material structure, physics and local damage processes.

6.3 Bibliography

[1] N. Selles, P. Cloetens, H. Proudhon, T. F. Morgeneyer, O. Klinkova, N. Saintier, and L. Laiarinandrasana, "Voiding Mechanisms in Deformed Polyamide 6 Observed at the Nanometric Scale," *Macromolecules*, vol. 50, no. 11, pp. 4372–4383, 2017. 172

[2] P.-A. Poulet, *Effet de la variabilité microstructurale sur le comportement d'un composite UD verre / PA11 : de la caractérisation expérimentale à la modélisation multi-échelle.* PhD thesis, PSL, 2017. 173

[3] L. Laiarinandrasana, "Stress Heterogeneity Leading to Void Nucleation within Spherulites for Semi-Crystalline Polymers," *Crystals*, 2019. 173

[4] B. Sixou, "Molecular dynamics simulation of the first stages of the cavitation process in amorphous polymers," *Molecular Simulation*, vol. 33, no. 12, pp. 965–973, 2007. 174

[5] M. A. Tschopp, J. L. Bouvard, D. K. Ward, and M. F. Horstemeyer, "Atomic Scale Deformation Mechanisms of Amorphous Polyethylene under Tensile Loading," *Supplemental Proceedings: Materials Fabrication, Properties, Characterization, and Modeling*, vol. 2, pp. 789–794, 2011. 174

[6] I. H. Sahputra and A. T. Echtermeyer, "Molecular dynamics simulations of strain-controlled fatigue behaviour of amorphous polyethylene," *Journal of Polymer Research*, vol. 21, no. 11, 2014. 174

[7] B. Monasse, S. Queyroy, and O. Lhost, "Molecular Dynamics prediction of elastic and plastic deformation of semi-crystalline polyethylene," *Int J Mater Form*, 2008. 174

[8] S. Lee and G. C. Rutledge, "Plastic deformation of semicrystalline polyethylene by molecular simulation," *Macromolecules*, vol. 44, no. 8, pp. 3096–3108, 2011.

[9] J. M. Kim, R. Locker, and G. C. Rutledge, "Plastic deformation of semicrystalline polyethylene under extension, compression, and shear using molecular dynamics simulation," *Macromolecules*, vol. 47, no. 7, pp. 2515–2528, 2014. 174

Chapter 7

Résumé étendu

7.1 Introduction

Depuis le milieu du XXe siècle, l'activité humaine a fait grimper les températures et les niveaux de dioxyde de carbone à des vitesses sans précédent alors que la biodiversité disparaît au rythme d'une extinction de masse.

Des lois et des réglementations sont donc nécessaires pour réduire l'impact de l'homme sur le climat et la Nature. Les législateurs ont donc œuvré pour une réduction des émissions dans l'industrie du transport.

Une façon de concevoir des véhicules moins polluants est de réduire leur masse totale. Les matériaux composites peuvent donc être utilisés pour remplacer certaines pièces métalliques et obtenir ainsi des voitures plus légères. Loin d'être une solution miracle au problème du changement climatique, il s'agit là d'une petite contribution à un problème beaucoup plus complexe.

Cependant, les fournisseurs de matériaux et les constructeurs automobiles doivent avoir une bonne connaissance des propriétés mécaniques et de la durabilité de ces nouveaux matériaux composites. L'étude de l'évolution des propriétés mécaniques et de l'endommagement sous chargement répété constitue l'objet de ce qu'on appelle la fatigue des matériaux.

L'étude la fatigue a commence dans la deuxième moitié du XIXe siècle pour les matériaux métalliques et est souvent liée aux études menées par Rankine et Whöler après l'accident ferroviaire de Meudon en 1842. Par la suite, des catastrophes dues à la fatigue ont déclenché des recherches et menés à des progrès conséquents dans la compréhensions des phénomènes de durabilité.

Avec l'industrialisation des plastiques et des matériaux composites au cours du XXe siècle, de nouvelles études sur les propriétés mécaniques et la physique sous-jacente de cette nouvelle classe de matériaux étaient nécessaires.

Après les premiers travaux sur la fatigue des polyamides renforcés de fibres de verre courtes dans les années 1990 par Sato et Horst, plusieurs équipes de recherche ont contribué à ce domaine comme par exemple Bernasconi en Italie, Sonsino en Allemagne, Fatemi aux États-Unis, etc. En France, plusieurs thèses ont également été con-

sacrées à ce sujet, y compris les travaux de Ghorbel, Arif, Klimkeit, Despringre, Giraudeau, Rolland et Fouchier. De plus, comme il existe des similitudes entre les chargements de fluage et de fatigue, la communauté française peut s'appuyer sur les nombreux travaux réalisés sur l'étude du fluage des matériaux polymères, principalement au Centre des Matériaux des Mines ParisTech.

Ce travail de doctorat fait partie d'un projet de recherche plus large qui comprend deux autres thèses de doctorat de Caroline Goutal et Prashanth Santharam respectivement à l'Institut Pprime et à l'ENSTA Bretagne. L'approche de Goutal est centrée sur l'optimisation d'un critère énergétique pour la fatigue multiaxiale, tandis que le travail de Santharam suit une approche thermomécanique.

Ce projet est réalisé en collaboration avec un certain nombre de partenaires industriels, entre autres : Solvay Perfomance Polyamides (qui a financé cette recherche), Trelleborg Vibracoustic, e-Xstream engineering, PSA et Promold.

Ce travail vise à compléter la description et la compréhension existantes du comportement en fatigue et de l'endommagement des polymères thermoplastiques renforcés de fibres de verre courtes. Il se focalise sur l'étude d'un paramètre basé sur la vitesse de déformation comme indicateur pertinent de la durabilité sous chargement de fatigue.

Dans cette étude multi-échelles, nous commencerons par un état de l'art de la recherche existante. Nous aborderons ensuite la réponse macroscopique des échantillons lisses et entaillés afin d'établir un critère de durabilité basé sur le taux de déformation. En passant à l'échelle microscopique, nous ferons la lumière sur les mécanismes d'endommagement sphérolitiques et leurs similitudes avec les dommages par fluage statique, où la vitesse de déformation est connue pour déterminer la durabilité. Cette analyse sera complétée par la micro-modélisation afin de confronter l'évaluation expérimentale des dommages locaux avec les champs mécaniques locaux calculés. Enfin, nous conclurons ce travail par un certain nombre de perspectives pour les recherches futures.

Enfin, notons que ce manuscrit de thèse s'appuie sur plusieurs articles déjà publiés ou à paraître prochainement:

- Rolland, H., Saintier, N., **Raphael, I.**, Lenoir, N., King, A., & Robert, G. (2018). "In-situ fatigue damage mechanisms in short fibre reinforced PA66 as observed by synchrotron X-ray microtomography". *Composites Part B: Engineering*, 143, 217–229.
  https://doi.org/10.1016/j.compositesb.2017.12.051

- **Raphael, I.**, Saintier, N., Robert, G., Béga, J., & Laiarinandrasana, L. (2019). "On the role of the spherulitic microstructure in fatigue damage of pure polymer and glass-fiber reinforced semi-crystalline polyamide 6.6". *International Journal of Fatigue*, 126, 44–54.
  https://doi.org/10.1016/j.ijfatigue.2019.04.036

- **Raphael, I.**, Saintier, N., Rolland, H., Robert, G., & Laiarinandrasana, L. (2019). "A mixed strain rate and energy based fatigue criterion for short fiber

reinforced thermoplastics". *International Journal of Fatigue*, 127, 131–143. https://doi.org/10.1016/j.ijfatigue.2019.06.003

- **Raphael, I.**, Saintier, N., Robert, G. & Laiarinandrasana, L. "Fatigue properties of notched short glass fiber reinforced polyamide 6,6 specimens".

- **Raphael, I.**, Saintier, N., Rolland, H., Mareau, C., Robert, G., & Laiarinandrasana, L. "Micro-mechanical modeling of fatigue damage mechanisms in short fiber reinforced thermoplastic".

7.2 État de l'Art

7.2.1 Polyamide 6,6 renforcé

Développé par les équipes de recherche de DuPont en 1935 le polyamide 6,6 (PA66) est rapidement commercialisé sous le nom de Nylon. D'abord principalement connu sous forme de fibre, le PA66 est ensuite progressivement utilisé pour la réalisation de matériaux composites.

Le PA66 est un polymère semi-cristallin, les macro-molécules peuvent donc se trouver à l'état amorphe ou sous forme cristalline. L'organisation la plus couramment décrite pour les matériaux semi-cristallins est la sphérolite[1] : les lamelles cristallines sont organisées de façon radiale autour d'un noyau, d'où la cristallisation a débuté. Entre ces lamelles les chaînes polymères sont à l'état amorphe. Il s'agit donc de structures radiales, souvent décrites à partir d'observations 2D, mais dont la structure tridimensionnelle reste mal décrite.

L'essor des composites à matrice thermoplastique renforcée de fibre de verre courtes s'explique notamment par leur mise en forme par injection. Ce procédé de moulage permet des cadences de production élevées et la réalisations de pièces de géométries complexes. En préparation de l'injection la matrice polymère est fondue et mélangées aux fibres de verre courtes. La matière est ensuite injectée dans le moule pour former la pièce désirée.

On parle ici de fibres de verres *courtes* car leur longueur est sub-millimétrique, typiquement entre 50 et 500 μm. Le taux de renforts est souvent considéré comme un paramètre clé pour caractériser les matériaux composites. Dans notre cas la fraction de fibres est de 30% en masse. Cependant le taux de renforts ne suffit pas à caractériser notre matériau car les fibres ne sont pas orientées aléatoirement.

En effet, le procédé d'injection d'injection induit une microstructure caractéristique dans le matériau composite, usuellement décrite comme *cœur - peau*. Dans la peau

[1] La question de savoir si le nom *sphérolite* est masculin ou féminin revient assez régulièrement dans les manuscrits de thèse et les conférences francophones... Pour le Dictionnaire Larousse et l'Encyclopædia Universalis, le terme est masculin. Le Trésor de la langue française informatisé est moins clair sur la question. Pour ma part le féminin semble plus naturel - sûrement car on parle d'*une* sphère - et sera donc d'usage ici.

(appelée *shell* en anglais), qui représente la majeure partie de l'épaisseur d'une plaque injectée, les fibres courtes sont orientées dans la direction d'injection. À cœur (*core* en anglais) les fibres sont orientées perpendiculairement à cette direction. Le procédé de mise en force confère donc au matériau une forte anisotropie.

7.2.2 Propriétés mécaniques

Les propriétés mécaniques des thermoplastiques renforcés de fibres de verre courtes dépendent de nombreux paramètres, qui peuvent être schématisés sous forme de diagramme.

7.2.2.1 Anisotropie du matériau

Pour étudier l'anisotropie induite par l'injection des enchantions sont usuellement prélevés dans trois directions par rapport à la direction d'injection (0°, 45°, 90°). Plus cet angle d'orientation augmente, plus la raideur et la résistance mécanique à la traction (UTS) diminuent, les fibres ne jouant plus entièrement leur rôle de renfort. En revanche l'élongation à rupture est plus importante.

En fatigue, la durabilité diminue avec l'augmentation des angles d'orientation, une fois de plus car les fibres ne jouent plus entièrement leur rôle de renfort. L'orientation des fibres impacte aussi directement la propagation de fissure dans le composite. En effet échantillons renforcés à 0° et 90° mènent à une fissure quasi perpendiculaire à la direction de chargement, alors que pour les échantillons 45° la fissure suit l'interface des fibres et a donc un chemin incliné.

7.2.2.2 Chargement mécanique

Le chargement mécanique appliqué influe également directement sur les propriétés du matériaux.

Sous chargement de fatigue à rapport de charge positif, la contrainte moyenne a un effet majeur sur le matériaux visco-élastique à température ambiante. Une contrainte moyenne élevée réduit la tenue en fatigue du matériau. Il est à noter que sous chargement de fatigue à contrainte moyenne positive, la déformation moyenne augmente au cours de l'essai. Ce phénomène de *fatigue-fluage* sera détaillé plus loin.

La fréquence du chargement cyclique impacte également la réponse mécanique du matériau sensible à la vitesse de déformation. Cette influence est complexe. À haute fréquence la durabilité diminue à cause principalement de l'auto-échauffement du matériau. À basse fréquence l'essai devient dominé par les interaction fatigue-fluage ce qui entraîne également un auto-échauffement accru. Il existe donc une fréquence de chargement *optimale*, autour de 1-2Hz, maximisant la durabilité du matériau.

7.2.2.3 Effet de l'environnement

L'influence de l'environnement sur les propriétés mécaniques des thermoplastiques renforcés est aussi bien documentée.

Une augmentation de la température réduit la durabilité du matériau. La pente de la courbe S-N diminue avec l'augmentation de la température jusqu'à la température de transition vitreuse T_g. Au-delà de T_g la pente devient indépendante de la température.

Le PA66 est un matériau hydrophile. L'absorption d'eau cause un gonflement et une prise de masse du matériau. Une humidité relative élevée rend le matériau plus ductile et réduit sa durabilité en fatigue. Cependant le matériau humide est plus à même de ralentir la progression d'une fissure: l'énergie nécessaire à l'avance de la fissure est plus importante et la vitesse de propagation est inférieure

7.2.2.4 Influence de la taille des sphérolites

La taille des sphérolite dans le matériau semi-cristalline a aussi une influence sur les propriétés mécaniques du matériau.

Karger-Kocsis a étudié le PA6 dans différentes conditions de température et de vitesse à l'injection afin d'obtenir diverses caractéristiques microstructurelles du matériau. En effectuant des essais de propagation de fissures de fatigue, il a été suggéré qu'une augmentation de la taille des sphérulites améliore la résistance à la propagation mais augmente la vitesse de propagation une fois que la fissure se propage.

Il faut cependant noter que la taille des sphérolites n'était pas le seul paramètre à varier en fonction du changement des conditions d'injection : l'épaisseur relative de la couche de peau et la cristallinité ont également été modifiées. Toute conclusion doit donc être faite avec prudence. De plus, l'auteur fait remarquer qu'il est fort probable que la résistance à la propagation passe par un maximum en fonction à la fois de la cristallinité et de la taille de la sphérolite.

Un équilibre entre l'effet de la microstructure (les sphérolites plus grosses sont plus cristallines et donc plus résistantes) et l'effet des frontières (les sphérolites plus grosses obtenues à des vitesses de refroidissement plus lentes ont des frontières plus faibles en raison de la formation de cavités et de la ségrégation des impuretés, la déformation est donc moins accommodée par les sphérolites et plus par de l'endommagement intersphérolitique).

7.2.2.5 Effet d'entaille

Les pièces industrielles ont des géométries souvent complexes, contenant nombre d'hétérogénéités structurelles (trous, entailles, etc.) qui induisent des concentrations de contraintes et réduisent la tenue mécanique de la pièce. Les entailles peuvent être moulées ou usinées, dans ce dernier cas l'orientation des renforts n'est pas affectée par la présence de l'entaille.

Sonsino a étudié des échantillons entaillés de PA66GF35 sous chargement alterné (R=-1). Les entailles ont été moulés au centre de la longueur utile avec différents rayons (de 5 à 0.2 mm) induisant un facteur de concentration de contrainte K_T variant de 1 à 9.8. Plusieurs observations ont été faites :

- La durée de vie de l'article est réduite avec l'augmentation de la gravité de l'entaille (plus K_T).

- La sévérité de l'entaille a peu d'effet sur la pente des courbes S-N, contrairement à ce qui est habituellement rapporté pour les métaux.

- La pente de la courbe S-N reste constante (jusqu'à 10^7 cycles).

- La sensibilité à l'entaille devient presque imperceptible à haute température ($T = 130°$ C).

7.2.2.6 Fluage cyclique

Sous chargement de fatigue avec une contrainte moyenne positive, la déformation moyenne augmente avec le nombre de cycles appliqués. Dans la suite de ce travail, ce phénomène sera appelé *le fluage cyclique* et est essentiel pour comprendre la réponse mécanique des polymères sous chargement de fatigue.

Le tracé de la déformation moyenne par cycle - ou *déformation cyclique* - par rapport au nombre de cycles de chargement donne une courbe similaire à celle qui serait obtenue pour un essai de fluage. Cependant, il faut noter que la *vitesse de déformation cyclique* est beaucoup plus élevé qu'elle ne le serait pour un essai de fluage stationnaire à la même contrainte (moyenne). Les paramètres de chargement cyclique (amplitude de contrainte, fréquence, etc.) ont un effet direct sur le fluage cyclique.

Comme pour le fluage, trois étapes peuvent être définies. Pendant le fluage primaire, la déformation cyclique augmente rapidement jusqu'à ce que la vitesse de déformation cyclique devienne presque constante. Le fluage secondaire est alors atteint. C'est l'étape la plus longue, où la déformation cyclique augmente régulièrement avec les cycles de charge appliqués. Enfin, à mesure que la déformation se localise et que les dommages macroscopiques commencent à s'étendre dans le matériau, le fluage tertiaire est atteint. Cette étape est plus prononcée pour le polymère pur que pour le matériau composite où la déformation est limitée par la présence de fibres. La déformation cyclique augmente rapidement, jusqu'à la rupture finale de l'échantillon.

7.2.3 Calculs de durée de vie

Plusieurs approches pour le calcul de durée de vie en fatigue ont été proposées dans la littérature. Ces approches peuvent être réparties en plusieurs catégories suivant le type de paramètres mécanique sur lesquelles elles sont basées.

Les approches en contrainte basées sur des adaptations des critères usuels (Sines, Crossland, Dang Van) donnent des résultats peu précis.

Des bon résultats ont été obtenus avec des formulations plus complexes (critère de Tsai-Hill modifié par Bernasconi, critère en amplitude de contrainte par Fatemi), mais nécessite une dépendance explicite à l'orientation des fibres dans la microstructure.

Launay a essayé une approche basée sur un critère de Manson-Coffin modifié, et basé l'amplitude de la déformation visco-plastique. Les résultats obtenus ne sont que peu concluants, comme noté par les auteurs.

Les approche énergétiques sont le plus souvent basées sur l'énergie anélastique, déterminée comme l'aire de la boucle d'hystérésis. Ces approches donne de bon résultats surtout si elles sont réalisées dans un cadre (au moins) visco-élastique et qu'une correction est réalisée pour la prise en compte de la contrainte moyenne.

Les approches actuellement les plus prometteuses sont basées sur la vitesse de déformation cyclique en régime secondaire.

7.2.4 Mécanismes d'endommagement

En ce qui concerne l'endommagement dans le polymère lors des essais de traction quasi-statiques, des observations en microscopie en polarisation croisée et en microscopie électronique à transmission sur des coupes minces ont montré que " les régions équatoriales des sphérolites sont particulièrement sensibles aux mécanismes de microcavitation.

La transition ou la concurrence entre les différents types de micro-mécanismes (glissement de chaîne, démêlage, cavitation, plasticité cristalline, fragmentation des lamelles) est complexe. La complexité provient de l'échelle d'étude et de la complexité de la structure sphérolitique où se déroulent ses phénomènes.

Pourtant, il est maintenant établi que la nano-cavitation est induite par la présence locale d'un état de contrainte triaxial et que des cavités micrométriques plus grandes sont ensuite développées lorsque la structure lamellaire est transformée en une structure fibrillaire.

La fissuration est une transition entre l'apparition de dommages et la croissance de microfissures et est largement décrite dans la littérature d'un point de vue expérimental ainsi que théorique. La fissuration se produit lorsque des chaînes de polymères amorphes s'orientent sous la contrainte appliquée. Le glissement peut alors se produire dans les lamelles cristallines, ainsi que la scission en chaîne ou le démélage. Les ponts se brisent progressivement et l'endommagement progresse, jusqu'à devenir une fissure qui finira par mener à la défaillance.

Les premiers marqueurs d'endommagent en fatigue, tels que la cavitation et les microfissures, ont été étudiés dans le polymère pur dans trois travaux antérieurs qui ont tenté de relier ces marqueurs de dommages avec la microstructure sphérolitique du polymère.

Le premier concerne le travail antérieur de Andrews et Walker concernant la rupture par fatigue dans le PE sous faible fréquence de charge (0.01-1Hz). Ils ont observé des coupes d'échantillons endommagés et ont rapporté "de courtes fissures s'étendant en ligne droite sur des distances comparables à la taille de la sphérolite et fréquemment le long des limites entre sphérolites".

Plus tards Bretz suggère que les polymères semi-cristallins se fracturent à la fois de manière intersphérolitique et intrasphérolitique (aussi appelé *trans-sphéroliitique* par les auteurs). Les auteurs ont effectué des essais de fatigue uniaxiale à $10Hz$, mais les conditions de charge précises ne sont pas claires. La qualité des images n'est pas suffisamment détaillée pour tirer des conclusions définitives et, comme l'ont fait

remarquer les auteurs eux-mêmes, il reste encore beaucoup à faire dans ce domaine.

Plus récemment, les travaux de Mourglia-Seignobos se sont concentrés sur l'initiation des dommages à l'échelle nano- et microscopique, au sein du polymère semi-cristallin. À l'aide de mesures SAXS, Mourglia-Seignobos a signalé la présence de cavitation dans des domaines orientés perpendiculairement à la contrainte. Les auteurs suggèrent que ce dommage est un *très probablement* situé dans le plan équatorial des sphérolites, entre les lamelles cristallines.

Lors d'un chargement de traction uniaxial quasi-statique sur le matériau composite, il est possible d'observer des cavités et des endommagements dans le matériau par tomographie in-situ.

Quatre mécanismes principaux ont été décrits dans la littérature :

- **L'endommagement en bout de fibre** est le principal type de dommage. Elle s'explique à la fois par le manque d'adhérence entre le polymère et le verre, et par le fait que la fibre agit comme un concentrateur local de contraintes. Il en résulte une croissance précoce et continue des dommages dans ces zones, jusqu'à la défaillance finale.

- **La rupture de fibre** est aussi un type de dommage majeur lors d'un chargement quasi statique. Environ les deux tiers des fibres finissent par se briser pendant le chargement. La rupture se produit préférentiellement aux points de croisement entre les fibres, où les concentrations de contraintes sont importantes. Il est à noter que des fibres à 90° peuvent même se rompre transversalement à la direction de la charge de traction, sur toute leur longueur.

- **La décohésion** à l'interface fibre-matrice se produit assez tard pendant le test. Elle est probablement déclenchée par une concentration locale de contraintes due au confinement de la matrice polymère. Le décollement peut ensuite progresser le long de l'interface.

- **L'endommagement matriciel** dans la majeure partie du matériau s'initie à partir des autres mécanismes de dommage mentionnés ci-dessus et peut atteindre de grands volumes, la plupart du temps avec une forme sphérique, jusqu'à la défaillance de l'échantillon.

Les mécanismes d'endommagement en fatigue du composite ont longtemps été décrits à l'aide d'observations MEB post-mortem. Cela a permis Sato et plus tard Horst d'identifier un premier scénario de dommages :

- Les dommages s'amorcent aux extrémités des fibres.

- Le micro-endommagement progresse le long de l'interface fibre-matrice.

- Des bandes de déformation plastique apparaissent dans la matrice polymère.

- Les fissures s'ouvre et progresse lentement.

- Propagation rapide des fissures conduisant à une défaillance complète.

Ces observations ont été plus récemment étayées et complétées par des données tomographiques, donnant accès à des données quantitatives dans le matériau. Les mécanismes élémentaires se produisant pendant la fatigue du PA6.6 renforcé de fibres de verre courtes a été mise en évidence : rupture de la fibre, decohesion ou endommagement aux extrémités de la fibre et dommages de la matrice (cavitation, fibrillation et formation de fissures).

Les essais in-situ par tomographie synchrotron à rayons X à haute résolution ont été particulièrement utiles pour étudier les tout premiers stades de l'endommagement par fatigue et établir la séquence complète menant à la défaillance finale. En particulier, la cavitation de la matrice a joué un rôle majeur dans l'apparition des dommages dus à la fatigue dans la majeure partie du matériau.

Le processus de cavitation se développe dans deux types de régions :

- Il s'agit de zones fortement renforcées où la présence de fibres tassées induit des champs de contraintes triaxiales élevées.
- Il s'agit de zones peu renforcées où les niveaux de déformation peuvent être plus élevés, ce qui permet d'augmenter la déformation de la matrice.

Il a été conclu que le contrôle du comportement de cavitation du polymère peut conduire à une amélioration significative des propriétés de fatigue du matériau composite.

7.3 Approfondissement des mécanismes d'endommagement

La description usuelle des mécanismes d'endommagement en fatigue dans les polyamides renforcés est complétée avec de nouvelles observations en micro-tomographie et microscopie électronique à balayage (MEB). L'accent est notamment mis sur la compréhension des mécanismes d'endommagement dans la matrice polymère et des essais sont donc également réalisés sur des échantillons de PA66 purs.

7.3.1 Endommagement sphérolitique

Les observations tomographiques réalisés lors d'essais de fatigue in-situ montrent une progression de l'endommagement dans la matrice avec une longueur caractéristique de $25 - 30\mu m$. Cette longueur correspondant à la taille des sphérolites dans le matériau, l'hypothèse avait été faite que ces mécanismes d'endommagement étaient liés à la microstructure semi-cristalline.

Des analyses complémentaires de ces données de tomographie permettent de montrer que l'endommagement progresse sous forme de disques plats, d'un diamètre de $25 - 30\mu m$, qui s'ouvrent en pointe de fissure pour permettre l'avance de celle-ci. Ces structures d'endommagement peuvent être retrouvées à la fois dans le matériau composite et dans le polymère non renforcé. Ces observations suggèrent une ouverture des sphérolites dans leur plan équatorial sous l'effet du chargement de fatigue.

Des observations complémentaires au MEB réalisées sur les faciès de rupture permettent d'avoir la résolution nécessaire pour confirmer ce scénario. En effet sur ces faciès les marques des structures sphérolitiques peuvent être reconnues sur le trajet de la fissure de fatigue. On observe ainsi un ensemble clairement les sphérolites ouvertes en deux par la fissure de fatigue. Cette ouverture a lieu dans le plan équatorial de la sphérolite, on peut en effet clairement observer le noyau -structure centrale de la sphérolite- sur le faciès de rupture.

Des essais complémentaires sont réalisés: une fois que la fissure de fatigue commence à propager l'essai est interrompu et suivi d'une cryo-fracture, le faciès étant ensuite observé au MEB. En amont du front de fissure de fatigue on peut nettement observer une sphérolite déjà ouverte au moment de la cryo-fracture, sa structure est donc quasi-intacte.

D'autres fractographies montrent de plus que cet endommagement a non seulement lieu en amont du front de fissure mais qu'il est progressif à partir du noyau au centre de la sphérolite se fait alors de manière radiale jusqu'à ouverture complète de la structure dans son plan équatorial. Ces dernières observations permettent donc d'établir un scénario d'endommagement en fatigue pour les polymères semi-cristallins.

7.3.2 Structure de la sphérolite orientée

La structure sphérolitique est souvent décrite comme étant une structure purement radiale. Ces constats sont essentiellement basées sur des observations réalisées sur des films minces.

En réalité la compréhension de la structure tri-dimensionnelle des sphérolites reste fortement incomplète, qui plus est sur le matériau industriel, issus du procédé d'injection.

En se servant de la rupture en fatigue comme d'un *outil* pour permettre l'observation des sphérolites, des fractographies ont été réalisées après rupture par fatigue sur des échantillons de PA66 purs prélevés à différentes orientations par rapport à la direction d'injection. En observant le noyau de sphérolites sur les faciès de rupture on observe alors nettement que pour les échantillons à 0° il apparait comme un disque alors que pour les échantillons à 90° il apparait comme un "rectangle". Le noyau a donc une forme cylindrique, orientée dans le sens de l'injection.

On peut donc en déduire le scenario suivant pour la formation des structures semi-cristallines dans les thermoplastiques injectés. Lors de l'injection, une parties des chaines polymères sont étirées dans la direction de l'écoulement. Ces chaines sont localement alignées et constituent les structures pré-sphérolitiques. Lors du refroidissement, les sphérolites croissent ensuite radialement autour de ces noyaux fortement orientés.

Ces *sphérolites orientées* sont donc des structures intermédiaires entre les sphérolites purement radiales usuellement décrites et les shish-kebab unidirectionnels.

7.3.3 Retour au matériau composite

Les fractographies réalisées sur le matériau composite après rupture par fatigue permettent également d'observer les structures sphérolitiques. Cela confirme le scenario pour le matériau renforcé. Les observations sont cependant moins évidentes que pour le PA66 pur car les fibres ont un diamètre proche de la taille des sphérolites. De plus, la proximité entre les fibres rend probablement la structure tridimensionnelle des sphérolites plus complexe et donc plus difficile à observer sur les faciès.

7.4 Échelle Macroscopique

7.4.1 Critère mixte

Sous chargement cyclique à charge imposée, la déformation moyenne augmente tout au long de l'essai. Cet effet existe quelle que soit la durée de vie ou l'orientation des fibres. Un critère basé sur la vitesse de déformation cyclique s'est avéré efficace pour unifier dans une certaine mesure les résultats de fatigue. La durée de vie a été estimée à partir du taux de déformation cyclique au milieu de la durée de vie en fatigue :

$$N_f = A \left(\frac{\dot{\varepsilon}_{cycl}}{\dot{\varepsilon}_0} \right)^n \tag{7.1}$$

Ce critère s'est avéré efficace pour unifier les résultats de fatigue pour des échantillons provenant de différentes positions sur une plaque injectées, pour différentes températures d'essai, pour différentes fréquences de chargement et pour toutes les orientations de fibres et une large gamme de rapports de charge positifs.

Bien qu'il donne de très bons résultats pour des rapports de charge positifs, ce critère basé sur le taux de déformation cyclique est beaucoup moins précis quand il s'agit des rapports de charge négatifs. Le but de cette section est de proposer une version améliorée du critère afin d'améliorer encore la qualité de sa prédiction.

Le critère fondé sur la vitesse de déformation cyclique de l'équation est moins précis pour les rapports de charge négatifs. Cependant, il a été démontré que l'énergie anélastique W_{an} est un paramètre unifiant les résultats pour ces rapports de charge. En étudiant le nombre de cycles à rupture en fonction de la vitesse de déformation cyclique et de l'énergie anélastique nous pouvons distinguer deux régimes :

- pour les rapports de charge positifs, la durabilité est principalement déterminée par la vitesse de fluage cyclique.
- pour des rapports de charge négatifs, en raison de l'amplitude élevée des contraintes, le comportement dissipatif devient dominant. La durée de vie en fatigue est alors principalement déterminée par un paramètre énergétique.

Il convient de noter que le présent travail porte sur les rapports de charge positifs allant jusqu'à 0,7. Un rapport de charge égal à 1 correspondrait à un essai de fluage statique et n'est pas traité ici.

Dans une première approche, nous considérons que chacun de ces régimes ne dépend que d'un seul paramètre ($\dot{\varepsilon}_{cycl}$ or W_{an} respectivement). Ces deux régimes sont donc définis par :

$$N_f^I = A\left(\frac{\dot{\varepsilon}_{cycl}}{\dot{\varepsilon}_0}\right)^n \tag{7.2}$$

$$N_f^{II} = B\left(\frac{W_{an}}{W_0}\right)^m \tag{7.3}$$

Les paramètres A et n (resp. B et m) sont déterminés par ajustement des données expérimentales pour les rapports de charge positifs (resp. négatifs).

Une fonction de pondération f est introduite pour permettre un passage continu d'un domaine à l'autre :

$$f = \frac{1}{2}\left\{1 + \tanh[\gamma(\alpha_0 - \alpha(\dot{\varepsilon}_{cycl}, W_{an}))]\right\} \tag{7.4}$$

avec $\alpha_0 = \left(\frac{B}{A}\right)^{\frac{1}{n}}$ et:

$$\alpha(\dot{\varepsilon}_{cycl}, W_{an}) = \frac{\dot{\varepsilon}_{cycl}}{\dot{\varepsilon}_0}\left(\frac{W_{an}}{W_0}\right)^{-\frac{m}{n}} \tag{7.5}$$

Le paramètre α_0 indique la limite entre les deux régimes. Les valeurs pour m et n font l'objet d'un processus d'optimisation. Le paramètre γ détermine la vitesse de transition entre les deux régimes.

Nous pouvons alors déterminer le nombre de cycles à rupture par :

$$N_f = (1-f)\cdot A\left(\frac{\dot{\varepsilon}_{cycl}}{\dot{\varepsilon}_0}\right)^n + f\cdot B\left(\frac{W_{an}}{W_0}\right)^m \tag{7.6}$$

Les paramètres A, n, B et m sont optimisés pour minimiser l'écart entre le N_f estimé et le N_f expérimental sur l'ensemble des données. À noter que les valeurs de α_0 et α sont mises à jour pendant le processus d'optimisation avec les valeurs correctes des paramètres n et m. Ceci donne, pour $\gamma = 10^4$:

$$A = 0.851,\ n = -0.660$$
$$B = 123.9,\ m = -3.247$$

L'amélioration notable de la prédiction pour tous les rapports de charge a été possible avec le critère mixte, permettant de prendre en compte le comportement dissipatif du matériau sous de fortes amplitudes de contrainte. Ce critère donne des résultats particulièrement en accords avec les données expérimentales. Maintenant que les mécanismes d'endommagement en régime de fluage cyclique sont bien compris, il serait intéressant d'étudier les mécanismes d'endommagement du régime dissipatif. Cela pourrait étayer l'utilisation d'un critère mixte correspondant à deux mécanismes.

7.4.2 Étude expérimentale des éprouvettes entaillées

Les pièces industrielles ont des géométries complexes comprenant des hétérogénéités structurelles (entailles, trous, etc.). Leur prise en compte passe donc par l'établissement d'un critère de durabilité *local*.

Des mesures expérimentales de la vitesse de déformation cyclique sont réalisée par corrélation d'image. La prise d'image est cadencée avec la machine d'essai afin de photographier l'échantillon à intervalles réguliers, au sommet d'un cycle de charge.

L'analyse du profil de vitesse de déformation cyclique entre les entailles à mi-durée de vie fournit quelques informations supplémentaires :

- La longueur affectée par le fluage cyclique est d'environ 1,5 mm à partir de la racine de l'entaille.
- La géométrie de l'encoche a peu d'effet sur cette longueur (fig. 4.19(a)).
- L'orientation des fibres et le chargement ont peu d'effet sur cette longueur.

Un critère *non-local* est proposé avec pour objectif d'unifier les résultats de fatigue en utilisant les paramètres identifiés sur éprouvettes lisses :

$$N_f = A_{smooth} \left(\frac{\dot{\varepsilon}_{VMm}}{\dot{\varepsilon}_0} \right)^{n_{smooth}} \tag{7.7}$$

avec donc les paramètres suivants:

$$A_{smooth} = 1.29 \text{ and } n_{smooth} = -0.674$$

et avec $\dot{\varepsilon}_{VMm}$ la déformation cyclique non-locale équivalente calculée avec :

$$\dot{\varepsilon}_{VMm} = \frac{1}{R} \int_0^R \dot{\varepsilon}_{VM}(s) ds \tag{7.8}$$

avec la distanc R=1.5mm basée sur les données présentes en fig. 4.20, et:

$$\dot{\varepsilon}_{VM} = \frac{\partial \varepsilon_{VM}}{\partial N} \tag{7.9}$$

avec ε_{VM} la valeur de la déformation équivalente de von Mises moyenne par cycle durant le stade de fluage secondaire.

Ce critère a donné de bons résultats, la plupart des points de données étant inclus entre deux bandes de dispersion de facteur deux. L'estimation est moins précise (mais conservative) pour les deux points à des durées de vie en fatigue plus élevées ($N_f \approx 10^5$). Cela pourrait s'expliquer par la très faible déformation cyclique qui rend la mesure expérimentale par corrélation d'image moins précise.

7.4.3 Modélisation par Éléments-Finis

7.4.3.1 Le modèle

Le modèle utilisé par Boisot pour modéliser le fluage du PA11 est également utilisé dans ce travail.

Le matériau est supposé elasto-visco-plastique, avec la partition usuelle de la déformation totale $\underline{\underline{\varepsilon}}$:

$$\underline{\underline{\varepsilon}} = \underline{\underline{\varepsilon}}^e + \underline{\underline{\varepsilon}}^{vp} \tag{7.10}$$

avec $\underline{\underline{\varepsilon}}^e$ la déformation élastique $\underline{\underline{\varepsilon}}^{vp}$ la déformation visco-platique. La déformation viscoélastique est négligée en tant que contribution indépendante à la déformation totale (autrement, un quatrième terme serait ajouté à l'expression eq. (7.10)).

La vitesse de déformation plastique est calculée par une loi de Norton :

$$\dot{p} = \dot{\varepsilon}_0 \left(\frac{\phi}{K} \right)^n \tag{7.11}$$

avec $\varepsilon_0 = 1s^{-1}$. Le paramètre K (MPa) contrôle l'intensité du taux de déformation plastique, n contrôle la non-linéarité du comportement visco-plastique et ϕ est la surface de charge définie par :

$$\phi = \sigma_* - \sigma_y(p) \tag{7.12}$$

avec σ_* la contrainte effective (fonction de la fraction de vide dans le matériau, et égale à la contrainte de von Mises s'il n'y a pas de porosité - voir eq. (1.25) dans section 1.5.2.2) et $\sigma_y(p)$ la limite élastique du matériau.

$\sigma_y(p)$ est définie avec un modèle d'écrouissage isotrope:

$$\sigma_y(p) = \sigma_0 + Q\,(1 - \exp(-bp)) \tag{7.13}$$

Plusieurs paramètres doivent donc être identifiés :

- paramètres pour le comportement élastique linéaire : le module de Young E et le coefficient de Poisson ν.
- paramètres de la loi de Norton pour le comportement visqueux : K et n.
- paramètres du modèle d'écrouissage isotrope : σ_0, Q et b.

L'identification des paramètres est d'abord effectuée pour des échantillons de PA66 purs en utilisant un algorithme génétique sur des essais quasi-statiques à $\dot{\varepsilon} = 10^{-2}s^{-1}$ et $\dot{\varepsilon} = 10^{-3}s^{-1}$ afin d'obtenir de bonnes prédictions de la courbe contrainte-déformation et de l'ouverture d'entaille.

Un protocole similaire a été suivi pour le matériau composite. Un modèle simple *trois couches* a été utilisé pour représenter la microstructure Peau-Cœur-Peau (fig. 4.23(b)).

Les paramètres ont été considérés identiques pour une phase donnée (ex. pour la phase 0°), qu'il s'agisse de la peau ou du cœur de l'échantillon.

Les paramètres de la phase 0° ont d'abord été identifiés à l'aide d'essais expérimentaux effectués sur un échantillon 0° (contenant donc un cœur à 90°). La contribution mécanique du cœur à 90° a été négligée. Les paramètres de la phase 90° ont ensuite été identifiés à l'aide des essais expérimentaux effectués sur un échantillon 90° (contenant donc un cœur à 0°).

Les résultats sont satisfaisants dans les deux cas.

7.4.3.2 Vitesse de déformation cyclique et critère

L'objectif est ensuite d'identifier un modèle capable de donner une valeur précise pour la vitesse de déformation cyclique sous chargement cyclique. Les paramètres identifiés pour le chargement quasi-statique sont ajustés avec pour but l'obtention d'une valeur correcte pour la vitesse de déformation axiale cyclique.

Cependant afin d'obtenir un critère de durabilité basé sur la vitesse de déformation applicable à des géométries complexes, notre modèle doit fournir des valeurs précises pour la vitesse de déformation cyclique locale pendant le fluage cyclique secondaire.

En traçant les champs de vitesse de déformation cyclique locale issus du calcul en surface des échantillons, on montre que l'estimation réalisée par le modèle est correcte. L'évaluation de la précision des champs mécaniques calculés pour l'intérieur du matériau est difficile, notamment sur le matériau composite. En effet il faudrait des données expérimentale de comparaison ; ces dernières pourraient être issues de corrélation d'image volumique bien que cela soit peu trivial pour des données de fatigue.

L'estimation des vitesses de déformation cyclique étant correcte, le critère introduit en eq. (7.8) peut être appliqué sur les résultats de la modélisation Éléments-Finis.

La vitesse de déformation cyclique non locale de von Mises a été déterminée en surface de l'éprouvette après 1000 cycles de chargement calculés. Le nombre estimé de cycles à rupture N_f a ensuite été calculé en utilisant le critère eq. (7.8). Cela a donné les courbes S-N qui peuvent être comparées aux courbes expérimentales présentées sur fig. 4.38(a).

À N_f faible, les prédictions sont relativement précises et dans une bande de dispersion de facteur 2 par rapport aux données expérimentales (fig. 4.38).

Cependant, pour des durées de vie plus longue (par exemple $N_f > 10^4$), la prédiction devient moins précise car le modèle sous-estime le nombre de cycles à rupture. Ceci pourrait être dû au fait que le critère a été appliqué après 1000 cycles de charge calculés, ce qui apparaîtrait comme était trop tôt dans la durée de vie de ces éprouvettes. La vitesse de déformation cyclique est beaucoup plus élevé après 1000 cycles qu'à mi-vie et le N_f estimé basé sur ces vitesses trop élevées est donc trop faible.

La même explication pourrait être donnée pour le modèle qui surestime la durabilité pour les faibles N_f (ex. pour les éprouvettes non renforcées U0.5). Dans ce cas, après 1000 cycles calculés, la vitesse de déformation peut être inférieur à celui à mi-vie, ce qui donne une valeur estimée de N_f plus élevée que prévu.

Deux approches pourraient mener à de meilleurs résultats. Premièrement, l'étude de la vitesse de déformation cyclique au cours de la première étape du chargement pourrait conduire à un critère de durabilité établi dès les premiers cycles appliqués. Pour ce faire, il faudrait toutefois modéliser correctement l'évolution de la vitesse de déformation cyclique pendant le régime transitoire. Deuxièmement, le comportement du matériau pourrait être identifié durant le régime secondaire stabilisé. L'utilisation de ce comportement stabilisé pourrait donner directement accès à la vitesse de déformation cyclique en régime secondaire sans pour autant calculer tous les cycles de charge. Ces deux perspectives pourraient en fin de compte réduire considérablement le temps de calcul et ainsi rendre ce critère plus facilement applicable pour les pièces industrielles

de grande tailles ou à géométries complexes.

7.4.3.3 Modèle GTN

Afin de modéliser la perte des propriétés mécaniques sous chargement mécanique, un modèle d'endommagement peut être ajouté à la simulation numérique. Comme la cavitation s'est avérée être le précurseur de nombreux autres types de mécanismes d'endommagement par fatigue, l'introduction d'un modèle d'endommagement par cavitation est cruciale.

Plusieurs de ces modèles et variantes existent dans la littérature et Boisot a fourni une analyse détaillée du développement progressif de ces travaux depuis la fin des années 1960.

Le modèle GTN est basé sur le travail original de Gurson sur une cavité sphérique unique dans une matrice plastique. Le critère original a ensuite été modifié par Tvergaard et Needleman afin de tenir compte de l'interaction entre plusieurs vides et la croissance de ces vides.

Ceci donne le critère suivant, tel qu'implémenté dans le code éléments-finis ZéBuLoN :

$$\Phi(\underline{\underline{\Sigma}}, f_*, \sigma_*) = \frac{\Sigma_{eq}^2}{\sigma_*^2} + 2q_1 f \cosh\left(\frac{q_2 \Sigma_{kk}}{2\sigma_*}\right) - 1 - q_1^2 f^2 = 0 \tag{7.14}$$

Avec Σ_{eq} l'équivalent macroscopique du stress de von Mises, Σ_{kkk} la trace du tenseur de stress macroscopique, et f la porosité. L'identification des paramètres q_1 et q_2 est entièrement empirique et varie selon les auteurs.

L'équation eq. (1.25) définit σ_*, la contrainte effective scalaire, en fonction de la porosité et de la contrainte macroscopique.

Ceci donne l'expression de la surface de charge ϕ en fonction de σ_*, et la limite d'élasticité de la matrice σ_y :

$$\phi = \sigma_* - \sigma_y(p) \tag{7.15}$$

avec σ_* la contrainte effective (fonction de la fraction de vide dans le matériau, et égale à la contrainte de von Mises en l'absence de porosité - voir eq. (1.25)) et $\sigma_y(p)$ la limite élastique du matériau.

$\sigma_y(p)$ est définie à l'aide d'un modèle d'écrouissage isotrope :

$$\sigma_y(p) = \sigma_0 + Q\,(1 - \exp(-bp)) \tag{7.16}$$

Les premiers résultats semblent montrer un bon accord entre la localisation de l'endommagement calculée dans le polymère pur et celle issue des observations tomographiques. Ces observations restent compliquées en fatigue car les cavités sont de très faibles tailles (inférieure ou proche de celle des voxels). Les comparaisons sont pour le moment qualitatives mais semblent prometteuses.

7.5 Échelle Microscopique

7.5.1 Calculs FFT

7.5.1.1 Mise en place

Afin d'effectuer des calculs FFT, la microstructure doit être correctement segmentée à partir de données tomographiques. Pour cette segmentation, les données tomographiques sont d'abord rééchantillonnées à partir d'une résolution voxel de 0,65 μm à 1,1 μm ou 1,3 μm.

Une première segmentation grossière des fibres est réalisée en appliquant successivement un filtre médian 3D, trois fois, afin de lisser l'image parfois buitée, et un seuil de 35000 sur les niveaux de gris, ne conservant que les valeurs élevées correspondant aux fibres de verre plus denses.

L'étape finale consiste à s'assurer que chaque fibre était segmentée avec précision. Ceci a été fait en séparant manuellement les fibres dans les régions où elles étaient en contact ou trop près pour être séparées par la valeur de seuillage. Cette étape, bien que longue, était nécessaire pour obtenir une microstructure représentative dans les régions où le confinement des fibres est le plus élevé, d'autant plus que ce sont ces régions qui sont les plus sujettes à l'initiation de l'endommagement.

Le choix d'une région d'intérêt (ROI) pour effectuer une modélisation micro-mécanique est dicté par plusieurs facteurs. Tout d'abord, des endommagements doivent être vus à l'intérieur du ROI sur les scans de tomographie effectué pendant la durée de vie en fatigue. De plus, le ROI segmenté doit être suffisamment important pour être représentatif de la microstructure locale qui a causé les dommages observés. Enfin, le volume doit être suffisamment petit pour que les simulations puissent être effectuées à l'aide de ressources informatiques raisonnables et dans un délai acceptable.

En conséquence, chaque volume segmenté était un cube de 119 à 140 voxels de côté, contenant environ 100 segments de fibres. Les calculs ont duré environ 40 heures chacun.

Pour calculer les champs mécaniques locaux à l'aide d'un algorithme FFT, le volume doit être périodique. Comme une microstructure réelle segmentée n'est pas périodique, le volume est enfermé dans une boîte plus grande en ajoutant une couche homogène englobante, de 20 voxels d'épaisseur, sur les six côtés du cube segmenté. Cette couche tampon supplémentaire est homogène et isotrope. Cela donne un volume cubique total de 154 μm à 208 μm, contenant jusqu'à 4 096 000 voxels.

L'identification des paramètres des modèles de comportement est réalisée de manière directe sur des essais quasi-statiques à vitesse de déformation imposée à $\dot{\varepsilon} = 10^{-4}s^{-1}$. Les paramètres de chaque phase (fibre, matrice et couche homogène) sont identifiés indépendamment. Il est à noter qu'une identification par une méthode inverse sur le matériau composite est également théoriquement possible. Cependant, il faudrait effectuer plusieurs calculs de microstructure pour chaque itération dans la boucle d'optimisation. Mais comme chaque calcul de microstructure prend au moins 30 heures, la méthode inverse n'est guère appropriée dans notre cas.

7.5.1.2 Champs mécaniques dans la matrice

La distribution des champs mécaniques locaux dans la matrice peut être étudiée pour différentes orientations de fibres et d'humidité relative (RH).

A contrainte macroscopique imposée donnée, la distribution des contraintes de von Mises est directement influencée par le RH. Plus le RH est faible, plus l'écart-type est faible et plus la valeur moyenne est élevée. L'influence de l'orientation des fibres est minimale, sauf à 0° où la distribution est plus plate et plus étalée. Dans ce dernier cas, pour une microstructure à 0° à RH50 et RH80, un petit pic à la limite supérieure de la distribution peut être remarqué. Les voxels ici sont situés près des pointes des fibres. A une macro-déformation donnée, ces voxels sont déjà chargés à la valeur maximale. Cette valeur *saturation* est directement liée au modèle de la matrice.

La distribution de contrainte hydrostatique est influencée à la fois par l'humidité relative et l'orientation des fibres. Pour une orientation donnée des fibres, plus le RH est faible, plus l'écart-type est faible et plus la contrainte hydrostatique moyenne est élevée. À RH donné, la valeur moyenne de la contrainte hydrostatique est plus élevée pour les spécimens de 90° que pour ceux de 45° et 0°. Cependant, les distributions sont beaucoup plus dispersées pour les spécimens à 0°.

Contrairement à la contrainte de von Mises, la distribution du taux de triaxilité est principalement influencée par l'orientation des fibres. Pour les échantillons de 90°, l'écart-type est plus faible et la valeur moyenne est plus élevée que pour les échantillons de 45° et de 0°. L'influence du RH est minime entre les échantillons RH50 et RH80. Pour les échantillons RH0, l'écart-type est plus faible. Cependant, aucune tendance claire ne peut être observée pour la valeur moyenne.

7.5.1.3 Principaux mécanismes d'endommagement

La rupture des fibres a longtemps été négligée en tant que mécanisme d'endommagement se produisant avant les tout derniers stades de la rupture par fatigue. Cependant, des études récentes basées sur des données tomographiques suggèrent que certaines fibres se cassent tôt dans la vie du matériau. Il est donc important de mieux comprendre pourquoi et où les fibres se cassent.

La contrainte principale maximale est tracée le long de l'axe central d'une fibre alignée avec la direction de chargement. Les niveaux de gris le long de son axe central sur l'image tomographique sont également tracés afin d'obtenir la position de la rupture marquée par une forte baisse des niveaux de gris (fig. 5.7). En les comparant les courbes, on observe que la rupture de la fibre s'est produite dans une zone de contrainte maximale. La présence de la fibre $n°2$ croisant la fibre $n°1$ induit une concentration de contrainte dans la matrice polymère et dans la fibre.

Deux informations principales peuvent être déduites de ces résultats :

- La modélisation micro-mécanique peut simuler la concentration de contraintes se produisant dans les fibres et conduisant à la rupture des fibres.
- La concentration de contrainte dans une fibre est induite par la proximité des fibres voisines. Ceci souligne l'importance de tenir compte d'un volume représentatif lors de la modélisation d'une microstructure.

La fibrillation des thermoplastiques amorphes se développe perpendiculairement à la déformation normale la plus élevée. De nombreux critères de fissuration peuvent être trouvés dans la littérature. Celle utilisée dans cette étude a été calculée comme proposé par Argon et Hannoosh. Il s'agit d'un critère local en contrainte. On observe une bonne corrélation entre le critère et les endommagement observés expérimentalement.

7.5.1.4 Cas de la cavitation

La cavitation dans la matrice thermoplastique est l'un des premiers signes d'endommagement du matériau lors d'un chargement de fatigue. Ces petits vides peuvent être détectés dans les données tomographiques s'ils ont un diamètre supérieur au micron.

On sait que des cavités se forment en phase amorphe, entre lamelles cristallines, sur le plan équatorial des sphérolites. Les volumes sujets à la formation de cavités sont habituellement séparés en deux catégories :

- Dans des volumes très confinés et le long des fibres de verre, où le rapport de triaxialité de contrainte est plus élevé.
- Dans les volumes mal renforcés, où la déformation de la matrice est plus importante.

Nous avons calculé l'incrément de déformation cyclique $\frac{\Delta\varepsilon_{11}}{\Delta N}$ à chaque cycle et pour chaque voxel du volume, un paramètre qui est connu pour être clé dans l'évaluation de la vie en fatigue à l'échelle macroscopique.

On montre ainsi que les cavités semblent se former principalement dans les zones où l'incrément maximal de déformation cyclique est le plus élevé, que ce soit à proximité d'une fibre ou dans une région peu renforcée. Cependant quelques cavités ne semblent pas obéir à cette règle, il peut s'agir de cavités formées lors du processus d'injection et déjà présentes dans la matière vierge ou de cavités formées sur des défauts de la matrice non pris en compte dans notre modélisation.

7.5.2 Calculs Éléments-Finis

7.5.2.1 Mise en place

La modélisation par éléments finis a été réalisée pour fournir un aperçu supplémentaire sur les résultats fournis par le calcul FFT, principalement par l'utilisation d'un modèle mécanique des milieux poreux pour la matrice polymère.

Le protocole de segmentation était un peu différent de celui décrit pour FFT. L'algorithme d'apprentissage machine de Weka a été entrainer pour séparer efficacement les fibres, donnant en beaucoup moins de temps des résultats comparables à ceux qui auraient été obtenus par segmentation semi-automatique. Une couche homogène est également utilisée autour du volume d'intérêt afin de réduire les effets de bord. Une fois segmenté, le maillage 3D est réalisée en utilisant Gmsh.

Les ROI sont des cubes, $120\mu m$ par côté, contenant chacun environ 150.10^3 éléments tétraédriques linéaires à quatre noeuds (c3d4). Bien que cela donne un maillage assez

grossier, cela permet d'effectuer des calculs cycliques dans un délai raisonnable (p. ex. environ deux cycles de charge calculés par heure).

Comme dans le cas de la FFT, on fait l'hypothèse que les paramètres identifiés à l'échelle macroscopique sur spécimens entiers sont valides à l'échelle microscopique. Le modèle de comportement élasto-visco-plastique et le modèle d'endommagement GTN utilisés ici sont donc les mêmes que ceux identifiés pour le PA66.

Pour la modélisation par éléments finis, un chargement cyclique sinusoïdal est imposé à la microstructure. Cependant, le chargement s'effectue ici sous contrôle de charge. La fréquence de charge est de 0,5 Hz et le rapport de charge est fixé à R=0,1. Le niveau de contrainte maximal est fixé à $\sigma_{max} = 0.21$ (normalisée) pour limiter les problèmes de convergence du solveur. Dans ce cas, les conditions de chargement sont clairement indiquées avec les résultats.

L'exécution du calcul sous contrôle de charge permet au fluage cyclique de se produire sans être contraint par une contrainte globale imposée.

7.5.2.2 Résultats

La croissance calculée des cavités débute aux extrémités des fibres. Outre les effets de bord, la localisation des dommages calculés est donc cohérente avec les observations expérimentales.

Cependant, notre modélisation ne tient pas compte de l'organisation sphérolitique de la matrice qui joue pourtant un rôle majeur dans l'endommagement par fatigue du polymère semi-cristallin. Cela pourrait aussi expliquer pourquoi, outre les faibles niveaux de contrainte et le faible nombre de cycles de charge, certaines caractéristiques de l'endommagement de la matrice, caractéristiques des dommages sphérolitiques, ne semblent pas correctement modélisées.

La bonne concordance entre les emplacements de l'endommagement, calculés et observés, confirme l'hypothèse selon laquelle le taux de déformation est à l'origine de l'endommagement à l'échelle locale et qu'un modèle basé sur ce paramètre donne des résultats prometteurs.

7.6 Conclusion

Dans ce travail, nous avons d'abord montré la nécessité d'une meilleure compréhension et d'une meilleure modélisation du comportement à la fatigue du polyamide 6,6 renforcé de fibres de verre courtes. L'approche choisie était fondée sur les nombreuses similitudes entre la fatigue et le fluage. En effet, sous un chargement répété avec une contrainte moyenne positive la déformation moyenne augmente progressivement, un phénomène appelé *fluage cyclique*. Comme pour les approches développées pour le fluage, l'accent a été mis sur la vitesse de déformation au cours de l'étape secondaire. Dans le cas du chargement de fatigue, nous avons décidé de l'appeler vitesse de déformation *cyclique*.

À l'échelle macroscopique, nous avons d'abord cherché à améliorer un critère de durabilité pour les éprouvettes lisses en l'étendant aux rapports de charge négatifs. Dans ce cas, nous avons introduit un critère mixte basé sur la vitesse de déformation

cyclique et sur l'énergie anélastique. Il s'est avéré très efficace pour unifier les résultats pour les trois orientations d'échantillons, dans une large gamme de rapports de charge ($-0,5$ à $+0,7$).

L'accent a ensuite été mis sur les éprouvettes entaillées usinées, car les pièces industrielles présentent souvent des géométries complexes. Un critère de fatigue non local a été proposé sur la base de mesures expérimentales de la vitesse de déformation cyclique locale par corrélation d'image. Il s'est avéré efficace pour les trois orientations d'éprouvettes et les deux géométries d'entailles qui ont été testées. Les paramètres d'un modèle de comportement élasto-visco-plastique ont été identifiés afin de capturer correctement les vitesses de fluage cyclique. Cela a permis d'appliquer le critère de durabilité aux modèles d'éléments finis et a donné des résultats prometteurs.

À l'échelle microscopique, nous avons étudié les mécanismes d'endommagement du matériau à l'échelle locale et leurs similitudes avec les observations antérieures faites pour le chargement de fluage. Sur la base d'analyses tomographiques et microscopiques détaillées, nous avons établi un scénario d'endommagement en fatigue pour les thermoplastiques injectés. L'endommagement s'initie le long du noyau orienté, au centre de la structure sphérolitique. Il progresse ensuite vers l'extérieur, dans le plan équatorial, jusqu'à l'ouverture complète de la sphérulite et l'avance de la microfissure.

De plus des modélisation micro-mécaniques ont été réalisées en utilisant les méthodes FFT et EF sur des microstructures réelles segmentées à partir de données tomographiques. Les calculs ont permis d'étudier l'influence de l'orientation des fibres et du taux d'humidité sur les champs mécaniques locaux dans la microstructure. Ils ont également montré que la cavitation croit préférentiellement dans les zones où la vitesse de déformation cyclique est élevée.

Tout au long de ce travail, nous avons donc montré que l'endommagement sphérulitique sous chargement de fatigue présentent de fortes similarités avec l'endommagement par fluage. De plus, nous avons démontré qu'un seul paramètre - le taux de déformation cyclique - est pertinent pour la description des dommages par fatigue et de la durabilité à l'échelle macroscopique et microscopique. L'explication se trouve probablement à l'échelle nanoscopique, à l'origine de la nature visqueuse du polymère, où la vitesse de déformation est directement responsable de l'initiation de l'endommagement lorsque les chaînes polymères ne peuvent plus se réorganiser pour accommoder la déformation.

Pour clôturer ce résumé étendu, il convient de rappeler la nécessité pour les travaux futurs de ne pas omettre l'étude du matériau et de sa microstructure. Beaucoup trop d'études se contentent d'une approche mécanique purement macroscopique, mais la clé d'une bonne compréhension et modélisation d'un matériau aussi complexe ne peut être trouvée que dans une connaissance approfondie de la structure du matériau et de la physique des processus locaux d'endommagement.

Appendix A

Processing of tomographic data

Computed X-ray tomography has been increasingly used in the past decade to gain valuable insight on the internal structure of materials as well as on the deformation and damage process under aging (be it mechanical, environmental, etc.). It might seem - and was sometimes presented as - a turnkey solution, almost a magic tool. While very powerful, this is not the case.

Computed tomography (CT) brings new challenges both in the experimental setup used for in-situ testing and the processing of the acquired data. In this appendix we will give a short outlook on the processing of tomographic data, which is quite a thankless task as it require long hours of image observation and analysis in order to produce the final segmented image.

A.1 The tomographic image

A.1.1 A 3D volume

Computed tomography relies on the reconstruction of a 3D volume from a set of 2D projections. The final reconstructed volume is composed of an array of voxels (*volumetric pixels*) that usually range from a few tens of microns by side down to a few tens of nanometers for the most advanced setups. The usual volume is around 2048 voxels by side, depending on the image sensor used, and the resulting field of view thus thus depends on the voxel size. The image is thus a balance between a large field of view and a good spatial resolution.

Every voxel has a gray level encoded in 8, 16 or 32 bits[1]. This gray level corresponds to the computed local attenuation coefficient of the matter but also to a number of artifacts.

[1] A number of authors (and colleagues!) obtain 16 or 32 bits data using synchrotron tomography and convert it down to 8 bits before processing. They then use a number of advanced algorithms to segment small details in the data, such as micrometric cavities or thin cracks. Maybe it would be more useful to try simpler segmentation algorithm but on the full dynamic range provided by the detector. It requires more powerful computers but segmenting between the 65,536 levels of gray of a 16-bits image is much more precise than in an 8-bits image with only 256 gray levels.

A.1.2 Information and artifacts

Segmentation and analysis of a tomographic image is based on the separation of different phases in the material (defects, inclusions, porosities, etc.). These phases can be distinguished if they do not appear with the same gray level on the image, i.e. if they have a distinct attenuation coefficient for X-rays, i.e. if their chemical composition is different enough.

However, besides the useful information regarding the material, the reconstructed image also contains a number of artifacts. They are often extensively described in the medical literature, where for clinical CT these artifacts "may obscure or simulate pathology" [1]. They include: noise, beam hardening, scatter, pseudoenhancement, motion, cone beam, helical, rings, and metal artifacts.

For material science the relevant artifacts that are usually considered are: noise, rings, beam hardening and phase contrast. Other artifacts can also appear during the reconstruction of the tomographic data. A good introduction with many illustrated example can be found in the work of Davis [2].

Like for any imaging technique, noise is due to the low number of particles hitting the sensor, resulting in random brighter and darker voxels, even in an homogeneous material. Noise can make proper segmentation difficult, especially when analyzing small objects in the material like small cavities close to the voxel size.

Rings artifacts are caused by a defective or miscalibrated element on the detector. They result in distinctive rings centered on the center of rotation of the sample.

Beam hardening is observed when using polychromatic X-ray sources. As the X-ray passes through the material, low energy X-ray photons are attenuated more easily than the remaining high energy photons. Beam transmission therefore does not follow a simple exponential decay as would be obtained with a monochromatic X-ray source. Filtering the incident beam can filter the low-energy photons and reduce the artifact.

Phase contrast is observed when using synchrotron tomography where the light source is coherent. As the beam passes through the sample it encounters interfaces where the phase of the wave changes. In the output beam, if the distance to the detector is high enough, the out-of-phase rays will interfere and cause distinctive artifacts. This phase contrast can be very useful and intended, but can also lead to difficulties in the segmentation of thin interfaces (e.g. fatigue cracks in metals).

Although some of these artifacts can be removed or mitigated during acquisition or reconstruction, the acquired image still needs to be filtered in order to properly segment the useful information.

A.2 Usual filtering and segmentation tools

A.2.1 Denoising

Reducing the impact of the noise on the segmentation of the image is the most important filtering step. A large number of denoising algorithms can be found in the

image-processing literature [3] and are implemented in the usual image processing. The most typical is probably the simple median filter.

The median filter consists in replacing the value for a given voxel by the median value of neighboring voxels. The nature (shape, size) of neighboring region considered (called the *window*) cans be adjusted.

The use of a median filter greatly improves an image with high level of noise by smoothing the gray levels. It is worth noting that the median filter is quite effective in preserving the edges in the image while performing the denoising. This is particularly important in order to avoid degrading the imaging of the interfaces in the material.

A.2.2 Thresholding

Thresholding is the most common way to segment an image. By placing various thresholds on the gray levels, every voxel can be affected to a certain phase. The choice of these thresholds is thus important and influences the outcome of the process.

Cosmi [4] proposed to set the threshold separating glass fibers from a polyamide matrix by imposing that the segmented volume fraction of each phase matches the known composition of the material. They the use a threshold value based on the staistical distribution of gray levels in the matrix in order to segment the micro-voids.

Rolland [5] set the different threshold values based on a visual analysis of the histograms. In this work, thresholding was performed in a similar manner but mostly based on our experience in analyzing CT data to determine the appropriate threshold value for a given batch of scans.

A.2.3 Morphological operations

Once a binary image is obtained after segmentation, morphological operation can be applied in order to *clean* or *repair* the data before analysis. Basics operators in binary morphology are: erosion, dilation, opening and closing. They all rely on the choice of structuring element.

The structuring element act as a probe that scans the image, and check how this element fits or misses the shapes in the image. Typical structuring elements are 3x3 square and a simple cross (in $\mathbb{Z}^2$) or a disk of a given radius (in $\mathbb{R}^2$). Extension to the 3^{rd} dimension is direct by using cubes, spheres, etc.

Erosion of a binary image by a given structuring element produces a new binary image with 1 in all locations of a structuring element's origin where it fits the input image, and 0 otherwise. Erosion shrinks the image, removing a layer of pixels from the boundaries of regions. The holes and gaps between different regions become larger, and small details are eliminated.

The dilation by a structuring element produces a new binary image with 1 in all locations of a structuring element's origin where that structuring element hits the input image, and 0 otherwise. Dilation adds a layer of pixels to the boundaries of regions.

Holes enclosed by a single region and gaps between different regions become smaller, and small intrusions into boundaries of a region are filled in.

Opening is an erosion followed by a dilation. It can open up a gap between objects connected by a thin bridge of pixels, hence its name. Opening is thus useful to separate two fibers still bound by a few voxels.

Closing is a dilation followed by an erosion. It can fill holes in the regions while keeping the initial region sizes. Closing is thus useful to remove small holes in a fiber due to improper segmentation.

A.3 Analysis tools

A.3.1 Quantitative analysis

Quantitative analysis of segmented data can be performed in a number of different ways depending on the object studied. Typical analysis for short fiber reinforced materials is to compute the position, orientation and morphology of the segmented fibers.

First step is thus to *label* the binary image, i.e. to group adjacent voxels into a single object. Adjacency can be defined as a contact between faces only, faces and edges, or faces, edges and vertices, giving 6, 18 or 26 neighbors for a given voxel.

Analysis is then performed on every of the identified label in order to compute the desired information such as position of the barycenter, spatial orientation, length, aspect ratio, etc.

Similar analysis can for example be performed on damage markers such as segmented cavities, to follow the growth of damage during an in-situ test.

It is worth noting that some quantitative analysis can also be performed on the tomographic data without segmentation as for example when performing Digital Volume Correlation.

A.3.2 Toward numerical modeling

The step between the tomographic data and numerical modeling is far from being trivial when wanting to perform finite element computation on a real microstructure[2]. Obtaining a proper mesh requires to clean the data from any unwanted imperfection (e.g. badly segmented voxel). Element size in the mesh should be refined enough to properly model the microstructure while still allowing for a fast enough computation.

In our case the surfaces of the segmented fibers were extracted in the Avizo software and remeshed using the available tools. The surfacic mesh was then exported to Gmsh for 3D meshing of the microstructure. Final export was made to ZebuLon for FE computation.

[2]This step is far easier when performing FFT modeling that precisely relies on a binary desciption of the microstructure in a voxel grid.

This kind of computation yield precious information as results can be compared directly with experimental tomographic data. Yet they bring an number of challenge in meshing the microstructure and in the boundary conditions of this non-periodic region of interest.

A.4 Bibliography

[1] F. E. Boas and D. Fleischmann, "CT artifacts: Causes and reduction techniques," *Imaging Med.*, vol. 4, pp. 229–240, 2012. II

[2] G. R. Davis and J. C. Elliott, "Artefacts in X-ray microtomography of materials," *Materials Science and Technology*, vol. 22, no. 9, pp. 1011–1018, 2006. II

[3] A. Buades, B. Coll, J.-m. Morel, and J.-m. M. A, "A review of image denoising algorithms , with a new one .," *Multiscale Modeling and Simulation: A SIAM Interdisciplinary Journal, Society for Industrial and Applied Mathematics,*, vol. 4, no. 2, pp. 490–530, 2005. III

[4] F. Cosmi and C. Ravalico, "Threshold identification for micro-tomographic damage characterisation in a short-fibre-reinforced polymer," *Strain*, vol. 51, no. 3, pp. 171–179, 2015. III

[5] H. Rolland, N. Saintier, P. Wilson, J. Merzeau, and G. Robert, "In situ X-ray tomography investigation on damage mechanisms in short glass fi bre reinforced thermoplastics : Effects of fibre orientation and relative humidity," *Composites Part B*, vol. 109, pp. 170–186, 2017. III

Appendix B

Molecular dynamics

The Molecular Dynamics (MD) simulations that were presented in the conclusion of this thesis were performed a bit on the side of the main research project for two reasons. First, I felt it gave a good, physics-based, explanation on why the cyclic-strain rate drives the durability of polymers. Second, it was pretty interesting to spend a bit of time doing some literature review on the topic, and quite fun to give it a try!

B.1 The force field

In order to compute movement of the atoms in an MD simulation, we have to iteratively solve Newton's second law of motion [1].

Forces can be calculated using quantum physics (*ab initio* MD) or from a set of empirical inter-atomic potentials called a force field (the classical approach that we will use). Various types of force fields have been proposed for different specific types of MD simulations [2] to describe the interactions between atoms.

These can be bonded or non-bonded (distance) interactions. A schematic of basic interactions is given in fig. B.1. The simpler the molecule, the less types of bonds and interactions the model will have to account for.



(a) Bond stretch (b) Bond bend (c) Bond torsion (d) Bond inversion



(e) Van der Vaals (f) Electrostatic (g) Hydrogen bond

Figure B.1: Bonded (figs. B.1(a) to B.1(d)) and non-bonded (figs. B.1(e) to B.1(g)) interactions between atoms.

In our case the generic DREIDING force field [3] was used:

$$\underbrace{E}_{\text{Potential Energy}} = \underbrace{E_{val}}_{\text{Valence interactions}} + \underbrace{E_{nb}}_{\text{Non-Bonded interactions}} \tag{B.1}$$

With:

$$\underbrace{E_{val}}_{\text{Valence interactions}} = \underbrace{E_B}_{\text{Bond stretch}} + \underbrace{E_A}_{\text{Bend}} + \underbrace{E_T}_{\text{Torsion}} + \underbrace{E_I}_{\text{Inversion}} \tag{B.2}$$

$$\underbrace{E_{nb}}_{\text{Non-Bonded interactions}} = \underbrace{E_{vdw}}_{\text{VdW}} + \underbrace{E_Q}_{\text{Electrostatic}} + \underbrace{E_{hb}}_{\text{Hydrogen Bonds}} \tag{B.3}$$

And:

$$E_B = \frac{1}{2}\, k_e\, (R - R_e)^2 \tag{B.4}$$

$$E_A = E_{IJK} = \frac{1}{2}\, C_{IJK}\, (\theta_{IJK} - \theta_J)^2 \tag{B.5}$$

$$E_T = \sum_n A_n \cos^{n-1}(\varphi) \tag{B.6}$$

$$E_I = E^d_{IJK} = \frac{1}{2}\, C_I\, (\cos\psi - \cos\psi_I)^2 \tag{B.7}$$

$$E_{vdw} = A\, R^{-12} - B\, R^{-6} \tag{B.8}$$

$$E_Q = 322.0637\, \frac{Q_i Q_j}{\varepsilon R_{ij}} \tag{B.9}$$

$$E_{hb} = D_{hb}\, [5(R_{hb}/R_{DA})^{12} - 6(R_{hb}/R_{DA})^{10}] \cos^4(\theta_{DA}) \tag{B.10}$$

B.2 The PE model

The model for calculations is based on the work and online tutorials by Tschopp [4]. The model for amorphous bulk PE contained 10 polymer chains with 1000 CH_2 pseudo-atoms each. The use of pseudo-atoms limits the type and number of interactions to take into account.

Parameters used for the model are given in table B.1.

Stretch	$k_e = 350$	$R_e = 1.53$		
Bend	$C_{IJK} = 60$	$\theta_J = 109.5$		
Torsion	$A_1 = 1.73$	$A_2 = -4.49$	$A_3 = 0.776$	$A_4 = 6.99$
Van der Waals	$A = 0.112$	$B = 4.01$	$L_{cut} = 10.5$	

Table B.1: DREIDING force field parameters for PE.

At first an equilibration sequence is performed to relaxes any high energy configurations due to initial arbitrary positioning of the atoms. The sequence is composed of four steps [4]. The simulation is first run for 10,000 timesteps ($\Delta t = 1fs$) using NVT[1] dynamics at 500 K. Next step is a relaxation for 50,000 timesteps ($\Delta t = 0.5fs$) using NPT dynamics at 500 K. Following computations in NPT dynamics cool the structure down to 100K (the temperature at which calculation will be later performed) for 50,000 timesteps and further relax the system for 50,000 timesteps at the same temperature.

The system is then deformed under a uniaxial at an imposed strain rate with a zero-pressure condition for the two lateral simulation cell faces.

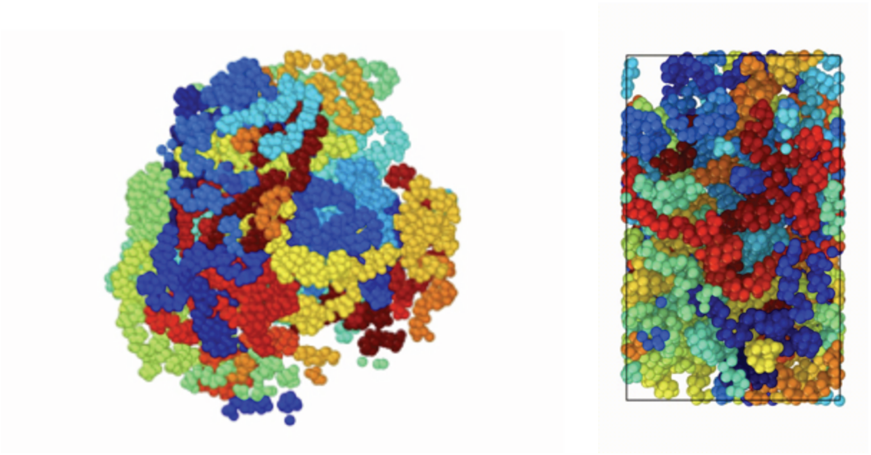
B.3 For a PA66 model

B.3.1 A full model of the polymer chain

The PA66 polymer chain is more complex than the PE. A blunt way to perform MD calculation on a PA66 polymer chain would be to model the entire structure of the polymer, with 38 atoms in the monomer, 5 types of bonds, 20 types of angles, 12 types of dyhedral angles, and non-bonding interaction including hydrogen bonds. It requires thus the appropriate data on the different types of bonding and interaction to be available in the literature.

A preliminary test using LAMMPS was performed with the physical parameters of the polymer chain given by Colclough [5] and Dasgupta [6]. It proved effective in modeling a random coil of polymer chains (fig. B.2(a)). However some issues appeared at the upper and lower boundaries when the volume is strained (fig. B.2(b)), and more work would be needed to obtain a fully operational model.

[1] NVT and NPT are the formal designations for two ensembles and acronyms for the system variables that are regulated or conserved in each case. These variables are particle number (N) usually constant, volume (V), pressure (P) and temperature (T). In NVT, T is regulated via a thermostat, here a Langevin thermostat. Whereas for NPT pressure is usually controlled using a piston.



(a) Random coil (b) Tensile test

Figure B.2: MD calculation of a PA66 model with 50 polymer chains and 5 monomers per chain.

B.3.2 A coarse-grain approach

Similar to what was used for PE CH_2 pseudo-atoms, it would be possible to use a coarse-grain (CG) approach in order to reduce the complexity of the problem.

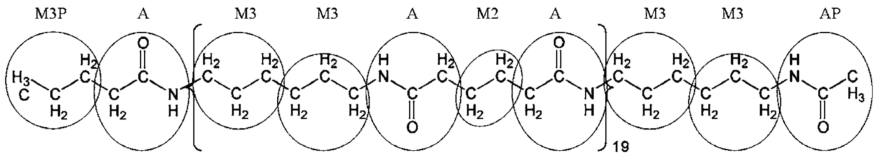


Figure B.3: Mapping between atomistic and CG models of PA66. The circles denote which atoms are joined into CG beads. From Karimi-Varzaneh [7].

I have not attempted a CG approach on PA66 but it would probably be the way forward. However caution should be taken in order to properly model the complex interaction of the polymer chain, especially the hydrogen bonding. The work of Karimi-Varzaneh [7] introduces an algorithm to reinsert the atomistic details neglected in the CG description and thus accounting for these interactions, crucial to the properties of the material.

B.4 The time-scale in MD calculations

Time scales in MD calculations are very limited with time steps around the femtosecond. Imposed strain rates are thus huge (around $10^{10}s^{-1}$). Any conclusion should thus be made with caution, especially for polymers where time is such an important factor in the behavior of the material.

B.5 The choice of boundary conditions

Usually MD simulations are performed on simple loading cases (tension, shear...). However if we want to model the loading conditions seen by a small volume of matter in the semi-crystalline, we need to model a more complex multiaxial loading. The question thus arises -and I don't have the answer- of what would be a good set of boundary conditions.

Once again this would probably require to gain a good understanding of the 3D structure of the spherulite.

B.6 Bibliography

[1] I. Newton, *Philosophiae naturalis principia mathematica*. 1687. VII

[2] J. P. Ewen, C. Gattinoni, F. M. Thakkar, N. Morgan, H. A. Spikes, and D. Dini, "A comparison of classical force-fields for molecular dynamics simulations of lubricants," *Materials*, vol. 9, no. 8, pp. 1–17, 2016. VII

[3] S. L. Mayo, B. D. Olafson, and W. A. Goddard, "DREIDING: A generic force field for molecular simulations," *Journal of Physical Chemistry*, vol. 94, no. 26, pp. 8897–8909, 1990. VIII

[4] M. A. Tschopp, J. L. Bouvard, D. K. Ward, and M. F. Horstemeyer, "Atomic Scale Deformation Mechanisms of Amorphous Polyethylene under Tensile Loading," *Supplemental Proceedings: Materials Fabrication, Properties, Characterization, and Modeling*, vol. 2, pp. 789–794, 2011. IX

[5] M. L. Colclough and R. Baker, "Polymorphism in nylon 66," *Journal of Materials Science*, vol. 13, no. 12, pp. 2531–2540, 1978. IX

[6] S. Dasgupta, W. B. Hammond, and W. A. Goddard, "Crystal structures and properties of nylon polymers from theory," *Journal of the American Chemical Society*, vol. 118, no. 49, pp. 12291–12301, 1996. IX

[7] H. A. Karimi-Varzaneh, P. Carbone, and F. Müller-Plathe, "Fast dynamics in coarse-grained polymer models: The effect of the hydrogen bonds," *Journal of Chemical Physics*, vol. 129, no. 15, pp. 1–11, 2008. X, XIX

List of Figures

1.1 Injection molding process. 9
1.2 Structure of spherulites in a semi-crystalline thermoplastic as usually described. 10
1.3 Spiral growth of spherulite. 11
1.4 PA610 spherulites as observed using cross-polarized microscopy. From Magill [29]. 12
1.5 Shish-kebab structure in semi-crystalline thermoplastics. 13
1.6 Heterogeneous fiber orientation in an injection molded plate. From Rolland [43]. 15
1.7 Fiber-matrix interface in fiber reinforced polymers. 16
1.8 Specimen orientation in an injection molded plate. 17
1.9 Results from tensile testing for different specimen orientations. From Bernasconi [50]. 18
1.10 Results from fatigue testing for different specimen orientations - RH50, R=0.1, 4Hz. From Bernasconi [50]. 19
1.11 Fatigue cracks in 0°, 45° and 90° notched specimens of under R=0.1. From Tanaka [51]. 19
1.12 Schematics of fatigue crack propagation mechanisms. 20
1.13 Haigh diagram: Relationship between stress amplitude σ_a and mean stress σ_m, with modified Gerber equation. From Mallick [52]. 21
1.14 Effect of loading frequency in fatigue life. 0° specimens, R=0.1. From Zhou [58]. 21
1.15 Influence of temperature on the S-N curves of RH0 PA66GF33. From Handa [60]. 22
1.16 Model of displacement of sorbed water in PA6. From Puffr [62]. A. Dry amorphous polyamide. B. Wet polyamide at saturated vapor pressure: 1, firmly bound water; 2, loosely bound water; 3, sites for capillary condensed water. 23
1.17 S-N curves for PA66GF30, R=-1, f=10Hz, T=23°C. From Barbouchi [66]. 23
1.18 Influence of the spherulite size on the material properties. 26

1.19 Schematic diagrams of Point, Line, and Area methods in TCD. From Luo [74]. 27
1.20 Influence of notches on the fatigue strength of PA66GF35. From Sonsino [75]. 28
1.21 Schematic of a typical evolution of the cyclic strain and cyclic strain rate during fatigue loading, with controlled load. (For cyclic loading with controlled displacement, cyclic stress relaxation would be observed). 29
1.22 Usual mechanical parameters. 30
1.23 Study on tubular and dogbone specimens. From Launay [86]. 32
1.24 Comparison between experimental and assessed fatigue lives using a Principal Stress criterion on PBT-PET GF30 specimens at R=0.1. From Klimkeit [83]. 33
1.25 Equivalent stress amplitude vs. fatigue life for PBT and PA6 specimens at various temperatures - R=-1 - 0°, 18°, 45°, 90°. From Fatemi [56]. . 33
1.26 Study of PA66GF30 specimens - RH50 - f = 3Hz - forced convection. From Rolland [43] 36
1.27 Section of polyethylene after fatigue showing "many inter-spherulitic cracks". From Andrews [79]. 40
1.28 Spherulitic creep damage mechanisms. 41
1.29 Damage at fiber tip and fiber failure as observed during in situ microtomography tensile testing. From Rolland [104] 42
1.30 Failure mechanisms in fatigue. From Horst [37] 43
1.31 Fatigue damage mechanisms as observed by synchrotron tomography. . 43
1.32 Microcracks observed by micro-tomography and proposed damage mechanism as a function of spherulite organization - RH50 - 0° specimen - $N_f = 2468$ cycles. From Rolland [26]. 44
1.33 Creep rate vs. Applied stress. Adapted from Selles [103]. 46
1.34 Computed void volume fraction for PA6 axisymmetric specimens. From Selles [103] 48
1.35 Plot of the von Mises stress along a fiber. From Klimkeit [121]. 50
1.36 Deformations at the fiber end. Overall imposed strain are indicated. From Horst [37]. 51
1.37 Comparison between X-Ray CT micrograph (a-c) and reconstructed model in the FEM code (b-d). Arrows indicate the direction of maximum principal stress during tensile loading. From Belmonte [122]. . . 51
1.38 Comparison of the crazing criterion with the damage observed by tomography. Tensile test on a 45° RH50 specimen. From Rolland [43]. . 52
1.39 Snapshot during an crystallization of a polymer (upper row) and numerical simulation of the crystallization process using the multi-phase field method (lower row). In the simulation initial germs are located identically to the the experimentation. From Gong [130]. 53
1.40 Different spherulite models, loading direction is vertical. 55

2.1 Fiber length and orientation distribution in the composite material. From Rolland [1]. 68

2.2 Segmented fibers at the center of a 0° specimen as observed using synchrotron tomography. The core layer is visible, but only part of the shells can be seen in the field of view. 68
2.3 Spherulites in PA66 observed using polarized light microscopy on thin slices obtained by microtomy. 69
2.4 Spherulites observed using polarized light microscopy on thin slices of reinforced PA66 obtained by microtomy. 70
2.5 Position of the specimens in the plates. Note that they are the same for smooth and notched specimens. 71
2.6 Geometry for smooth specimens. 72
2.7 Dimensions of notched specimens, stress concentration factor K_T and stress triaxiality ratio η (see definitions given in section 2.2.1.4). 73
2.8 Experimental setup for fatigue testing. 74
2.9 Timed image acquisition with fatigue loading. 75
2.10 Position of the virtual extensometer on a notched U2 specimen for NOD measurement. 76
2.11 Example of the *cyclic strain* measurement for cyclic-creep evaluation during fatigue loading. 77
2.12 Experimental setups for in-situ testing, on the PSICHE beamline. . . . 78
2.13 Transmission polarized light microscopy. 79
2.14 Secondary electron imagery in SEM. 80
2.15 Micro-tomography. 82
2.16 Atomic Force Microscopy. 82

3.1 Damage at fiber ends and crazing - RH50 - 0° specimen - $N_f = 2468$ cycles. Cavitation is evidenced by arrows. From ROLLAND [1]. 86
3.2 Fiber failure induced by the proximity of a crossing fiber in the shell - U2 0° specimen - RH50 - f=0.5Hz - R=0.1 - Normalized $\sigma_{max} = 0.54$ - $N_f = 6206$. 86
3.3 Sequence of fibre failure as observed by microtomography. Note how difficult it can be to determine if, where and when adjacent fibers are actually in contact. 87
3.4 Evidences of contact inducing damage and failure of fibers during fatigue loading - U2 0° specimen - RH50 - f=0.5Hz - R=0.1 - Normalized $\sigma_{max} = 0.54$ - $N_f = 6206$. 87
3.5 Cavity distribution by diameter as obtained by various methods. 88
3.6 Detail view of cavitation ahead of crack tip in neat PA66 - U0.5 specimen - RH50 - f=0.5Hz - R=0.1 - Normalized $\sigma_{max} = 0.30$ - $N_f = 2123$. . . . 89
3.7 Early stage of debonding at the interface, seen here at $N/N_f = 20.3\%$ in a RH50 0° specimen - $N_f = 2468$. Note how difficult it can be to distinguish debonding from the phase contrast at the fiber-matix interface. 89
3.8 Damage at the interface along a transversely broken fiber after fatigue loading - 0° specimen. 90
3.9 Damage at the interface around broken fibers after fatigue loading - 0° specimen. 90

3.10 Crack tip in a 0° PA66GF30 specimen as observed by microtomography - f=3Hz - RH50 - Normalized $\sigma_{max} = 0.69$ - $N = 2462$. 91
3.11 Geometries and S-N curves for the notched specimens. 92
3.12 Tomographic observation and segmentation of the crack tip in a PA66 notched specimen, test interrupted at 4221 cycles and 90% of estimated fatigue life. 94
3.13 Crack tip in a PA66 notched specimen as observed by microtomography, test interrupted at 2531 cycles and 95% of estimated fatigue life. 95
3.14 Short cracks in a 45° PA66GF30 smooth specimen as observed by microtomography, test interrupted at 1500 cycles and 98% of estimated fatigue life. 95
3.15 Advance of the crack tip, segmented in a RH50 0° specimen and viewed in the plane orthogonal to the loading direction. 96
3.16 Fracture surface of a notched PA66 specimen after fatigue testing - Normalized $\sigma_{max} = 0.29$ - $N_f = 917$. 97
3.17 SEM fractography of a notched PA66 specimen ($N_f = 917$). 98
3.18 Spherulitic damage ahead of the fatigue crack in a notched U0.5 PA66 specimen after cryofractography, test interrupted at 4221 cycles and 90% of estimated fatigue life. 99
3.19 Schematic of the influence of the spherulitic structure of the polymer on fatigue crack advance. 100
3.20 Orientation of the 40 nuclei observed on 3 different PA66 specimens after fatigue testing. 101
3.21 SEM observations of the nuclei for three different specimens orientation ($N_f \approx 1500$). 101
3.22 Oriented spherulitic structure induced by the injection molding. 102
3.23 SEM fractography a notched "tomo" PA66 specimen - $N/N_f = 73\%$ - f=0.5Hz - Normalized $\sigma_{max} = 0.36$. 103
3.24 Complementary SEM fractography of a notched "tomo" PA66 specimen showing damage initiating from the nucleus - $N/N_f = 73\%$ - f=0.5Hz - Normalized $\sigma_{max} = 0.36$. 103
3.25 Fatigue damage progress in oriented spherulite. 103
3.26 SEM fractography a notched U0.5 90° PA66GF30 specimen - f=0.5Hz - Normalized $\sigma_{max} = 0.34$ - $N_f = 24565$. 105

4.1 Evolution of the mean strain for several load ratios and fatigue lives on smooth 0° PA66GF30 specimens - RH50 - f = 3Hz - forced convection. 108
4.2 Estimated fatigue life using eq. (4.1) vs. experimental number of cycle to failure on smooth PA66GF30 45° specimens - f = 0.5Hz - free convection. Scatter band of factor 2 is marked in dashed lines. 109
4.3 Analysis to establish a relationship between the number of cycle to failure N_f, the anelastic energy W_{an} and the cyclic strain rate $\dot{\varepsilon}_{cycl}$ - RH50 specimens - f = 3Hz - forced convection - all fiber orientations. 110

4.4 Estimated fatigue life using eq. (4.4) vs. experimental number of cycle to failure - RH50 specimens - f = 3Hz - forced convection - all fiber orientations. Scatter bands of factor 2 and 10 are marked in dashed and dotted lines respectively. . . . 111
4.5 Weight function f for various values of the parameter γ. . . . 112
4.6 Weight function f and estimated fatigue life using the mixed criterion [eq. (4.7)] for all fiber orientations. Scatter bands of factor 2 and 10 are marked in dashed and dotted lines respectively. . . . 113
4.7 Relative error on N_f using the mixed criterion eq. (4.7) identified on various datasets. . . . 114
4.8 Relative error on N_f using several criteria. . . . 116
4.9 Quasi-static tensile tests for notched PA66 specimens. Note that U2 and U0.5 refers to the notch geometry as defined in fig. 2.7. . . . 117
4.10 Nominal stress vs. notch opening factor . . . 117
4.11 Tomographic slice of a notched "tomo" PA66 specimens during in-situ quasi-static tensile testing, at $\dot{\varepsilon} = 10^{-3}s^{-1}$. . . . 118
4.12 Tensile test on notched PA66GF30 specimens at $\dot{\varepsilon} = 10^{-3}s^{-1}$. . . . 119
4.13 S-N curves for PA66 notched specimens. . . . 120
4.14 Cyclic strain evolution and local strain rate as measured by timed DIC in a PA66 specimen - U0.5 notch - Normalized $\sigma_{max} = 0.26$. . . . 120
4.15 Fatigue damage in a "tomo" notched PA66 specimen as observed by micro-tomography. . . . 121
4.16 Segmented fatigue cracks in 3 interrupted notched "tomo" PA66 specimens as observed by micro-tomography - Number corresponds on the number of applied loading cycles before the test was interrupted for tomographic imaging - Normalized $\sigma_{max} = 0.36$. . . . 122
4.17 SEM fractography of a notched U0.5 PA66 specimen - $N_f = 917$. . . . 122
4.18 S-N curves for notched reinforced PA66 specimens. . . . 123
4.19 Maximum principal cyclic strain rate as measured on the surface of the specimens by timed DIC. . . . 124
4.20 Maximum principal cyclic strain rate between notched at $N_f/2$. . . . 124
4.21 Tomographic evaluation of fatigue damage in a notched "tomo" 0° specimen - Normalized $\sigma_{max} = 0.60$. . . . 126
4.22 Identification of several fatigue criteria for notched PA66GF30 specimens - R=0.1 - 0.5 Hz. Scatter band of factor 2 is marked in dotted lines. . . . 128
4.23 Finite-element model. . . . 130
4.24 Normalized stress vs. NOD for a U2 notched PA66 specimen during tensile testing. . . . 131
4.25 Shell-Core geometry and stress-strain curves for U2 notched PA66GF30 specimens during tensile testing at $\dot{\varepsilon} = 10^{-3}s^{-1}$. . . . 132
4.26 Cyclic loading of a notched U2 PA66 specimen with parameters from the quasi-static loading identification and the readjusted parameters for improved cyclic strain rate calculation - f=0.5Hz - R=0.1 - Normalized σ_{max}=0.36. . . . 133

4.27 Global axial cyclic strain rate for notched PA66 specimens (R=0.1 - f=0.5Hz), determined experimentally from the crosshead displacement and the top surface displacement in the numerical model. 134
4.28 Global axial cyclic strain rate for notched PA66GF30 specimens. 135
4.29 Profile of the axial cyclic strain rate between notches during at $N = N_f/2$. 136
4.30 Notch opening rate for notched PA66 specimens. 136
4.31 Process to plot local cyclic strain rate maps, here on a U2 specimen. . . 137
4.32 Axial cyclic strain rate fields measured at $N = N_f/2$ and calculated at the corresponding number of computed cycles. 138
4.33 Principal cyclic strain rate in composite specimens - U2 notch - Normalized $\sigma_{max} = 0.36$. 138
4.34 Principal cyclic strain rate in a 0° specimen during the secondary stage of cyclic creep - U2 notch - Normalized $\sigma_{max} = 0.36$. 139
4.35 Computed void volume fraction f in a notched PA66 "tomo" specimen - Normalized $\sigma_{max} = 0.36$. 140
4.36 Computed void volume fraction f and corresponding tomographic slice. Notched PA66 "tomo" specimen - Normalized $\sigma_{max} = 0.36$. 140
4.37 Cyclic strain rate and computed void volume fraction after 500 loading cycles in notched "tomo" specimens - Normalized $\sigma_{max} = 0.36$. 141
4.38 Comparison between computed N_f and experimental values. 142

5.1 Fiber segmentation from micro-tomography data. Slicing is made perpendicularly to the fiber direction. 146
5.2 Example of segmented microstructure for FFT micro-modeling. 147
5.3 Boundary conditions for FFT and FE modeling. 149
5.4 Strain rate distribution in the matrix and sensitivity of the matrix model to the imposed macroscopic strain rate - FFT modeling. 150
5.5 Experimental stress-strain curves *vs.* microstructure calculation - FFT modeling. 151
5.6 Local mechanical fields distribution in the matrix for different RH and fiber orientation at iso-macroscopic axial strain $\varepsilon = 3.6\%$ after loading at $\dot{\varepsilon} = 10^{-4}s^{-1}$ - FFT modeling. 152
5.7 Study of a short glass fiber failure - FFT modeling. 154
5.8 Modeling voiding at fiber end by an extra phase with degraded properties - FFT modeling. Small oscillations in the computed fields come from an aliasing effect as the conditions of the Nyquist-Shannon are not formally respected (high contrast between the phases). 155
5.9 Results for monotonic tensile loading of a RH 50 - 0° specimen at $\dot{\varepsilon} = 10^{-4}s^{-1}$ until a global strain of $\varepsilon = 3.6\%$- FFT modeling. 156
5.10 Hydrostatic stress in two microstructures after quasi-static loading at $\dot{\varepsilon} = 10^{-4}s^{-1}$ until a global strain of $\varepsilon = 3.6\%$. At this imposed strain, different stresses are reached depending on the fiber orientation. 157
5.11 Cavitation in a RH50 90° specimen after 2500 loading cycles - 3Hz - R=0.1 - Normalized $\sigma_{max} = 0.37$, and computed stress triaxiality ratio. 158
5.12 Calculation of the local cyclic strain rate. 159

5.13 Cartography of $\frac{\Delta\varepsilon_{11}}{\Delta N}_{max}$, with the locations of the cavities observed on the corresponding tomographic slice, in a RH 50 - 45° specimen - FFT modeling. 160
5.14 Example of segmentation using the Weka machine learning algorithm. . 161
5.15 Example of meshed microstructures for FE modeling. 162
5.16 Cyclic strain evolution for FE microstructure modeling - 0° - RH50 - R=0.1 - f=0.5Hz - Normalized $\sigma_{max} = 0.21$. 163
5.17 Calculated void volume fraction after 10 loading cycles at a normalized $\sigma_{max} = 0.21$ overlaid on the corresponding tomographic slice, in a RH50 - 0° specimen after 1500 loading cycles at a normalized $\sigma_{max} = 0.69$ - FEM modeling. 165
5.18 Calculated void volume fraction at a normalized $\sigma_{max} = 0.21$ overlaid on the corresponding tomographic slice, in a RH 50 - 0° specimen after 1500 loading cycles at a normalized $\sigma_{max} = 0.69$ - FEM modeling. . . . 166

6.1 S-N curves for normal and nucleated matrix in composite material specimens. 171
6.2 AFM imaging of a fatigue fracture surface in PA66. 172
6.3 Influence of the exposition to synchrotron radiation on the failure mode of PA66 under cyclic loading. 174
6.4 Molecular dynamics tensile test on amorphous PE at different imposed strain rates. 10 polymer chains, 1000 atoms per chain. 175

B.1 Bonded (figs. B.1(a) to B.1(d)) and non-bonded (figs. B.1(e) to B.1(g)) interactions between atoms. VIII
B.2 MD calculation of a PA66 model with 50 polymer chains and 5 monomers per chain. X
B.3 Mapping between atomistic and CG models of PA66. The circles denote which atoms are joined into CG beads. From Karimi-Varzaneh [7]. . X

Fatigue-fluage du Polyamide 6,6 renforcé

RESUMÉ: Ce travail vise à compléter la description et la compréhension actuelles du comportement en fatigue et des mécanismes d'endommagement des polymères thermoplastiques renforcés de fibres de verre courtes.

Après une revue de l'état de l'art, le travail se concentre sur l'évaluation des mécanismes d'endommagement fatigue dans le composite tels qu'observés par micro-tomographie et microscopie. Afin de mieux comprendre les mécanismes d'endommagement de la matrice du composite, des observations supplémentaires sont effectuées sur le polymère et mettent en évidence un scénario complet de l'endommagement intra-sphérolitique sous chargement de fatigue. Le calcul de microstructure est utilisé pour compléter cette approche et améliorer la compréhension des mécanismes d'endommagement grace au calcul de champs mécaniques locaux. En se basant sur les similitudes entre les mécanismes d'endommagement en fatigue et ceux observés en fluage, un modèle d'évaluation de la durée de vie en fatigue basé sur la vitesse de déformation cyclique est proposé. Il s'avère très efficace pour unifier les durée de vie en fatigue du composite dans une large gamme de conditions de chargement, y compris l'effet du rapport de charge R, l'effet de fréquence, l'effet d'orientation des fibres et l'humidité. Le critère proposé est également adapté pour application aux échantillons entaillés et donne des résultats prometteurs.

Mots-clés: Endommagement en fatigue, Matériau composite, Endommagement intra-sphérolitique, Critère de fatigue, Modélisation de la microstructure

Cyclic-creep of reinforced Polyamide 6,6 under fatigue loading

ABSTRACT: This work aims at completing the existing description and understanding of the fatigue behavior and damage mechanisms of short-glass fibers reinforced thermoplastic polymers.

After a state of the art review the work focuses on the evaluation of fatigue and quasi-static damage mechanisms in SFRP as observed by micro-tomography and microscopy. In order to fully address the polymer damage mechanisms additional observations are performed on the neat polymer matrix and evidence a full scenario of intra-spherulitic fatigue damage growth. Microstructure modeling is used to complete the understanding of damage mechanisms accordingly to local mechanical fields. Based on the similarities of fatigue damage mechanisms with those observed for creep loading, a fatigue life assessment model based on the cyclic strain rate is introduced. It proved very effective at unifying the SFRP fatigue behavior over a wide range of loading conditions including R ratio effect, frequency effect, fiber orientation effect and humidity. The proposed criterion is also adapted for application to notched specimens and yielded promising results.

Keywords: Fatigue damage, Composite material, Spherulitic damage, Fatigue criterion, Microstructure modeling



Arts et Métiers Institute of Technology

ParisTech
INSTITUT DES SCIENCES ET TECHNOLOGIES
PARIS INSTITUTE OF TECHNOLOGY